Energy flux paths and air-water exchange in freshwater ecosystems

by Sofya Guseva

from Moscow, Russia

Accepted dissertation thesis for the partial fulfillment of the requirements for

the degree of Doctor of Natural Sciences

Fachbereich 7: Natur- und Umweltwissenschaften

Universität Koblenz-Landau

Thesis examiners:

Prof. Dr. Andreas Lorke

Prof. Dr. Alfred Johny Wüest

07 October 2022

Publications

This dissertation is based on the following manuscripts and publications (ordered by date of publication or submission):

1. Guseva, S., Aurela, M., Cortés, A., Kivi, R., Lotsari, E., MacIntyre, S., Mammarella, I., Ojala, A., Stepanenko, V., Uotila, P., Vähä, A., Vesala, T., Wallin, M. B., & Lorke, A. (2021). Variable physical drivers of near-surface turbulence in a regulated river. *Water Resources Research*, 57, e2020WR027939. doi: https://doi.org/10.1029/2020WR027939.

2. Guseva, S., Casper, P., Sachs, T., Spank, U., & Lorke, A. (2021). Energy flux paths in lakes and reservoirs. *Water*, 13(22), 3270. *MDPI AG*. doi: http://dx.doi.org/10.3390/w13223270.

3. Guseva, S., Armani, F., Desai, A. R., Dias, N. L., Friborg, T., Iwata, H., Jansen, J., Lükő, G., Mammarella, I., Repina, I., Rutgersson, A., Sachs, T., Scholz, K., Spank, U., Stepanenko, V. M., Torma, P., Vesala, T., & Lorke A. (2022) Bulk transfer coefficients estimated from eddy-covariance measurements over lakes and reservoirs. *Submitted to Journal of Geophysical Research: Atmospheres*. Preprint doi: https://doi.org/10.1002/essoar.10511514.1.

Table of Contents

Abstract

This thesis was motivated by the need to advance the knowledge on the variability and dynamics of energy fluxes in lakes and reservoirs, as well as about the physical processes that regulate the fluxes at both the air and water side of the air-water interface.

In the first part, I re-examine how mechanical energy, resulting from its major source – the vertical wind energy flux - distributes into the various types of water motions, including turbulent flows and surface and internal waves. Although only a small fraction of the wind energy flux from the atmosphere is transferred to the water, it is crucial for physical, biogeochemical and ecological processes in lentic ecosystems. Based on extensive air- and water-side measurements collected at two small water bodies (< 10 km^2), we estimated the energy fluxes and energy content in surface and in internal waves. Overall, the estimated energy fluxes and energy content agree well with results reported for larger water bodies, suggesting that the energetics driving the water motions in enclosed basins is similar, independently of the basin size. Our findings highlight the importance of the surface waves that receive the largest fraction of the wind energy flux, which strongly nonlinearly increases for wind speeds exceeding 3 m s^{-1}. We found that the existing parameterization of the wave height as a function of wind speed and fetch length did not reproduce the measured wave amplitude in lakes. On average, the highest energy content was observed in basin-scale internal waves, together with high-frequency internal waves exhibiting seasonal variability and varies among the aquatic systems. During our analysis, we discovered the diurnal variability of the energy dissipation rates in the studied lake, suggesting biogenic turbulence generation, which appears to be a widespread phenomenon in lakes and reservoirs.

In the second part of the thesis, I addressed current knowledge gaps related to the bulk transfer coefficients (also known as the drag coefficient, the Stanton number and the Dalton number), which are of a particular importance for the bulk estimation of the surface turbulent fluxes of momentum, sensible and latent heat in the atmospheric boundary layer. Their inaccurate representation may lead to significant errors in flux estimates, affecting, for example, the weather and climate predictions or estimations of the near-surface current velocities in lake hydrodynamic models. Although the bulk transfer coefficients have been extensively studied over the past several decades (mainly in marine and large-lake environments), there has been no systematic analysis of measurements obtained at lakes of different size. A significant increase of the transfer coefficients at low wind speeds (< 3 m s^{-1}) has been observed in several studies, but, to date, it has remained unexplained. We evaluated

the bulk transfer coefficients using flux measurements from 31 lakes and reservoirs. The estimates were generally within the range reported in previous studies for large lakes and oceans. All transfer coefficients increased substantially at low wind speeds, which was found to be associated with the presence of gusts and capillary waves (except the Dalton number). We found that the Stanton number is systematically higher than the Dalton number. This challenges the assumption made in the Bowen-ratio method, which is widely used for estimating evaporation rates from micrometeorological measurements. We found that the variability of the transfer coefficients among the lakes could be associated with lake surface area. In flux parameterizations at lake surfaces, it is recommended to consider variations in the drag coefficient and the Stanton number due to wind gustiness and capillary wave roughness while the Dalton number could be considered as constant at all wind speeds.

In the third part of the thesis, I address the key drivers of the near-surface turbulence that control the gas exchange in a large regulated river. As all inland waters, rivers are an important natural source of greenhouse gases. The effects of the widespread alteration and regulation of river flow for human demands on gas exchange is largely unknown. In particular, the near-surface turbulence in regulated rivers has been rarely measured and its drivers have not been identified. While in lakes and reservoirs, near-surface turbulence is mainly related to atmospheric forcing, in shallow rivers and streams it is generated by bottom friction of the gravity-forced flow. The studied large regulated river represents a transition between these two cases. Atmospheric forcing and gravity were the dominant drivers of the near-surface turbulence for a similar fraction of the measurement period. Based on validated scalings, we derived a simple model for estimating the relative contributions of wind and bottom friction to near-surface turbulence in lotic ecosystems with different flow depths. Large diel variability in the near-surface energy dissipation rates due to flow regulation leads to the same variability in gas exchange. This suggests that estimates of gas fluxes from rivers are biased by measurements performed predominantly during daytime.

In addition, the novelty in all the analyses described above is the use of the turbulent surface fluxes measured directly by the eddy-covariance technique – at the moment of writing, the most advanced method. Overall, this thesis is of a potential interest for a broad range of scientific disciplines, including limnology, micrometeorology and open channel hydraulics.

1 Introduction

1.1   Energy partition in lakes and reservoirs

The spatial and temporal distribution of the *mechanical energy available for mixing* in lakes or reservoirs is crucial for a wide range of ecological processes. Mechanical energy is subdivided into *potential* and *kinetic* energy. There are two main sources of mechanical energy in lakes: *surface shear* created by the wind acting on the water surface and convection-inducing *heat flux*. In terms of ability to set water in motion, wind forcing is the dominant driver for internal lake circulation as well as for creating the surface waves (Imboden, 2003). The dynamic interplay between the wind- and convective-driven turbulence regulates the heat, moisture and gas exchange at the *air-water interface*. The transfer of heat and moisture across the air-water interface can have a significant impact on the local weather, e.g., intensifying precipitation (Changnon & Jones, 1972; Kato & Takahashi, 1981). The emissions of such gases as carbon dioxide (CO_2) and methane (CH_4) from lakes are recognized as an important part of the global carbon cycle that can affect the climate (Bastviken et al., 2011; DelSontro et al., 2018). The gas exchange can be accelerated by wind-driven surface waves at the water surface (Perolo et al., 2021).

During summer, lakes often experience density and thermal stratification. It is important to distinguish the terminology used in the literature to describe the stratified conditions in lakes. From a classical point of view, the water column can be subdivided into a three-layer structure (from surface to bottom): *epilimnion*, *metalimnion* and *hypolimnion* (Wetzel, 2001). Epilimnion is also known as *the surface mixed layer* which extends to the depth determined by the strength and history of winds, heating or cooling. In addition, it is common to distinguish the *thermocline*, which is defined as the surface of a maximum rate of decrease in temperature with the water depth. Moreover, based on the field measurements of turbulence, in terms of turbulent activity the water column consists of three layers that only partially intersect with those mentioned above: the surface boundary layer (SBL), interior and the bottom boundary layer (BBL) (Wüest & Lorke, 2003). Imberger (1998), however, defines a four-layer structure in lakes using different terminology: the surface mixing layer, the subsurface mixing layer, the main water column, the benthic boundary layer. A term the surface mixed layer (or epilimnion) differs from the surface mixing layer as it forms during longer time scale. In this upper nearly isothermal layer, energetic mixing controls the water quality and biological rate processes, for example, providing oxygen and light for the growth of the planktonic organisms (MacIntyre, 1993; Huisman et al., 2004; Peeters et al., 2007). In the lake interior (hypolimnion) the

turbulence is suppressed by stratification. However, the internal waves that develop as a result of the complex influence of both wind and stratification in the metalimnion are the important mediator of nutrients from the bottom to the surface layer. It affects both the phytoplankton community and overall water quality (MacIntyre & Jellison, 2001). Turbulence generated along the boundaries in the BBL affects the oxygen consumption of sediments (Lorke et al., 2003), therewith the rate of carbon burial and methane production (Sobek et al., 2009), and nutrient release.

Different kinds of motions generated mainly by wind have various time and space scales. Smith (1979) well observed an analogy with atmospheric circulation and noted that these lake movements form part of the "underwater weather". The literature suggests exploring the lake dynamics in terms of *energy fluxes* (energy per unit area per unit time, in W m^{-2}) and *energy content* stored in different motions (energy per unit area, in J m^{-2}) (Imboden & Wüest, 1995). Typical values of the downward wind energy flux into the lake (also called "a wind energy input", P_{10} [W m^{-2}]) span several orders of magnitude (from $5 \cdot 10^{-3}$ to 7 W m^{-2}) for small and medium to large-sized lakes with a surface area (A_s [km^2]) ranging between 5 and $31.7 \cdot 10^3$ km^2 (Ravens et al., 2000; Wüest et al., 2000; Imboden, 2003; Woolway & Simpson, 2017; Fernández Castro et al., 2021). A general scheme of the fate of the non-dissipated wind energy flux and the energy content is shown in **Figure 1**. The largest portion of the wind energy flux is fed to the surface waves: 1.5-3.5% according to (Simon, 1997). Subsequently, the largest energy content among all water motions (up to 10^3 J m^{-2}, according to (Imboden, 2003)) is stored in the surface waves.

Only a small fraction of the wind energy input is transferred into the lake (~0.13-2% according to (Wüest et al., 2000; Imboden, 2003; Woolway & Simpson, 2017; Fernández Castro et al., 2021)). Energy transfer from wind to water was found to be more efficient during the stratified season compared to periods of full mixing (Woolway & Simpson, 2017). Most of the wind energy input (1.5% out of ~2% mentioned above) is dissipated in the surface layer (Wüest et al., 2000). According to different sources, the typical order of magnitude for the dissipation rates in this layer varies between 10^{-9} and 10^{-4} W kg^{-1} for small and medium-sized lakes (Wüest et al., 2000; Imboden, 2003). 0.42% or 1% of P_{10} is transferred to the internal waves according to (Wüest et al., 2000; Imboden, 2003), respectively. Ultimately, 90% of that energy is dissipated within the BBL.

Given the various terminology in the literature, it is important to clarify that the internal waves with wavelengths of the same order as the lake diameter are also known as the *basin-scale internal waves* (or *standing wave modes*, or *internal seiches*). Sub-basin-scale internal

waves resulting from the degeneration of the basin-scale internal waves are called *propagating high-frequency* internal waves. The latter appear at frequencies equal to some fraction of the maximum buoyancy frequency, which is a quantity characterizing the strength of the vertical density stratification (Heyna & Groen, 1958; Boegman et al., 2005; Preusse et al., 2010). The energy stored in the basin-scale internal waves is the result of the interrelation between kinetic energy produced by wind and potential energy represented by the vertical isothermal displacement relative to their equilibrium position. Under the assumption that the motions in lakes are not affected by planetary rotation, the principle of equipartition between kinetic and potential energy is valid (Kundu et al., 2012). Thus, for simplicity, the total energy in the basin-scale internal waves (sum of the kinetic and potential energy) is often estimated as two times the averaged potential energy (Wüest et al., 2000). The total energy in the basin-scale internal waves is typically one or several orders of magnitude less than the energy stored in the surface waves ($10^{-3} - 196$ J m^{-2}) (Wüest et al., 2000; Imboden, 2003; Fernández Castro et al., 2021). The estimates of the energy content in the high-frequency internal waves are so far limited.

The integrated potential energy stored in the vertical density stratification is referred to as *Schmidt stability* and its typical value for the lakes is approximately 10^3 J m^{-2} during the periods of strong stratification (Imboden & Wüest, 1995). For a medium-sized temperate lake ($A_s = 24$ km^2), the annual average value is equal to approximately 60 J m^{-2} (Yang et al., 2016). The net surface heat flux is the sum of the radiative heat fluxes due to solar radiation (shortwave radiation) and to the infrared radiation emitted from the atmosphere and from the water surface (longwave radiation), the non-radiative heat fluxes due to convection (sensible heat flux) and evaporation or condensation (latent heat flux). The annual mean for lakes is 60 W m^{-2} (Imboden & Wüest, 1995). All these estimates of energy fluxes and energy content described above were based on the limited number of studies and mainly on the information compiled from asynchronously conducted measurements in different systems (Imboden, 2003). The generality of current figures, their transferability to water bodies of different sizes and depth, and their temporal dynamics remain largely unexplored. Moreover, all existing estimates are based on bulk parameterization of wind energy fluxes, since observations lack direct measurements of atmospheric fluxes (Simon, 1997; Wüest et al., 2000; Imboden, 2003; Woolway & Simpson, 2017; Simpson et al., 2021). Direct flux measurements are carried out by the eddy-covariance (EC) technique, which is based on the covariations between the turbulent velocity components and scalar air properties at a specified height (Smith, 1979; Foken, 2008; Burba & Anderson, 2010). Using this technique, one can obtain the spatial and

temporal average of turbulent fluxes originating from an area called the footprint. Nowadays, the EC method is commonly applied for measurements above lakes (Blanken et al., 2000; Vesala et al., 2006; Nordbo et al., 2011; Mammarella et al., 2015; Spank et al., 2020). The role of surface waves in the energy budget appears to be constraint by observations, which are restricted to a single study in a large lake (Simon, 1997; Imboden, 2003).
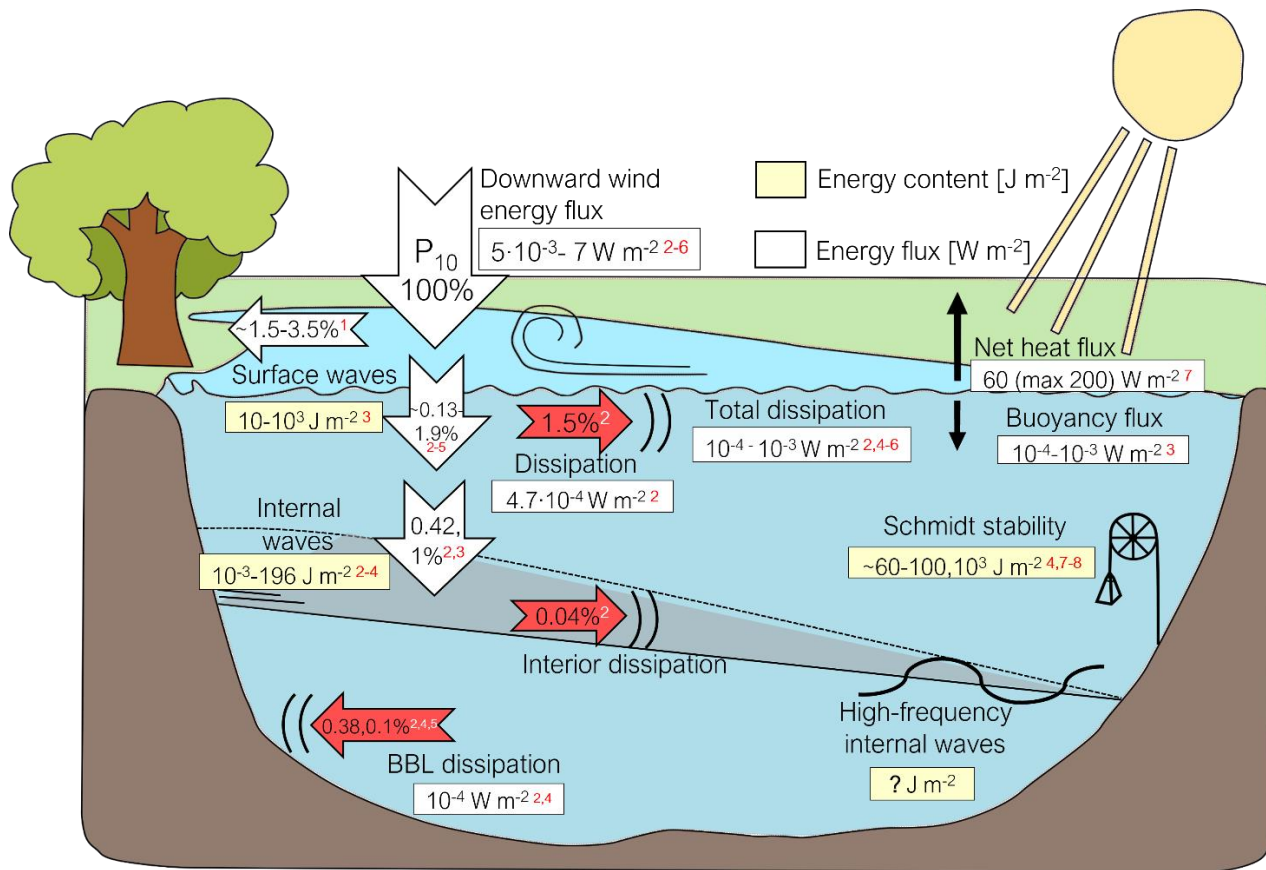

Figure 1. Scheme of the energy fluxes and energy content according to the recent studies. Superscript numbers in red and white colors correspond to the following studies: 1 - (Simon, 1997); 2 - (Wüest et al., 2000); 3 - (Imboden, 2003); 4 - (Fernández Castro et al., 2021); 5 (Woolway & Simpson, 2017); 6 - (Ravens et al., 2000); 7 - (Imboden & Wüest, 1995); 8 - (Yang et al., 2016). Large arrows show the main flux paths of the downward wind energy flux (P_{10}) and the percentage which is attributed to different type of motions. White and yellow rectangles contain the typical magnitude of the fluxes (in W m^{-2}) and energy content (in J m^{-2}), respectively.

1.2 Air-water interface as key boundary for lake-atmosphere interaction

1.2.1   Turbulent surface fluxes in the atmospheric surface boundary layer

In the section above, we mainly introduced the overall energy partition in lakes and reservoirs providing the overview of the major water motions. Here, we focus on the key boundary – *the air-water interface* – which separates two layers: the atmospheric and the water surface boundary layers (**Figure 2**). The air-water interface is crucial for the lake-atmosphere interaction including the input of momentum and the exchange of heat and volatile substances, such as dissolved gases. With focus on the atmospheric boundary layer, we aimed to explore in detail the exchange of momentum, heat and water vapor, expressed via the momentum, sensible and latent heat fluxes (see *Appendix II*). An accurate evaluation of these fluxes above the lake ecosystems is important, as lakes are known to have an impact on local weather and climate. For example, lakes affect the stability of the atmosphere above (Sun et al., 1997), leading to the formation of clouds and precipitation on the shores (Changnon & Jones, 1972; Kato & Takahashi, 1981; Eerola et al., 2014; Thiery et al., 2016). The past three decades have seen a rapid development of lake models (Stepanenko et al., 2014) and their incorporation into numerical weather and climate prediction models (Ljungemyr et al., 1996; Mironov et al., 2010; Salgado & Le Mogne, 2010). Experiments on the coupling of lake and the atmospheric models revealed improved performance of weather prediction (Balsamo et al., 2012).

Momentum, sensible and latent heat fluxes are commonly parametrized by the bulk formulations. Bulk formulas are based on gradient approaches utilizing transfer coefficients (bulk transfer coefficients) and easy to measure meteorological and limnological variables, i.e., wind speed, air temperature, air humidity and water surface temperature (Stull, 1988). The bulk transfer coefficients of momentum, heat and water vapor are known as the drag coefficient (C_{DN}), the Stanton number (C_{HN}) and the Dalton number (C_{EN}). In the notations, "N" stands for "neutral" transfer coefficients, corresponding to the neutral thermal stability of the atmosphere. These bulk transfer coefficients are among the key parameters in atmospheric and lake models. They are often considered as model tuning parameters (Stepanenko et al., 2014), despite the fact that their incorrect representation can lead to errors in the bulk flux estimates. Therefore, much effort has been put into developing their correct parameterizations. A lot of research has been dedicated to the drag coefficient (overview in Garratt (1977) and Kantha & Clayson (2000)). Fewer studies analyzed the other transfer coefficients (Harbeck, 1962; Hicks, 1972; Xiao et al., 2013). The first studies mainly investigated the transfer coefficients for large lakes

and marine environments. While the drag coefficient is known to be dependent on wind speed, atmospheric stability and the surface roughness length, which could be a function of the surface wave field, the research is still ongoing. Although early marine studies agreed that the drag coefficient increases nearly linearly with the increasing wind speed (Kantha & Clayson, 2000), more recent studies revealed a significant increase at wind speed below 3 m s^{-1} (Grachev et al., 1998; Wüest & Lorke, 2003; Wei et al., 2016). This increase could be up to ten times higher than the constant value of 1.3·10^{-3}, which corresponds to the typical value of open water surface roughness and is widely accepted in models (Foken, 2008).

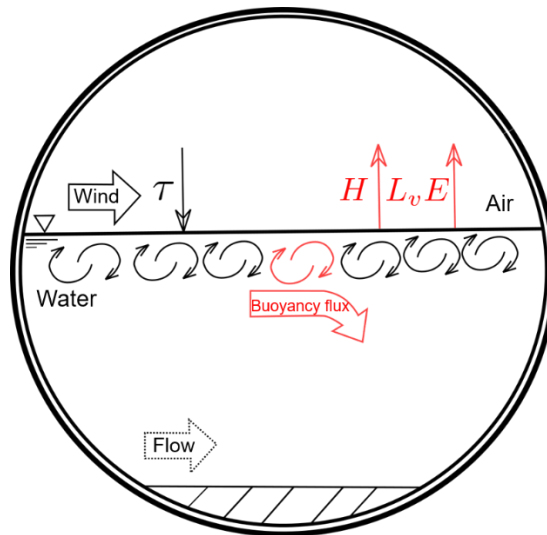**Figure 2**. Air-water interface: the key boundary in lake-atmosphere interaction. Momentum, sensible and latent heat fluxes (denoted by τ, H and L_vE, respectively, where L_v is the latent heat of vaporization) are marked as narrow arrows. The standard sign convention is that the momentum flux is defined as positive downward, while sensible and latent heat fluxes are defined as positive upward. Large arrows indicate the main driving forcing mechanisms for the near-surface turbulence: wind, surface buoyancy flux and flow for the regulated rivers (transitional case between lentic and lotic ecosystems, see *Section 1.2.2* and *Appendix III*).

Despite the fact that there have been many attempts to address the reasons for such an increase, there is still no consensus in the scientific community. Researchers tried to find possible explanations by looking at the surface roughness parameterization. The low wind speed regime was first described as the aerodynamically smooth flow and the surface roughness is described as a function of the thickness of this layer (Schlichting, 1968). On

the contrary, Wu (1988) proposed that at low winds the flow is aerodynamically rough and capillary waves are the main drivers. The surface roughness length in that case is described as a function of the water surface tension. As an additional possible mechanism for the increase of the drag coefficient at low winds, Grachev et al. (1998) and Fairall et al. (2003) suggested the influence of gusts – large convective eddies. Instead of the standard formulation of the drag coefficient, Grachev et al. (1998) described an alternative approach for its estimation, which accounted for the effect of gusts. Similar to Grachev et al. (1998), Sahlée et al. (2014) and Liu et al. (2020) related the increase of the drag coefficient to nonlocal effects such as the penetration of large eddies into the surface layer from the atmosphere above. Liu et al. (2020) introduced the factor describing this effect (however, over the land surface and only for neutral atmospheric stability). None of the processes mentioned above could explain such a strong increase of the drag coefficient estimated from measurements above a relatively large lake (Wei et al., 2016). However, their study indicated that this increase at low wind speeds was associated with enhanced turbulent kinetic energy due to buoyancy flux.

At wind speeds exceeding 3-4 m s^{-1}, surface waves start to develop (Ataktürk & Katsaros, 1999; Simon, 1997; Guseva et al., 2021). In the most simplified way, the drag coefficient for this wind speed regime was first described by parameterization of the surface roughness, called the Charnock relationship (Charnock, 1955). In that case, the surface waves were assumed to be fully developed, and the surface roughness was a function of the wind stress. However, later on, Donelan (1990) and Geernaert (1990) summarized that this assumption might not hold for lakes with limited wind fetch. Consideration of surface wave development expressed by wave age in the surface roughness length parameterization was beneficial for the drag coefficient estimation (Donelan, 1982; Ataktürk & Katsaros, 1999). Vickers & Mahrt (1997) reported that for a given wind speed, the drag coefficient tends to be larger for young steeper waves representative of short wind fetches than for longer fetches. However, very often the surface wave measurements are not available for lakes and Charnock relationship is used as a first approximation.

Several studies focused on the possible relationship between the bulk transfer coefficients and different lake properties such as lake surface area (Harbeck, 1962; Brutsaert & Yeh, 1970; Read et al., 2012; Woolway et al., 2017), lake depth at the measurement location (Panin et al., 2006), wind fetch at the measurement location (Lükő et al., 2020) and lake biota, e.g., submerged macrophytes (Xiao et al., 2013). According to those studies, the transfer coefficients tend to decrease with increasing water depth, lake area, fetch and in the presence

of water plants at the water surface. Note that Panin et al. (2006) and Woolway et al. (2017) revealed a correlation between the transfer coefficients and the lake parameters, but their estimates of the transfer coefficients were based either on bulk parameterization (Woolway et al., 2017) or were compared to other studies where there were no direct flux measurements (Panin et al., 2006).

Despite the fact that in the marine studies the Stanton and Dalton numbers also showed an increase at low wind speeds, both transfer coefficients were considered as being approximately constant with a value of $1.1 \cdot 10^{-3}$ (Kantha & Clayson, 2000). The first measurements carried out in lakes revealed that this value was higher and equal to $\sim 1.5 \cdot 10^{-3}$ (Harbeck, 1962; Hicks, 1972) or $1.9 \cdot 10^{-3}$ (Strub & Powell, 1987). From the most recent studies (Xiao et al., 2013; Li et al., 2016; Wei et al., 2016; Dias & Vissotto, 2017), there is evidence that both transfer coefficients depend on the wind speed and that the Stanton number is higher than the Dalton number by approximately a factor of 1.3. This indicates that the earlier assumption of the equality of both transfer coefficients may not be valid for lakes.

1.2.2 Near-surface turbulence in the water surface boundary layer

The dynamics in the *water surface boundary layer* in lake ecosystems is closely related to the forcing mechanisms in the atmospheric boundary layer above the lake. Here, we focus on the physical processes in this layer. Currently, many studies explore a "hot" topic – the gas exchange at the air-water interface - because the inland waters produce, receive, transport and process carbon and, relative to their surface area, are disproportionally important for regional and carbon cycling (Cole et al., 2007; Tranvik et al., 2009; Aufdenkampe et al., 2011). A key parameter that regulates the gas exchange across the air-water interface is the gas transfer velocity, which is mainly controlled by turbulence on the water side of the interface. Such theories as surface renewal and thin-film models result in a dependence of the gas transfer velocity on the dissipation rate of the turbulent kinetic energy near the water surface (Lamont & Scott, 1970; Zappa et al., 2007; Katul & Liu, 2017). While in lentic aquatic ecosystems, such as lakes and reservoirs, near-surface turbulence is mainly driven by atmospheric forcing including wind shear, convective cooling and surface wave breaking (MacIntyre et al., 1995, 2010), in shallow lotic ecosystems, such as streams, turbulence is generated by bed shear induced by gravity-driven flows (**Figure 2**) (Lorke & MacIntyre, 2009). Turbulence generated by wind and the surface buoyancy flux in the surface boundary layer can be described by the model (Tedford et al., 2014) proposed for lakes. Turbulence in rivers due to bed friction (in the following sections we refer to as "bottom-generated turbulence") can be described in three ways: either assuming the constant shear over the water column (Lorke & MacIntyre, 2009), or assuming that the shear decreases toward the water surface and is equal to zero at the water surface (Nezu, 1977), or by combining the latter assumption with a logarithmic profile of the mean flow velocity (Nikora & Smart, 1996).

Alin et al. (2011) proposed a conceptual scheme in which the physical driver of the gas transfer velocity in rivers undergoes a transition from the dominance of the wind control in large rivers and estuaries toward increasing dominance of flow and depth in smaller streams. With a growing number of the altered rivers worldwide (Grill et al., 2019), *regulated rivers* are of great importance for studying the near-surface dynamics (controlling the gas exchange), as they also can represent a unique transitional case between lentic and lotic ecosystems.

Currently, there is a limited number of studies that involve measurements of turbulence as well as the gas exchange velocities in streams and the existing measurements are mostly restricted to estuaries and tidal rivers. Some studies focused on gas exchange only and provided empirical relations between the gas exchange velocity and bulk flow properties, such

as channel slope, discharge, mean flow speed, and water depth (Raymond et al., 2012; Wallin et al., 2018; Ulseth et al., 2019). These formulas are derived for streams but they are applied to large rivers, as measurements are lacking.

2 Objectives and Hypotheses

The aim of this thesis is to advance existing knowledge about the energy partition in lakes and reservoirs with a focus on physical processes either in the water column of the water body, or, in particular, at the air-water interface separating two boundary layers: atmospheric and water. Regulated rivers are considered as a special environment that combines the hydrodynamics of both lakes and rivers. The main research objectives and hypotheses (**H**) of the thesis are:

(1) Identify the most relevant components of the total mean energy budget for two small (< 10 km^2) water bodies: a lake and a reservoir.

H1.1 The partitioning of the kinetic energy into surface and internal waves, boundary-layer turbulence depends on the lake surface area and varies seasonally with density stratification.
H1.2 Hydrodynamic processes (e.g., presence of different types of internal waves) in a lake and a reservoir are different as the reservoir experiences the water level fluctuations.
H1.3 The role of the surface waves in the energy budget is significant. The fraction of the wind energy attributed to the surface waves depends on the wind speed.

(2) Investigate dependence of the bulk transfer coefficients on the wind speed and lake characteristics over multiple lakes and reservoirs.

H2.1 All bulk transfer coefficients strongly increase at wind speeds less than 3 m s^{-1}. Increase in the drag coefficient can be associated with either one of the physical mechanisms: the effect of the viscous sublayer resulting in a smooth flow, the effect of capillary waves or the effect of the large convective eddies from the atmosphere above.
H2.2 Bulk transfer coefficients at high wind speeds (>3 m s^{-1}) depend on such lake properties as lake surface area, wind fetch and depth at the measurement location.
H2.3 The transfer coefficients of heat and water vapor (Stanton number and Dalton number) are on average equal for all water bodies.

13

(3) Identify the key drivers for near-surface turbulence in a large regulated river.

H3.1 Near-surface turbulence in a regulated river is generated by an interplay between the dominant forcing mechanisms associated with large rivers (wind or bed friction due to gravity-driven flow). The relative importance of the dominant forcing mechanisms depends on the magnitudes of the dissipation rates associated with them. In a simplified way, their relative contribution to the near-surface turbulence can be presented as a function of mean wind speed, flow velocity and water depth.
H3.2 The temporal dynamics of the dissipation rates (and, therefore, gas transfer velocities) is affected by the flow regulation.

3 Outline

The thesis is organized in line with the objectives and hypotheses stated above and, therefore, consists of three parts. Each part represents an article describing the investigation and findings. The three articles are attached as *Appendices*: two of them have been published (*Appendix I, III*) and one is currently under the second stage of peer-review (*Appendix II*).

To address the objectives and test hypotheses in the first and the third parts, we conducted field campaigns at the three sites: Lake Dagow (A_s = 0.3 km^2, Germany), Bautzen Reservoir (A_s = 5.3 km^2, Germany) and the River Kitinen (181 m wide at measurement location, Finland). At all three study sites, a similar set of instruments was installed to carry out simultaneous water- and air- side measurements. A general scheme of these measurements is shown in **Figure 3**.

All field campaigns were carried out in a close cooperation with our scientific partners (see *Acknowledgments* and *Appendices*). The air-side measurements included the EC system (see *Section 1.1*) which provided the wind speed and flux data. The water-side measurements consisted of measurements of flow velocity, vertical water temperature profile and surface waves properties.

Using this dataset, we quantified the energy fluxes and energy content in various types of water motions in response to wind energy flux, compiling the energy budgets for two small water bodies (Lake Dagow, Bautzen Reservoir, **H1.1**, *Appendix I*). Taking advantage of the wave measurements covering a nearly complete annual cycle, we investigated the surface wave characteristics and their dependence on wind speed (**H1.3**) and fetch. The predominant modes of the basin-scale internal waves and the presence of the high-frequency internal waves were examined (**H1.2**).

Based on the field measurements in the large regulated River Kitinen, the hypotheses were tested (**H3.1 - H3.2**, *Appendix III*). The dataset was used to quantify the observed dissipation rates. The dominance of the forcing mechanisms was identified via comparison of the magnitude of the dissipation rates (associated with different forcing) estimated using the validated approaches.

In the second part (*Appendix II*), we took advantage of the growing number of the EC flux measurements above lakes and reservoirs. We compiled a large dataset consisting mostly of published data for 31 water bodies of various sizes and located in different climate zones.

We used this dataset to obtain the typical values of the bulk transfer coefficients over the lakes and reservoirs in order to investigate their dependence on wind speed (**H2.1 – H2.2**) and to explain their variability among water bodies via relating them to different lake characteristics (**H2.3**).
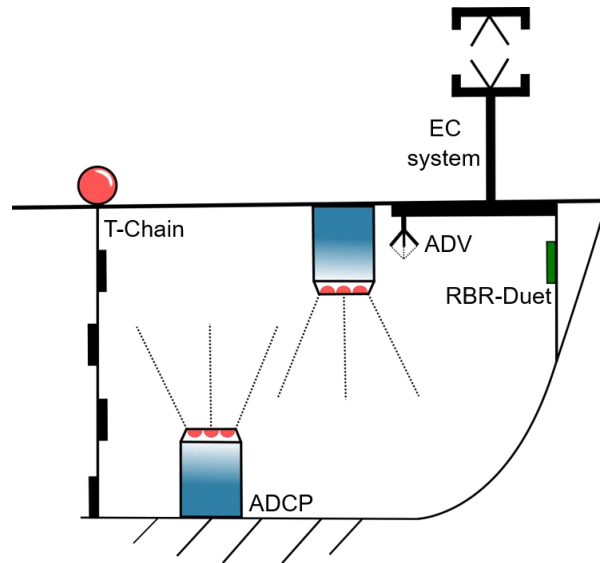

Figure 3. A general scheme of the measurements carried out to obtain the data used in the thesis. The water-side measurements included the flow velocity measured by an acoustic Doppler current profiler (ADCP) installed either on the lake bottom facing up or at the platform facing down and an acoustic Doppler velocimeter (ADV). The ADV and the ADCP provided the pointwise and profile velocity measurements, respectively. The vertical water temperature profile was measured using a thermistor chain (T-Chain). The surface wave measurements were made by a wave recorder (RBR-Duet). The EC system consisted of a sonic anemometer and a gas analyzer and was installed at different sites by our scientific partners (see *Acknowledgments* and *Appendices I, II, III*).

The articles and the corresponding parts mentioned above are listed below. Note that articles are sorted here not by the date of publication but following the logic of the thesis.

Part 1

Appendix I –

Guseva, S., Casper, P., Sachs, T., Spank, U., & Lorke, A. (2021). Energy flux paths in lakes and reservoirs. *Water*, 13(22), 3270. *MDPI AG*. doi: http://dx.doi.org/10.3390/w13223270.

Part 2

Appendix II –

Guseva, S., Armani, F., Desai, A. R., Dias, N. L., Friborg, T., Iwata, H., Jansen, J., Lükő, G., Mammarella, I., Repina, I., Rutgersson, A., Sachs, T., Scholz, K., Spank, U., Stepanenko, V. M., Torma, P., Vesala, T., & Lorke A. (2022) Bulk transfer coefficients estimated from eddy-covariance measurements over lakes and reservoirs. *Submitted to Journal of Geophysical Research: Atmospheres*. Preprint doi: https://doi.org/10.1002/essoar.10511514.1.

Part 3

Appendix III –

Guseva, S., Aurela, M., Cortés, A., Kivi, R., Lotsari, E., MacIntyre, S., Mammarella, I., Ojala, A., Stepanenko, V., Uotila, P., Vähä, A., Vesala, T., Wallin, M. B., & Lorke, A. (2021). Variable physical drivers of near-surface turbulence in a regulated river. *Water Resources Research*, 57, e2020WR027939. doi: https://doi.org/10.1029/2020WR027939.

4 Discussion

In this thesis, I investigated the energy flux paths in freshwater ecosystems (mainly, lakes and reservoirs) within the water column and at the air-water interface. For the analysis (*Appendix I and III*), I used the dataset collected during intensive field measurements over all seasons except winter for most of the study sites (**Figure 4a**). These kinds of measurements are especially valuable because they link water column energetics to air-side flux measurements and, to the best of my knowledge at the moment of writing this thesis, are unique (**Figure 3**). In the following sections, I summarize and discuss the implications of our most important findings.

4.1 Energy partition in small water bodies

Based on simultaneous measurements in the atmospheric boundary layer and in the water column in two small water bodies, we compiled mean energy budgets in various types of water motions (**Figure 4c**, *Appendix I*). Here, I outline the assessments and highlight some of the important findings discovered during the analysis which supported or rejected the formulated hypotheses.

Despite the fact that one study site was a lake and the other a reservoir with surface area larger by one order of magnitude, both water bodies experienced similar hydrodynamic processes and energy flux paths (contrary to **H1.2**). In both water bodies, we found the presence of the basin-scale and high-frequency internal waves. According to our estimates, average wind energy fluxes for both the lake and the reservoir were of the same order of magnitude (10^{-2} W m^{-2}), and thus was within the range reported by multiple studies for lakes of similar size (Wüest et al., 2000) and for larger lakes (Ravens et al., 2000; Imboden, 2003; Woolway & Simpson, 2017; Fernández Castro et al., 2021) (for comparison, see **Figure 1**). Most of this wind energy flux (~95%) is dissipated in the atmospheric boundary layer and is not transported into the lake. The remaining energy is distributed into different types of water motions. Unlike the results reported by Woolway & Simpson (2017) and Simpson et al. (2021) for Lake Windermere (United Kingdom, lake surface area, A_s = 14.7 km^2), there was no evidence of intensification of the energy transfer from wind to water during the stratified season compared to the period of lake mixing (in contrast to the dependence suggested in **H1.1**).

The efficiency of the wind energy was found to be within the values reported for non-stratified conditions (Woolway & Simpson, 2017).
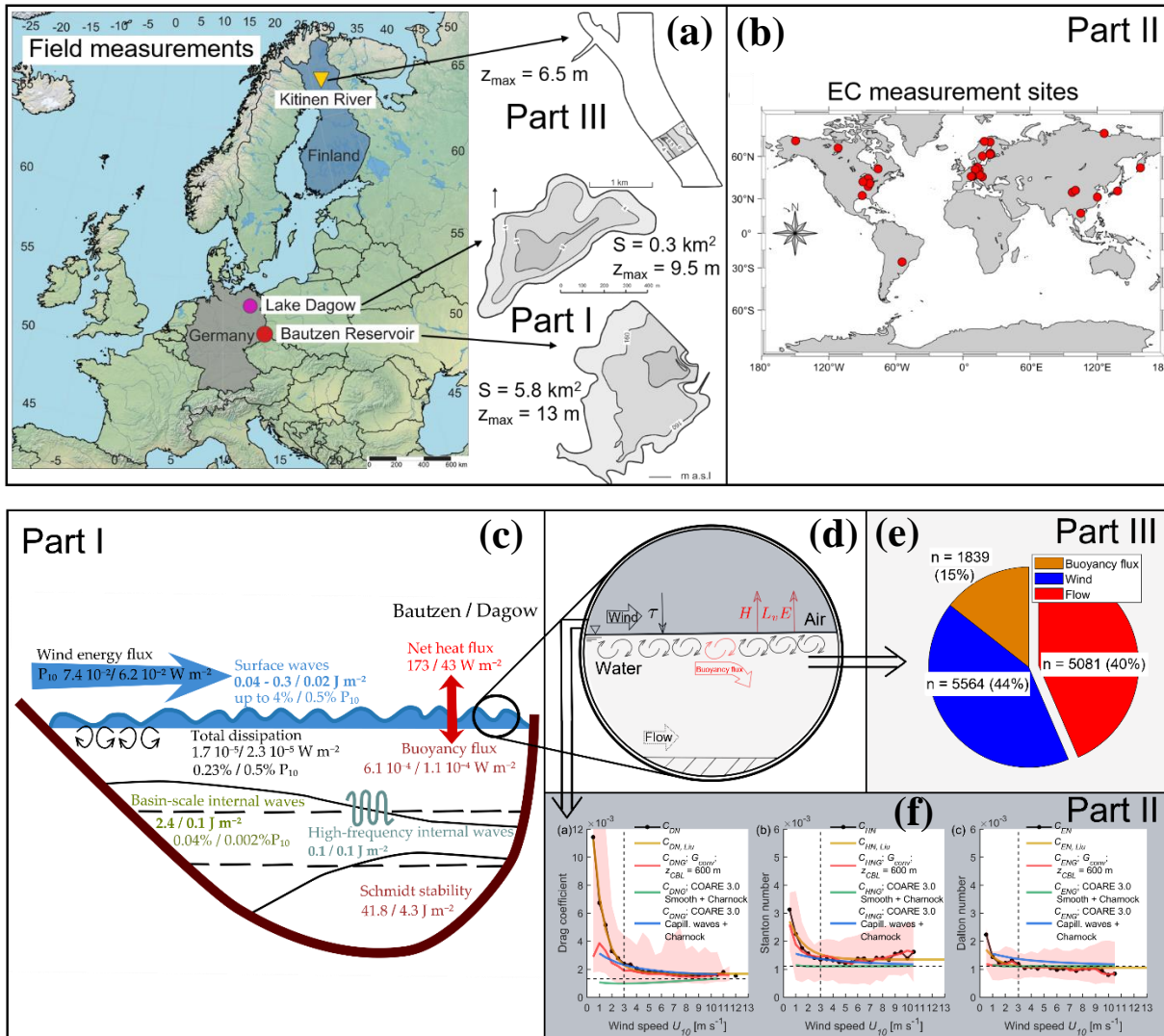

Figure 4. Plots summarizing **(a)** the study sites where field measurement campaigns took place (Lake Dagow, Bautzen Reservoir in Germany, and the River Kitinen in Finland); **(b)** study sites with existing EC measurements; **(c)** key findings in this thesis related to energy fluxes and energy content in different water motions in lakes and reservoirs (taken from *Appendix I*) as well as related to the air-water exchange at the air-water interface (taken from *Appendix II, III*) **(d)**, **(e)**, **(f)**. Parts I, II, III indicate the structure of the thesis as well as the corresponding *Appendices*.

The largest portion of the wind energy flux (up to 4% on average) was transferred to surface waves (in support of **H1.3**). This estimate was within the range (1.5%-3.5%) reported by Simon (1997) based on the measurements in Lake Neuchâtel, a large lake in Switzerland (A_s = 218 km^2). In our case, this fraction strongly increased with wind speed exceeding 3 m s^{-1} and depended on the sampling location (supports **H1.3**). The energy content was on average less than that reported by Imboden (2003) for a large lake (~10^{-2} -10^{-1} J m^{-2} versus 10 J m^{-2} for weak winds). However, our estimates reached 10^3 J m^{-2}, which was consistent with the range reported in study by Imboden (2003). One of the interesting results was that, based on our wave measurements, we found similar features specified by Simon (1997) for a large lake: significant wave height strongly increased for wind speed higher than 3-4 m s^{-1} and it could not be predicted with the JONSWAP model based on the wind speed and fetch length (Hasselmann et al., 1973), which is widely used for its estimation. This model significantly overestimated the wave heights at low wind speeds. Therefore, the synthesis of the wave observations is required to investigate the relationship between the wave characteristics and wind speed and to improve the predictions of the wave height and energy flux in lakes and reservoirs.

The estimated average depth-integrated energy dissipation rate was of the same order of magnitude in both water bodies (10^{-5} W m^{-2}) and represented the largest fraction of the wind energy flux transferred into the lake (0.2% - 0.5%). In general, our estimate was one order of magnitude less than reported in (Wüest et al., 2000), and the averaged dissipation over the water column for both water bodies (5·10^{-9} W kg^{-1}) was at the lower limit of ranges specified for weak winds by Imboden (2003). We found two possible explanations. The first one is the fact that the flow velocities were generally very low and the bottom boundary layer was not captured within the ADCP profiling range (due to instrument installation). Therefore, the dissipation rates estimated using the velocity closest to the bottom could be underestimated (e.g., on average by one or two orders of magnitude in comparison to the dissipation rates in the surface layer). The second possible explanation for the dissipation rate bias is the evidence of biogenic activity in Lake Dagow, which has received a lot of attention from the scientific community over the past decade (Simoncelli et al., 2017; Kunze, 2019). In contrast to the studies where higher dissipation rates were found at the depth of the high acoustic backscatter (Ishikawa et al., 2021; Simpson et al., 2021), we observed enhanced dissipation rates in the presence of low acoustic backscatter. The difference in dissipation rates between day and night was up to two orders of magnitude. While the first type of behavior can be associated with the vertical migration of the zooplankton (Lorke et al., 2004), the second type may be

related to small fish activity (Lorke et al., 2008). The most recent study by Fernández Castro et al. (2022) revealed that the turbulence associated with the aggregation of fish might be especially important in strongly stratified ecosystems. Both types of biogenic activity disturb the ADCP measurements and leads to enhanced dissipation rates. The increasing number of reported biogenic turbulence in inland waters and marine environment calls for future synthesis of such measurements and development of new ways of dissipation rate estimation.

The energy flux to the basin-scale internal waves can constitute to 0.1% of the wind energy flux but was on average one or two orders of magnitude smaller than that reported for the alpine lake (0.04% versus 0.42%, 1% in (Wüest et al., 2000; Imboden, 2003), respectively). The largest energy content was observed in the basin-scale internal waves in the reservoir, exceeding on average by one order of magnitude the energy content, stored in the surface waves and in the high-frequency internal waves (2.4 J m^{-2} versus 0.3 J m^{-2}, 0.1 J m^{-2}). In the small lake, the energy content was of comparable magnitude for all types of waves. These estimates were lower than the values reported in (Wüest et al., 2000) (22±3 J m^{-2}) and slightly higher than those reported in (Imboden, 2003) (10^{-2} - 10^{0} J m^{-2}). We assume that this difference can be related to the strength of the stratification and the lake depth. The alpine lakes studied in (Wüest & Lorke, 2003) and (Imboden, 2003) showed persistent large-amplitude internal seiching, while at our study sites it occurred only sporadically and with smaller amplitudes. We also found that the energy content in both basin-scale and high-frequency internal waves strongly varied with the season (in support of **H1.1**); for example, during the stratified period, high-frequency waves can contain on average twice as much energy than during the rest of the year. This fact is associated with the deepening of the thermocline and the way the energy content is estimated, with the thermocline depth being the upper limit for vertical integration.

Generally, the energy content in water motions was small compared to the potential energy of stratification (Schmidt stability), which on average differed by one order of magnitude between the reservoir and the lake (41.8 J m^{-2} and 4.3 J m^{-2}). Both estimated net heat flux and surface buoyancy flux fell into the range provided by (Imboden & Wüest, 1995) and (Imboden, 2003), respectively. The average wind energy flux in the atmosphere exceeded the average buoyancy flux by two orders of magnitude in both water bodies.

It should be noted that, despite a thorough research, there are several limitations and issues that could be improved in future analysis. Our single-point measurements were unable to spatially resolve the internal waves. Additional measurements along the direction of the

internal waves may be beneficial for precise estimation of the potential and kinetic energy in basin-scale internal waves. The measurements can be combined with numerical models in future studies. We did not account for the potential effects of water level variation in the reservoir; it is however difficult to separate it from the seasonal change in the lake thermal structure without additional modeling. Finally, spatial meteorological measurements would be necessary to confirm the assumption of horizontal homogeneity of the wind field over the lake, which was used in estimation of the wind and wave energy fluxes.

4.2 Bulk transfer coefficients over lakes and reservoirs

Given the aforementioned objectives, the focus of the thesis now shifts to the processes near the air-water interface (**Figure 4d, f**, *Appendix II*). In particular, I focus on the atmospheric side - the turbulent surface fluxes in the atmospheric boundary layer. Based on the compiled dataset consisting of the published EC data for 23 lakes and 8 reservoirs of different sizes and locations, we estimated the bulk transfer coefficients and investigated their dependence on wind speed and different lake characteristics (**H2.1 – H2.3**). All bulk transfer coefficients tended to increase towards low wind speeds (supports **H2.1**) and remained relatively constant at wind speeds exceeding 3 m s^{-1} (**Figure 4f**). The values averaged over all data at lowest winds of 0-0.5 m s^{-1} were higher by up to one order of magnitude for the drag coefficient, factor of three and factor of two for the Stanton and Dalton numbers, respectively, in comparison with the values reported in the literature (1.3·10^{-3}; 1.1·10^{-3}). This increase confirmed the results of previous studies for individual lakes (e.g., Simon, 1997; Xiao et al., 2013; Wei et al., 2016). While Wei et al. (2016) suggested that the contribution of the gusts was not significant for their dataset, we found that the different formulation of the drag coefficient involving the gustiness factor (Grachev et al., 1998; Fairall et al., 2003) could reduce its values by up to a factor of two at wind speeds of 0.5 m s^{-1} (**Figure 4f**). This finding suggests that non-local effects such as the large convective eddies intruding the atmospheric surface layer from the atmosphere above can partially explain the enhanced momentum transfer into the lakes (partially supports **H2.1**). Similar trend was observed for the Dalton number but not for the Stanton number. While the Dalton number with the gustiness correction remained relatively constant with a value of 1·10^{-3} throughout all ranges of wind speed, the drag coefficient and the Stanton number still showed the increase. This increase was found to be explained reasonably well by the capillary wave parametrization of the surface roughness (Wu, 1994) (partially supports **H2.1**). The Dalton number was well described by the smooth flow parametrization.

The parameterization of gustiness involves some additional data (e.g., the virtual sensible heat flux) which is not always available from EC-measurements. In a simplified approach, one can use an empirical function that was originally proposed for the land surface (Liu et al., 2020). The bulk transfer coefficients calculated in a standard way were described well by this function with the fitted coefficients (see details in *Appendix II*).

Unexpectedly, our results revealed the significant increase of the drag coefficient with increasing lake surface area as well as with increasing measurement height for winds less

than 2 m s^{-1} (contrary to **H2.2**). This result is counterintuitive since the dependence on the lake surface area may only be expected when surface waves develop (at wind speed of 3 m s^{-1}) and not at weak winds. It may be also related to development of the thermal internal boundary layer above lakes but a further investigation is required to explain the exact mechanism.

The lower bound for the transfer coefficients among water bodies at wind speed exceeding 3 m s^{-1} was within the range reported in previous studies – either for large lakes or reservoirs (A_s > 200 km^2, (Kuznetsova et al., 2016; Wei et al., 2016)) or for marine environments: classical open ocean measurements (Large & Pond, 1981; Fairall et al., 2003) and coastal ocean sites under fetch-limited conditions (Lin et al., 2002). Indeed, in our dataset we also considered large lakes (e.g., Lake Erie, Lake Taihu), which were expected to have the smallest transfer coefficients, as they had the largest wind fetch. The averaged drag coefficient at high wind speeds corresponded to an upper limit for the water surface roughness reported by Foken (2008) but was two times higher than the values reported for oceans (Fairall et al., 2003). The estimated drag coefficients were also higher than that predicted using the Charnock relationship. This difference was expected because for the fetch-limited conditions the assumption of fully developed waves may not be valid (overview in (Ataktürk & Katsaros, 1999)). We were able to attribute this difference to the lake surface area which supported our proposed hypothesis **H2.2**. We found that all bulk transfer coefficients were highest in small water bodies and decreased with increasing lake surface area at high wind speeds (in support of **H2.2**). We showed a significant correlation between the drag coefficient, the Stanton number and lake surface area. We did not observe a bilinear dependence for the drag coefficient as described in (Woolway et al., 2017) and our estimates were on average twice as high. This difference can be associated with the way they estimated the transfer coefficients using the parametrization of the surface roughness (smooth flow, Charnock relationship). In contrast to the results reported in (Panin et al., 2006), we did not find evidence of the dependence of the bulk transfer coefficients on the lake water depth at any wind speeds (contrary to **H2.2**).

The bulk transfer coefficients are often considered constant or as tuning parameters in hydrodynamic lake models may lead to significant errors in flux estimation. In addition, inadequate values of the drag coefficient result in biased estimates of current velocity in lake models. Therefore, to provide the most accurate flux parameterizations at lake surfaces it is beneficial to use the gustiness approach together with capillary wave parameterization of the surface roughness. Our results may also be important for the Bowen-ratio method, which is frequently used in the micrometeorology community in order to estimate the evaporation.

We found that for all lakes the Stanton number was on average 1.3 times higher than the Dalton number (even with the correction for gustiness), which violates the common assumption of their equality (contrary to suggested in **H2.3**). The physical mechanism underlying this difference requires further investigation.

4.3 Key drivers of the near-surface turbulence in a regulated river

While I investigated energy fluxes in lakes and reservoirs in previous sections, in what follows I focus on a different environment – a regulated river, which can be seen as a transitional case between lentic and lotic ecosystems in terms of flow dynamics. In the following, I describe the main findings related to the assessment of the key drivers of near-surface turbulence in the water surface boundary layer.

Based on our measurements in the River Kitinen, a large regulated river in Finland, we were the first to identify the dominant forcing mechanisms of near-surface turbulence and their dynamics from minutes to seasonal time scales (**Figure 4d, e**, *Appendix III*). Bed friction of the gravity flow and wind shear contributed equally to near-surface turbulence and were the dominant forcing mechanisms throughout 40% and 44% of the total observational period, respectively (supports **H3.1**). While wind shear was the dominant driver when wind speeds exceeded 3 m s^{-1}, bottom-generated shear was dominant when flow velocities exceeded 0.09-0.1 m s^{-1}. The latter were strongly affected by flow regulation resulting in diel variability. The reduction of flow velocities due to hydropower production demand was frequently associated with a transition from bottom-generated to atmospheric-generated turbulence and a change of the water body from lotic to a more lentic-type of the system. The indication of this transition can also be observed in our overall estimates of the dissipation rates ranging from 10^{-10} to 10^{-5} W kg^{-1}. While for smaller streams and tidal estuaries the dissipation rate estimates near the surface can be at the higher limit of this range (10^{-6}–10^{-4} W kg^{-1}) (Zappa et al., 2007; Chickadel et al., 2011) or several orders of magnitude higher (Kokic et al., 2018), in lakes they typically vary between 10^{-9} and 10^{-5} W kg^{-1} (Wüest & Lorke, 2003; Tedford et al., 2014). Surface buoyancy flux driven by convective cooling dominated energy dissipation rates only during 15% of the measurement period (was not proposed in **H3.1**). The contribution of surface waves was found to be insignificant, probably due to the small amplitude of the observed waves. The observed weak thermal stratification caused a slight suppression of turbulence and the estimation of the dissipation rates in that case is challenging and requires separate investigation.

Quantification of dominant forcing mechanisms was possible after comparing the dissipation rates estimated from the velocity measurements with the ones obtained using different models. We found that two models - the similarity scaling by Tedford et al. (2014) for cases when atmospheric forcing dominated and the law-of-the-wall scaling for the bottom-generated turbulence - reproduced the dissipation rates in a close agreement with

the observations (supports **H3.1**). While the former is commonly applied for lakes and oceans and is expected to be applicable for the low-flow regime, the latter was not expected to work for the high-flow regime in rivers as it assumes constant shear stress throughout the water column. Classical empirical and theoretical approaches with the assumption of linearly decreasing shear stress are commonly applied in the open-channel flow scientific community (Nezu, 1977; Nikora & Smart, 1996). Possible explanations were a subject of long discussions with scientists during the peer-review process, but they remained unknown. Given the relative insignificance of convectively driven turbulence during the measurement period, we proposed a concept that could assess the relative importance of wind and bottom-generated turbulence for rivers of arbitrary depth. We combined the two scaling approaches mentioned above and derived the expression for a mean "critical" wind speed as a function of the mean flow velocity and water depth (in support of **H3.1**). For wind speeds exceeding this value, near-surface turbulence is expected to be controlled by wind, in contrast to the predominance of bed friction for wind speed below this value.

As near-surface turbulence constitutes the primary controlling factor of the gas transfer velocity at the air-water interface, our results may have implications for the accurate assessment of the global carbon dioxide emissions from regulated rivers. For example, if we compare the gas transfer velocity estimated from our observed mean dissipation rate using the surface renewal model, we obtain values four times lower than the one reported for a river of the same Strahler order in a global analysis (Raymond et al., 2013). Moreover, the large variability of the dissipation rates spanned over four orders of magnitude theoretically corresponds to temporal variation in the gas transfer velocity of one order of magnitude (supports **H3.2**). To date, sub-daily variability of the gas transfer velocity has not been resolved in larger-scale models of riverine carbine dioxide emissions, and our findings indicate that the estimated fluxes could be biased. Future field observations and modeling efforts are required to analyze to what extent the diel variability affects the emission rates. Overall, our findings confirm the conceptual scheme of Alin et al. (2011) describing a transition of the physical control of the gas transfer velocities from the dominance of the wind control in estuaries and large rivers toward increasing importance of the flow velocity and depth at smaller streams (as suggested **H3.1**). The River Kitinen appeared to be located in the transition zone, where wind and water currents are of equal importance.

5 Conclusion

In the following, I summarize the main conclusions of this thesis related to the energy flux paths in small lakes and reservoirs as well as to the process of air-water exchange:

i. For the first time, we compiled the energy budget for a lake and a reservoir using direct measurements of atmospheric fluxes. Although the two studied water bodies were expected to be governed by different hydrodynamic processes due to water level change in a reservoir, we did not find any significant differences in energy fluxes. Overall, the estimated energy fluxes and energy content in various types of water motion agree well with the results reported for larger water bodies, suggesting that the energetics governing the water motions in enclosed basins is similar, independent of basin size.

We emphasize the importance of surface waves that receive the largest fraction of the wind energy flux into the water and have mostly been neglected in previous studies. Wave energy increases strongly non-linearly for wind speeds exceeding 3 m s^{-1}. We showed that existing parameterizations of wave height as a function of wind speed and fetch length failed to reproduce the observed wave amplitudes in small water bodies. Future wave measurements and investigation of such a dependence are required. While the energy content in the basin-scale internal waves was found to be within the range reported for larger lakes, it seems to vary strongly among lakes with different size and depth. Internal waves appear to be more important in mean energy budgets in larger and deeper lakes.

The dissipation rates of the turbulent kinetic energy have a similar structure and are of comparable magnitude in water bodies of different size. Depth-integrated dissipation rates increase strongly for wind speeds exceeding 3 m s^{-1}. In the lake, we observed a pronounced diurnal pattern in dissipation rates, indicating biogenic activity such as vertically migrating organisms. In future studies, the reliability of commonly applied measurement and analysis methods for estimation of dissipation rates in the presence of biogenic turbulence should be validated.

ii. For the first time, we analyzed the bulk transfer coefficients of momentum, sensible and latent heat from the directly measured atmospheric fluxes above many lakes and reservoirs of different sizes. All transfer coefficients have a pronounced increase at low winds (< 3 m s^{-1}) and have relatively constant values at high winds (> 3 m s^{-1}).

29

Alternative calculation of the transfer coefficients involving gustiness approach could reduce the drag coefficient and the Dalton number at low wind speeds. The remaining increase of the drag coefficient and the Stanton number at low wind speeds could be associated with the physical mechanism, including the capillary wave approach. It is recommended to use the gustiness approach in calculation of the transfer coefficients. In a simplified approach, the bulk transfer coefficients can be calculated without consideration of gustiness by using empirical function that has been proposed for the land surface and that we fitted to data measured over lake and reservoir surfaces.

At high wind speeds the drag coefficient and the Stanton number decreased with increasing surface area of the water body, whereas the opposite (for the drag coefficient only) was found at low winds. Despite the fact that the estimated bulk transfer coefficients generally agreed with previous studies, the Stanton number was on average higher by a factor of 1.3 than the Dalton number. This inequity has consequences for the Bowen-ratio method used for evaporation estimation and requires further investigation.
We underline the need for experimental confirmation of the validity of assumptions underlying eddy-covariance flux measurements at low wind speed.

iii. Based on the first continuous turbulence measurements in a large regulated river, we described the key drivers of the near-surface turbulence and quantified their contributions. We found nearly equal contributions from wind forcing and bed friction to near-surface dissipation rates, with wind being the dominant driver for wind speeds exceeding 3 m s^{-1}, and bottom-generated turbulence when flow speeds exceeded 0.1 m s^{-1}. This finding confirms the fact that the regulated river is a transitional environment between lotic and lentic-type ecosystems combining the hydrodynamics of both. Based on the validated models, we proposed a scaling approach to quantify the relevance of the dominant forcing mechanisms using the critical value of the wind speed, which depends on the mean flow velocity and the river depth. As flow regulation appears to be important for the temporal dynamics of the near-surface turbulence, future studies should focus on the daily and sub-daily flow variations and how they affect the temporal dynamics of biogeochemical cycling in such rivers.

6 References

Alin, S. R., Rasera, M. de F. F. L., Salimon, C. I., Richey, J. E., Holtgrieve, G. W., Krusche, A. V., & Snidvongs, A. (2011). Physical controls on carbon dioxide transfer velocity and flux in low-gradient river systems and implications for regional carbon budgets. *Journal of Geophysical Research*, *116*(G1), G01009. https://doi.org/10.1029/2010JG001398

Ataktürk, S. S., & Katsaros, K. B. (1999). Wind Stress and Surface Waves Observed on Lake Washington. *Journal of Physical Oceanography*. *29*(4), 633–650. https://doi.org/10.1175/1520-0485(1999)029<0633:WSASWO>2.0.CO;2

Aufdenkampe, A. K., Mayorga, E., Raymond, P. A., Melack, J. M., Doney, S. C., Alin, S. R., Aalto, R. E., & Yoo, K. (2011). Riverine coupling of biogeochemical cycles between land, oceans, and atmosphere. *Frontiers in Ecology and the Environment*, *9*(1), 53–60. https://doi.org/10.1890/100014

Balsamo, G., Salgado, R., Dutra, E., Boussetta, S., Stockdale, T., & Potes, M. (2012). On the contribution of lakes in predicting near-surface temperature in a global weather forecasting model. *Tellus A: Dynamic Meteorology and Oceanography*, *64*(1), 15829. https://doi.org/10.3402/tellusa.v64i0.15829

Bastviken, D., Tranvik, L. J., Downing, J. A., Crill, P. M., & Enrich-Prast, A. (2011). Freshwater Methane Emissions Offset the Continental Carbon Sink. *Science*, *331*(6013), 50–50. https://doi.org/10.1126/science.1196808

Blanken, P. D., Rouse, W. R., Culf, A. D., Spence, C., Boudreau, L. D., Jasper, J. N., Kochtubajda, B., Schertzer, W. M., Marsh, P., & Verseghy, D. (2000). Eddy covariance measurements of evaporation from Great Slave Lake, Northwest Territories, Canada. *Water Resources Research*, *36*(4), 1069–1077. https://doi.org/10.1029/1999WR900338

Boegman, L., Ivey, G. N., & Imberger, J. (2005). The energetics of large-scale internal wave degeneration in lakes. *Journal of Fluid Mechanics*, *531*, 159–180. https://doi.org/10.1017/S0022112005003915

Brutsaert, W., & Yeh, G.-T. (1970). Implications of a Type of Empirical Evaporation Formula for Lakes and Pans. *Water Resources Research*, *6*(4), 1202–1208. https://doi.org/10.1029/WR006i004p01202

Burba, G. G., & Anderson, D. J. (2010). *A Brief Practical Guide to Eddy Covariance Flux Measurements: Principles and Workflow Examples for Scientific and Industrial Applications*. LI-COR Biosciences.

Changnon, S. A., & Jones, D. M. A. (1972). Review of the influences of the Great Lakes on weather. *Water Resources Research*, *8*(2), 360–371. https://doi.org/10.1029/WR008i002p00360

Charnock, H. (1955). Wind stress on a water surface. *Quarterly Journal of the Royal Meteorological Society*, *81*(350), 639–640. https://doi.org/10.1002/qj.49708135027

Chickadel, C. C., Talke, S. A., Horner-Devine, A. R., & Jessup, A. T. (2011). Infrared-Based Measurements of Velocity, Turbulent Kinetic Energy, and Dissipation at the Water Surface in a Tidal River. *IEEE Geoscience and Remote Sensing Letters*, *8*(5), 849–853. https://doi.org/10.1109/LGRS.2011.2125942

References

Cole, J. J., Prairie, Y. T., Caraco, N. F., McDowell, W. H., Tranvik, L. J., Striegl, R. G., Duarte, C. M., Kortelainen, P., Downing, J. A., Middelburg, J. J., & Melack, J. (2007). Plumbing the Global Carbon Cycle: Integrating Inland Waters into the Terrestrial Carbon Budget. *Ecosystems*, *10*(1), 172–185. https://doi.org/10.1007/s10021-006-9013-8

DelSontro, T., Beaulieu, J. J., & Downing, J. A. (2018). Greenhouse gas emissions from lakes and impoundments: Upscaling in the face of global change. *Limnology and Oceanography Letters*, *3*(3), 64–75. https://doi.org/10.1002/lol2.10073

Dias, N. L., & Vissotto, D. (2017). The effect of temperature-humidity similarity on Bowen ratios, dimensionless standard deviations, and mass transfer coefficients over a lake: Temperature-Humidity Similarity over a Lake. *Hydrological Processes*, *31*(2), 256–269. https://doi.org/10.1002/hyp.10925

Donelan, A. (1990). Air-sea interaction. In *The Sea* (Vol. 9, pp. 239–292). Environment and Climate Change Canada.

Donelan, M. (1982). The dependence of the aerodynamic drag coefficient on wave parameters. *Proc.. First Int. Conf. on Meteorology and Air-Sea Interaction of the Coastal Zone*, 381–387.

Eerola, K., Rontu, L., Kourzeneva, E., Pour, H. K., & Duguay, C. (2014). Impact of partly ice-free Lake Ladoga on temperature and cloudiness in an anticyclonic winter situation – a case study using a limited area model. *Tellus A: Dynamic Meteorology and Oceanography*, *66*(1), 23929. https://doi.org/10.3402/tellusa.v66.23929

Fairall, C. W., Bradley, E. F., Hare, J. E., Grachev, A. A., & Edson, J. B. (2003). Bulk Parameterization of Air–Sea Fluxes: Updates and Verification for the COARE Algorithm. *Journal of Climate*, *16*(4), 571–591. https://doi.org/10.1175/1520-0442(2003)016<0571:BPOASF>2.0.CO;2

Fernández Castro, B., Bouffard, D., Troy, C., Ulloa, H. N., Piccolroaz, S., Sepúlveda Steiner, O., Chmiel, H. E., Serra Moncadas, L., Lavanchy, S., & Wüest, A. (2021). Seasonality modulates wind-driven mixing pathways in a large lake. *Communications Earth & Environment*, *2*(1), 215. https://doi.org/10.1038/s43247-021-00288-3

Fernández Castro, B., Peña, M., Nogueira, E., Gilcoto, M., Broullón, E., Comesaña, A., Bouffard, D., Naveira Garabato, A. C., & Mouriño-Carballido, B. (2022). Intense upper ocean mixing due to large aggregations of spawning fish. *Nature Geoscience*, *15*(4), 287–292. https://doi.org/10.1038/s41561-022-00916-3

Foken, T. (2008). *Micrometeorology*. Springer Berlin Heidelberg. https://doi.org/10.1007/978-3-540-74666-9

Garratt, J. R. (1977). Review of Drag Coefficients over Oceans and Continents. *Monthly Weather Review*, *105*(7), 915–929. https://doi.org/10.1175/1520-0493(1977)105<0915:RODCOO>2.0.CO;2

Geernaert, G. L. (1990). Bulk Parameterizations for the Wind Stress and Heat Fluxes. In G. L. Geernaert & W. L. Plant (Eds.), *Surface Waves and Fluxes* (pp. 91–172). Springer Netherlands. https://doi.org/10.1007/978-94-009-2069-9_5

Ghan, S., Crawford, J., Langematz, U., Leung, R., Li, Z., Russell, L., Steiner, A., & Zhang, C. (2016). Author contributions can be clarified. *Journal of Geophysical Research: Atmospheres*, *121*(14), 8155–8155. https://doi.org/10.1002/2016JD025417

Grachev, A. A., Fairall, C. W., & Larsen, S. E. (1998). On the Determination of the Neutral Drag Coefficient in the Convective Boundary Layer. *Boundary-Layer Meteorology*, *86*(2), 257–278. https://doi.org/10.1023/A:1000617300732

Grill, G., Lehner, B., Thieme, M., Geenen, B., Tickner, D., Antonelli, F., Babu, S., Borrelli, P., Cheng, L., Crochetiere, H., Ehalt Macedo, H., Filgueiras, R., Goichot, M., Higgins, J., Hogan, Z., Lip, B., McClain, M. E., Meng, J., Mulligan, M., … Zarfl, C. (2019). Mapping the world's free-flowing rivers. *Nature*, *569*(7755), 215–221. https://doi.org/10.1038/s41586-019-1111-9

Guseva, S., Casper, P., Sachs, T., Spank, U., & Lorke, A. (2021). Energy Flux Paths in Lakes and Reservoirs. *Water*, *13*(22), 3270. https://doi.org/10.3390/w13223270

Harbeck, G. E. (1962). *A Practical Field Technique for Measuring Reservoir Evaporation Utilizing Mass-Transfer Theory*. 101–105.

Hasselmann, K. F., Barnett, T., Bouws, E., Carlson, H., Cartwright, D., Enke, K., Ewing, J., Gienapp, H., Hasselmann, D., Meerburg, A., Mueller, P., Olbers, D., Richter, K., Sell, W., & Walden, H. (1973). *Measurements of wind-wave growth and swell decay during the joint North Sea wave project (JONSWAP)*. *12*. http://hdl.handle.net/21.11116/0000-0007-DD3C-E

Heyna, B., & Groen, P. (1958). On short-period internal gravity waves. *Physica*, *24*(1–5), 383–389. https://doi.org/10.1016/S0031-8914(58)95455-7

Hicks, B. B. (1972). Some evaluations of drag and bulk transfer coefficients over water bodies of different sizes. *Boundary-Layer Meteorology*, *3*(2), 201–213. https://doi.org/10.1007/BF02033919

Huisman, J., Sharples, J., Stroom, J. M., Visser, P. M., Kardinaal, W. E. A., Verspagen, J. M. H., & Sommeijer, B. (2004). Changes in turbulent mixing shift competition for light between phytoplankton species. *Ecology*, *85*(11), 2960–2970. https://doi.org/10.1890/03-0763

Imberger, J. (1998). Flux paths in a stratified lake: A review. In *Physical processes in lakes and oceans* (pp. 1–17).

Imboden, D. M. (2003). The Motion of Lake Waters. In P. E. O'Sullivan & C. S. Reynolds (Eds.), *The Lakes Handbook, Volume 1* (pp. 115–152). Blackwell Science Ltd. https://doi.org/10.1002/9780470999271.ch6

Imboden, D. M., & Wüest, A. (1995). Mixing Mechanisms in Lakes. In A. Lerman, D. M. Imboden, & J. R. Gat (Eds.), *Physics and Chemistry of Lakes* (pp. 83–138). Springer Berlin Heidelberg. https://doi.org/10.1007/978-3-642-85132-2_4

Ishikawa, M., Bleninger, T., & Lorke, A. (2021). Hydrodynamics and mixing mechanisms in a subtropical reservoir. *Inland Waters*. https://doi.org/10.1080/20442041.2021.1932391

Kantha, L., & Clayson, C. (2000). *Small Scale Processes in Geophysical Fluid Flows* (1st Edition, Vol. 67). Academic Press.

Kato, H., & Takahashi, H. (1981). Local Climate near the Small Lake. *Journal of Agricultural Meteorology*, *37*(1), 29–37. https://doi.org/10.2480/agrmet.37.29

Katul, G., & Liu, H. (2017). Multiple mechanisms generate a universal scaling with dissipation for the air-water gas transfer velocity. *Geophysical Research Letters*, *44*(4), 1892–1898. https://doi.org/10.1002/2016GL072256

Kokic, J., Sahlée, E., Sobek, S., Vachon, D., & Wallin, M. B. (2018). High spatial variability of gas transfer velocity in streams revealed by turbulence measurements. *Inland Waters*, *8*(4), 461–473. https://doi.org/10.1080/20442041.2018.1500228

Kundu, P. K., Cohen, I. M., & Dowling, D. R. (2012). Gravity Waves. In *Fluid Mechanics* (pp. 253–307). Elsevier. https://doi.org/10.1016/B978-0-12-382100-3.10007-1

Kunze, E. (2019). Biologically Generated Mixing in the Ocean. *Annual Review of Marine Science*, *11*(1), 215–226. https://doi.org/10.1146/annurev-marine-010318-095047

Kuznetsova, A., Baydakov, G., Papko, V., Kandaurov, A., Vdovin, M., Sergeev, D., & Troitskaya, Y. (2016). Field and numerical study of the wind-wave regime on the Gorky Reservoir. *GEOGRAPHY, ENVIRONMENT, SUSTAINABILITY*, *9*(2), 19–37. https://doi.org/10.15356/2071-9388_02v09_2016_02

Lamont, J. C., & Scott, D. S. (1970). An eddy cell model of mass transfer into the surface of a turbulent liquid. *AIChE Journal*, *16*(4), 513–519. https://doi.org/10.1002/aic.690160403

Large, W. G., & Pond, S. (1981). *Open ocean momentum flux measurements in moderate to strong winds*. *11*(3), 324–336. https://doi.org/10.1175/1520-0485(1981)011<0324:OOMFMI>2.0.CO;2

Li, Z., Lyu, S., Zhao, L., Wen, L., Ao, Y., & Wang, S. (2016). Turbulent transfer coefficient and roughness length in a high-altitude lake, Tibetan Plateau. *Theoretical and Applied Climatology*, *124*(3–4), 723–735. https://doi.org/10.1007/s00704-015-1440-z

Lin, W., Sanford, L. P., Suttles, S. E., & Valigura, R. (2002). Drag Coefficients with Fetch-Limited Wind Waves*. *Journal of Physical Oceanography*, *32*(11), 3058–3074. https://doi.org/10.1175/1520-0485(2002)032<3058:DCWFLW>2.0.CO;2

Liu, C., Li, Y., Gao, Z., Zhang, H., Wu, T., Lu, Y., & Zhang, X. (2020). Improvement of Drag Coefficient Calculation Under Near-Neutral Conditions in Light Winds Over land. *Journal of Geophysical Research: Atmospheres*, *125*(24). https://doi.org/10.1029/2020JD033472

Ljungemyr, P., Gustafsson, N., & Omstedt, A. (1996). Parameterization of lake thermodynamics in a high-resolution weather forecasting model. *Tellus A*, *48*(5), 608–621. https://doi.org/10.1034/j.1600-0870.1996.t01-4-00002.x

Lorke, A., & MacIntyre, S. (2009). The Benthic Boundary Layer (in Rivers, Lakes, and Reservoirs). In *Encyclopedia of Inland Waters* (pp. 505–514). Elsevier. https://doi.org/10.1016/B978-012370626-3.00079-X

Lorke, A., McGinnis, D. F., Spaak, P., & Wuest, A. (2004). Acoustic observations of zooplankton in lakes using a Doppler current profiler. *Freshwater Biology*, *49*(10), 1280–1292. https://doi.org/10.1111/j.1365-2427.2004.01267.x

Lorke, A., Müller, B., Maerki, M., & Wüest, A. (2003). Breathing sediments: The control of diffusive transport across the sediment-water interface by periodic boundary-layer turbulence. *Limnology and Oceanography*, *48*(6), 2077–2085. https://doi.org/10.4319/lo.2003.48.6.2077

Lorke, A., Weber, A., Hofmann, H., & Peeters, F. (2008). Opposing diel migration of fish and zooplankton in the littoral zone of a large lake. *Hydrobiologia*, *600*(1), 139–146. https://doi.org/10.1007/s10750-007-9183-1

Lükő, G., Torma, P., Krámer, T., Weidinger, T., Vecenaj, Z., & Grisogono, B. (2020). Observation of wave-driven air–water turbulent momentum exchange in a large but fetch-limited shallow lake. *Advances in Science and Research*, *17*, 175–182. https://doi.org/10.5194/asr-17-175-2020

MacIntyre, S. (1993). Vertical mixing in a shallow, eutrophic lake: Possible consequences for the light climate of phytoplankton. *Limnology and Oceanography*, *38*(4), 798–817. https://doi.org/10.4319/lo.1993.38.4.0798

MacIntyre, S., & Jellison, R. (2001). Nutrient fluxes from upwelling and enhanced turbulence at the top of the pycnocline in Mono Lake, California. *Hydrobiologia*, *466*(1/3), 13–29. https://doi.org/10.1023/A:1014563914112

MacIntyre, S., Jonsson, A., Jansson, M., Aberg, J., Turney, D. E., & Miller, S. D. (2010). Buoyancy flux, turbulence, and the gas transfer coefficient in a stratified lake: Turbulence and gas evasion in lakes. *Geophysical Research Letters*, *37*(24), n/a-n/a. https://doi.org/10.1029/2010GL044164

MacIntyre, S., Wanninkhof, R., & Chanton, J. P. (1995). Trace gas exchange across the air–water interface in freshwater and coastal marine environments. In *Biogenic trace gasses: Measuring emissions from soil and water* (eds Matson, P. A. & Harris, R. C., pp. 52–97).

Mammarella, I., Nordbo, A., Rannik, Ü., Haapanala, S., Levula, J., Laakso, H., Ojala, A., Peltola, O., Heiskanen, J., Pumpanen, J., & Vesala, T. (2015). Carbon dioxide and energy fluxes over a small boreal lake in Southern Finland: CO_2 and Energy Fluxes Over Lake. *Journal of Geophysical Research: Biogeosciences*, *120*(7), 1296–1314. https://doi.org/10.1002/2014JG002873

Mironov, D., Heise, E., Kourzeneva, E., Ritter, B., Schneider, N., & Terzhevik, A. (2010). *Implementation of the lake parameterization scheme FLake into the numerical weather prediction model COSMO*. *15*, 218-- 230.

Nezu, I. (1977). *Turbulent structure in open-channel flows*. Kyoto University.

Nikora, V. I., & Smart, G. M. (1996). A Simple Model of Turbulence Intensity and Turbulence Scale Distribution in Gravel Bed Rivers. In S. Gavrilakis, L. Machiels, & P. A. Monkewitz (Eds.), *Advances in Turbulence VI* (Vol. 36, pp. 171–174). Springer Netherlands. https://doi.org/10.1007/978-94-009-0297-8_47

Nordbo, A., Launiainen, S., Mammarella, I., Leppäranta, M., Huotari, J., Ojala, A., & Vesala, T. (2011). Long-term energy flux measurements and energy balance over a small boreal lake using eddy covariance technique. *Journal of Geophysical Research*, *116*(D2), D02119. https://doi.org/10.1029/2010JD014542

Panin, G. N., Nasonov, A. E., & Foken, T. (2006). Evaporation and heat exchange of a body of water with the atmosphere in a shallow zone. *Izvestiya, Atmospheric and Oceanic Physics*, *42*(3), 337–352. https://doi.org/10.1134/S0001433806030078

Peeters, F., Straile, D., Lorke, A., & Ollinger, D. (2007). Turbulent mixing and phytoplankton spring bloom development in a deep lake. *Limnology and Oceanography*, *52*(1), 286–298. https://doi.org/10.4319/lo.2007.52.1.0286

Perolo, P., Fernández Castro, B., Escoffier, N., Lambert, T., Bouffard, D., & Perga, M.-E. (2021). *Accounting for surface waves improves gas flux estimation at high wind speed in a large lake* [Preprint]. Dynamics of the Earth system: interactions. https://doi.org/10.5194/esd-2021-30

Preusse, M., Peeters, F., & Lorke, A. (2010). Internal waves and the generation of turbulence in the thermocline of a large lake. *Limnology and Oceanography*, *55*(6), 2353–2365. https://doi.org/10.4319/lo.2010.55.6.2353

Ravens, T. M., Kocsis, O., Wüest, A., & Granin, N. (2000). Small-scale turbulence and vertical mixing in Lake Baikal. *Limnology and Oceanography*, *45*(1), 159–173. https://doi.org/10.4319/lo.2000.45.1.0159

Raymond, P. A., Hartmann, J., Lauerwald, R., Sobek, S., McDonald, C., Hoover, M., Butman, D., Striegl, R., Mayorga, E., Humborg, C., Kortelainen, P., Dürr, H., Meybeck, M., Ciais, P., & Guth, P. (2013). Global carbon dioxide emissions from inland waters. *Nature*, *503*(7476), 355–359. https://doi.org/10.1038/nature12760

Raymond, P. A., Zappa, C. J., Butman, D., Bott, T. L., Potter, J., Mulholland, P., Laursen, A. E., McDowell, W. H., & Newbold, D. (2012). Scaling the gas transfer velocity and hydraulic geometry in streams and small rivers: Gas transfer velocity and hydraulic geometry. *Limnology and Oceanography: Fluids and Environments*, *2*(1), 41–53. https://doi.org/10.1215/21573689-1597669

Read, J. S., Hamilton, D. P., Desai, A. R., Rose, K. C., MacIntyre, S., Lenters, J. D., Smyth, R. L., Hanson, P. C., Cole, J. J., Staehr, P. A., Rusak, J. A., Pierson, D. C., Brookes, J. D., Laas, A., & Wu, C. H. (2012). Lake-size dependency of wind shear and convection as controls on gas exchange. *Geophysical Research Letters*, *39*(9). https://doi.org/10.1029/2012GL051886

Sahlée, E., Rutgersson, A., Podgrajsek, E., & Bergström, H. (2014). Influence from Surrounding Land on the Turbulence Measurements Above a Lake. *Boundary-Layer Meteorology*, *150*(2), 235–258. https://doi.org/10.1007/s10546-013-9868-0

Salgado, R., & Le Mogne, P. (2010). *Coupling the FLake model to the Surfex externalized surface model*. *15*, 231-- 244.

Schlichting, H. (1968). *Boundary-Layer Theory* (6th Edition). McGraw-Hill Book Company.

Simon, A. (1997). *Turbulent mixing in the surface boundary layer of lakes* [Dissertation No 12272]. Swiss Federal Institute of Technology.

Simoncelli, S., Thackeray, S. J., & Wain, D. J. (2017). Can small zooplankton mix lakes?: Can small zooplankton mix lakes? *Limnology and Oceanography Letters*, *2*(5), 167–176. https://doi.org/10.1002/lol2.10047

Simpson, J. H., Woolway, R. I., Scannell, B., Austin, M. J., Powell, B., & Maberly, S. C. (2021). The Annual Cycle of Energy Input, Modal Excitation and Physical Plus Biogenic Turbulent Dissipation in a Temperate Lake. *Water Resources Research*, *57*(6). https://doi.org/10.1029/2020WR029441

Smith, I. R. (1979). Hydraulic conditions in isothermal lakes. *Freshwater Biology*, *9*(2), 119–145. https://doi.org/10.1111/j.1365-2427.1979.tb01496.x

Sobek, S., Durisch-Kaiser, E., Zurbrügg, R., Wongfun, N., Wessels, M., Pasche, N., & Wehrli, B. (2009). Organic carbon burial efficiency in lake sediments controlled by oxygen exposure time and sediment source. *Limnology and Oceanography*, *54*(6), 2243–2254. https://doi.org/10.4319/lo.2009.54.6.2243

Spank, U., Hehn, M., Keller, P., Koschorreck, M., & Bernhofer, C. (2020). A Season of Eddy-Covariance Fluxes Above an Extensive Water Body Based on Observations from a Floating Platform. *Boundary-Layer Meteorology*, *174*(3), 433–464. https://doi.org/10.1007/s10546-019-00490-z

Stepanenko, V., Jöhnk, K. D., Machulskaya, E., Perroud, M., Subin, Z., Nordbo, A., Mammarella, I., & Mironov, D. (2014). Simulation of surface energy fluxes and stratification of a small boreal lake by a set of one-dimensional models. *Tellus A: Dynamic Meteorology and Oceanography*, *66*(1), 21389. https://doi.org/10.3402/tellusa.v66.21389

Strub, T. P., & Powell, T. M. (1987). The exchange coefficients for latent and sensible heat flux over lakes: Dependence upon atmospheric stability. *Boundary-Layer Meteorology*, *40*(4), 349–362. https://doi.org/10.1007/BF00116102

Stull, R. B. (Ed.). (1988). *An Introduction to Boundary Layer Meteorology*. Springer Netherlands. https://doi.org/10.1007/978-94-009-3027-8

Sun, J., Lenschow, D. H., Mahrt, L., Crawford, T. L., Davis, K. J., Oncley, S. P., MacPherson, J. I., Wang, Q., Dobosy, R. J., & Desjardins, R. L. (1997). Lake-induced atmospheric circulations during BOREAS. *Journal of Geophysical Research: Atmospheres*, *102*(D24), 29155–29166. https://doi.org/10.1029/97JD01114

Tedford, E. W., MacIntyre, S., Miller, S. D., & Czikowsky, M. J. (2014). Similarity scaling of turbulence in a temperate lake during fall cooling. *Journal of Geophysical Research: Oceans*, *119*(8), 4689–4713. https://doi.org/10.1002/2014JC010135

Thiery, W., Davin, E. L., Seneviratne, S. I., Bedka, K., Lhermitte, S., & van Lipzig, N. P. M. (2016). Hazardous thunderstorm intensification over Lake Victoria. *Nature Communications*, *7*(1), 12786. https://doi.org/10.1038/ncomms12786

Tranvik, L. J., Downing, J. A., Cotner, J. B., Loiselle, S. A., Striegl, R. G., Ballatore, T. J., Dillon, P., Finlay, K., Fortino, K., Knoll, L. B., Kortelainen, P. L., Kutser, T., Larsen, Soren., Laurion, I., Leech, D. M., McCallister, S. L., McKnight, D. M., Melack, J. M., Overholt, E., … Weyhenmeyer, G. A. (2009). Lakes and reservoirs as regulators of carbon cycling and climate. *Limnology and Oceanography*, *54*(6part2), 2298–2314. https://doi.org/10.4319/lo.2009.54.6_part_2.2298

Ulseth, A. J., Hall, R. O., Boix Canadell, M., Madinger, H. L., Niayifar, A., & Battin, T. J. (2019). Distinct air–water gas exchange regimes in low- and high-energy streams. *Nature Geoscience*, *12*(4), 259–263. https://doi.org/10.1038/s41561-019-0324-8

Vesala, T., Huotari, J., Rannik, Ü., Suni, T., Smolander, S., Sogachev, A., Launiainen, S., & Ojala, A. (2006). Eddy covariance measurements of carbon exchange and latent and sensible heat fluxes over a boreal lake for a full open-water period. *Journal of Geophysical Research*, *111*(D11), D11101. https://doi.org/10.1029/2005JD006365

Vickers, D., & Mahrt, L. (1997). Fetch Limited Drag Coefficients. *Boundary-Layer Meteorology*, *85*(1), 53–79. https://doi.org/10.1023/A:1000472623187

Wallin, M. B., Campeau, A., Audet, J., Bastviken, D., Bishop, K., Kokic, J., Laudon, H., Lundin, E., Löfgren, S., Natchimuthu, S., Sobek, S., Teutschbein, C., Weyhenmeyer, G. A., & Grabs, T. (2018). Carbon dioxide and methane emissions of Swedish low-order streams—A national estimate and lessons learnt from more than a decade of observations. *Limnology and Oceanography Letters*, *3*(3), 156–167. https://doi.org/10.1002/lol2.10061

Wei, Z., Miyano, A., & Sugita, M. (2016). Drag and Bulk Transfer Coefficients Over Water Surfaces in Light Winds. *Boundary-Layer Meteorology*, *160*(2), 319–346. https://doi.org/10.1007/s10546-016-0147-8

Wetzel, R. G. (2001). *Limnology: Lake and river ecosystems*. http://site.ebrary.com/id/10606261

Woolway, R. I., & Simpson, J. H. (2017). Energy input and dissipation in a temperate lake during the spring transition. *Ocean Dynamics*, *67*(8), 959–971. https://doi.org/10.1007/s10236-017-1072-1

Woolway, R. I., Verburg, P., Merchant, C. J., Lenters, J. D., Hamilton, D. P., Brookes, J., Kelly, S., Hook, S., Laas, A., Pierson, D., Rimmer, A., Rusak, J. A., & Jones, I. D. (2017). Latitude and lake size are important predictors of over-lake atmospheric stability: Atmospheric Stability Above Lakes. *Geophysical Research Letters*, *44*(17), 8875–8883. https://doi.org/10.1002/2017GL073941

Wu, J. (1988). Wind-Stress Coefficients at Light Winds. *Journal of Atmospheric and Oceanic Technology*, *5*(6), 885–888. https://doi.org/10.1175/1520-0426(1988)005<0885:WSCALW>2.0.CO;2

Wu, J. (1994). The sea surface is aerodynamically rough even under light winds. *Boundary-Layer Meteorology*, *69*(1–2), 149–158. https://doi.org/10.1007/BF00713300

Wüest, A., & Lorke, A. (2003). Small-Scale Hydrodynamics in Lakes. *Annual Review of Fluid Mechanics*, *35*(1), 373–412. https://doi.org/10.1146/annurev.fluid.35.101101.161220

Wüest, A., Piepke, G., & Van Senden, D. C. (2000). Turbulent kinetic energy balance as a tool for estimating vertical diffusivity in wind-forced stratified waters. *Limnology and Oceanography*, *45*(6), 1388–1400. https://doi.org/10.4319/lo.2000.45.6.1388

Xiao, W., Liu, S., Wang, W., Yang, D., Xu, J., Cao, C., Li, H., & Lee, X. (2013). Transfer Coefficients of Momentum, Heat and Water Vapour in the Atmospheric Surface Layer of a Large Freshwater Lake. *Boundary-Layer Meteorology*, *148*(3), 479–494. https://doi.org/10.1007/s10546-013-9827-9

Yang, Y., Colom, W., Pierson, D., & Pettersson, K. (2016). Water column stability and summer phytoplankton dynamics in a temperate lake (Lake Erken, Sweden). *Inland Waters*, *6*(4), 499–508. https://doi.org/10.1080/IW-6.4.874

Zappa, C. J., McGillis, W. R., Raymond, P. A., Edson, J. B., Hintsa, E. J., Zemmelink, H. J., Dacey, J. W. H., & Ho, D. T. (2007). Environmental turbulent mixing controls on air-water gas exchange in marine and aquatic systems. *Geophysical Research Letters*, *34*(10), L10601. https://doi.org/10.1029/2006GL028790

Author Contributions

This thesis is based on three original research articles provided in *Appendices I-III* which were created in collaboration with all of the authors. I am the corresponding author of all three articles (Parts 1, 2, and 3 of the thesis). The contributions of all authors based on the so-called CrediT standard (Ghan et al., 2016) are explained in the following:

Part 1

Guseva, S., Casper, P., Sachs, T., Spank, U., & Lorke, A. (2021). Energy flux paths in lakes and reservoirs. *Water*, 13(22), 3270. *MDPI AG*. doi: http://dx.doi.org/10.3390/w13223270.

Conceptualization: SG, AL

Methodology: SG, AL

Software: SG, AL

Formal Analysis: SG

Investigation: SG, AL

Resources: SG, US, PC, TS

Data Curation: SG, TS, US, PC

Writing—Original Draft Preparation: SG

Writing—Review and Editing: AL, PC, TS,

Visualization: SG

Supervision: AL

Project Administration: SG

Funding Acquisition: AL

Part 2

Guseva, S., Armani, F., Desai, A. R., Dias, N. L., Friborg, T., Iwata, H., Jansen, J., Lükő, G., Mammarella, I., Repina, I., Rutgersson, A., Sachs, T., Scholz, K., Spank, U., Stepanenko, V. M., Torma, P., Vesala, T., & Lorke A. (2022) Bulk transfer coefficients estimated from eddy-covariance measurements over lakes and reservoirs. *Submitted to Journal of Geophysical Research: Atmospheres*. Preprint doi: https://doi.org/10.1002/essoar.10511514.1.

Conceptualization: SG, AL

Methodology: SG, AL, HI, ARD

Software: SG

Formal Analysis: SG

Investigation: SG, AL, HI, ARD

Resources: SG, FA, ARD, NLD, TF, JJ, IR, IM, AR, TS, KS, US, PT, TV

Data Curation: SG, FA, HI, JJ, GL, IR, AR, KS, US, PT

Writing—Original Draft Preparation: SG

Writing—Review and Editing: AL, FA, A NLD, TF, HI, JJ, GL, IM, IR, AR, TS, KS, VS, PT, TV

Visualization: SG

Supervision: AL

Project Administration: SG

Funding Acquisition: AL

Part 3

Guseva, S., Aurela, M., Cortés, A., Kivi, R., Lotsari, E., MacIntyre, S., Mammarella, I., Ojala, A., Stepanenko, V., Uotila, P., Vähä, A., Vesala, T., Wallin, M. B., & Lorke, A. (2021). Variable physical drivers of near-surface turbulence in a regulated river. *Water Resources Research*, 57, e2020WR027939. doi: https://doi.org/10.1029/2020WR027939.

Conceptualization: SG, AL, SM

Methodology: SG, AL, VS, SM

Software: SG, AL, SM, AC, VS

Formal Analysis: SG, AC, VS

Investigation: SG, AL, SM

Resources: SG, MA, RK, EL, SM, IM, AO, VS, AV, TV, MBW, AL

Data Curation: SG, SM, AV, AC, MA

Writing—Original Draft Preparation: SG

Writing—Review and Editing: AL, SM, IM, VS, TV, MA, AC, RK, EL, AO, PU, AV, MBW

Visualization: SG, AV, EL

Supervision: AL, SM

Project Administration: SG

Funding Acquisition: AL

Declaration

I hereby declare that the thesis entitled "*Energy flux paths and air-water exchange in freshwater ecosystems*" is the result of my own work except where otherwise indicated. It has not been submitted for any other degree at another university or scientific institution.

Landau, 07 October 2022   ……………………………………………

Curriculum Vitae

Name: Sofya Guseva
Url: https://www.researchgate.net/profile/Sofya-Guseva

History of the academic career:

2001 – 2011	Moscow Secondary school №315
2011 – 2015	Lomonosov Moscow State University (LMSU) Meteorology and Climatology Department, Faculty of Geography - Bachelor's programme of higher education; awarded the degree of Bachelor in the field of study "Hydrometeorology"
2015 – 2017	Lomonosov Moscow State University (LMSU) Meteorology and Climatology Department, Faculty of Geography - Master's programme of higher education; awarded the degree of Master in the field of study "Hydrometeorology". Title of the Master's thesis: "Numerical simulation of greenhouse gases in fresh water bodies"
2017 – Curr.	University of Koblenz-Landau Institute for Environmental Sciences PhD candidate - Dissertation topic: "Energy flux paths and air-water exchange in freshwater ecosystems"

Publications and science activity:

2016	Guseva, S., Stepanenko, V., Shurpali, N., Biasi, C., Marushchak, M. E., & Lind, S. E. (2016). Numerical simulation of methane emission from subarctic lake in Komi Republic (Russia). *Geography, Environment, Sustainability*, 9(2), 58-74. *https://doi.org/10.24057/2071-9388-2016-9-2-11-20*

2017	Poster "Harp Lake model intercomparison experiment: focus on vertical gas transfer". Participation in conference *Physical Processes in Natural Waters (PPNW)*, held on 21-25 August 2017, Finland.
2018	Participation in "*Block course Physical Limnology*" held on 2-6 April 2018, Heidelberg.
2020	Guseva, S., Bleninger, T., Jöhnk, K., Polli, B. A., Tan, Z., Thiery, W., ... & Stepanenko, V. (2020). Multimodel simulation of vertical gas transfer in a temperate lake. *Hydrology and Earth System Sciences*, 24(2), 697-715. *https://doi.org/10.5194/hess-24-697-2020*
2020	Oral presentation with a topic "Variable physical drivers of near-surface turbulence in a regulated river" in Workshop on Physical Processes in Natural Waters (PPNW), held on 15-18 June 2020, online.
2020	Oral presentation with a topic "Variable physical drivers of near-surface turbulence in a regulated river" in *American Geophysical Union (AGU) Fall Meeting*, held on 1-17 December 2020, online. *https://agu.confex.com/agu/fm20/meetingapp.cgi/Paper/661928*
2021	Guseva, S., Aurela, M., Cortés, A., Kivi, R., Lotsari, E., MacIntyre, S., …& Lorke, A. (2021). Variable physical drivers of near-surface turbulence in a regulated river. *Water Resources Research*, 57, e2020WR027939. *https://doi.org/10.1029/2020WR027939*
2021	Guseva, S., Casper, P., Sachs, T., Spank, U., & Lorke, A. (2021). Energy Flux Paths in Lakes and Reservoirs. *Water*, 13(22), 3270. *https://doi.org/10.3390/w13223270*
2022	Guseva, S., Armani, F., Desai, A. R., Dias, N. L., …& Lorke, A. (2022) Bulk Transfer Coefficients Estimated from Eddy-Covariance Measurements over Lakes and Reservoirs. *Submitted to Journal of Geophysical Research: Atmospheres*. Doi of the preprint: https://doi.org/10.1002/essoar.10511514.1

Acknowledgements

This thesis could not exist without many people who supported and helped me throughout the research. First and foremost, I want to thank my supervisor Andreas Lorke for the endless support. I was often amazed by his ability to capture the scientific essence and connect things in whatever area was discussed. Our discussions were interesting, productive and inspiring, even though at the beginning they were challenging for me since I had much to learn. During our field campaigns, I learned from Andreas to carefully prepare everything in advance and be ready to improvise if something goes wrong. I am also grateful to my previous supervisor Victor Stepanenko, who originally encouraged me to pursue a career in science and supported me throughout the research.

Among other brilliant scientists I met, was Sally MacIntyre, who always inspired me and burst with energy in every situation. Together with her husband and a great scientist John Melack, Sally helped me during the field campaign at the River Kitinen, sharing the knowledge about how field measurements should be prepared and carried out. They also helped me with the review of the first article.

I would like to thank Angelika Holderle, Christoph Bors, Aki Vähä, Daniela Franz, Risto Taipale, Rigel Kivi, Mika Aurela, Anders Lindroth, John Melack, Peter Casper, Gonzalo Santaolalla, Jens Nejstgaard, Tim Walles, Christian Wille, Philipp Keller, Matthias Koschorreck, Christian Bernhofer, Heiko Prasse, Uwe Eichelmann, Markus Hehn and Martin Wieprecht, without whom the field campaigns in the River Kitinen, Bautzen Reservoir and Lake Dagow would not be possible. Special thanks to Uwe Spank for showing me how thorough, careful and well-planned measurements can be. And of course, I am grateful to Timo Vesala for organizing the River Kitinen campaign and the "Physical Processes in Natural Waters" workshop in 2017 at such a high level. Additionally, I would like to thank Werner Eugster, Ivan Mammarella, Hiroki Iwata, Ankur R. Desai, Nelson L. Dias, Torsten Sachs, Thomas Friborg, Joachin Jansen, Rafael de Carvalho Bueno, Gabriella Lükő, Péter Torma, Katharina Scholz, Irina Repina, Anna Rutgersson, Fernando Armani, Marcus B. Wallin, Anne Ojala, Alicia Cortés and Eliisa Lotsari for the fruitful collaboration.

I would like to thank my co-examiner Prof. Alfred Johny Wüest and the chair of the dissertation committee Mirco Bundschuh for thoughtful questions and for making my doctoral defense possible.

I also want to thank Alexander Shamanskiy, my friend at the beginning and my husband at the end; without his tremendous support I could not make it all the way through this PhD. He gave an inspiring example by finishing a PhD himself, motivated me to improve my imperfect writing and provided mathematical advice. And I really appreciate the support of all my large family and friends who always believed in me.

Finally, I thank all my colleagues at the university: Mayra Ishikawa and Lianghong Long, with whom we brain-stormed many issues at the beginning (for example, how to estimate the energy dissipation rates from the data); Jihyeon Kim who impressed me with her absolute energy and passion for science and experiments and Christian Noss, Jeremy Wilkinson, Pascal Bodmer, Liu Liu, Lorenzo Rovelli, Gerrit Rau, Clara Mendoza-Lera, Lediane Marcon, with whom I always had great scientific discussions. Overall, I count here more than fifty people who were of great importance to me during the creation of this work, and I am eternally grateful for their support.

Appendices

Appendix I

Energy flux paths in lakes and reservoirs

S. Guseva[1], P. Casper[2], T. Sachs[3], U. Spank[4], and A. Lorke[1]

[1] Institute for Environmental Sciences, University of Koblenz-Landau, 76829 Landau, Germany;
[2] Department of Experimental Limnology, Leibniz-Institute of Freshwater Ecology and Inland Fisheries, 12587 Berlin, Germany;
[3] GFZ German Research Centre for Geosciences, 14473 Potsdam, Germany;
[4] Institute of Hydrology and Meteorology, Chair of Meteorology, Technische Universität Dresden, 01069 Dresden, Germany.

Please click on the following link to read the publication

Energy Flux Paths in Lakes and Reservoirs

Sofya Guseva [1,*], Peter Casper [2], Torsten Sachs [3], Uwe Spank [4] and Andreas Lorke [1]

[1] Institute for Environmental Sciences, University of Koblenz-Landau, 76829 Landau, Germany; lorke@uni-landau.de
[2] Department of Experimental Limnology, Leibniz-Institute of Freshwater Ecology and Inland Fisheries, 12587 Berlin, Germany; pc@igb-berlin.de
[3] GFZ German Research Centre for Geosciences, 14473 Potsdam, Germany; torsten.sachs@gfz-potsdam.de
[4] Institute of Hydrology and Meteorology, Chair of Meteorology, Technische Universität Dresden, 01069 Dresden, Germany; Uwe.Spank@tu-dresden.de
[*] Correspondence: guseva@uni-landau.de

Abstract: Mechanical energy in lakes is present in various types of water motion, including turbulent flows, surface and internal waves. The major source of kinetic energy is wind forcing at the water surface. Although a small portion of the vertical wind energy flux in the atmosphere is transferred to water, it is crucial for physical, biogeochemical and ecological processes in lentic ecosystems. To examine energy fluxes and energy content in surface and internal waves, we analyze extensive datasets of air- and water-side measurements collected at two small water bodies (<10 km^2). For the first time we use directly measured atmospheric momentum fluxes. The estimated energy fluxes and content agree well with results reported for larger lakes, suggesting that the energetics governing water motions in enclosed basins is similar, independent of basin size. The largest fraction of wind energy flux is transferred to surface waves and increases strongly nonlinearly for wind speeds exceeding 3 m s^{-1}. The energy content is largest in basin-scale and high-frequency internal waves but shows seasonal variability and varies among aquatic systems. At one of the study sites, energy dissipation rates varied diurnally, suggesting biogenic turbulence, which appears to be a widespread phenomenon in lakes and reservoirs.

Keywords: energy fluxes; energy content; lakes; reservoirs; internal waves; surface waves; biogenic turbulence

1. Introduction

The spatial distribution and temporal dynamics of mechanical energy play vital roles in the physical, biogeochemical and ecological functioning of lentic ecosystems. At the water surface, wind-generated turbulence regulates the vertical distribution of heat that is exchanged with the atmosphere, affects thermal stratification [1] and controls gas exchange with the atmosphere [2], which can be enhanced by surface waves [3]. Vertical turbulent mixing in the surface layer controls the exposure of planktonic organisms to light, therewith regulating primary production and community composition of phytoplankton [4–6]. Wind-induced upwelling [7,8], as well as internal waves [9], affect phytoplankton and water quality by transporting nutrients from the stratified hypolimnion to the surface layer. The state of mixing of water bodies can result in the persistence of harmful cyanobacteria in the thermocline throughout summer stratification [10]. At the bottom of lakes and reservoirs, boundary layer turbulence controls the oxygen flux into the sediments [11] and therewith the rate of carbon burial and methane production [12], as well as the internal loading of the lake with nutrients [13].

The major source of mechanical energy in lentic systems is wind, which exerts a shear force at the water surface. However, only a small fraction of the vertical wind energy flux in the atmospheric boundary layer is transferred to water motions (~1.9% according to [14] and ~22% including surface waves in [15]). Water motions are distributed over

a wide range of temporal and spatial scales ranging from low to high frequencies of the energy spectrum [15]. Recently, energy transfer from wind to water has been found to be more efficient when the lake is thermally stratified, resulting in an enhancement of mean kinetic energy throughout the water column during seasonal stratification [16,17]. The majority of the wind energy flux is dissipated in the atmospheric and water surface boundary layers. A considerable part of the non-dissipated wind energy (~20%) is fed to the surface wave field [15]. In [18], however, this percentage is lower—1.5–3.5%, although both estimates were derived from the same set of observations conducted in a Swiss lake. Approximately 1% of the energy input is stored in large-scale currents such as basin-scale internal waves [15]. Shear instabilities lead to the degeneration of large-scale internal waves into propagating high-frequency internal waves. They appear at frequencies being some fraction of the maximum buoyancy frequency, which is related to the strength of vertical density stratification [19–21]. It has been estimated that about 90% of the energy in the internal waves is dissipated within the bottom boundary layer [14,15].

Current knowledge about the partitioning and distribution of energy fluxes in lakes and reservoirs described above is mainly based on observations from the same lake [16,17], or information compiled from asynchronously conducted measurements in different systems [15]. The generality of current figures, their transferability to water bodies of different size and depth, and their temporal dynamics remain largely unexplored. Moreover, all existing estimates are based on bulk parameterization of wind energy fluxes, as observations lack direct measurements of atmospheric fluxes [14–18]. The role of surface waves in the energy budget appears to be constraint by observations, which are restricted to a single study in a large lake [15,18].

To address these gaps in research, we analyze the most relevant components of energy fluxes and energy content in various types of water motions in response to wind energy fluxes in two small (<10 km^2) water bodies. The study sites, a lake and a reservoir, differ in surface area by one order of magnitude, but have comparable water depth (~10 m). Given the difference in surface area and the fact that the reservoir experiences water level variations, we expect the hydrodynamic processes in these two water bodies to be different. The selected lake is considered representative of a large number of small lakes, belonging to the most abundant size class which contributes 54% of the global lake surface area [22,23]. To overcome shortcomings of previous studies, we used direct measurements of momentum fluxes in the atmosphere above the water surface for the estimation of the wind energy flux into the lakes. We investigate the wind speed and fetch dependence on the surface wave characteristics based on measurements covering nearly a complete annual cycle. The predominant modes of basin-scale internal waves and the presence of high-frequency internal waves are identified and examined. The data are used to complement and to re-examine mean energy budgets of small lentic systems, their temporal dynamics, and their variation with water body size.

2. Materials and Methods

2.1. Study Sites and Measurements

Measurements were conducted at a small reservoir (Bautzen Reservoir, surface area: 5.33 km^2, volume: 39.2×10^6 m^3, maximum depth: 12.2 m) and a small lake (Lake Dagow, surface area: 0.3 km^2, volume: 1.2×10^6 m^3, maximum depth: 9.5 m)—both situated in Germany. Bautzen Reservoir is a part of the dammed river Spree in southeastern Germany, with a mean water residence time of 164 days [24]. It can be classified as a small storage-type reservoir [25,26] with additional purposes of flood control and leisure activities. Besides, the reservoir is used to regulate the water supply for wetlands and power stations located downstream of the river. The outlet tower located near the dam regulates water discharge through the bottom of the reservoir. Major water withdrawal in summer is associated with a gradual decrease of water level [27]. The reservoir is often not persistently stratified throughout the summer due to a lack of shelter against strong winds and experiences several full mixing events [24,28]. Lake Dagow is a glacial lake in the Lake Stechlin area in

northern Germany. It is a small eutrophic lake with a water residence time of 5 years [29]. The lake develops persistent density stratification every year leading to anoxic conditions in its hypolimnion [29]. Lake Dagow was impacted by wastewater, duck and carp farming in the 1960–1970s, with restoration activities in the 1980s.

At both water bodies, a similar set of instruments was installed for a period resolving the seasonal dynamics of stratification and mixing in Bautzen Reservoir (3 April until 3 December in 2018) and the transition from stratified to mixed conditions during the autumn overturn in Lake Dagow (11 September until 25 November in 2017). Meteorological measurements, including radiation fluxes and eddy covariance (EC) measurements of vertical momentum fluxes, were conducted from floating platforms (Points A and E, Figure 1). The platform was 3 × 3 m in size in Bautzen Reservoir and about 2.5 × 5 m in size in (Lake Dagow). Both platforms were attached with steel chains (Bautzen Reservoir) or guy wires (Lake Dagow) to four concrete anchors at the bottom. Vertical profiles of flow velocity in the water column, including turbulent velocity fluctuations, were measured by acoustic Doppler current profilers (ADCP), which were mounted downward-facing at the platforms (see Table 1). In Bautzen reservoir, the profiling range of the platform-mounted ADCP did not cover the entire water column and an additional ADCP was deployed at the bottom at ~10 m distance from the platform. The bottom-mounted instrument did not resolve turbulent velocity fluctuations and provided mean flow velocity profiles only. In Lake Dagow, there were three sequential ADCP deployments with time gaps in between. The ADCP was installed at the bottom during the second and third deployments. Thermistor chains were deployed at the platform in Bautzen Reservoir and in the middle of Lake Dagow to observe vertical temperature stratification in water. Wave recorders (high-frequency pressure loggers) were placed near the shore at both locations and an additional wave recorder was installed at the platform in Bautzen Reservoir. The measurement campaign lasted from 3 April until 3 December in 2018 in Bautzen Reservoir and from 11 September until 25 November in 2017 in Lake Dagow.
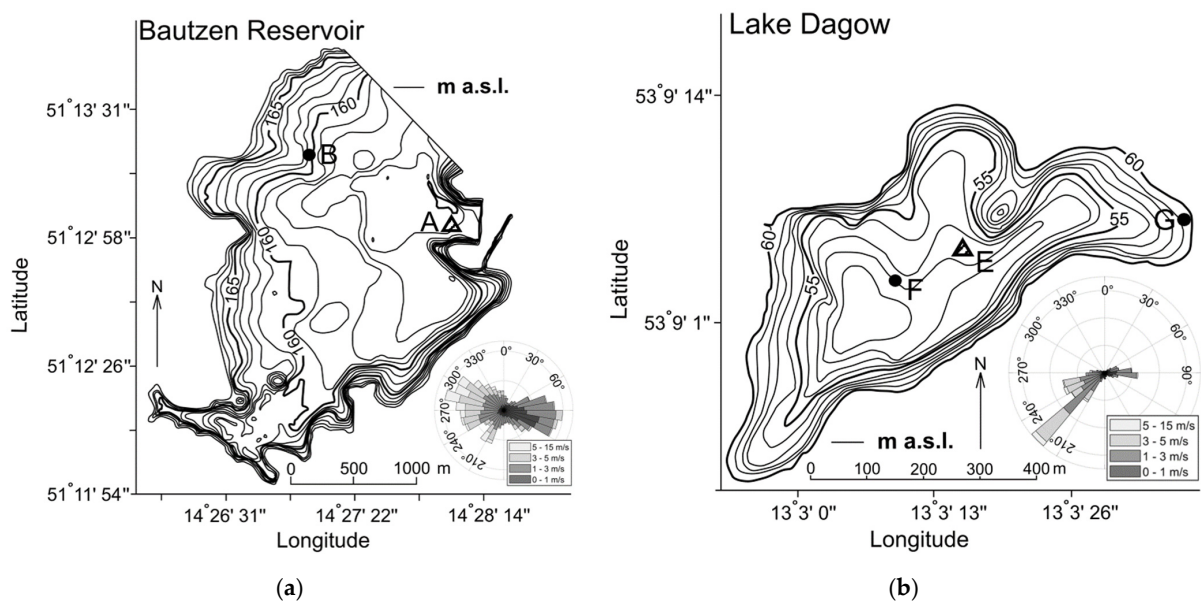

Figure 1. Bathymetric maps of the study sites: (**a**) Bautzen Reservoir; (**b**) Lake Dagow. The plots were created based on the published maps in [24,29]. Black lines show isolines with equal elevation in meters above sea level (m a.s.l.). Small panels on the right show wind roses with wind directions and windspeed. The locations of the instruments are indicated by triangles and circles labeled with capital letters. Points A and E (triangles) mark the locations of the platforms for micrometeorological measurements and the acoustic Doppler current profiler (ADCP). The ADCPs were deployed at the bottom, at a distance of approximately 10 m from the platforms. Points A and F mark the locations of the thermistor chains. A, B and G mark the location of the surface wave observations (pressure sensors).

Table 1. Instrumentation and resolution for the water-side and atmospheric measurements conducted in Bautzen Reservoir and Lake Dagow.

Type of Measurements	Water Body	Instrument	Resolution	Location on the Map (Figure 1)
Flow velocity	Bautzen Reservoir	(a) ADCP RDI Workhorse 600 kHz (range: 1.4–10 m); (b) Workhorse 1200 kHz (range: 0.8–4.7 m)	(a) 10 min with 200 pings with 0.25 m bin size; (b) 1 s with 0.1 m bin size	(a) Bottom deployment (facing upward) ~10 m from southern corner of the platform; (b) platform deployment (facing down, southwest corner)
	Lake Dagow	ADCP RDI Workhorse 600 kHz (3 deployments, range: (1) 0.5–6.8 m; (2–3) 0.8–7.1 m)	5 s with 12 pings with 0.1 m bin size	3 deployments: (1) platform (facing down, west corner), point E; (2–3) ~6–7 m from northern corner of the platform (facing upward)
Water temperature	Bautzen Reservoir	(a) Thermocouples (type T, Copper/Constantan)	10 min averages from measurements in 30 s intervals	Platform, point A
	Lake Dagow	RBR solo	10 s	Point F
Wave measurements	Bautzen Reservoir Lake Dagow	RBR duet	10 min with 512 measurements of 16 Hz	Platform, point A; shore, point B Shore, point G
Wind speed	Bautzen Reservoir	Campbell Scientific, CSAT3 (1.8 m)	20 Hz, as well as 10 min and 30 min averages	Platform, point A
	Lake Dagow	Gill Instruments HS-50 (1.97 m)	20 Hz	Platform, point E
Radiation	Bautzen Reservoir	Kipp and Zonen, CNR1	10 and 30 min averages from measurements in 30 s intervals	Platform, point A
	Lake Dagow	Kipp and Zonen, CNR4	measured at 1 Hz, logged at 1 min averages	Platform, point E

Detailed information about instrumentation and resolution is provided in Table 1. As described in the following sections, the collected data were analyzed to characterize energy fluxes from wind to water and the energy content in different types of water motion. Meteorological data were screened based on plausibility limits, logged information about maintenance work at the measurement station, and by detection of errors and outliers. ADCP velocity data were filtered using a threshold for signal correlation (>70 (-)) and were despiked following [30,31]. All final parameters were estimated with a temporal resolution of 30 min.

2.2. Energy Content

2.2.1. Internal Waves

Standing, basin-scale internal waves (internal seiches) are characterized by oscillations of the vertical density structure that appears due to wind forcing acting on the stratified lake. Waves are typically present in the form of one or several energetic modes depending on the density layer structure [32]. In our study, we identified the major modes of internal waves using the "Internal Wave Analyzer" software (IWA) [33] and selected wave "events" when visual evidence of their presence was observed. Visual evidence appeared in vertical displacements of isotherms and as a pronounced peak in the power spectral density estimated for variations in isothermal depths and for the selected velocity components. Similarly, events were identified for propagating (high frequency) internal waves, which were mainly present in the spectra of the vertical velocity component and displacement of isotherms during the stratified season. The high-frequency limit of the wave band in spectra is limited by the maximum buoyancy frequency N_{max} (Hz) [19,34]:

$$N_{\mathrm{max}} = \mathrm{max}\left[\left(-\frac{g}{\rho_{\mathrm{w0}}}\frac{\partial\rho_{\mathrm{w}}}{\partial z}\right)^{\frac{1}{2}}\right] \tag{1}$$

where g (m s^{-2}) is gravitational acceleration, ρ_{w} (kg m^{-3}) is water density, ρ_{w0} (kg m^{-3}) is the mean water density, z (m) is the height above the bottom with positive direction upwards. The conversion from temperature to density was done based on the freshwater equation of state following [35].

The energy content in a linear internal wave field is equally partitioned into potential energy and kinetic energy [36]. An appropriate approach for estimation of the energy is calculation of the locally available potential energy (APE (J m^{-3})) from temporal variations of water density observed at a single mooring location [37,38]:

$$APE = \int_{z-\zeta}^{z} g[\rho_{\mathrm{w}}(z) - \rho_{\mathrm{w0}}(z\prime)]dz\prime \tag{2}$$

where ζ (m) is the vertical displacement of a fluid particle and z' is the integration variable. We estimated potential energy at 30 min resolution (or 1 min for high-frequency internal waves) by using different time intervals for estimating the mean (background) density stratification. As a rule of thumb, we considered 10 periods of the observed wave, either the basin-scale or high-frequency internal wave, for calculating mean density profiles. In addition, for basin-scale internal waves we estimated kinetic energy from the spectra of the three velocity components within the frequency band corresponding to the range of the wave periods provided by IWA. For high-frequency internal waves a fixed frequency range from 1×10^{-3} to 6.1×10^{-3} Hz was selected.

For comparison with surface energy fluxes, we integrated the volumetric energy content over depth. Both integrated potential and kinetic energies (as well as dissipation rate described in Section 2.4), were normalized by depth-dependent surface area, i.e., for a given quantity X, integration over the water column was computed as:

$$\frac{1}{A_{\mathrm{surf}}}\int_{0}^{H} X(z)\ A(z)\ dz \tag{3}$$

where A_{surf} is the surface area of the water body, H is the water depth, A is the depth-dependent cross-sectional area.

Following [14], we used the depth of the thermocline as the upper limit of integration for APE (APE in J m^{-2}), which was estimated using the "Lake Analyzer" software [39].

2.2.2. Surface Waves

Significant wave height H_{sig} (m) and energy content in surface waves E_{wave} (J m^{-2}) were calculated from pressure fluctuations measured by the wave recorders. The calculation was carried out following standard procedures based on linear wave theory [40] by using the "Ruskin" software provided by the manufacturer [41]. The calculations take into account the attenuation of wave-induced pressure fluctuations at the sampling depth of the sensor. Significant wave height is defined as the average height of the highest one third of the waves during each sampling interval. Mean wave energy was calculated from the variance of water surface elevation. Note that for Bautzen Reservoir we used only those wave measurements that corresponded to the acceptable wind directions (195–355°) to avoid the possible sheltering effect of the measurement platform (the sensor was deployed at the south-western corner).

2.2.3. Schmidt Stability

The Schmidt stability Sc (J m^{-2}) describes the integrated potential energy in vertical density stratification of the entire basin. It is equivalent to the work required for vertical mixing, i.e., the energy required to move the vertical coordinate of the center of mass of all water in the basin to the corresponding center of volume z_v:

$$Sc = \frac{g}{A_{\text{surf}}} \int_0^H (z - z_V)\rho_w(z)A(z)dz \tag{4}$$

$$z_V = \frac{1}{V}\int_0^H A(z)z dz, \quad V = \int_0^H A(z)dz \tag{5}$$

where V is the volume of the basin.

2.3. Energy Fluxes

2.3.1. Wind Energy Flux and Rate of Working

The vertical energy flux at a standard height of 10 m above the water surface P_{10} (W m^{-2}) is equivalent to the vertical shear stress multiplied by the horizontal wind velocity [42]:

$$P_{10} = \tau_s U_{10} = \rho_a u_{*a}^2 U_{10} \tag{6}$$

where $\tau_s = \rho_a u_{*a}^2$ (kg m^{-1} s^{-1}) is the shear stress, u_{*a} (m s^{-1}) is the atmospheric friction velocity and ρ_a (kg m^{-3}) is air density. In our analysis, we estimated u_{*a} from measurements of turbulent velocity fluctuations in the atmospheric boundary layer using the eddy-covariance (EC) method [43]. The mean wind speed measured at a height of 1.8 m (Bautzen Reservoir) and 1.97 m (Lake Dagow) above the water surface was corrected to a standard height of 10 m (U_{10} (m s^{-1})) by considering atmospheric stability [44,45]. We calculated the fraction of the wind energy that is transferred to the water as the total rate of working RW (W m^{-2}) following [16]:

$$(\tau_x, \tau_y) = C_{DN10}\rho_a U_{10}(U, V) \tag{7}$$

$$RW = \tau_x u + \tau_y v \tag{8}$$

where the wind (U, V) and flow velocity (u,v) components were rotated along the wind direction averaged over 12 h since the shape of two water bodies does not have any preferred elongated direction. The drag coefficient C_{DN10} was first determined as $C_{D10} = u_*^2/U_{10}^2$ (-) and then corrected to its neutral counterpart $C_{DN10} = C_{D10}\left(1 + C_{D10}^{1/2}\kappa^{-1}\psi(10/L)\right)^{-2}$, where $\kappa = 0.4$ (-) is the von Kármán constant, L is the Monin-Obukhov length scale and ψ are the stability functions described in [44]. Note that, we used the first acceptable measurement of flow velocity below the surface: for Bautzen Reservoir, it corresponds to ~1 m depth, for Lake Dagow ~0.6 m (first deployment), ~1.3 m (second and third deployment).

2.3.2. Surface Wave Energy Flux

The horizontal wave energy flux per unit length of the wave crest of surface waves (P_{wave} (W m^{-1})) was calculated as the product of the wave energy and the wave group velocity. The group velocity is a function of wave period, which we assign to the period corresponding to the maximum in the wave spectrum. The estimation of the wave energy flux proceeds in the same way as in [46]. To compare P_{wave} with the wind energy flux P_{10}, we considered the ratio $P_{\text{wave}}/(P_{10} \times F)$ 100 (%), where F (m) is the wind fetch at the wave measurement location. The wind fetch is interpolated from distances obtained from the map corresponding to the standard grid of wind direction. Note that, as in Section 2.2.2, we disregarded data with unacceptable wind directions for Bautzen Reservoir.

2.3.3. Surface Heat Flux and Buoyancy Flux

The net surface energy flux in form of heat and radiation H_{net} (W m^{-2}) is expressed as the sum of net shortwave radiation Q_{SW}, longwave radiation Q_{LW}, and latent and sensible heat fluxes H_L, H_S (W m^{-2}). Latent and sensible heat fluxes were calculated following the standard EC methodology using the "Eddy Pro Version 6.2.1" software (LI-COR, Inc., Lincoln, NE, USA).

The surface buoyancy flux J_{BO} (W m^{-2}) was calculated as:

$$J_{BO} = z_V \frac{g\alpha}{c_p} H_{net} \tag{9}$$

where α (K^{-1}) is the temperature-dependent thermal expansion coefficient of water and c_p (J kg^{-1} K^{-1}) is the specific heat capacity of water.

2.3.4. Energy Flux to Basin-Scale Internal Waves

For the estimation of the fraction of the wind energy input attributed to basin-scale internal waves, we manually selected isolated episodes with solitary wind event and corresponding enhancement of the available potential energy in internal waves. This fraction (%) was calculated as a ratio of APE averaged over one cycle of the wave right after the wind event to the wind energy flux integrated over the time for the respective wind event.

2.4. Dissipation Rates

Dissipation rates of turbulent kinetic energy ε (W kg^{-1}) were estimated following two methods: inertial subrange fitting (ISF) [47] and second-order structure function (SF) [48]. Both methods have been widely applied and validated for obtaining dissipation rates from velocity data measured by ADCP [49–52]. Under the assumption of isotropic turbulence, the theoretical power spectrum of turbulent velocity fluctuations S (m^3 s^{-2} rad^{-1}) is expressed as:

$$S(k) = C_1 \alpha_K \, \varepsilon^{2/3} k^{-5/3} \tag{10}$$

where $\alpha_K = 1.5$ (-) is the universal Kolmogorov constant, k (rad m^{-1}) is the spatial wavenumber and C_1 (-) is the isotropy constant, which depends on the direction of the velocity component $18/55 \leq C_1 \leq 4/3 \times 18/55$. We used a constant value of $C_1 = 18/55$ as we used beam-averaged velocity spectra from the ADCP, which measures along-beam velocity fluctuations without directional information [53]. Power spectra estimated from measurements were fitted to Eq. 10 to estimate the dissipation rates. The upper wavenumber limit for the fit was found as a breakpoint where the power spectral density became smaller than the level of noise. The noise level was determined as the logarithmically averaged high-frequency end of the spectra at frequencies higher than 0.2 Hz. To find the lower frequency limit for inertial subrange fitting, we used the optimization procedure described in [54]. We used three criteria for quality assurance for calculated dissipation rates: validity of Taylor's frozen turbulence hypothesis, coefficient of determination of the fit (for both—see [47]) and the length of observed inertial subrange (set to a minimum of 10/8 of decade). The application of these quality criteria led to significant reduction in dissipation rate estimated using ISF (~70% of the data were removed).

Due to the presence of surface waves in velocity spectra, we could not apply ISF for the entire period of measurements. We manually selected velocity spectra where no sur-face wave peak was observed. For periods when no inertial subrange could be observed in the spectra, we applied the SF method, which can be corrected for the case when surface waves are present [55]:

$$D(z,r) = C_2 \varepsilon^{2/3} r^{2/3} + C_3 \left(r^{2/3}\right)^3 + N_m \tag{11}$$

where $D(z,r)$ (m² s⁻²) is the mean squared velocity difference at two locations separated by the distance r (m), $C_2 = 2.1$ (-) is a constant, C_3 (-) is a coefficient describing wave orbital motion and N_m (m² s⁻²) is the measurement noise. C_3, $C_2 \, \varepsilon^{2/3}$ and N_m were determined using least square fits of measured along-beam velocity fluctuations to Equation (11). We used fixed numbers of ADCP bins for the fitting. First, we applied the procedure with 5 bins (for the purpose of the calculations the number of bins should be odd). We noticed that noise could be negative in cases when the theoretical structure function was not long enough to reach its "plateau". Therefore, we used the procedure with seven bins and replaced the values of dissipation rates from the previous step for cases when the noise was negative. We disregarded fits, if either N_m, $C_2 \, \varepsilon^{2/3}$, the difference between the first point of the structure function and the noise, or the difference between the second and first point of the structure function were negative. The application of these criteria led to ~51% and ~30% reduction of the dissipation rate estimates for Bautzen Reservoir and Lake Dagow, respectively.

The dissipation rates obtained from both ISF and SF methods agreed reasonably well (see Figure S1, Supplementary Material). However, the scatter at low dissipation rates increases towards the bottom and the structure function estimates were a factor of 2 to 3 lower than the ISF estimates for dissipation rates exceeding 1×10^{-8} W kg⁻¹. The final dissipation rates combined both estimates using ISF and SF techniques considering the ISF calculations as default value and gap-filling with estimates from SF.

The ISF method could be applied for the full depth range of the velocity measurements. Application of the SF method results in dissipation profiles that lack several bins at the beginning and at the end of the profiling range due to the calculation procedure but could be applied in the presence of surface waves. Thus, we combined the advantages of both methods. However, this procedure was applied and validated for Bautzen Reservoir data, while for Lake Dagow only the SF method was used. That was because there were only few periods during which the velocity spectra were not affected by surface waves during the first deployment and application of the ISF method was not possible for most of the time.

Logarithmic velocity profiles in the bottom boundary layer (BBL) were not resolved by our ADCP measurements at both locations due to the limited profiling range. Visual observation of the flow velocity profiles revealed that the BBL extended up to ~2 m distance above the bottom. Dissipation rates in the BBL were calculated using the flow velocity u_m (m s⁻¹) at the measurement depth (ADCP bin) closest to the bottom using the law of the wall [56]:

$$\varepsilon = \frac{u_{*w}^3}{\kappa z} \tag{12}$$

where $u_{*w} = \left(C_{Db} u_m^2 \right)^{\frac{1}{2}}$ (m s⁻¹) is the bottom friction velocity. Following [56], the bottom drag coefficient C_{Db} was corrected for the distance from the bottom at which the flow speed was measured, using a standard value of 1.5×10^{-3} at 1 m height. Resulting dissipation rate profiles were integrated over depth as in Equation (3) and multiplied by density of the water ρ_w to obtain areal estimates of depth-integrated dissipation rates (in W m⁻²).

3. Results

3.1. Overview of the Measurements

The measurements include both stratified and mixed conditions throughout 243 days in Bautzen Reservoir and the transition from seasonal summer stratification to mixed conditions during the autumn overturn (76 days) in Lake Dagow (Figure 2). In Bautzen Reservoir, the temperature stratification during summer was occasionally disrupted by winds exceeding 7 m s⁻¹. These mixing events are consistent with observations at this reservoir reported in previous studies [24,28,57]. The maximum temperature at the water surface was 29.2 °C (4 August) in Bautzen Reservoir and 18 °C (11 September) in Lake Dagow. The maximum temperature difference between surface and bottom was 15.2 °C (10 June) and 8 °C (12 September) in Bautzen Reservoir and Lake Dagow, respectively.

In Lake Dagow, the thermocline was located close to the bottom and the thickness of the hypolimnion was only ~0.7 m. Average Schmidt stability was 4.3 and 41.8 J m^{-2} and maximum values were 21 J m^{-2} (17 September) and 178 J m^{-2} (01 June) in Lake Dagow and Bautzen Reservoir, respectively. The heat and buoyancy fluxes varied between -155 and 1113 W m^{-2} (-5.1×10^{-4} and 4.2×10^{-3} W m^{-2}) in Bautzen Reservoir and between -130 and 763 W m^{-2} (-2.6×10^{-4} and 3.1×10^{-3} W m^{-2}) in Lake Dagow (buoyancy flux in parenthesis, Table S1, Figure S8, Supplementary Material).
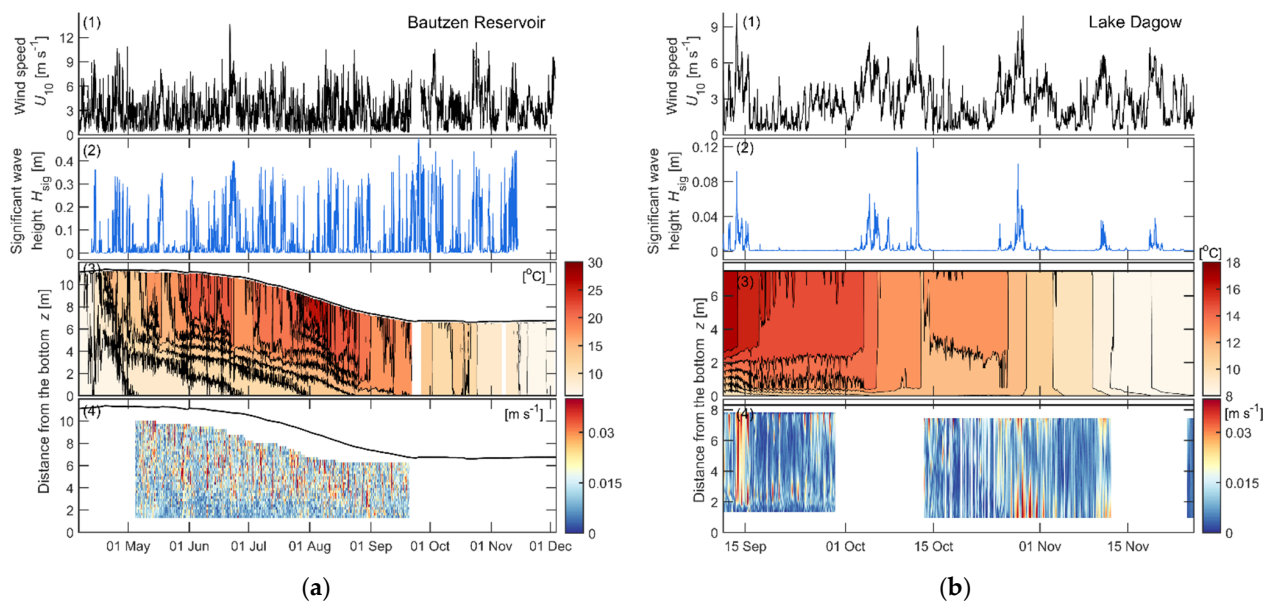
Figure 2. Overview of wind forcing and hydrodynamic conditions in (**a**) Bautzen Reservoir and (**b**) Lake Dagow. From the top to the bottom: (1) wind speed corrected to a height of 10 m; (2) significant wave height; (3) temperature profile (color denotes temperature, lines show isothermal depths); (4) flow velocity profiles (velocity magnitude). The black lines mark the location of the water surface. All data are shown at 30 min resolution.

Wind forcing in both systems was of the same order of magnitude: the wind speed at 10 m height was 3.0 ± 1.9 and 2.7 ± 1.7 m s^{-1} (here and further, $\pm$ denotes standard deviation) with maximum values of 13.7 and 10.1 m s^{-1} in Bautzen Reservoir and Lake Dagow, respectively. West-northwestern (280–300°) and south-western (220–240°) wind directions were predominant for Bautzen Reservoir and Lake Dagow, respectively. The water level continuously declined throughout the study period from 11.2 m to 6.8 m at the platform location in Bautzen Reservoir, while in Lake Dagow it remained constant (~8.3 m at the ADCP location). Water discharge at the inflow and at the outlet tower varied between 0.6 and 3.9 m^3 s^{-1}, with mean values of 1.2 and 1.9 m^3 s^{-1}, respectively (Figure S2, Supplementary Material). In both water bodies, flow velocities were relatively small for most of the time (~0.01–0.02 m s^{-1}). The maximum flow speed was 0.1 m s^{-1} in Bautzen Reservoir and 0.07 m s^{-1} in Lake Dagow. The mean significant wave height H_{sig} was $(3.9 \pm 9.6) \times 10^{-3}$ m and $(1.9 \pm 2.7) \times 10^{-2}$ m at shore sampling locations (Point B in Bautzen Reservoir, Point G in Lake Dagow, see Figure 1) and $(7.4 \pm 9.9) \times 10^{-2}$ m at the platform in Bautzen Reservoir. The maximum value of significant wave height was 0.1 and 0.2 m for the shore sampling locations in Lake Dagow and Bautzen Reservoir, respectively, and 0.5 m at the platform in Bautzen Reservoir.

3.2. Wind Energy Flux and Rate of Working

The ratio of the wind energy flux at 10 m height (P_{10}) to the rate of working associated with shear stress in the surface layer of the water column (RW) provides an estimate of the efficiency of the energy transfer from wind to water. We analyzed the ratio separately for mixed and for stratified conditions, but we did not find significant differences between both

conditions (Figure 3). We used a fixed, although arbitrary, threshold for Schmidt stability ($Sc = 5$ J m^{-2}) to distinguish between mixed and stratified conditions. Distributions of the ratio of *RW* to P_{10} for periods when the Schmidt stability was smaller or larger than 5 J m^{-2} were in close agreement (Figure S3, Supplementary Material). The median values of the ratio were 1.8×10^{-3} and 1.6×10^{-3} in Bautzen Reservoir, and 1.7×10^{-3} and 0.7×10^{-3} in Lake Dagow for non-stratified and stratified conditions, respectively. We applied linear regressions of RW as a function of P_{10} considering P_{10} less than 2 W m^{-2}, as most of the data belonged to this interval. Different values of the threshold in Schmidt stability to distinguish stratified and mixed conditions did not result in significant changes in slopes. However, we noticed that the slope of the regression was sensitive to the inclusion of few high-magnitude values. The slope coefficient for all data, which describes the efficiency of energy transfer is equal to $(1.3 \pm 0.1) \times 10^{-3}$ and $(2.61 \pm 0.05) \times 10^{-3}$ ($\pm$ here denotes standard error for the slope) for Bautzen Reservoir and Lake Dagow, respectively. Data from Bautzen Reservoir were additionally filtered based on the same wind directions as for surface waves (Section 2.2.2) to avoid potential sheltering by the measurement platform. These values were comparable to the mean efficiency of 1.3×10^{-3} estimated under mixed conditions in a lake by [16].
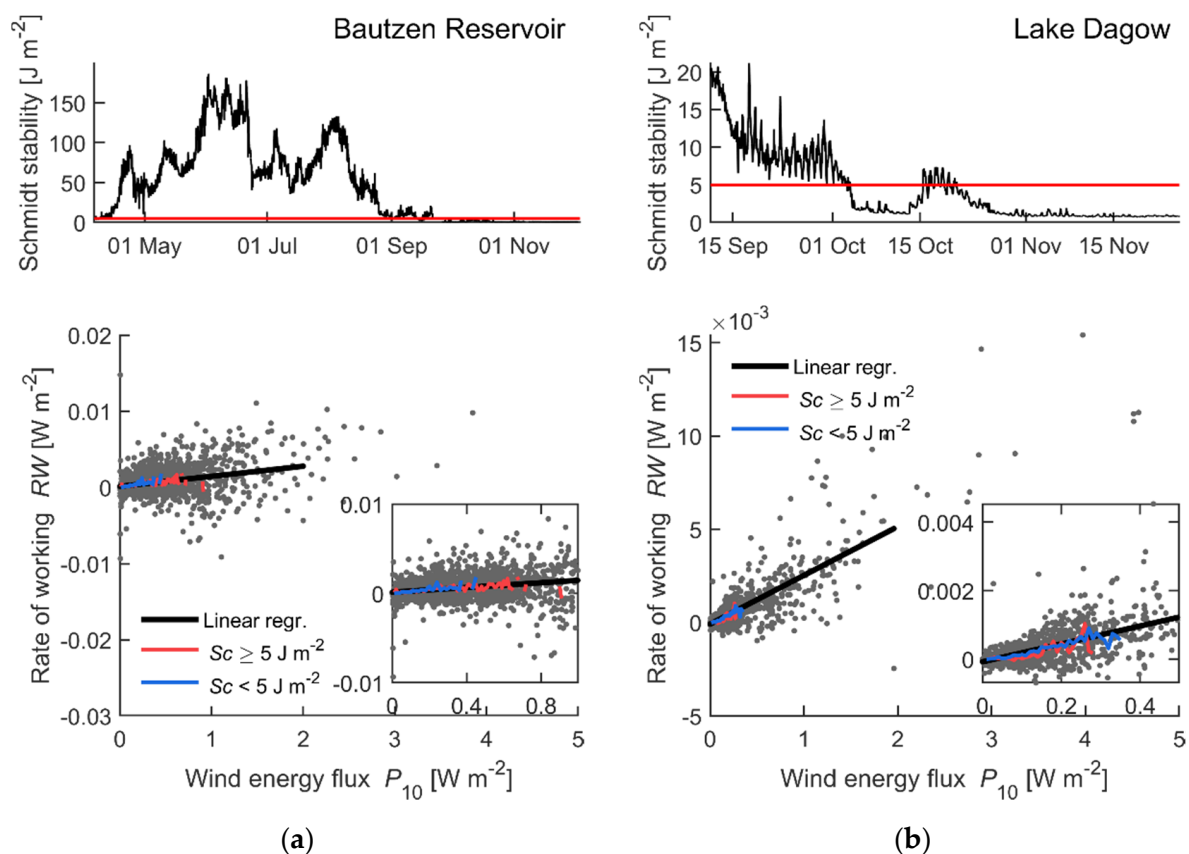

Figure 3. Potential energy in stratification and efficiency of energy transfer from wind to water in (**a**) Bautzen Reservoir and (**b**) in Lake Dagow. From top to bottom: (1) the black line shows the time series of Schmidt stability (*Sc*). The horizontal red lines mark the threshold value (5 J m^{-2}) to separate mixed and stratified conditions. (2) Relationship between rate of working *RW* and wind energy input P_{10}. Gray dots show all data. Red and blue lines represent bin-averages for two selected cases: $Sc \geq 5$ and $Sc < 5$ J m^{-2}—indicating stratified and mixed conditions, respectively. A minimum of 5 data points was considered for the bin-averaging. The black line shows a linear regression for all data with $P_{10} < 2$ W m^{-2}. Inset graphs in the lower panels show a detailed view of the data at small energy fluxes. The slope coefficient, i.e., the efficiency of energy transfer from wind to water is equal to $(1.3 \pm 0.1) \times 10^{-3}$ and $(2.61 \pm 0.05) \times 10^{-3}$ for Bautzen Reservoir and Lake Dagow, respectively.

3.3. Surface Waves

We examined the relationship between significant wave height and wind speed at 10 m height (Figure 4a) and compared our wave measurements with the only—to the best of our knowledge—other existing dataset of significant wave height in relation to wind speed in a lake. These data were measured in a large lake in Switzerland over a two-week period [18]. Although the significant wave height reached higher values in [18] (~0.5 m) than in our measurements (~0.3 m, at the platform location in Bautzen Reservoir), the wind-speed dependence is remarkably consistent in both datasets. Wave heights were relatively small ($<1 \times 10^{-2}$ m) with weak dependence on wind speed for winds below ~3 m s^{-1}, while wave heights strongly increased for wind speeds exceeding 3–4 m s^{-1}. Significant wave heights measured at the shore locations were generally smaller in amplitude and showed a weaker increase with increasing wind compared to open-water measurements (Figure 4a). This could be related to the interference with waves reflected from the shore and shallow water depth at the sampling locations.
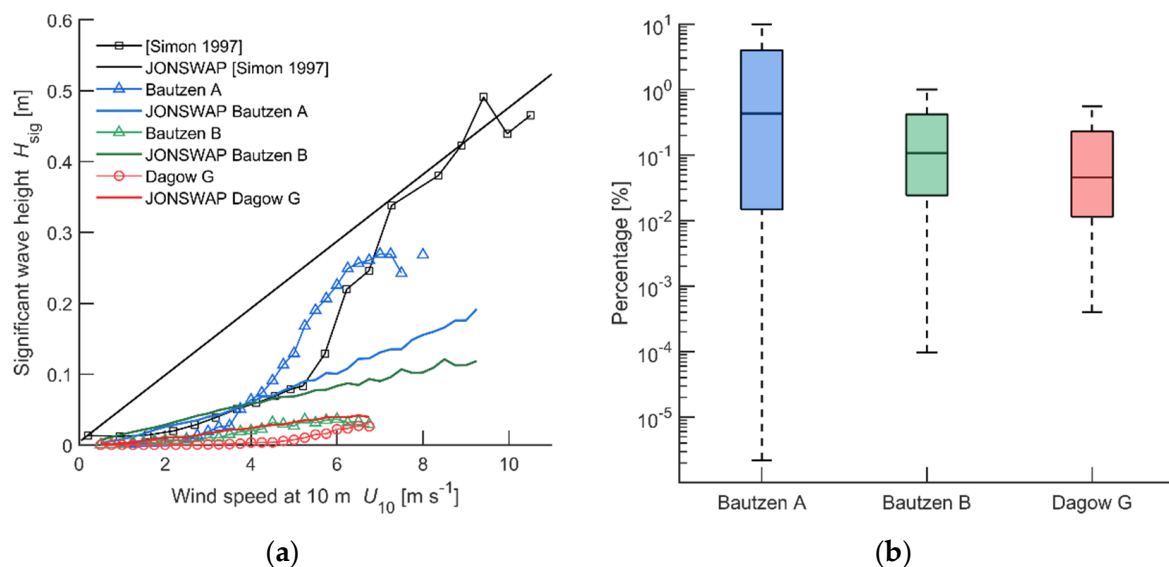

(a) **(b)**

Figure 4. (**a**) Significant wave H_{sig} as a function of wind speed U_{10}. Lines with markers represent measurements: black color shows data from [18]. Blue, green and red colors represent the bin-averaged data from the present study: Bautzen Reservoir A (platform), B (shore) and Dagow Lake G (shore). Solid lines show a commonly applied empirical parameterization of the significant wave height based on the wind speed and fetch length (JONSWAP). The parameterization was applied to the observed wind speed and direction with a resolution of 30 min. (**b**) Boxplots showing the percentages of the ratio of wave energy flux per unit length of wave crest (P$_{wave}$) to the fetch-integrated wind energy flux (approximated as P$_{10}$ multiplied by the fetch length) for three measurement locations. The central horizontal line in boxes indicates the median; the bottom and top edges of the boxes denote the 25th and 75th percentiles; the whiskers extend to the largest data points which are not considered outliers.

We applied an empirical approach for the prediction of significant wave height based on the wave frequency, wind speed and fetch length, which was originally derived from measurements in the North Sea but is also commonly used in lake models (the Joint Sea Wave Project or JONSWAP, [58]). The parameterization overestimated the significant wave height up to wind speeds of approximately 4 m s^{-1} and underestimated wave heights for higher wind speeds (see blue lines, Figure 4a). This supported the earlier finding of [18]; however, their "breakpoint" was at around 6 m s^{-1} and the JONSWAP predictions agreed well with the measurements at higher wind speed. The authors of [18] note that the possible reasons for underestimation at low wind speeds could either be insufficient sensor accuracy to resolve the small amplitude of waves, or a failure to compute the wind fetch correctly as the variability in wind direction at low wind speeds is very high. The wind fetch indeed varied considerably due to the variations in wind direction; however,

smoothing of the calculated fetch prior to applying the wave model did not significantly reduce the predicted values at low wind speeds. The JONSWAP model overestimated the significant wave height for both measurements at shore locations.

Energy content in surface waves varied between 1.3×10^{-4} and 9.1×10^2 J m^{-2} with a log-averaged value of 0.3 J m^{-2} for the measurements at the platform in Bautzen Reservoir. In Lake Dagow, it varied between 1.6×10^{-4} and 1.1×10^1 J m^{-2} with a log-averaged value of 1.5×10^{-3} J m^{-2}. Wave energy measured at the shore in Bautzen Reservoir (1.3×10^{-4}–2.1×10^1 J m^{-2} with log-averaged value 2×10^{-2} J m^{-2}) was comparable in magnitude to the shore measurements in Lake Dagow. Wave energy showed strong dependence on the wind speed exceeding 3 m s^{-1} with a power-law exponent of ~8–9 (Figure S4, Supplementary Material).

The median values of the fraction of the wind energy input attributed to the surface waves (see Section 2.3.2) varied between 0.05% and 0.4% between sampling locations (Figure 4b). Mean values varied between 0.5% and 4%. The fraction strongly increased for wind speeds exceeding 3 m s^{-1}.

3.4. Internal Waves

Basin-scale and high-frequency internal waves were observed in both water bodies. The prevailing mode of basin-scale waves was the second vertical mode/first horizontal mode (V2H1), with a period of approximately 8–9 and 12 h and maximum amplitude of 1–2 m and 0.5–1 m in Bautzen Reservoir and Dagow Lake, respectively (Figure 5). Note, that we also observed waves with a period of approximately 21 h in both water bodies; however, they occurred only once during a short period of time. Although a clear periodic structure of the waves was present below the thermocline (Figure 5a), close to the surface it was often masked by wind-driven flow and mixed layer dynamics. Unlike basin-scale internal waves, high-frequency internal waves occurred not only during summer stratification but also during autumn and spring mixing. The period of the major wave peak in the power spectra of velocity and isothermal depths varied throughout the measurements from 5–6 min during the stratified season up to 15–20 min during mixing in spring and autumn. High-frequency internal waves appeared in the frequency range 0.02–0.2 N, which was lower than values reported for larger lakes (0.1–0.7 N) [59–62].

Energy content in basin-scale and high-frequency internal waves is comprised of available potential energy (APE) and kinetic energy (see Section 2.2.1). We analyzed its seasonal dynamics, using the long-term measurement from Bautzen Reservoir (Figure 6a). During the deepening of the upper mixed layer in spring, the average APE during internal wave events (for the definition of "event" see Section 2.2.1) had a maximum of 6.7 J m^{-2}, while it remained nearly constant below 1 J m^{-2} during most of the time. Its average value for 13 analyzed internal wave events was 1.2 ± 1.0 J m^{-2}. Note that the periods of the internal waves in the two last events (October and November, see Figure 6a) were not supported by the predictions of the Internal Wave Analyzer; however, we visually observed internal waves as a peak in the velocity spectrum. The average APE in high-frequency internal waves evaluated for 210 events reached its maximum value of 0.45 J m^{-2} in summer during the strongest stratification (end of June–beginning of September). The average value over the entire measurement period was 0.06 ± 0.05 J m^{-2}.
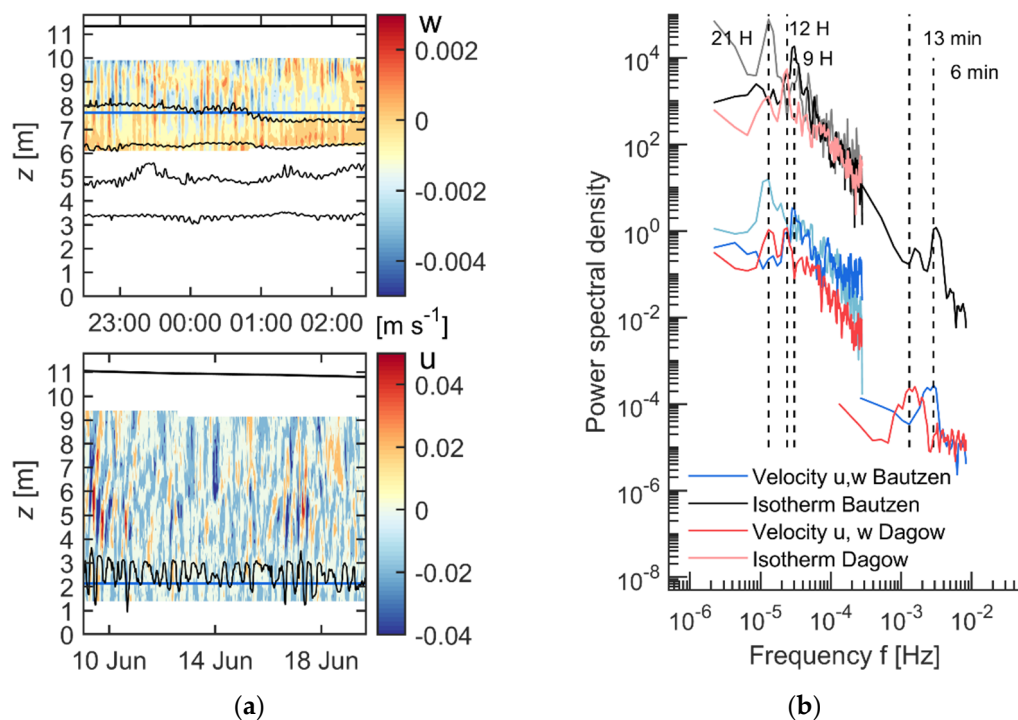
Figure 5. (**a**) Sample data from Bautzen Reservoir illustrating high-frequency internal waves with a period of 6 min (upper panel) and basin-scale internal waves with the period of 9 h (lower panel). The upper and lower panels show vertical (*w*) and horizontal (*u*) velocity components, respectively. Black lines show temperature isotherms; blue lines show the distance above the bed for which the velocity power spectra are shown in panel (**b**). (**b**) Power spectral density estimates for flow velocity components (m^2 s^{-1}) and isotherms (m^2 s). Blue, light blue and red solid lines show velocity spectra; gray, black and light red show isotherm spectra for Bautzen Reservoir and Lake Dagow, respectively. Internal waves are associated with distinct spectral peaks and vertical dashed lines denote major internal wave periods.
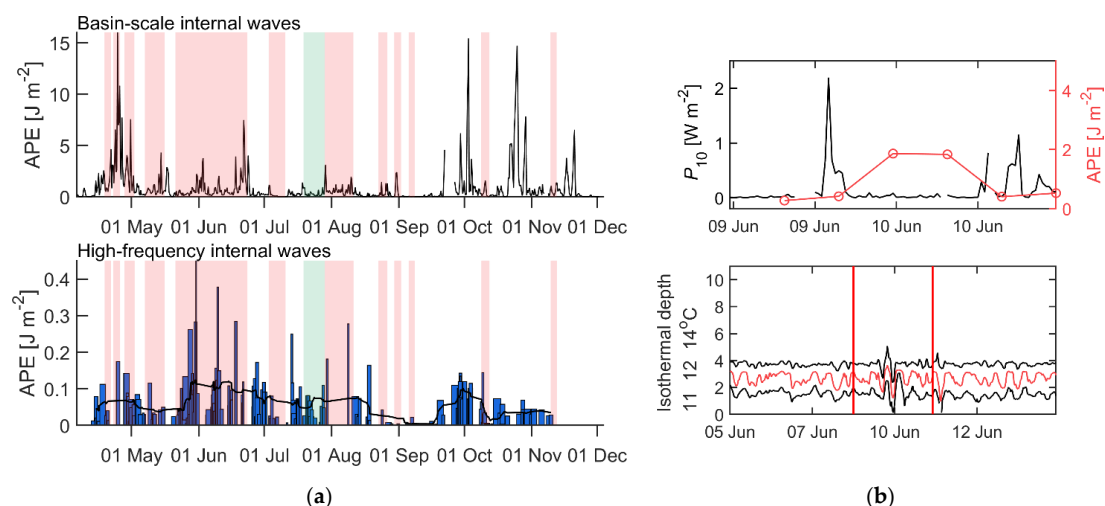
Figure 6. (**a**) Average available potential energy (APE) in basin-scale internal waves (upper panel) and in high-frequency internal waves (lower panel) throughout the measurement period in Bautzen Reservoir. The red-shaded areas correspond to the presence of the basin-scale waves with 8–9 h period, the green-shaded area shows the presence of a wave with 21 h period. The width of the bars is not to scale but is proportional to the event duration (i.e., narrow bars indicate shorter events where waves are present, and wider bars indicate longer events). The black line in the lower panel (**a**) shows a moving average of the APE. (**b**) Sample data demonstrating the transfer of wind energy to basin-scale internal waves. The upper panel shows the time series of P_{10} and APE averaged over one wave cycle. After the wind event stopped, APE grows first and then decays after three wave cycles. The lower panel shows isothermal depths with the event duration marked by red vertical lines.

The mean kinetic energy during the selected basin-scale internal wave events was on average a factor of four smaller than the APE. This inconsistency with linear wave theory can be explained by the location of measurements relative to the lake center. In standing waves, the kinetic energy is higher near the center, whereas the potential energy is higher along the edges. However, for high-frequency internal waves, the average kinetic energy for all selected events was 0.05 J m^{-2}, which was comparable to the APE (note that the difference between them is greater during April to August, probably because velocity measurements cover only the upper part of the water column). In Lake Dagow, we identified only one event with basin-scale internal wave activity and the corresponding APE of 0.05 J m^{-2} was two orders of magnitude smaller than in Bautzen Reservoir because the thermocline was close to the bottom. Following [14], we used the double value of APE as a measure of the total energy in internal waves.

The fraction of the wind energy flux, which is transferred to basin-scale internal waves was estimated based on nine selected episodes with solitary wind events in Bautzen Reservoir and three in Lake Dagow (see Section 2.3.4). One example is presented in Figure 6b, which demonstrates how waves are energized by a wind event. The average percentage of wave energy and integrated wind energy flux amounted up to 0.1% with an average value of 0.04 ± 0.03%. In Lake Dagow, the energy flux to internal waves was 0.002%, which is one order of magnitude lower than the average value in Bautzen.

3.5. Dissipation Rate in Surface and Bottom Boundary Layers

The log-averaged dissipation rates of turbulent kinetic energy were of the same order of magnitude (~10^{-8} W kg^{-1}) in Bautzen Reservoir and Lake Dagow (Figure 7). They tended to increase towards the water surface, while remaining nearly constant in the middle of the water column. Estimates of dissipation rate in the bottom boundary layer (Equation (12)) were on average one (Bautzen Reservoir) and two (Lake Dagow) orders of magnitude smaller than dissipation rates in the interior and the surface layer.
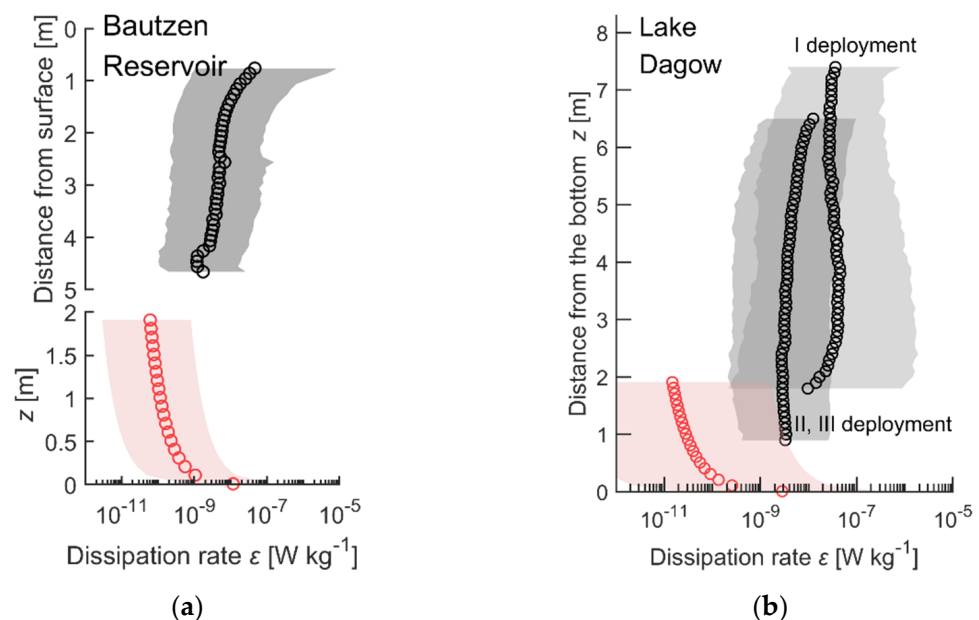

Figure 7. Vertical profiles of log-averaged energy dissipation rates (ε) for all available data (gray and red shaded areas show the 5th to 95th range of data): (**a**) combined data with dissipation rates calculated using the structure function and inertial subrange fitting methods (black circles, the platform-mounted ADCP facing downward) and using bottom boundary layer approach (see Section 2.4, red circles, the ADCP deployed at the bottom) in Bautzen Reservoir. The vertical axis is split into two subaxes with identical scaling: The lower axis corresponds to the distance from the bottom,

the upper—to the distance from the surface. Thus, we avoid averaging over the entire water column because the water level change was significant throughout the measurements. Data are based on measurements in Bautzen Reservoir. (**b**) Dissipation rate calculated using the structure function method and the BBL approach based on measurements in Lake Dagow (separately for the first and for the following two ADCP deployment periods).

In Lake Dagow, the BBL approach may not be appropriate as there was a possible influence of biogenic activity, which may contribute additional turbulence or interfere with the analysis method. We observed a strong diurnal variation in the dissipation rate (primarily during the first deployment; see Figures S5 and S8, Supplementary Material). However, in contrast to similar observations [17,63], we observed high acoustic backscatter during the night (see Figure S5b, Supplementary Material) and an increase in dissipation rates and vertical velocity occurred during the day (Figure S5b, Supplementary Material). It is important to note that high dissipation rates were present in the entire water column and not just close to the bottom where elevated acoustic backscatter was observed. We also observed a "trace" of high dissipation rates starting from midnight when migrating zooplankton species begin to swim towards the bottom. We suggest that strong acoustic backscatter during the night and high dissipation rate and vertical flow velocity patterns during the day (see average profiles for days and nights in Figure S5, Supplementary Material) are related to diurnal migrations of different types of organisms. The pronounced diurnal pattern of dissipation rates and backscatter strength became less obvious in the second and third ADCP deployments suggesting the reduction of the number of species in autumn.

Depth-integrated dissipation rates were typically three orders of magnitude smaller than the wind energy flux (Figures S6–S8, Supplementary Material). The dissipation rates integrated over the BBL were on average two orders of magnitude lower than the dissipation rates integrated over the interior and surface boundary layer (Figure S7, Supplementary Material). The share of the wind energy input that was dissipated in turbulence increased with wind speed. In Bautzen Reservoir, highest values of depth-integrated dissipation rates were comparable in magnitude to the corresponding wind energy flux (Figure S6a, Supplementary Material). We observed a strong relationship between the integrated dissipation rate and wind energy flux with a power-law exponent of ~2.6 for wind speeds exceeding ~3 m s^{-1} in Bautzen Reservoir (Figure S7). We did not find this relationship in the data from Lake Dagow, where the wind energy flux reached comparable magnitude, but integrated dissipation rates remained below the high values observed in Bautzen Reservoir. However, rare events with high integrated energy dissipation rates did not contribute to mean conditions. The average ratio of total integrated dissipation rate and wind energy flux was 0.23% and 0.5% for Bautzen Reservoir and Lake Dagow, respectively. Similarly, the mean values of depth-integrated dissipation rates were a factor of two lower in Bautzen (1.7×10^{-5} W m^{-2}) compared to Lake Dagow (3.4×10^{-5} W m^{-2}).

4. Discussion

4.1. Overall Energy Budget

Based on simultaneous measurements of energy fluxes in the atmospheric boundary layer and along the water column in two small water bodies, we compiled energy budgets in terms of energy fluxes and energy content in different types of water motions (Figure 8, Table S1, Supplementary Material). Despite having different origin and differing in size by one order of magnitude, the reservoir and the lake feature similar hydrodynamic processes and energy flux paths. Most of the vertical energy flux at 10 m above the water surface is dissipated in the atmospheric boundary layer (~95% of the wind energy flux) and is not transferred to the water body. The remaining fraction is distributed into various types of water motions.
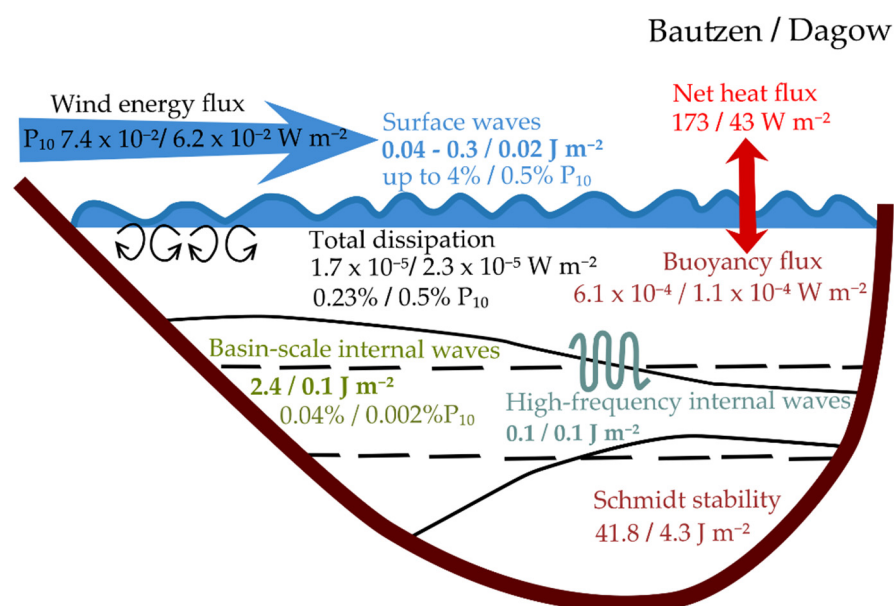
Figure 8. Scheme showing mean energy fluxes in (W m^{-2}) and mean energy content (J m^{-2}) for the two studied water bodies. Numbers written before/after a slash correspond to the values obtained from Bautzen Reservoir and Lake Dagow measurements, respectively. Solid and dashed lines illustrate the motion and equilibrium positions of vertical layers of water with the same density.

The largest fraction of wind energy flux (0.5–4%) is transferred to surface waves. Energy dissipation in turbulent flows accounted for 0.2–0.5% of the wind energy flux, while one order of magnitude less energy is transferred to basin-scale internal waves (0.002–0.04%). The energy content is largest in basin-scale internal waves in Bautzen Reservoir, where it is about one order of magnitude higher than the energy content in surface waves, as well as in high-frequency internal waves. Lake Dagow, the energy content is of comparable magnitude in all type of waves. Generally, the energy content in water motions is small compared to the potential energy in thermal stratification (Schmidt stability), which differed on average by one order of magnitude between both water bodies. The average wind energy flux in the atmosphere exceeded the average buoyancy flux by two orders of magnitude in both water bodies (Figure 8).

Some important components of the energy budget are lacking, including turbulent kinetic energy and kinetic energy in large-scale water motions such as water currents (except for waves). As discussed in the following sections, our results revealed a number of important findings related to specific energy flux paths, as well as to the potential generalization of the derived energy budget to other lakes and reservoirs.

4.2. Energy Transfer Efficiency

The estimated efficiency of energy transfer from wind to water derived from wind energy flux and rate of working in the surface layer was in close agreement for both water bodies, despite their difference in surface area. The estimated rate of wind working can be considered as an independent estimate of the energy transfer from wind to water. It can be obtained by summing up the relevant components of the energy budget (Table S1). Taking the mean shear and flow velocity at the water surface into account, the RW should be equal to the sum of all energy fluxes, except for surface waves, which are not resolved in the estimation of the RW. The sum of the components was dominated by depth-integrated energy dissipation rates (0.23–0.5% of P_{10}), which were slightly higher but of the same order of magnitude as RW (0.14–0.27% of P_{10}). Generally, this agreement supports the magnitudes of the energy fluxes compiled in Figure 8.

In contrast to earlier studies on Lake Windermere [16,17], there was no evidence of intensification of the energy transfer from the wind to the water during the stratified season compared to the period of lake mixing. The efficiency of wind energy input for both water bodies was found to be within the values reported for non-stratified conditions [14]. However, we did find a strong, non-linear increase of the efficiency with increasing wind speed in Bautzen reservoir. This fact was in line with our finding that estimates of a mean transfer efficiency are sensitive to including the few largest observations. We observed a close agreement between the mean transfer efficiencies estimated in the present study for two water bodies differing by an order of magnitude in surface area and those reported in [14] for Lake Windermere South Basin, which is slightly larger in size than Bautzen Reservoir but considerably deeper. This agreement suggests that the values represent a robust order-of-magnitude estimate for aquatic systems of small to medium size.

4.3. Surface and Internal Waves

The fraction of the wind energy flux attributed to surface waves was up to 4% on average and within the range reported by [13,16] based on measurements in a large (214 km^2) lake in Switzerland. However, this fraction strongly increased with the wind speed exceeding 3 m s^{-1} and depended on the sampling location. We demonstrated that the JONSWAP model for the estimation of the significant wave height may not be an appropriate approach for estimating significant wave heights in smaller lakes and reservoirs as it significantly overestimated wave height at low wind speed. At high wind speed, we found an extremely strong increase of wave energy with a power-law coefficient of ~8–9 with wave height exceeding the JONSWAP predictions. More wave observations in different lakes and reservoirs and further detailed investigation of the relationship between the wave characteristics and wind speed are needed to improve predictions of wave height and wave energy fluxes in lakes and reservoirs.

The energy content in basin-scale internal waves was on average lower than values reported for a larger and deeper alpine lake in [14] (0.1–2.4 J m^{-2} versus 22 $\pm$ 3 J m^{-2}) and slightly higher than the values in [15] (10^{-2}–1 J m^{-2}). We assume that this difference can be related to the strength of stratification and lake depth. The alpine lakes studied in [14] and [15] showed persistent and large-amplitude internal seiching, which occurred rather sporadically and with smaller amplitudes in Bautzen and Dagow. In addition, the energy content in basin-scale internal waves varied with season and was on average five-fold higher in spring than for the remaining sampling period in Bautzen Reservoir. This can be explained by the deepening of the thermocline and the way of calculation of the energy content with the thermocline depth being the upper limit for vertical integration. Also, lake bathymetry can affect the seasonal variation of the internal waves [64]. The energy flux to the basin-scale internal waves can be up to 0.1% of the wind energy flux but is on average two orders of magnitude smaller than that reported for the alpine lake (0.04% versus 1% in [13]). Energy content in high-frequency internal waves was on average one order of magnitude smaller than in basin-scale internal waves (Bautzen Reservoir) and comparable with basin-scale internal waves in Lake Dagow. During the stratified season, high-frequency waves can contain on average twice as much energy than during the remaining period.

4.4. Energy Dissipation Rates

Average energy dissipation rates were of the same order of magnitude in both water bodies (~5 $\times$ 10^{-9} W kg^{-1}). More energy was dissipated with increasing wind energy flux. Although in Bautzen Reservoir at high wind speeds almost all of the wind energy flux was dissipated, this was not observed at Lake Dagow, which may be related to the smaller size of the lake and the sheltering effect of the surrounding forest. On average, a similar percentage of the wind energy flux was dissipated in both water bodies. However, the dissipation rates estimated for the bottom boundary layer were on average one (Bautzen Reservoir) and two (Lake Dagow) orders of magnitude smaller than those calculated for the

remaining water column. This can potentially be explained by the fact that flow velocities were generally very low, and the boundary layer may not be observed within the ADCP profiling range, making an underestimation of the dissipation rates possible.

The other possible explanation for such a difference in the dissipation rates in Lake Dagow is biogenic activity. We observed high acoustic backscatter in the upper part of the water column during the night and at larger depth during daytime, suggesting diurnal vertical migration of zooplankton [65]. Recent studies found higher dissipation rates at depths of high acoustic backscatter [17,63], suggesting a contribution of migrating organisms to energy dissipation. In contrast to these observations, we observed enhanced dissipation rates at depths and at times of low acoustic backscatter. The difference in dissipation rates between day and night can be up to two orders of magnitude. As pointed out in [65], the acoustic backscatter strength is affected by both the abundance and the acoustic properties of the scatterers and can be dominated by organisms containing gas bubbles. Other organisms, such as small fish, may follow opposing migration patterns, which remain hidden in the volume backscatter strengths [66]. Aggregations of small swimming fish with densities of 5–8 m^{-3} have been shown to enhance dissipation rates by one order of magnitude [67]. The role of biogenic turbulence in marine in inland waters has been widely discussed and analyzed in the past decade (see reviews in [68,69]). The main conclusion was that although small swimmers may generate additional flow and energy dissipation, they are unlikely to contribute to vertical mixing. Small swimmers generate flow disturbances at the scale of some multiple body length [70]. The dissipation rate estimates from ADCP are limited by the relatively large size of the sampling volume (bin size) and are theoretically based on turbulent energy transfer from large to small scales. These limitations may challenge the measurement of energy dissipation rates with ADCP in the presence of small swimmers. The increasing reporting of diurnal patterns in energy dissipation rates in relation to acoustic backscatter in recent studies calls for careful validation of these estimates using alternative methods for estimating dissipation rates, such as microstructure profiling and particle image velocimetry.

4.5. Study Limitations

In addition to the methodological limitations and uncertainties mentioned above, a number of limitations of our analysis should be noted. We made single-point measurements, and internal waves were not spatially resolved. Additional measurements along the direction of the internal wave may allow to estimate the potential and kinetic energy in wave motions more precisely. To assess the possible effect of lake bathymetry and morphology on internal wave structure and seasonal variability, spatially resolved flow measurements can be combined with numerical models in future studies.

In addition, we did not analyze the potential impact of the water level variation in Bautzen Reservoir on the energy fluxes. Reduction of the water level in a medium-sized reservoir shortens the stratification period [71,72]. This would affect the energy content in the basin-scale internal waves, at least in the way we calculated it. Possible interference of the internal waves with the lakebed may cause more turbulence in the bottom boundary layer. However, it is difficult to distinguish between the effect of water level variation and the seasonal change in the lake thermal structure without additional modeling.

Furthermore, we assumed that the wind speed is horizontally homogeneous over the lake for all sampling locations. This may not be applicable and additional, spatially resolving meteorological measurements should be included in future studies. The uncertainties in the estimation of dissipation rates could be related to the selection of the constants (in inertial subrange fitting and structure function methods). For example, [52,73] showed that these constants depend on the distance from the boundary and the use of the "canonical" constants may lead to significant errors. In addition, it remains unclear how flow and energy dissipation generated by small swimming organisms affect measurements and bulk parameterizations of energy dissipation rates.

5. Conclusions

For the first time, we related observations of energy content and fluxes in different types of water motion to simultaneously measured energy fluxes in the atmospheric boundary layer. Although the two studied water bodies were expected to be governed by contrasting hydrodynamic processes and conditions, we did not find any significant differences in energy fluxes. The observed and estimated energy fluxes and energy content agree well with results reported for larger water bodies, suggesting that the energetics governing water motions in enclosed basins is similar, independent of basin size.

Only a small fraction (<5%) of the vertical wind energy flux in the atmosphere is transferred to water motions. By disregarding surface waves, the efficiency of energy transfer does not differ strongly between various water bodies of different sizes. The transfer efficiency increases with increasing wind energy flux, but we could not observe significant differences of the energy efficiency under stratified and mixed conditions, as it has been reported for a deeper lake.

Our measurements highlight the importance of surface waves, which receive the largest share of the wind energy flux into the water and have mostly been neglected in previous studies. The wave energy flux increases strongly nonlinearly with increasing wind speed for wind speed exceeding $3 \, \text{m s}^{-1}$. Existing parametrizations of wave height as a function of wind speed and fetch length fail to reproduce observed wave amplitudes in small water bodies.

The largest energy content was observed in basin-scale internal waves, which was found to be within the range reported for larger lakes. However, the energy fluxes and energy content in internal waves seem to vary strongly among lakes having different size and depth. Internal waves appear to be more important in mean energy budgets in larger and deeper lakes.

Dissipation rates of turbulent kinetic energy show similar structure and dynamics and are of comparable magnitude in water bodies of different size. Similar to surface waves, depth-integrated dissipation rates increase strongly nonlinearly if the wind energy flux exceeds a threshold value, which corresponds to a wind speed of $3 \, \text{m s}^{-1}$. We observed a pronounced diurnal pattern in dissipation rates at one of our study sites, which is most likely related to vertically migrating organisms. The reliability of commonly applied measurement and analysis procedures for estimating energy dissipation rates in the presence of swimming organisms needs to be confirmed in future studies.

Supplementary Materials: The following are available online at https://www.mdpi.com/article/10.3390/w13223270/s1, Figure S1: Dissipation rate estimated using structure function method (SF) versus dissipation rate calculated using inertial subrange fitting method (ISF) at ~1.5 m depth for measurements in Bautzen Reservoir (gray dots). Figure S2: Discharge of the inflow (red line) and outflow (at the outlet tower) of Bautzen reservoir. The data was provided by the the Landestalsperren-Verwaltung Sachsen (LTV). Figure S3: Probability distribution of the ratio of rate of working (RW) to wind energy flux (P10) selected for two cases: Schmidt stability (Sc) < 5 J m^{-2} (area shown in gray, corresponding to non-stratified conditions) and Sc $\geq$ 5 J m^{-2} (area shown in red, corresponding to stratified conditions) for (a) Bautzen Reservoir. The median values are 1.8×10^{-3} and 1.6×10^{-3}, the average values ($\pm$standard deviation) are $(2 \pm 4) \cdot 10^{-3}$ and $(0.6 \pm 21.6) \cdot 10^{-2}$, for non-stratified and stratified conditions, respectively. (b) Lake Dagow. Figure S4: Surface wave energy versus wind speed at 10 m height at the platform location in Bautzen Reservoir (gray dots). Wave energy shows strong dependence on wind speed exceeding 2–3 m s^{-1}. The black line shows bin-average data, the red line represents a power-law relationship with an exponent of nine. The latter was obtained from a linear regression of log-transformed data. Figure S5: (a) Dissipation rates of turbulent kinetic energy averaged over night and over daytime during the first ADCP deployment in Lake Dagow. (b) Acoustic backscatter strength recorded by the ADCP (upper panel), vertical flow velocity (middle panel), dissipation rate (lower panel). Figure S6: Depth-integrated dissipation rate (including surface and bottom boundary layers and interior of the water bodies) versus the vertical wind energy flux above the water surface in (a) Bautzen Reservoir; (b) Lake Dagow. Figure S7: Dissipation rate integrated over the bottom boundary layer (the thickness of 2 m, light gray dots) and over the rest of

the water column where the ADCP measurements are available (dark gray dots) using data from (a) Bautzen Reservoir; (b) Lake Dagow. The gray solid line represents a 1:1 relationship. Figure S8: Temporal dynamics of wind energy flux (black line, upper panel), dissipation rates integrated over the water depth (red dots, upper panel) and buoyancy flux (lower panel) for data measured in (a) Bautzen Reservoir; (b) Lake Dagow. Note the pronounced diurnal pattern in integrated energy dissipation rates in Lake Dagow during the first ADCP deployment (cf. Figure S4). Table S1: Energy content and energy fluxes.

References

1. Imberger, J. Flux paths in a stratified lake: A review. In *Physical Processes in Lakes and Oceans*; American Geophysical Union: District of Columbia, WA, USA, 1998; pp. 1–17.
2. Jähne, B.; Haußecker, H. Air-Water Gas Exchange. *Annu. Rev. Fluid Mech.* **1998**, *30*, 443–468. [CrossRef]
3. Perolo, P.; Fernández Castro, B.; Escoffier, N.; Lambert, T.; Bouffard, D.; Perga, M.-E. Accounting for Surface Waves Improves Gas Flux Estimation at High Wind Speed in a Large Lake. In *Dynamics of the Earth System*; Interactions: Franklin, MA, USA, 2021.
4. MacIntyre, S. Vertical Mixing in a Shallow, Eutrophic Lake: Possible Consequences for the Light Climate of Phytoplankton. *Limnol. Oceanogr.* **1993**, *38*, 798–817. [CrossRef]
5. Huisman, J.; Sharples, J.; Stroom, J.M.; Visser, P.M.; Kardinaal, W.E.A.; Verspagen, J.M.H.; Sommeijer, B. Changes in Turbulent Mixing Shift Competition for Light between Phytoplankton Species. *Ecology* **2004**, *85*, 2960–2970. [CrossRef]
6. Peeters, F.; Straile, D.; Lorke, A.; Ollinger, D. Turbulent Mixing and Phytoplankton Spring Bloom Development in a Deep Lake. *Limnol. Oceanogr.* **2007**, *52*, 286–298. [CrossRef]
7. Corman, J.R.; McIntyre, P.B.; Kuboja, B.; Mbemba, W.; Fink, D.; Wheeler, C.W.; Gans, C.; Michel, E.; Flecker, A.S. Upwelling Couples Chemical and Biological Dynamics across the Littoral and Pelagic Zones of Lake Tanganyika, East Africa. *Limnol. Oceanogr.* **2010**, *55*, 214–224. [CrossRef]
8. Bocaniov, S.A.; Schiff, S.L.; Smith, R.E.H. Plankton Metabolism and Physical Forcing in a Productive Embayment of a Large Oligotrophic Lake: Insights from Stable Oxygen Isotopes: Plankton Metabolism and Physical Forcing. *Freshw. Biol.* **2012**, *57*, 481–496. [CrossRef]
9. MacIntyre, S.; Jellison, R. Nutrient Fluxes from Upwelling and Enhanced Turbulence at the Top of the Pycnocline in Mono Lake, California. *Hydrobiologia* **2001**, *466*, 13–29. [CrossRef]
10. Sepúlveda Steiner, O. *Mixing Processes and Their Ecological Implications: From Vertical to Lateral Variability in Stratified Lakes*; EPFL: Lausanne, Switzerland, 2020.

11. Lorke, A.; Müller, B.; Maerki, M.; Wüest, A. Breathing Sediments: The Control of Diffusive Transport across the Sediment-Water Interface by Periodic Boundary-Layer Turbulence. *Limnol. Oceanogr.* **2003**, *48*, 2077–2085. [CrossRef]
12. Sobek, S.; Durisch-Kaiser, E.; Zurbrügg, R.; Wongfun, N.; Wessels, M.; Pasche, N.; Wehrli, B. Organic Carbon Burial Efficiency in Lake Sediments Controlled by Oxygen Exposure Time and Sediment Source. *Limnol. Oceanogr.* **2009**, *54*, 2243–2254. [CrossRef]
13. Søndergaard, M.; Jensen, J.P.; Jeppesen, E. Role of Sediment and Internal Loading of Phosphorus in Shallow Lakes. *Hydrobiologia* **2003**, *506–509*, 135–145. [CrossRef]
14. Wüest, A.; Piepke, G.; Van Senden, D.C. Turbulent Kinetic Energy Balance as a Tool for Estimating Vertical Diffusivity in Wind-Forced Stratified Waters. *Limnol. Oceanogr.* **2000**, *45*, 1388–1400. [CrossRef]
15. Imboden, D.M. The Motion of Lake Waters. In *The Lakes Handbook, Volume 1*; O'Sullivan, P.E., Reynolds, C.S., Eds.; Blackwell Science Ltd.: Malden, MA, USA, 2003; pp. 115–152. ISBN 978-0-470-99927-1.
16. Woolway, R.I.; Simpson, J.H. Energy Input and Dissipation in a Temperate Lake during the Spring Transition. *Ocean Dyn.* **2017**, *67*, 959–971. [CrossRef]
17. Simpson, J.H.; Woolway, R.I.; Scannell, B.; Austin, M.J.; Powell, B.; Maberly, S.C. The Annual Cycle of Energy Input, Modal Excitation and Physical Plus Biogenic Turbulent Dissipation in a Temperate Lake. *Water Res.* **2021**, *57*, e2020WR029441. [CrossRef]
18. Simon, A. Turbulent Mixing in the Surface Boundary Layer of Lakes. Ph.D. Thesis, Swiss Federal Institute of Technology, Zürich, Switzerland, 1997.
19. Heyna, B.; Groen, P. On Short-Period Internal Gravity Waves. *Physica* **1958**, *24*, 383–389. [CrossRef]
20. Boegman, L.; Ivey, G.N.; Imberger, J. The Energetics of Large-Scale Internal Wave Degeneration in Lakes. *J. Fluid Mech.* **2005**, *531*, 159–180. [CrossRef]
21. Preusse, M.; Peeters, F.; Lorke, A. Internal Waves and the Generation of Turbulence in the Thermocline of a Large Lake. *Limnol. Oceanogr.* **2010**, *55*, 2353–2365. [CrossRef]
22. Downing, J.A.; Prairie, Y.T.; Cole, J.J.; Duarte, C.M.; Tranvik, L.J.; Striegl, R.G.; McDowell, W.H.; Kortelainen, P.; Caraco, N.F.; Melack, J.M.; et al. The Global Abundance and Size Distribution of Lakes, Ponds, and Impoundments. *Limnol. Oceanogr.* **2006**, *51*, 2388–2397. [CrossRef]
23. Choulga, M.; Kourzeneva, E.; Zakharova, E.; Doganovsky, A. Estimation of the Mean Depth of Boreal Lakes for Use in Numerical Weather Prediction and Climate Modelling. *Tellus A Dyn. Meteorol. Oceanogr.* **2014**, *66*, 21295. [CrossRef]
24. Rinke, K.; Hübner, I.; Petzoldt, T.; Rolinski, S.; König-Rinke, M.; Post, J.; Lorke, A.; Benndorf, J. How Internal Waves Influence the Vertical Distribution of Zooplankton. *Freshw. Biol.* **2007**, *52*, 137–144. [CrossRef]
25. Poff, N.L.; Hart, D.D. How Dams Vary and Why It Matters for the Emerging Science of Dam Removal. *BioScience* **2002**, *52*, 659. [CrossRef]
26. Tundisi, J.G. *Limnology*; CRC Press: Boca Raton, FL, USA, 2017; ISBN 978-1-138-07204-6.
27. Kerimoglu, O.; Rinke, K. Stratification Dynamics in a Shallow Reservoir under Different Hydro-Meteorological Scenarios and Operational Strategies. *Water Resour. Res.* **2013**, *49*, 7518–7527. [CrossRef]
28. Wagner, A.H.; Janssen, M.; Kahl, U.; Mehner, T.; Benndorf, J. Initiation of the Midsummer Decline of Daphnia as Related to Predation, Non-Consumptive Mortality and Recruitment: A Balance. *Arch. Hydrobiol.* **2004**, *160*, 1–23. [CrossRef]
29. Casper, S.J. *Lake Stechlin: A Temperate Oligotrophic Lake*; Springer: Berlin/Heidelberg, Germany, 2012; Volume 58.
30. Goring, D.G.; Nikora, V.I. Despiking Acoustic Doppler Velocimeter Data. *J. Hydraul. Eng.* **2002**, *128*, 117–126. [CrossRef]
31. Wahl, T.L. Discussion of "Despiking Acoustic Doppler Velocimeter Data" by Derek G. Goring and Vladimir I. Nikora. *J. Hydraul. Eng.* **2003**, *129*, 484–487. [CrossRef]
32. Münnich, M.; Wüest, A.; Imboden, D.M. Observations of the Second Vertical Mode of the Internal Seiche in an Alpine Lake. *Limnol. Oceanogr.* **1992**, *37*, 1705–1719. [CrossRef]
33. De Carvalho Bueno, R.; Bleninger, T.; Lorke, A. Internal Wave Analyzer for Thermally Stratified Lakes. *Environ. Model. Softw.* **2021**, *136*, 104950. [CrossRef]
34. Antenucci, J.P.; Imberger, J. On Internal Waves near the High-Frequency Limit in an Enclosed Basin. *J. Geophys. Res.* **2001**, *106*, 22465–22474. [CrossRef]
35. Chen, C.-T.A.; Millero, F.J. Thermodynamic Properties for Natural Waters Covering Only the Limnological Range. *Limnol. Oceanogr.* **1986**, *31*, 657–662. [CrossRef]
36. Kundu, P.K.; Cohen, I.M.; Dowling, D.R. Gravity Waves. In *Fluid Mechanics*; Elsevier: Amsterdam, The Netherlands, 2012; pp. 253–307. ISBN 978-0-12-382100-3.
37. Holliday, D.; Mcintyre, M.E. On Potential Energy Density in an Incompressible, Stratified Fluid. *J. Fluid Mech.* **1981**, *107*, 221. [CrossRef]
38. Kang, D.; Fringer, O. On the Calculation of Available Potential Energy in Internal Wave Fields. *J. Phys. Oceanogr.* **2010**, *40*, 2539–2545. [CrossRef]
39. Read, J.S.; Hamilton, D.P.; Jones, I.D.; Muraoka, K.; Winslow, L.A.; Kroiss, R.; Wu, C.H.; Gaiser, E. Derivation of Lake Mixing and Stratification Indices from High-Resolution Lake Buoy Data. *Environ. Model. Softw.* **2011**, *26*, 1325–1336. [CrossRef]
40. RBR Ltd. Wave Parameters. Available online: https://docs.rbr-global.com/support/ruskin/ruskin-features/waves/wave-parameters (accessed on 25 July 2021).
41. Ruskin Software. Available online: https://rbr-global.com/products/software (accessed on 25 July 2021).
42. Imboden, D.M.; Wüest, A. Mixing Mechanisms in Lakes. In *Physics and Chemistry of Lakes*; Lerman, A., Imboden, D.M., Gat, J.R., Eds.; Springer: Berlin/Heidelberg, Germany, 1995; pp. 83–138. ISBN 978-3-642-85134-6.
43. Foken, T.; Nappo, C.J. *Micrometeorology*; Springer: Berlin/Heidelberg, Germany, 2008; ISBN 978-3-540-74665-2.

44. Paulson, C.A. The Mathematical Representation of Wind Speed and Temperature Profiles in the Unstable Atmospheric Surface Layer. *J. Appl. Meteorol. Climatol.* **1970**, *9*, 857–861. [CrossRef]

45. Large, W.G.; Pond, S. Open Ocean Momentum Flux Measurements in Moderate to Strong Winds. *J. Phys. Oceanogr.* **1981**, *11*, 324–336. [CrossRef]

46. Hofmann, H.; Lorke, A.; Peeters, F. The Relative Importance of Wind and Ship Waves in the Littoral Zone of a Large Lake. *Limnol. Oceanogr.* **2008**, *53*, 368–380. [CrossRef]

47. Bluteau, C.E.; Jones, N.L.; Ivey, G.N. Estimating Turbulent Kinetic Energy Dissipation Using the Inertial Subrange Method in Environmental Flows: TKE Dissipation in Environmental Flows. *Limnol. Oceanogr. Methods* **2011**, *9*, 302–321. [CrossRef]

48. Wiles, P.J.; Rippeth, T.P.; Simpson, J.H.; Hendricks, P.J. A Novel Technique for Measuring the Rate of Turbulent Dissipation in the Marine Environment. *Geophys. Res. Lett.* **2006**, *33*, L21608. [CrossRef]

49. Guerra, M.; Thomson, J. Turbulence Measurements from Five-Beam Acoustic Doppler Current Profilers. *J. Atmos. Ocean. Technol.* **2017**, *34*, 1267–1284. [CrossRef]

50. McMillan, J.M.; Hay, A.E. Spectral and Structure Function Estimates of Turbulence Dissipation Rates in a High-Flow Tidal Channel Using Broadband ADCPs. *J. Atmos. Ocean. Technol.* **2017**, *34*, 5–20. [CrossRef]

51. Lorke, A. Boundary Mixing in the Thermocline of a Large Lake. *J. Geophys. Res.* **2007**, *112*, C09019. [CrossRef]

52. Jabbari, A.; Rouhi, A.; Boegman, L. Evaluation of the Structure Function Method to Compute Turbulent Dissipation within Boundary Layers Using Numerical Simulations. *J. Geophys. Res. Oceans* **2016**, *121*, 5888–5897. [CrossRef]

53. Lorke, A.; Wüest, A. Application of Coherent ADCP for Turbulence Measurements in the Bottom Boundary Layer. *J. Atmos. Ocean. Technol.* **2005**, *22*, 1821–1828. [CrossRef]

54. Guseva, S.; Aurela, M.; Cortes, A.; Kivi, R.; Lotsari, E.S.; Macintyre, S.; Mammarella, I.; Ojala, A.; Stepanenko, V.M.; Uotila, P.; et al. Variable Physical Drivers of Near-Surface Turbulence in a Regulated River. *Water Resour. Res.* **2021**, *57*. [CrossRef]

55. Scannell, B.D.; Rippeth, T.P.; Simpson, J.H.; Polton, J.A.; Hopkins, J.E. Correcting Surface Wave Bias in Structure Function Estimates of Turbulent Kinetic Energy Dissipation Rate. *J. Atmos. Ocean. Technol.* **2017**, *34*, 2257–2273. [CrossRef]

56. Lorke, A.; MacIntyre, S. The Benthic Boundary Layer (in Rivers, Lakes, and Reservoirs). In *Encyclopedia of Inland Waters*; Elsevier: Amsterdam, The Netherlands, 2009; pp. 505–514. ISBN 978-0-12-370626-3.

57. Benndorf, J.; Kranich, J.; Mehner, T.; Wagner, A. Temperature Impact on the Midsummer Decline of *Daphnia galeata*: An Analysis of Long-Term Data from the Biomanipulated Bautzen Reservoir (Germany): Temperature Impact on Midsummer Decline. *Freshw. Biol.* **2001**, *46*, 199–211. [CrossRef]

58. Hasselmann, K.F.; Barnett, T.; Bouws, E.; Carlson, H.; Cartwright, D.; Enke, K.; Ewing, J.; Gienapp, H.; Hasselmann, D.; Meerburg, A.; et al. Measurements of Wind-Wave Growth and Swell Decay during the Joint North Sea Wave Project (JONSWAP). *Ergänzungsheft zur Dtsch. Hydrogr. Z. Reihe A* **1973**, *12*, 1–95. Available online: http://hdl.handle.net/21.11116/0000-0007-DD3C-E (accessed on 14 October 2021).

59. Mortimer, C.H.; McNaught, D.C.; Stewart, K.M. Short Internal Waves near Their High-Frequency Limit in Central Lake Michigan. In Proceedings of the 11th Annual Conference on Great Lakes Research, Milwaukee, WI, USA, 18–20 April 1968; pp. 454–469.

60. Thorpe, S.A. High-Frequency Internal Waves in Lake Geneva. *Phil. Trans. R. Soc. Lond. A* **1996**, *354*, 237–257. [CrossRef]

61. Stevens, C.L. Internal Waves in a Small Reservoir. *J. Geophys. Res.* **1999**, *104*, 15777–15788. [CrossRef]

62. Gímez-Giraldo, A.; Imberger, J.; Antenucci, J.P.; Yeates, P.S. Wind-Shear-Generated High-Frequency Internal Waves as Precursors to Mixing in a Stratified Lake. *Limnol. Oceanogr.* **2008**, *53*, 354–367. [CrossRef]

63. Ishikawa, M.; Bleninger, T.; Lorke, A. Hydrodynamics and Mixing Mechanisms in a Subtropical Reservoir. *Inland Waters* **2021**, *11*, 286–301. [CrossRef]

64. Fricker, P.D.; Nepf, H.M. Bathymetry, Stratification, and Internal Seiche Structure. *J. Geophys. Res.* **2000**, *105*, 14237–14251. [CrossRef]

65. Lorke, A.; McGinnis, D.F.; Spaak, P.; Wuest, A. Acoustic Observations of Zooplankton in Lakes Using a Doppler Current Profiler. *Freshw. Biol.* **2004**, *49*, 1280–1292. [CrossRef]

66. Lorke, A.; Weber, A.; Hofmann, H.; Peeters, F. Opposing Diel Migration of Fish and Zooplankton in the Littoral Zone of a Large Lake. *Hydrobiologia* **2008**, *600*, 139–146. [CrossRef]

67. Lorke, A.; Probst, W.N. In Situ Measurements of Turbulence in Fish Shoals. *Limnol. Oceanogr.* **2010**, *55*, 354–364. [CrossRef]

68. Kunze, E. Biologically Generated Mixing in the Ocean. *Annu. Rev. Mar. Sci.* **2019**, *11*, 215–226. [CrossRef]

69. Simoncelli, S.; Thackeray, S.J.; Wain, D.J. Can Small Zooplankton Mix Lakes? *Limnol. Oceanogr.* **2017**, *2*, 167–176. [CrossRef]

70. Wickramarathna, L.N.; Noss, C.; Lorke, A. Hydrodynamic Trails Produced by Daphnia: Size and Energetics. *PLoS ONE* **2014**, *9*, e92383. [CrossRef] [PubMed]

71. Nowlin, W.H.; Davies, J.-M.; Nordin, R.N.; Mazumder, A. Effects of Water Level Fluctuation and Short-Term Climate Variation on Thermal and Stratification Regimes of a British Columbia Reservoir and Lake. *Lake Reserv. Manag.* **2004**, *20*, 91–109. [CrossRef]

72. Bonnet, M.-P.; Poulin, M.; Devaux, J. Numerical Modeling of Thermal Stratification in a Lake Reservoir. Methodology and Case Study. *Aquat. Sci.* **2000**, *62*, 105. [CrossRef]

73. Jabbari, A.; Boegman, L.; Valipour, R.; Wain, D.; Bouffard, D. Dissipation of Turbulent Kinetic Energy in the Oscillating Bottom Boundary Layer of a Large Shallow Lake. *J. Atmos. Ocean. Technol.* **2020**, *37*, 517–531. [CrossRef]

74. Sachs, T.; Wille, C. FLUXNET-CH4 DE-Dgw Dagowsee, Dataset, 2015–2018. Available online: https://doi.org/10.18140/FLX/1669633 (accessed on 20 August 2021).

Appendix II

Bulk transfer coefficients estimated from eddy-covariance measurements over lakes and reservoirs

S. Guseva[1], F. Armani[2], A. R. Desai[3], N. L. Dias[4], T. Friborg[5], H. Iwata[6], J. Jansen[7,8],

G. Lükő[9], I. Mammarella[10], I. Repina[11,12], A. Rutgersson[13], T. Sachs[14], K. Scholz[15], U. Spank[16],

V. Stepanenko[12,17,18], P. Torma[9], T. Vesala[10,19], and A. Lorke[1]

[1] Institute for Environmental Sciences, University of Koblenz-Landau, 76829 Landau, Germany;
[2] Federal University of Paraná, Curitiba, PR, Brasil;
[3] Department of Atmospheric and Oceanic Sciences, University of Wisconsin-Madison, Madison, WI, USA;
[4] Department of Environmental Engineering, Federal University of Paraná, Curitiba, PR, Brasil;
[5] Department of Geosciences and Natural Resource Management, Oester Voldgade 10, 1350 Copenhagen K, Denmark;
[6] Department of Environmental Science, Faculty of Science, Shinshu University, Matsumoto, Japan;
[7] Department of Ecology and Genetics / Limnology, Uppsala University, Uppsala, Sweden;
[8] Département des Sciences Biologiques, Groupe de Recherche Interuniversitaire en Limnologie, Université du Québec à Montréal, Montréal, QC, Canada;
[9] Department of Hydraulic and Water Resources Engineering, Budapest University of Technology and Economics, Budapest, Hungary;
[10] Institute for Atmospheric and Earth System Research/Physics, Faculty of Science, University of Helsinki, Helsinki, Finland;
[11] A.M. Obukhov Institute of Atmospheric Physics, Moscow, Russia;
[12] Research Computing Center, Lomonosov Moscow State University, Moscow, Russia;
[13] Department of Earth Sciences, Uppsala University, Uppsala, Sweden;
[14] GFZ German Research Centre for Geosciences, Potsdam, Germany;
[15] Department of Ecology, University of Innsbruck, Innsbruck, Austria;
[16] Technische Universität Dresden, Faculty of Environmental Sciences, Institute of Hydrology and Meteorology, Chair of Meteorology, PF 1117, 01735 Tharandt, Germany.;
[17] Faculty of Geography, Lomonosov Moscow State University, Moscow, Russia;
[18] Moscow Center of Fundamental and Applied Mathematics, Moscow, Russia;
[19] Institute for Atmospheric and Earth System Research/Forest Sciences, Faculty of Agriculture and Forestry, University of Helsinki, Finland.

The first submitted version is available at

The second submitted version after the first revisions is attached below

Bulk Transfer Coefficients Estimated from Eddy-Covariance Measurements over Lakes and Reservoirs

S. Guseva[1], F. Armani[2], A. R. Desai[3], N. L. Dias[4], T. Friborg[5], H. Iwata[6], J. Jansen[7,8], G. Lükő[9], I. Mammarella[10], I. Repina[11,12], A. Rutgersson[13], T. Sachs[14], K. Scholz[15], U. Spank[16], V. Stepanenko[12,17,18], P. Torma[9], T. Vesala[10,19], and A. Lorke[1]

[1] Institute for Environmental Sciences, University of Koblenz-Landau, Landau, Germany.

[2] Federal University of Paraná, Curitiba, PR, Brazil.

[3] Department of Atmospheric and Oceanic Sciences, University of Wisconsin-Madison, Madison, WI, USA.

[4] Department of Environmental Engineering, Federal University of Paraná, Curitiba, PR, Brazil.

[5] Department of Geosciences and Natural Resource Management, Oester Voldgade 10, 1350 Copenhagen K, Denmark.

[6] Department of Environmental Science, Faculty of Science, Shinshu University, Matsumoto, Japan.

[7] Department of Ecology and Genetics / Limnology, Uppsala University, Uppsala, Sweden.

[8] Département des Sciences Biologiques, Groupe de Recherche Interuniversitaire en Limnologie, Université du Québec à Montréal, Montréal, QC, Canada.

[9] Department of Hydraulic and Water Resources Engineering, Budapest University of Technology and Economics, Budapest, Hungary.

[10] Institute for Atmospheric and Earth System Research/Physics, Faculty of Science, University of Helsinki, Helsinki, Finland.

[11] A.M. Obukhov Institute of Atmospheric Physics, Moscow, Russia.

[12] Research Computing Center, Lomonosov Moscow State University, Moscow, Russia.

[13] Department of Earth Sciences, Uppsala University, Uppsala, Sweden.

[14] GFZ German Research Centre for Geosciences, Potsdam, Germany.

[15] Department of Ecology, University of Innsbruck, Innsbruck, Austria.

[16] Technische Universität Dresden, Faculty of Environmental Sciences, Institute of Hydrology and Meteorology, Chair of Meteorology, PF 1117, 01735 Tharandt, Germany.

[17] Faculty of Geography, Lomonosov Moscow State University, Moscow, Russia.

[18] Moscow Center of Fundamental and Applied Mathematics, Moscow, Russia.

[19] Institute for Atmospheric and Earth System Research/Forest Sciences, Faculty of Agriculture and Forestry, University of Helsinki, Finland.

Corresponding author: Sofya Guseva (guseva@uni-landau.de)

Key Points:

- Bulk transfer coefficients exhibit a substantial increase at low wind speed

- The increase is explained by wind gustiness and capillary wave roughness

- At higher wind speed, drag coefficient and Stanton number decrease with lake surface area.

40 **Abstract**

41 The drag coefficient, Stanton number and Dalton number are of particular importance for
42 estimating the surface turbulent fluxes of momentum, heat and water vapor using bulk
43 parameterization. Although these bulk transfer coefficients have been extensively studied over the
44 past several decades in marine and large-lake environments, there are no studies analyzing their
45 variability for smaller lakes. Here, we evaluated these coefficients through directly measured
46 surface fluxes using the eddy-covariance technique over more than 30 lakes and reservoirs of
47 different sizes and depths. Our analysis showed that the transfer coefficients (adjusted to neutral
48 atmospheric stability) were generally within the range reported in previous studies for large lakes
49 and oceans. All transfer coefficients exhibit a substantial increase at low wind speeds (< 3 m s-1),
50 which was found to be associated with the presence of gusts and capillary waves (except Dalton
51 number). Stanton number was found to be on average a factor of 1.3 higher than Dalton number,
52 likely affecting the Bowen ratio method. At high wind speeds, the transfer coefficients remained
53 relatively constant at values of $1.6 \cdot 10^{-3}$, $1.4 \cdot 10^{-3}$, $1.0 \cdot 10^{-3}$, respectively. We found that the
54 variability of the transfer coefficients among the lakes could be associated with lake surface area.
55 In flux parameterizations at lake surfaces, it is recommended to consider variations in the drag
56 coefficient and Stanton number due to wind gustiness and capillary wave roughness while Dalton
57 number could be considered as constant at all wind speeds.

58 **Plain Language Summary**

59 In our study, we investigate the bulk transfer coefficients, which are of particular importance for
60 estimation the turbulent fluxes of momentum, heat and water vapor in the atmospheric surface
61 layer, above lakes and reservoirs. The incorrect representation of the surface fluxes above inland
62 waters can potentially lead to errors in weather and climate prediction models. For the first time
63 we made this synthesis using a compiled dataset consisting of existing eddy-covariance flux
64 measurements over 23 lakes and 8 reservoirs. Our results revealed substantial increase of the
65 transfer coefficients at low wind speeds, which is often not taken into account in models. The
66 observed increase in the drag coefficient (momentum transfer coefficient) and Stanton number
67 (heat transfer coefficient) could be associated with the presence of wind gusts and capillary waves.
68 In flux parameterizations at lake surface, it is recommended to consider them for accurate flux
69 representation. Although the bulk transfer coefficients were relatively constant at high wind
70 speeds, we found that the Stanton number systematically exceeds the Dalton number (water vapor
71 transfer coefficient), despite the fact they are typically considered to be equal. This difference may
72 affect the Bowen ratio method and result in biased estimates of lake evaporation.

73 **1 Introduction**

74 The major process that governs the interaction between the atmosphere and surface waters
75 is the turbulent exchange of momentum, heat and gases at the air-water interface. Although lakes
76 and reservoirs occupy only about 3% of the land surface area (Downing et al., 2006), they are
77 known to have an impact on local weather and climate. For example, lakes affect the stability of
78 the atmosphere above (Sun et al., 1997), leading to the formation of clouds and precipitation on
79 the shores (Changnon & Jones, 1972; Kato & Takahashi, 1981; Eerola et al., 2014; Thiery et al.,
80 2016). Furthermore, lakes and reservoirs are recognized as significant contributors to the global
81 carbon cycle by emitting significant amounts of carbon dioxide and methane (DelSontro et al.,
82 2018; Rosentreter et al., 2021).

83   The past three decades have seen a rapid development of lake models (Stepanenko et al.,
84 2014) and their incorporation into numerical weather and climate prediction models (Ljungemyr
85 et al., 1996; Salgado & Le Mogne, 2010; Mironov et al., 2010). Experiments on the coupling of
86 lakes and the atmospheric model revealed their beneficial impact on the weather prediction quality
87 (Balsamo et al., 2012). A number of case studies have demonstrated the importance of lakes for
88 extreme local weather phenomena, such as lake-effect snow over Great American lakes (Fujisaki-
89 Manome et al., 2020), deep hazardous convection over Great African lakes (Thiery et al., 2016),
90 wind speeds over Lake Superior (Desai et al., 2009), or stratiform cloudiness in winter over Lake
91 Ladoga (Eerola et al., 2014). Thus, an accurate representation of the exchange of momentum, heat
92 and water vapor at the air-water interface in water bodies is essential to understand those processes.

93   In state-of-the-art, momentum, sensible and latent heat fluxes are usually determined based
94 on gradient approaches utilizing transfer coefficients (also known as bulk transfer coefficients) and
95 easy to measure meteorological and limnological variables, i.e., wind speed, air temperature, air
96 humidity and water surface temperature (Stull, 1988). The exchange at the air-water interface and
97 therewith the bulk coefficients are controlled by boundary-layer turbulence. The bulk exchange
98 coefficient of momentum, known as the drag coefficient (C_D, C_{DN}) (Garratt, 1977), is of particular
99 importance for all air-water fluxes. The coefficients of heat (C_H, C_{HN}) and water vapor exchange
100 (C_E, C_{EN}) are also known as Stanton and Dalton numbers, respectively. Here, "N" stands for
101 "neutral" transfer coefficients, corresponding to the neutral thermal stability of the atmosphere.
102 The transfer coefficients depend on the measurement height of the mean wind speed, air
103 temperature and humidity, respectively, and for this reason, they are usually reported for the
104 reference meteorological height of 10 m.

105   A considerable amount of studies has been published on the momentum flux and the drag
106 coefficient starting from the early 1950s when the fundamental work, presenting the theory later
107 on named as Monin-Obukhov similarity theory, was published (Monin & Obukhov, 1954;
108 Obukhov, 1971). The theory aims at describing the structure of turbulence in the atmospheric
109 surface layer about several tens of meters thick with the assumption of the fluxes being constant
110 and independent of height. Similarity laws introduce functional relations to derive the universal
111 shapes for the vertical profiles of different quantities for atmospheric thermal stability other than
112 neutral. During the past decades, considerable effort has been devoted to define the exact form of
113 these similarity functions (Paulson, 1970; Businger et al., 1971; Högström, 1988; Zilitinkevich &
114 Calanca, 2010).

115   As the drag coefficient is one of the key parameters in atmospheric and lake models, the
116 errors in its parameterization lead to errors in the bulk flux estimates. Therefore, numerous early
117 studies focused on exploring different parameterizations of the drag coefficient over the land and
118 oceans in terms of wind speed, atmospheric stability, and surface roughness, which are a function
119 of the surface wave field (for oceans) (Garratt, 1977; Kantha & Clayson, 2000). Most of the
120 extensive field measurement campaigns over the oceans have been conducted during the last 30
121 years of the 20th century (Large & Pond, 1981; Godfrey & Beljaars, 1991; Smith et al., 1996;
122 Fairall et al., 1996). Several of these studies agreed that the drag coefficient linearly increases with
123 increasing wind speed ignoring the state of the wave field. More recent parameterizations of the
124 drag coefficient (e.g., the COARE algorithm by Fairall et al., (2003); Edson et al., (2013)),
125 however, include a wave dependence. There is still an ongoing scientific discussion concerning
126 the importance of waves and how their impact could be included in the models (Wu et al., 2019).

127   Along with the studies in the marine environment, the research started to focus on the drag
128   coefficient estimated from measurements over large and medium-sized lakes (e.g., Hicks, 1972;
129   Donelan, 1982; Graf et al., 1984; Simon, 1997). To date, in total, about two dozen studies focusing
130   on lakes have been published since the beginning of the 1970s. In reviewing these studies, we
131   separated them by the wind speed regime they were interested in. It is usually assumed that surface
132   wave development starts when the wind speed exceeds 3-4 m s^{-1} (Ataktürk & Katsaros, 1999;
133   Kantha & Clayson, 2000). This is also supported by wave measurements in several lakes (Simon,
134   1997; Guseva et al., 2021). Therefore, we intend to separate the two wind speed regimes using this
135   threshold.

136   At the "high" wind speed regime (wind speed exceeds 3 m s^{-1}), in the most simplified way,
137   the surface waves are assumed to be fully developed, and the surface roughness length is described
138   as a function of wind stress, which is commonly known as Charnock relationship (Charnock,
139   1955). However, this assumption might not hold for lakes with limited wind fetch (Donelan, 1990;
140   Geernaert, 1990). Thus, some research has been made to study the drag coefficient as a function
141   of the surface wave state, for example, taking into account wave characteristics such as the wave
142   age (Donelan, 1982; Ataktürk & Katsaros, 1999). Vickers & Mahrt (1997) reported that for a given
143   wind speed the drag coefficient tends to be larger for younger steeper waves representative of short
144   wind fetches than for longer fetches. Ataktürk & Katsaros (1999) could significantly reduce the
145   scatter in the estimated drag coefficients by considering waves in the parameterization of the
146   surface roughness length. However, these studies mainly examined large lakes and only a few were
147   performed in lakes with short fetch and young wave states (Babanin & Makin, 2008; Lükő et al.,
148   2020). Given the fact that the surface wave measurements in lakes are often not available, their
149   effect still could be investigated via analyzing the relationship between the drag coefficient and
150   fetch length.

151   At the "low" wind speed regime, several studies found that the neutral drag coefficient in
152   lakes and oceans tended to increase by an approximate factor of two up to ten compared to the
153   value of $1.3 \cdot 10^{-3}$ (corresponding to a typical value of open water surface roughness (Foken, 2008))
154   (Wüest & Lorke, 2003; Woolway et al., 2017). Although the wind speed dependence is obvious,
155   many numerical and empirical studies employ a constant value for the drag coefficient, which is
156   often considered as a model tuning parameter (Stepanenko et al., 2014). Despite the fact that there
157   have been many attempts to address the reasons of such increase, there is still no consensus in the
158   scientific community. The low wind speed regime was first described as the aerodynamically
159   smooth flow, when the surface waves are buried within the viscous sublayer and the surface
160   roughness is described as a function of the thickness of this layer (Schlichting, 1968). On the
161   contrary, Wu (1988) proposed that the flow is aerodynamically rough and that capillary gravity
162   waves play a key role at low wind speeds. Surface roughness length was described as a function
163   of the water surface tension. As an additional reason for the increase of the drag coefficient at low
164   wind speed, Godfrey & Beljaars (1991) and Grachev et al. (1998) considered the concept of
165   gustiness, which assumes that at "zero" wind speeds there are dry random convective motions –
166   gusts – in the convective boundary layer (CBL). Thus, the "traditional" formulation of the drag
167   coefficient has been modified using the scalar-averaged wind speed (not the vector-averaged wind
168   speed) to account for gusts. All the possible mechanisms mentioned above were addressed in the
169   recent work by Wei et al. (2016). They concluded that none of them explained the increase of the
170   drag coefficient at low wind speeds. However, they found it can be explained by the increase in
171   the turbulent kinetic energy due to buoyant energy production. Similar to Grachev et al. (1998),
172   Sahlée et al. (2014) and Liu et al. (2020) related the increase of the drag coefficient with nonlocal

effects, such as the penetration of large convective eddies into the surface layer from the atmosphere above. Liu et al. (2020) introduced the factor describing this effect and estimated it from two-level measurements of wind speed (however, over the land surface and only for neutral conditions). Another formulation of the drag coefficient at low wind speeds was done by Zhu & Furst (2013) relating the drag coefficient to the turbulent kinetic energy budget. However, their fitting coefficients for the drag coefficient formula were found to be site-specific (Liu et al., 2020).

Other studies on the bulk transfer coefficients in lakes branched off from the main direction – potential physical mechanisms – with a focus on the possible correlation between the bulk transfer coefficients and some lake characteristics. Among them are lake depth at the measurement location (Panin et al., 2006), lake surface area (Read et al., 2012; Woolway et al., 2017), wind fetch at the measurement location (Lükő et al., 2020) and lake biota, e.g, submerged macrophytes (Xiao et al., 2013). All studies showed a strong dependence of the transfer coefficients on these lake characteristics. The drag coefficient tends to decrease with increasing water depth, lake area, fetch and in the presence of water plants at the water surface. It is important to note that although Panin et al. (2006) and Woolway et al. (2017) revealed the correlation between the transfer coefficients and the lake parameters, the estimation of the transfer coefficients was based either on bulk parameterization (Woolway et al., 2017), or was compared to other studies where there were no direct flux measurements (Panin et al., 2006).

Fewer studies have been published on the Stanton and Dalton numbers. Although the measurements in the oceans showed their obvious increase at low wind speeds, both transfer coefficients were considered as fairly constant with a value of $1.1 \cdot 10^{-3}$ (review of these measurements in Kantha & Clayson (2000)). First measurements conducted in lakes revealed this value being higher and equal to $\sim 1.5 \cdot 10^{-3}$ (Harbeck, 1962; Hicks, 1972) or $1.9 \cdot 10^{-3}$ (Strub & Powell, 1987). Harbeck (1962) and Brutsaert & Yeh (1970) reported a dependence of the Dalton number on the lake surface area. Heikinheimo et al. (1999) summarized that the Dalton number is generally known to be less dependent on the wind speed. From the most recent studies (Xiao et al., 2013; Li et al., 2016; Wei et al., 2016; Dias & Vissotto, 2017), there is evidence that both coefficients depend on the wind speed and that the Stanton number is higher than the Dalton number by approximately a factor of 1.3. This indicates that the earlier assumption of the equality of both coefficients may not be valid for lakes.

The eddy-covariance (EC) technique is a micrometeorological method to directly measure momentum, heat, water vapor and greenhouse gas fluxes (Foken, 2008). It is based on the correlation between turbulent fluctuations of vertical wind speed and scalar air properties. Using this technique, one can obtain the spatial and temporal average of turbulent fluxes originating from an area called footprint and a period of meteorological stationarity (Lenschow et al., 1994; Sun et al., 2006; Burba & Anderson, 2010; Foken et al., 2012). Nowadays, the EC technique is commonly used over lakes (Blanken et al., 2000; Vesala et al., 2006; Nordbo et al., 2011; Lee et al., 2014; Mammarella et al., 2015; Spank et al., 2020; Golub et al., 2021). However, several studies reported difficulties in measuring the wind stress at weak winds, which resulted in large uncertainties (Kantha & Clayson, 2000). Low wind speed conditions are more relevant for lakes and specifically small lakes that are the most abundant inland water bodies (Downing et al., 2006).

In this study, we evaluate the first multiple water body estimates of bulk transfer coefficients and their dependencies on wind speed and water body characteristics using EC data measured above lakes. The analysis aimed at answering the following research questions: 1) what are the typical values for the bulk transfer coefficients and their variability among lakes and

218 reservoirs? 2) how do the values compare with the reported transfer coefficients for oceans and
219 other lakes? 3) can the mechanistic approaches mentioned above describe the transfer coefficients
220 at low wind speed regime? 4) is there a consistent dependence of the transfer coefficients on lake
221 characteristics, such as water depth, lake area and wind fetch? In the sections below, we examine
222 possible answers.

223 **2 Materials and Methods**

224   2.1. Eddy-covariance dataset

225   For this analysis, most of the existing EC data measured by various researchers over lakes
226 and reservoirs were extracted from open access databases and repositories of published papers.
227 The fluxes that are reported in the datasets were calculated using different software (e.g., EddyPro
228 (LI-COR, Inc, 2021), TK3 (Mauder & Foken, 2015), EddyUH (Mammarella et al., 2016)). In total,
229 we obtained data for 23 lakes and 8 reservoirs located in the arctic, subarctic, temperate and
230 subtropical zones (Figure 1, Table S1). The water bodies are located in different landscapes,
231 including mountains (e.g., Lake Lunz, Austria or Lake Klöntal, Switzerland), forests (e.g., Lake
232 Vanajavesi, Finland), and arctic landscapes. The EC mast at each lake or reservoir was installed
233 either on a floating or bottom-fixed platform, on shore, or on small islands. The measurement
234 height ranged between 1.3 m and 16.1 m with 2 m being the most frequent height among all
235 datasets. Elongated shapes of the lakes or shore/island locations were the subject of wind direction
236 filtering to ensure that the measured surface fluxes were originating from water. Approximately
237 half of the water bodies in this study had a surface area (A_s [km^2]) smaller than 10 km^2 with an
238 average wind fetch (F_{ave} [m]) ranging from 160 m to 1550 m. The fetch grid was estimated from
239 the map as the distance from the measurement location to the shore with the corresponding wind
240 direction. Then, the time series of the fetch was interpolated from this grid using the measured
241 wind directions. The average fetch was calculated as the mean distance for the filtered wind
242 directions. The rest of the lakes and reservoirs were larger: the maximum surface area of $2.6 \cdot 10^4$
243 km^2 and the maximum mean fetch of $2.6 \cdot 10^4$ m refer to one of the North-American Great Lakes –
244 Lake Erie in the USA. The maximum depth (D_{max} [m]) varied between 1.3 m (Lake Villasjön,
245 Sweden) and 89 m (Rappbode Reservoir, Germany). Each EC dataset contained the estimated
246 variables averaged over 30 min intervals.
247   The variables included wind speed (U_z [m s^{-1}]), wind direction (WD [$^\circ$]), friction velocity
248 (u_* [m s^{-1}]) as a quantity characterizing the momentum flux ($\tau = \rho_a u_*^2$ [kg m^{-1} s^{-2}], ρ_a – air density
249 [kg m^{-3}]), air temperature (T_a [$^\circ$C]), turbulent fluxes of sensible heat (H [W m^{-2}]), and latent heat
250 ($L_v E$ [W m^{-2}]), the latter referred to in this paper as water vapor heat flux as well. Water temperature
251 was provided either as skin surface temperature (T_s [$^\circ$C]) or bulk water temperature, measured at
252 0-0.5 m water depth (T_w [$^\circ$C]). The skin temperature was observed with an infrared thermometer
253 or calculated from outgoing longwave radiation, both corrected for the reflectance of incoming
254 longwave radiation. Some lakes or reservoirs had only momentum flux data, resulting in fewer
255 estimates of heat and water vapor transfer coefficients. Precipitation (parameter which was
256 considered as a factor for filtering the data) was not available for all datasets. The duration of the
257 EC measurements ranged from 11 days (Lake Wohlen, Switzerland) to 2243 days (or ~ 6.1 years,
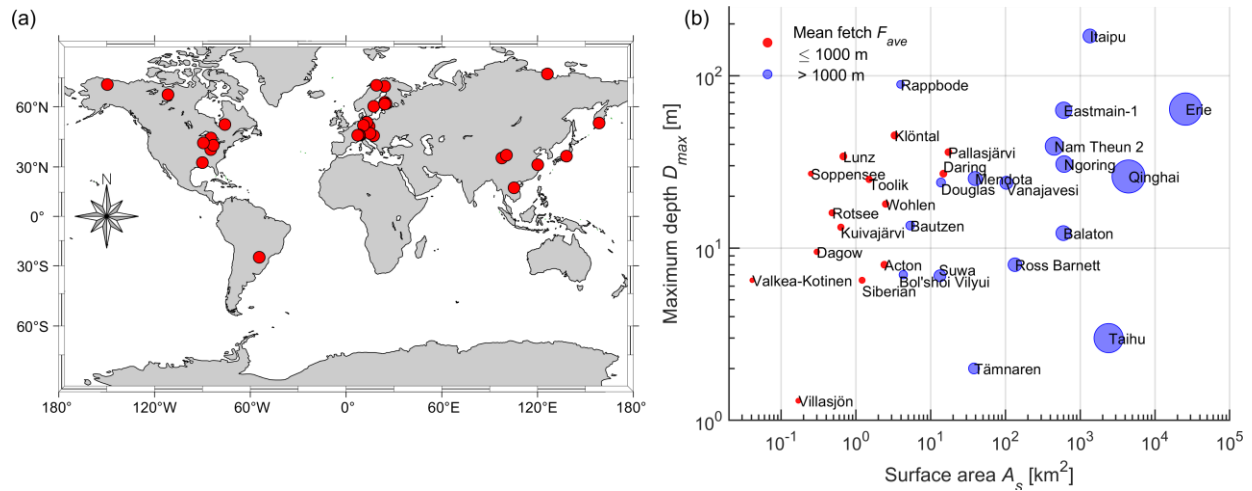258 Lake Dagow, Germany) with a median duration of 155 days.
259

Figure 1. (a) Geographical distribution of the eddy-covariance measurements over the lakes and reservoirs used in this study (red circles). Map was created using the software by Pawlowicz (2020). (b) The maximum depth versus surface area for each lake or reservoir. The circles in blue and red color show lakes with average wind fetch less than or more than 1000 m, respectively, with the lake name next to it. The diameter of the circle represents the relative average fetch: the larger diameter, the larger the average fetch is.

260

261   2.2. Data filtering and averaging

262   The individual datasets used in the analysis were subject to filtering with the following
263 different criteria:

264   a) filtering based on stationarity and integral turbulence test quality flags;
265   b) restriction of the wind directions to ensure >90% of footprint was originated from
266   water;
267   c) removing periods with ice cover;
268   d) removing periods with precipitation (if data on precipitation was available);
269   e) removing periods when the difference between water surface temperature (surface
270   water specific humidity) and air temperature (air specific humidity) is less than 0.2°C
271   ($1.5\cdot10^{-3}$ kg kg^{-1});
272   f) removing periods with floating vegetation on the water surface (only for Lake Suwa,
273   Japan).

274 Quality screening of EC data is known to be site- and instrument- specific (Burba & Anderson,
275 2010). The data were either available in filtered form, or they contained the quality flags provided
276 by the software. Non-filtered datasets included quality flags for each flux value (momentum,
277 sensible and latent heat fluxes) to ensure the stationarity of the time series (homogeneity of the
278 flow) and developed turbulent conditions (Foken et al., 2004; Foken & Wichura, 1996).

279   Removing wind directions was site-specific and we carefully studied each individual site.
280 We only accepted the data from periods when wind was blowing from the lake with sufficient
281 fetch. We specified the accepted wind directions for each site in Table S1. We focused on open-
282 water conditions and discarded ice-covered periods either using the water temperature time series
283 or interval camera data. For Lake Suwa we removed the approximate periods when floating
284 vegetation appeared on the water surface using interval camera data, however, for other sites this

285 kind of data was not available. For some sites, all erroneous data due to rain interference and site
286 maintenance were filtered by data providers, or we removed periods with precipitation (if data
287 were available). Based on the standard accuracy of temperature and humidity sensors, we also
288 applied a minimum threshold for temperature and specific humidity difference between water
289 surface and air. We describe the effect of these filters on the data in Text S1. Note, that in SI and
290 in the sections below all transfer coefficients are shown as median values following suggestions
291 from former studies (DeCosmo et al. (1996); Fairall et al. (2003)).

292   2.3. Transfer coefficients

293   Turbulent fluxes of momentum (τ), sensible heat (H) and latent heat (L_vE) at the water
294 surface are expressed as:
295

$$\tau = \rho_a[(\overline{u'w'})^2 + (\overline{v'w'})^2]^{1/2} = \rho_a u_*^2 = \rho_a C_D U_{10}^2, \tag{1a}$$
$$H = \rho_a c_p \overline{w'T'} = -\rho_a c_p T_* u_* = \rho_a c_p C_H U_{10}(T_s - T_{10}), \tag{1b}$$
$$L_vE = \rho_a L_v \overline{w'q'} = -\rho_a L_v q_* u_* = \rho_a L_v C_E U_{10}(q_s - q_{10}), \tag{1c}$$

296

297 where u', v', w' are the horizontal and vertical wind velocity fluctuations, respectively; $\overline{w'T'}$ [m s^{-1}
298 K], $\overline{w'q'}$ [m s^{-1} kg kg^{-1}] are the covariances of vertical wind velocity and air temperature (T') and
299 specific humidity (q') fluctuations. U_{10} [m s^{-1}] is wind speed at 10 m height, T_s and T_{10} [K] are the
300 surface water temperature and the air temperature at 10 m height, respectively, q_s and q_{10} [kg kg^{-1}
301] are the specific humidity at the air-water interface (estimated from surface temperature) and at
302 10 m height, respectively. c_p [J kg^{-1} K^{-1}] is the specific heat of air at constant pressure, and L_v [J
303 kg^{-1}] is the latent heat of vaporization. $T_* = \frac{-\overline{w'T'}}{u_*}$ and $q_* = \frac{-\overline{w'q'}}{u_*}$ are temperature and specific
304 humidity scales, respectively. The standard sign convention is that the momentum flux is defined
305 as positive downward, while sensible and latent heat fluxes as positive upward (Kaimal &
306 Finnigan, 1994). Equations 1a-1c are not the only way to describe the transfer coefficients. The
307 widely used COARE 3.0 bulk algorithm (Fairall et al., 2003) includes scalar-averaged wind speed
308 instead of U_{10} (vector-averaged wind speed) in Eq. 1a-1c, which includes the gustiness (will be
309 discussed below in Section 2.4.4).
310   Using measured flux data from the obtained EC datasets, the transfer coefficients can be
311 derived from Eq. (1a-c) as follows:
312

$$C_D = \frac{u_*^2}{U_{10}^2}, \tag{2a}$$

$$C_H = \frac{\overline{w'T'}}{U_{10}(T_s - T_{10})}, \tag{2b}$$

$$C_E = \frac{\overline{w'q'}}{U_{10}(q_s - q_{10})}. \tag{2c}$$

313
314 Wind speed, air temperature (T_z) and specific humidity (q_z) measured at a certain height z were
315 converted to a standard height of 10 m considering stability of the atmosphere following the
316 equations:

317

$$U_{10} = U_z - \frac{u_*}{\kappa}\left[\ln\left(\frac{z}{10}\right) - \psi_u\left(\frac{z}{L}\right) + \psi_u\left(\frac{10}{L}\right)\right], \tag{3a}$$

$$T_{10} = T_z - \frac{T_*}{\kappa}\left[\ln\left(\frac{z}{10}\right) - \psi_T\left(\frac{z}{L}\right) + \psi_T\left(\frac{10}{L}\right)\right], \tag{3b}$$

$$q_{10} = q_z - \frac{q_*}{\kappa}\left[\ln\left(\frac{z}{10}\right) - \psi_T\left(\frac{z}{L}\right) + \psi_T\left(\frac{10}{L}\right)\right], \tag{3c}$$

318

319 where κ is the von Kármán constant, L [m] is the Obukhov length, $\psi_u\left(\frac{z}{L}\right)$ is the stability function

320 which is the integral of the empirical universal function for the momentum flux and $\psi_T\left(\frac{z}{L}\right)$ – the

321 same for sensible and latent heat (Businger et al., 1971). In the literature, z/L is usually denoted

322 as the non-dimensional stability parameter ζ. To remove the effect of atmospheric stability on the

323 magnitude of the transfer coefficients, C_D, C_H, C_E are converted to their neutral counterparts

324 C_{DN}, C_{HN}, C_{EN} (i.e. for neutrally-stratified atmospheric conditions) (Large & Pond, 1981):

325

$$C_{DN} = \kappa^2\left[\ln\left(\frac{10}{z_0}\right)\right]^{-2} = C_D\left[1 + \kappa^{-1}C_D^{\frac{1}{2}}\psi_u\left(\frac{10}{L}\right)\right]^{-2}, \tag{4a}$$

$$C_{HN} = C_D\left[1 + \kappa^{-1}C_D^{\frac{1}{2}}\psi_u\left(\frac{10}{L}\right)\right]^{-1}\left[\frac{C_D}{C_H} + \kappa^{-1}C_D^{\frac{1}{2}}\psi_T\left(\frac{10}{L}\right)\right]^{-1}, \tag{4b}$$

$$C_{EN} = C_D\left[1 + \kappa^{-1}C_D^{\frac{1}{2}}\psi_u\left(\frac{10}{L}\right)\right]^{-1}\left[\frac{C_D}{C_E} + \kappa^{-1}C_D^{\frac{1}{2}}\psi_T\left(\frac{10}{L}\right)\right]^{-1}, \tag{4c}$$

326
327 where z_0 is the surface roughness length. For our calculations, we used the Kansas-type stability
328 functions (Businger et al., 1971) in the form of Högström (1988), which is the most frequently
329 applied form (Foken, 2008). C_{DN}, C_{HN}, C_{EN} were estimated for 31, 25, 23 water bodies under study,
330 respectively, depending on the flux data availability (see details about each lake or reservoir in
331 Table S1 and in data repository).
332   In the scientific community, there has been an ongoing discussion on the form of the
333 transfer coefficients to be presented. For example, some studies focused only on neutral values of
334 the drag coefficient (Li et al., 2016) or some considered the drag coefficient non-adjusted to their
335 neutral counterpart (C_D). Other studies addressed the so-called "effective" drag coefficient, which
336 was derived as the slope coefficient for the linear relationship between u_*^2 and U_{10}^2 (Xiao et al.,
337 2013). We examine the difference between C_D, C_H, C_E and C_{DN}, C_{HN}, C_{EN} in Section 3.1.

338   2.4. Parametrizations of the drag coefficient at low and high wind speeds

339   2.4.1. *Smooth flow*

340   Previous studies focused on the parameterizations of surface roughness length z_0 (see Eq.
341 4a) to assess wind speed dependence of the drag coefficient (e.g., Ataktürk & Katsaros (1999). In
342 our study, we compared C_{DN} estimated from measured momentum fluxes with the existing
343 approaches. One of the approaches is based on the smooth flow regime at low wind speed (< 3 m
344 s^{-1}), where the thickness of the viscous sublayer (δ_v) determines the aerodynamic roughness of the
345 interface (Schlichting, 1968), and not the physical roughness of the water surface:

346

$$\delta_\nu = z_0 = \alpha \frac{\nu}{u_*}, \tag{5}$$

347

348 where $\alpha = 0.11$ [-] and $\nu = 1.6 \times 10^{-5}$ [m^2 s^{-1}] is kinematic viscosity of air. z_0 can be derived
349 from Eq. 4a as:

350

$$z_0 = z \exp\left(-\frac{\kappa}{\sqrt{C_{DN}}}\right). \tag{6}$$

351
352

2.4.2. *Capillary waves*

354 As an alternative method to parameterize C_{DN} at low wind speeds, we considered the
355 approach proposed by Wu (1994). He suggested that the wind shear stress in the absence of large
356 gravity waves is related to the ripples (capillary waves). For the capillary waves, the roughness
357 length is related to surface tension (σ) as:

358

$$z_0 = \alpha_{Wu} \frac{\sigma}{\rho_w u_*^2}, \tag{7}$$

359 where $\alpha_{Wu} = 0.18$ [-] is an empirical constant and ρ_w [kg m^{-3}] is water density. Surface tension at
360 a temperature of 20°C is $\sigma = 7.28 \cdot 10^{-2}$ N m^{-1}.

2.4.3. *Charnock relationship*

362 With increasing wind speed, the thickness of the viscous sublayer becomes smaller, and
363 the aerodynamic roughness of the water surface (z_0) becomes minimal, before surface gravity
364 waves evolve. At wind speeds exceeding 3 m s^{-1}, waves protrude from the viscous sublayer and
365 surface roughness length increases with increasing wind speed, indicating the transition from a
366 smooth to a rough flow regime. Charnock, (1955) proposed the following equation for surface
367 roughness length over fully developed surface waves, which account for typical oceanic
368 conditions:

369

$$z_0 = \gamma \frac{u_*^2}{g}, \tag{8}$$

370

371 where γ ranges from 0.011 to 0.0185 [-] (Garratt, 1994), g [m s^{-2}] is the gravitational acceleration.
372

2.4.4. *The concept of gustiness*

374 Under strong convective conditions, the wind stress at the water surface is governed by
375 random convective motions - gusts - in the convective boundary layer (CBL), whereas the mean
376 wind speed vector can even become zero (Godfrey & Beljaars, 1991). These large convective
377 eddies embrace the entire CBL and affect the turbulence regime in the atmospheric surface layer.
378 Grachev et al. (1998) formulated an approach to estimate the drag coefficient using this concept.

379   In their study, the gustiness could explain the apparent increase of the drag coefficient estimated
380   using the traditional equation (Eq. 2a, 4a) at low wind speeds. The estimated drag coefficient
381   accounting for gusts was a factor of 1.5 to 6 smaller at wind speeds below 2 m s^{-1} in comparison
382   to the drag coefficient calculated from Eq. 2a, 4a. The gustiness concept is widely accepted and
383   used in the COARE algorithm to estimate air-sea fluxes (Fairall et al., 2003).
384   The gustiness factor, G corresponds to the ratio of the scalar-averaged ($\widetilde{U}_{10}$, for the
385   definition see (Grachev et al., 1998)) to vector-averaged wind speed:
386

$$G_{wind} = \frac{\widetilde{U}_{10}}{U_{10}}. \tag{9}$$

387

388   Taking into account that $\widetilde{U}_{10}^2 = U_{10}^2 + U_g^2$, where $U_g \cong \sigma_u^2 + \sigma_v^2$ is a gustiness velocity (σ_u, σ_v
389   are standard deviations of the wind speed components), the gustiness factor can be estimated as:
390

$$G_{wind}^2 = \frac{U_{10}^2 + U_g^2}{U_{10}^2} = \frac{U_{10}^2 + (\sigma_U^2 + \sigma_V^2)}{U_{10}^2} = 1 + \frac{(\sigma_U^2 + \sigma_V^2)}{U_{10}^2}. \tag{10}$$

391

392   Since the scalar-averaged wind speed is not a standard output parameter in the EC-software, the
393   estimation of G from velocity standard deviations allowed calculation of the transfer coefficients
394   for more lake datasets. Alternatively, G can be parameterized in terms of the convective velocity
395   scale w_* (Grachev et al., 1998; Fairall et al., 2003). We denote the gustiness factors derived from
396   measured wind speed and from CBL scaling as G_{wind} and G_{conv}, respectively:
397

$$G_{conv}^2 = 1 + \left(\frac{\beta w_*}{U_{10}}\right)^2, \tag{11}$$

398   where $\beta = 1.2$ [-] is an empirical constant (Beljaars, 1995) and w_* is expressed as:
399

$$w_* = \left(g z_{CBL} \frac{\overline{w'T_v'}}{T_v}\right)^{1/3}, \tag{12}$$

400

401   where, T_v [K] is the virtual temperature, z_{CBL} [m] is the CBL height, defined as the height of the
402   lowest inversion. Previous studies used the fixed height of the CBL equal to 600 m (Fairall et al.,
403   2003) or 1000 m (Beljaars, 1995). The neutral gustiness drag coefficient C_{DNG} and its gustiness
404   counterpart $\widetilde{C}_{DG}$ is:
405

$$C_{DNG} = \left[C_{DG}^{-1/2} G + \kappa^{-1}\psi_u\left(\frac{10}{L}\right)\right]^{-2}, \tag{13a}$$

406

407   and other gustiness transfer coefficients, C_{HNG} and C_{ENG}, can be derived as:
408

$$C_{HNG} = \left[C_{DG}^{-1/2} G + \kappa^{-1}\psi_u\left(\frac{10}{L}\right)\right]^{-1}\left[C_{DG}^{1/2} C_{HG}^{-1} + \kappa^{-1}\psi_T\left(\frac{10}{L}\right)\right]^{-1}, \tag{13b}$$

$$C_{ENG} = \left[C_{DG}^{-1/2} G + \kappa^{-1} \psi_u \left(\frac{10}{L} \right) \right]^{-1} \left[C_{DG}^{1/2} C_{EG}^{-1} + \kappa^{-1} \psi_T \left(\frac{10}{L} \right) \right]^{-1} , \qquad (13c)$$

409

410 where $C_{DG} = \left(\frac{\tilde{u}_*}{U_{10}} \right)^2$ and $\tilde{u}_*$ is the scalar-averaged friction velocity. The majority of the available
411 EC datasets from lakes did not contain the scalar-averaged friction velocity. Akylas et al. (2003)
412 investigated the combinations with different averaging procedures and suggested that vector-
413 averaged friction velocity u_* is more appropriate to use with scalar-averaged wind speed for all
414 wind speed classes. Thus, we used the vector-averaged friction velocity and therefore $C_{DG} = C_D$,
415 $C_{HG} = C_H, C_{EG} = C_E$.
416   In a first step, we applied the gustiness approach for the drag coefficient with the cases
417 corresponding to unstable atmospheric condition ($\zeta < 0$). We estimated two types of the gustiness
418 drag coefficient, using as G_{wind} and G_{conv} and we considered the former one as a reference. These
419 calculations were possible only for a subset of the datasets (11 lakes) for which both scalar-
420 averaged wind speed (or the standard deviations of the wind speed components) and virtual
421 sensible heat flux ($\overline{w'T_v'}$) were available. Then we fitted the coefficient β in Eq. 11 in order to get
422 best agreement between the parametrized C_{DNG} and the referenced one. As the second step, we
423 applied the parametrization of gustiness with the fitted β (Eq. 11) to larger subset of the data (26
424 lakes) for which the virtual sensible heat flux was available. Thus, we estimated all gustiness
425 transfer coefficients (Eq. 13a-13c).
426   We compared the gustiness transfer coefficients with the standard formulations (Eq. 4a-
427 4c) and with the results from the COARE 3.0 bulk algorithm (Fairall et al., 2003), which includes
428 the parameterization of gustiness (Eq. 11-12). In addition, the COARE algorithm considers the
429 effect of changing water surface roughness by using parameterizations of z_0 that combines the
430 smooth flow approach (Eq. 5) and Charnock's relationship (Eq. 8).
431

3 Results

433   3.1. Transfer coefficients over lakes

434   Bulk transfer coefficients for neutral atmospheric stability C_{DN}, C_{HN} and C_{EN} (Eq. 4a-4c)
435 were estimated using data from 23 lakes and 8 reservoirs (see data availability details in Table in
436 the data repository). The transfer coefficients varied between the water bodies and differed on
437 average by a factor of 2-3 for wind speeds exceeding 3 m s^{-1}. However, we identified three water
438 bodies for which the estimated drag coefficients (C_{DN}) were exceptionally large at all wind speeds
439 (up to a factor of five, Lake Quinghai, China, Nam Theun 2 Reservoir, Laos), or exceptionally low
440 (factor of four, Bol'shoi Vilyui Lake, Russia), when compared to other water bodies with similar
441 surface area. These three water bodies contributed largely to the variability among systems (Figure
442 S5a shows the estimates for individual water bodies). We did not find possible sources of errors
443 and considered these data as outliers. In the overall estimates and in the range of variability shown
444 in Figure 2a, we included the complete dataset.
445   All transfer coefficients showed a similar wind speed dependence (Figure 2a-c). At high
446 wind speeds (> 3 m s^{-1}), C_{DN}, C_{HN}, C_{EN} had relatively constant values of $1.8 \cdot 10^{-3}$, $1.4 \cdot 10^{-3}$, $10 \cdot 10^{-3}$
447 $^{-3}$, respectively. All transfer coefficients increased towards the lowest wind speeds. The strongest
448 increase was found for C_{DN}, which was one order of magnitude higher ($1.1 \cdot 10^{-2}$) at the lowest wind
449 speed (0.5 m s^{-1}, the first bin) compared to values at higher wind speeds. A similar, but less

450 pronounced increase was observed for C_{HN} and C_{EN}: their values at the lowest wind speed were
451 $3.1 \cdot 10^{-3}$ and $2.2 \cdot 10^{-3}$, respectively.

452 Unstable atmospheric conditions ($\zeta < 0$) prevailed over all water bodies, particular during
453 the evening and at night time, when $> 80\%$ of all data were obtained under unstable conditions
454 (Figure 2d). Stable atmospheric conditions occurred most frequent during the day (12-19 hours).
455 In addition, we estimated the percentage of time when the wind speed was less than 3 m s^{-1} (Figure
456 2e). Low wind speed conditions prevailed slightly during the evening and at night, when the
457 atmosphere was mostly unstable. This means that the significant increase of the transfer
458 coefficients at low wind speeds frequently coincides with unstable atmospheric conditions, when
459 the water is still warm and the atmosphere starts cooling at the end of the day.

460 To analyze the effect of atmospheric stability on the transfer coefficients, we compared the
461 transfer coefficients (C_D, C_H, C_E, Eq. 2a-2c) with their neutral counterparts (C_{DN}, C_{HN}, C_{EN}, Eq. 4a-
462 4c, Figure S6). We found that atmospheric stability did not significantly affect the values of C_D,
463 C_H and C_E at wind speeds exceeding 3 m s^{-1}: their values were in close agreement with C_{DN},
464 C_{HN} and C_{EN}. However, it is evident that at low wind speeds (0-2 m s^{-1}) these transfer coefficients
465 under in-situ conditions were systematically higher (up to a factor of 2-3) than their neutral
466 counterparts C_{DN}, C_{HN} and C_{EN}.

467 Estimation of C_H and C_E (Eq. 2b, 2c and Eq. 4b,4c) involves water surface temperature, for
468 which the skin temperature is the most appropriate measure. However, these measurements were
469 not available for some sites. Instead, we used water temperature measured at some depth (often
470 varying between 0 and 0.5 m between datasets). We compared three types of calculations of C_H
471 using two subsets which use: (a) only skin temperature (b) only water temperature and (c) the
472 combined lake dataset which includes either skin or water temperature (Figure S7). C_{HN} estimated
473 with water temperature tends to be slightly lower than the estimates using skin temperature (the
474 mean percentage difference is approximately 15%). As a result, we presented C_H and C_E (Figure
475 2b, c) calculated using all available data, independent of how water surface temperature was
476 measured. When both the skin and water temperatures were available for one site, the skin
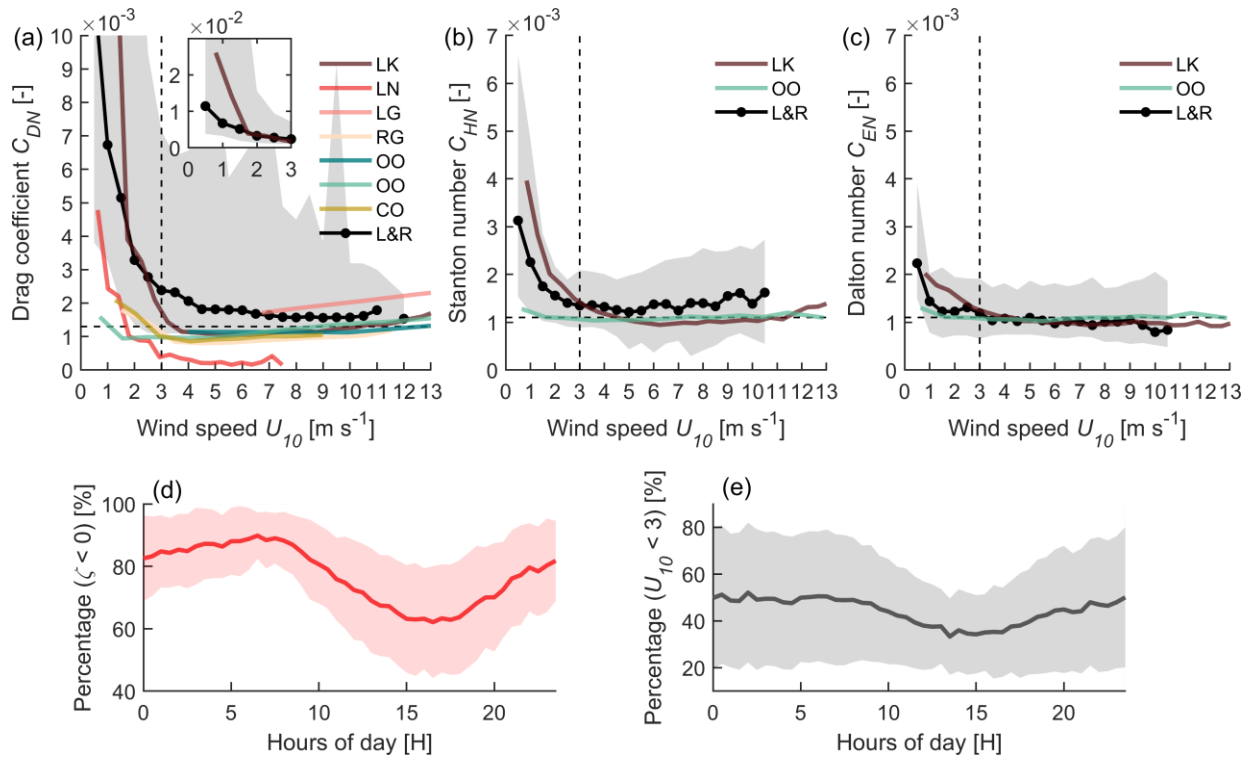477 temperature was used.

478

Figure 2. Neutral (a) drag coefficient (C_{DN}), (b) Stanton number (heat transfer coefficient, C_{HN}), (c) Dalton number (water vapor transfer coefficient, C_{EN}) versus wind speed at 10 m height. The shaded grey area indicates the variability among water bodies by marking the range from the 5th to the 95th percentiles of the median values estimated for each wind speed bin (0.5 m s^{-1}). The black line with circles, marked as L&R denoting "lakes and reservoirs", represents the median values for all lakes and reservoirs. The small inset in (a) shows the data beyond the scale. Vertical and horizontal black dashed lines mark a constant wind speed of 3 m s^{-1} and typical values of C_{DN}, $C_{HN} = C_{EN}$ 1.3·10[-3], 1.1·10[-3], respectively. Colored lines show the results from previous studies: LK, brown line – Lake Kasumigaura, Japan (eddy covariance, (Wei et al., 2016)); LN, red line – Lake Neuchâtel, Switzerland (dissipation method, (Simon, 1997)); LG, pink line – nearshore site at Lake Geneva, Switzerland (wind profile method, (Graf et al., 1984)); RG, light orange color – Reservoir Gorkiy, Russia (wind profile method, (Kuznetsova et al., 2016)); OO, dark green color – open ocean (eddy covariance, (Large & Pond, 1981)); OO, light green color – open ocean (eddy covariance, (Fairall et al., 2003)); CO, dark yellow color – coastal ocean at limited fetch conditions (eddy covariance, (Lin et al., 2002)). (d) Mean diel pattern of the percentage of time periods with unstable atmospheric conditions (stability parameter $\zeta < 0$). (e) Mean diel pattern of the percentage of time with low wind speed (< 3 m s^{-1}). The red and black lines in (d) and (e) show the mean value and the shaded area shows ± standard deviation of all data.

479

480   3.2. Parametrizations of the drag coefficient

481   As described in Section 2.4.4, we estimated drag coefficients accounting for gustiness
482 (C_{DNG}) using gustiness factors derived from measured scalar-averaged wind speed (G_{wind}), and

483 from the parametrization of convective velocities (G_{conv}). To test the applicability of the
484 parametrization, we compared C_{DNG} estimated using both approaches during unstable atmospheric
485 conditions for a subset containing 11 lake datasets with all required data (Figure S8). The estimated
486 C_{DNG} based on G_{conv} was slightly higher than the one based on G_{wind}. We obtained a coefficient
487 $\beta = 1.4$ (compared to a value of 1.2 suggested by Beljaars (1995)) for the best agreement between
488 both drag coefficients (minimum of the mean absolute value of their difference). Note, that for this
489 subset of lake dataset the gustiness drag coefficient was on a factor of two lower than C_{DN} (Figure
490 S8).
491   Using the fitted parameterization, we calculated C_{DNG}, C_{HNG} and C_{ENG} based on G_{conv} for
492 a larger subset of the data – 26 and 23 lakes (Figure 3). C_{DNG} and C_{ENG} decreased approximately
493 by a factor of two at wind speeds less than 1.5 m s^{-1} in comparison to the standard formulation
494 C_{DN} and C_{EN}. C_{ENG} was almost constant with a value of $1.0 \cdot 10^{-3}$ throughout all ranges of wind
495 speed. C_{HNG} decreases only slightly (~10%) in comparison with C_{HN} at low wind speeds. For wind
496 speeds exceeding 3 m s^{-1}, all gustiness transfer coefficients almost coincided with their standard
497 formulation, only C_{DNG} was slightly smaller: $\sim 1.6 \cdot 10^{-3}$.
498   We examined the possible mechanisms (Eq. 5, 7, Section 2.4) that could explain the
499 increase of the drag coefficient at low wind speed and the Charnock relationship (Eq. 8), which
500 describes its wind speed dependence at high wind speed. We applied the COARE 3.0 algorithm to
501 the same subset of the data (26 and 23 lakes) and compared the results with our estimates of the
502 gustiness transfer coefficients. It was evident that the smooth flow approach (together with
503 Charnock relationship) could not explain the increase of C_{DNG} at low wind speeds. However,
504 replacing this model with the approach which considers capillary waves (Eq. 7 with $\alpha_{Wu} = 0.8$) led
505 to reasonable agreement between the bulk parameterization and C_{DNG} estimated from measured
506 fluxes. In contrast, C_{ENG} calculated using this approach overestimated values of the EC-derived
507 C_{ENG}. There, the smooth flow was a more appropriate parameterization.
508   When analysing the standard formulation of the drag coefficient, we found that the
509 function describing the wind speed dependence of C_{DN} proposed by Liu et al. (2020) based on EC
510 measurements over terrestrial surfaces ($C_{DN} = b_1[1 + b_2 \exp(b_3 U_{10})]$), can also be applied to
511 observations over all lakes (Figure 3a). In a similar way, we applied this empirically derived
512 function to C_{HN} and C_{EN} estimates (Figure S7). The fitted coefficients for our data are provided in
513 Table 1.
514   The gustiness approach, together with increasing surface roughness due to capillary waves
515 allowed to explain the increase of the transfer coefficients at low wind speeds, suggesting that
516 these formulations of the transfer coefficients can provide most accurate flux parameterizations at
517 lake surfaces.
518   The mean ratio of C_{HNG} to C_{ENG} is 1.3 and has its maximum value of 2 at low wind speeds
519 (Figure 4). For wind speeds ranging from 2 to 9 m s^{-1} the ratio remained at relatively constant
520 value of 1.2.
521

Table 1. Coefficients for the empirical function $C = b_1[1 + b_2 \exp(b_3 U_{10})]$ (Liu et al., 2020)), describing the wind speed dependence of the bulk transfer coefficients of momentum (C_{DN}), heat (C_{HN}), and water vapor (C_{EN}). The coefficients were obtained from least-square fits of the function to the bin-averaged data shown in Fig. 3a to c.

	b_1	b_2	b_3
C_{DN}	$1.7 \cdot 10^{-3}$	1	-1.1
C_{HN}	$1.3 \cdot 10^{-3}$	1.5	-0.8

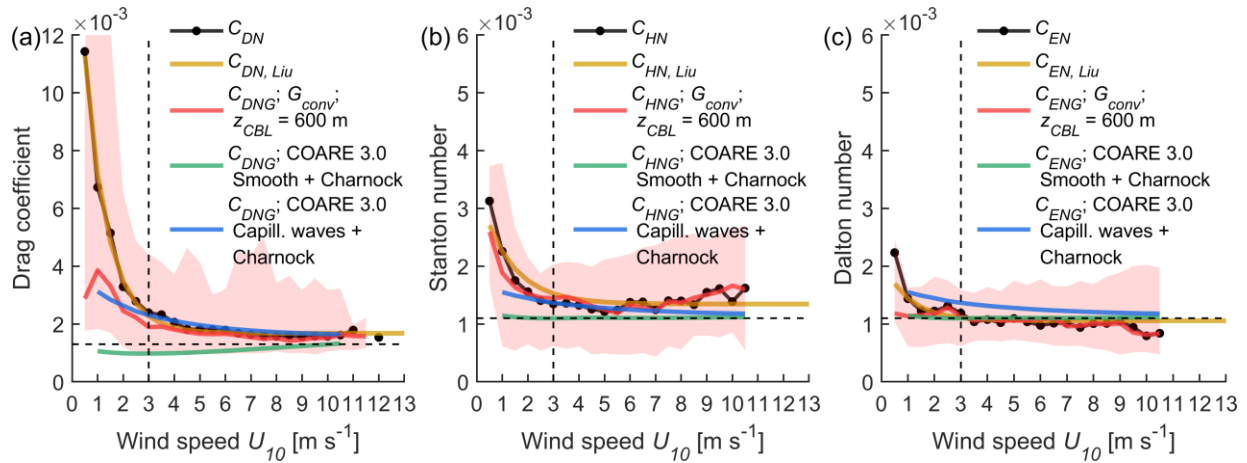| C_{EN}	$1.1 \cdot 10^{-3}$	1	-1

522

523

Figure 3. Neutral gustiness transfer coefficients (a) C_{DNG} , (b) C_{HNG} and (c) C_{ENG} (calculated using G_{conv} , see Section 2.4.4) versus U_{10} (red line) estimated for 26, 23 and 23 lakes, respectively. The red shaded area marks the range between the 5th and 95th percentiles. The black line with symbols shows estimates of C_{DN}, C_{HN} and C_{EN} from Figure 2. The dark yellow line in all plots shows the function $C_{DN} = b_1[1 + b_2\exp(b_3 U_{10})]$ proposed by Liu et al., (2020) with fitted coefficients (Table 1). The green and blue lines show transfer coefficients as they are used in the COARE 3.0 algorithm for bulk parameterizations. The green line shows the original COARE parameterization, which combines the effects of thesmooth flow approach (Eq. 5) and Charnock relationship (Eq. 8). The blue line shows a modified parameterization, which includescapillary wave roughness (Eq. 7 with $\alpha_{Wu}= 0.8$) and Charnock relationship.

524

525

526

527
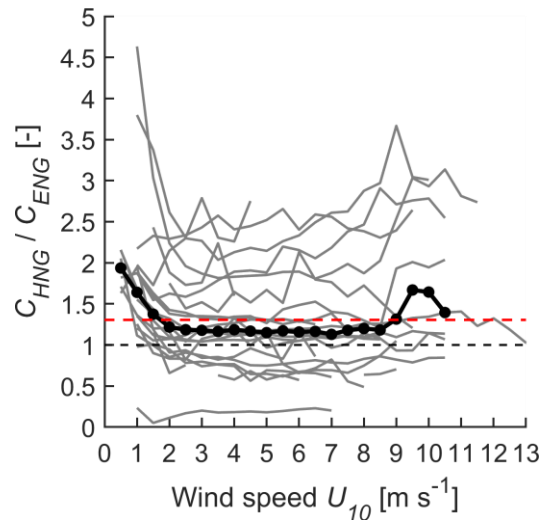
Figure 4. Ratio of C_{HNG} to C_{ENG} estimated for each individual dataset (21 water bodies, shown by grey lines). Black line with circles shows the median values for all datasets. The horizontal dashed black line shows a ratio of 1:1 and the horizontal dashed red line indicates the overall mean value of the ratio (1.3).

528

3.3. Dependence of the bulk transfer coefficients on the lake characteristics

530   We examined the dependencies of the bulk transfer coefficients accounting for gustiness
531   on lake characteristics, including the maximum and average water depth, water depth at the
532   measurement site, maximum and average wind fetch, and water surface area. As the transfer
533   coefficients at high wind speeds were relatively constant, we first analyzed effects of lake
534   characteristics on the median values of the transfer coefficients for wind speeds exceeding 3 m s^{-1}
535   estimated for each individual water body.

536   We found that C_{DNG} and C_{HNG} decreased significantly (Pearson correlation coefficient $r =$
537   -0.5, p-value < 0.05) with increasing lake surface area (Figure 5a, d). These relationships could be
538   expressed as power law dependencies ($y = x^A \exp(B \ln 10)$, where A and B are the slope and
539   intercept of the linear regression $\log_{10} y = A \log_{10} x + B$) with exponent of -0.06. Most variability
540   in C_{DNG} was found to be explained by the lake surface area (for log-transformed data the
541   coefficient of determination was $R^2 = 0.3$). The correlation between C_{DNG}, C_{HNG} amd C_{ENG} and
542   mean or maximum fetch was low ($r \sim$ -0.2, -0.3, Figure 5b,e,h, Figure S9a,d,g). A principal
543   component analysis revealed that lake surface area has a largest predictive power (Figure S10).
544   We did not find a significant correlation ($r \sim$ -0.3, p-value > 0.05) between C_{ENG} and surface area,
545   however, a similar trend as for C_{DNG} and C_{HNG} could be observed.

546   Using the principal component analysis, we identified that there was no significant
547   correlation of the transfer coefficients at high wind speeds with maximum, average or local water
548   depth (Figure 5c,f,i, Figure S9, S10). We used the exponential dependence from Panin et al. (2006)
549   to compare with our results. However, we did not have sufficient sites with larger depth to confirm
550   the depth dependence reported in their study.

551   At low wind speeds (< 3 m s^{-1}), the transfer coefficients were strongly wind speed
552   dependent (Figure 2a,b,c) and their relationships with lake characteristics are examined separately
553   for each different wind speed interval. Here we found that C_{DNG} significantly increased with

554   increasing water surface area for wind speeds between 0.5 m s^{-1} and 2 m s^{-1}. At higher wind speeds
555   these correlations become negative, as in the analysis for wind speed > 3 m s^{-1} presented above.
556   As an example, we show the transfer coefficients for a wind speed of 1 m s^{-1} in Figure S11. At the
557   same time, we found significant correlation of C_{DNG} with measurement height at low wind speeds,
558   which was not present at high wind speeds (Figure S11d). No correlation with measurement height
559   was found for C_{HNG} and C_{ENG}.
560   Additionally, we looked for a possible relationship between the averaged wind speed
561   (estimated over entire time series for each individual water body) and surface area. We found a
562   significant correlation between them in a double-logarithmic domain ($r = 0.5$, p-value < 0.05,
563   Figure S12), resulting in increasing mean wind speed with increasing lake size following a power-
564   law dependence $U_{10} = A_s^{0.05}\exp(0.5\ln 10)$.
565
566
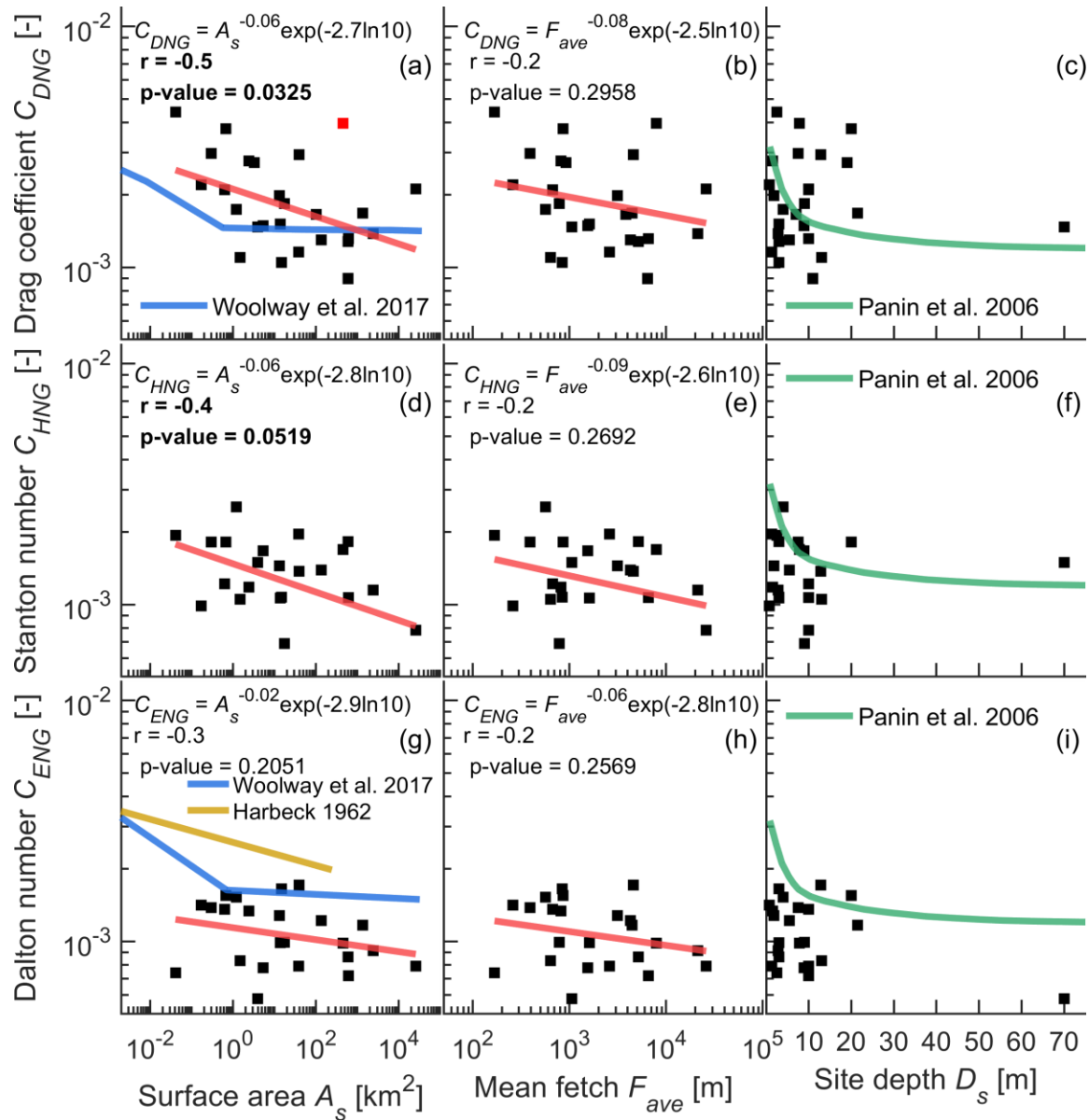
Figure 5. Neutral transfer coefficients accounting for gustiness (a, b, c) C_{DNG}; (d, e, f) C_{HNG}; (g, h, i) C_{ENG} versus surface area of the water body, mean fetch length, and water depth at the measurement site. Panels show the median values of the transfer coefficients for wind speeds exceeding 3 m s^{-1} for each individual water body. The red lines show the linear regressions of log-transformed transfer coefficients. The corresponding power laws as well as the Pearson correlation coefficient (*r*) and p-value are provided in the upper left corner of each panel. Significant correlation is marked by bold labels. The single red symbol in (a) marks the data from Nam Theun 2 Reservoir, which was not considered in the linear regression analysis and in the Pearson correlation as an obvious outlier. Blue, green and dark yellow lines show results from previous studies by Woolway et al., (2017; Panin et al. (2006; Harbeck, (1962), respectively.

567

4 Discussion

4.1. Bulk transfer coefficients estimated for lakes and reservoirs

We examined the bulk transfer coefficients describing the transport of momentum, heat and water vapor at the water surface estimated based on EC data collected at 23 lakes and 8 reservoirs of different size, depth, and location. At first, we used their standard formulations commonly used in literature (Eq. 4a-c). All transfer coefficients tended to increase towards low wind speeds and remained relatively constant at wind speeds exceeding 3 m s^{-1}. This increase was reported in previous studies for lakes (see, e.g., Wei et al., 2016; Xiao et al., 2013) and for the land surface (Grachev et al., 2011; Liu et al., 2020) and has been extensively investigated, yet remained unexplained up to now. Authors of Grachev et al. (2011) referred to lakes as an "intermediate" case between over-sea and over-land locations in terms of turbulent transfer. The lower bound for C_{DN}, C_{HN}, C_{EN} among the water bodies at high wind speeds were within the range reported by previous studies, including for large lakes (> 200 km^2, (Kuznetsova et al., 2016; Wei et al., 2016)), classical open ocean measurements (Fairall et al., 2003; Large & Pond, 1981) and coastal sites under fetch-limited conditions (Lin et al., 2002). Indeed, we also considered large lakes (Figure 1b) that were expected to have the smallest drag coefficient as they had the largest fetch (e.g., Lake Erie, Lake Taihu, Lake Balaton). The mean C_{DN} for winds exceeding 3 m s^{-1} was equal to $1.8 \cdot 10^{-3}$ and this value corresponded to an upper bound for the water surface roughness (0.001 m) reported by Foken (2008), but was a factor of two higher than the values reported for oceans and large lakes or reservoirs (Large & Pond, 1981; Fairall et al., 2003).

Values of C_{DN} varied considerably depending on the type of measurements used for its estimation. For example, in Simon (1997), C_{DN} was calculated from the dissipation rate of turbulent kinetic energy measured at the water side of the air-water interface in the relatively large Lake Neuchâtel (218 km^2, Switzerland). C_{DN} was significantly lower than our estimates (factor of ten) and the estimates from lakes or marine measurements (factor of five). However, these estimates also confirmed the increase of C_{DN} at low wind speeds. C_{DN} at high wind speeds calculated from the wind profile method at the nearshore site in Lake Geneva (Graf et al., 1984) was in close agreement with our estimates. The strong increase of C_{DN}, C_{HN}, C_{EN} at low wind speeds was similar to the one observed for a large lake using surface fluxes measured by EC method(Wei et al., 2016), but it was not supported by measurements in the marine environment.

4.2. Bulk transfer coefficients at low wind speed

Low wind speeds are typical conditions for lakes (Woolway et al., 2018), especially for smaller ones (Figure S10), which are most abundant by number (Downing et al., 2006). The most pronounced increase in bulk transfer coefficients at low wind speed was observed for C_{DN}, which was up to one order of magnitude higher at low wind speeds compared to its value at high wind speeds. We found less pronounced increases of C_{EN} and C_{EN}, yet their values at low wind speed can be larger compared to the constant values at high wind speed by up to factor of three and two, respectively. Periods with low wind speeds mostly corresponded to periods with unstable atmospheric conditions or enhanced convective transport, which is the most prevailing condition at all studied lakes during the ice-free period. It confirms former findings of Read et al. (2012) and Woolway et al. (2017).

While Wei et al., (2016) suggested that the contribution of gusts (different formulation of the C_{DN}) was not significant in their measurements obtained over a large lake, we found that the strong increase can partially be attributed to missing consideration of gustiness in the definition of

612   C_{DN}. Correction involving the gustiness factor (G_{conv}) could reduce the values of C_{DN} and C_{EN} by
613   up to a factor of two at wind speeds around 0.5 m s^{-1}. Thus, the gustiness approach is recommended
614   to be applied in bulk parametrizations of both fluxes in lakes.

615   It is important to note, that the CBL scaling requires knowledge about the height of the
616   unstable boundary layer, for which we used a fixed value of 600 m, as in other studies, including
617   the COARE algorithm for bulk parametrization of air-sea fluxes (Fairall et al., 2003). Over lakes,
618   convective motions can be associated with lake-land breeze circulation (Crosman & Horel, 2012),
619   which additionally depends on lake size and on the atmospheric conditions in the surrounding
620   landscape. Nevertheless, we found that the gustiness parameterization based on the convective
621   velocity scale (G_{conv}) agreed reasonably well with observed gustiness in wind speed fluctuations
622   (G_{wind}). Best agreement was obtained by using a slightly higher value of the empirical constant β
623   (Eq. 11), for which we estimated a value of 1.4 (compared $\beta = 1.2$ used in the COARE algorithm.
624   The close agreement between parameterized and measured guestiness suggests that the
625   parameterization can improve bulk parametrizations also under more complex CBL dynamics in
626   lakes in comparison to the open ocean.

627   Comparison of our measurements with the bulk parametrizations in the commonly used
628   COARE 3.0 algorithm, which includes the gustiness correction (Fairall et al., 2003), showed a
629   remaining underestimation of the parameterized C_{DNG} at low wind speed. Obviously, the
630   remaining increase in the gustiness-corrected drag coefficient at low wind could not be described
631   by the smooth flow parametrization (Eq. 5), which is applied in the COARE 3.0. Instead, we
632   applied the capillary wave approach for parametrizing the surface roughness at low wind speed
633   (Eq. 7) and found reasonable agreement between observed and parameterized gustiness drag
634   coefficients. For C_{ENG} the smooth flow model performed better, as it became a nearly constant
635   value after applying the gustiness approach. The effect of gustiness was not significant for C_{HNG}
636   and similar to C_{DNG} the capillary wave parametrization performed better than smooth flow
637   approach.

638   The wind speed dependence of the bulk transfer coefficients in their standard formulation
639   (especially at low winds), could be well described by an empirical function that was originally
640   proposed for the land surface (Liu et al., 2020). This suggests that this function can be used to
641   describe the transfer coefficients without consideration of gustiness.

642   Unexpectedly, we found that the gustiness drag coefficient significantly increase with
643   increasing lake surface areaat wind speeds less than 2 m s^{-1}. This result is counterintuitive, because
644   at low winds we did not expect a dependence on lake surface area or fetch, as it should only be
645   important for the development of surface waves, which appears only at wind speeds exceeding 3
646   m s^{-1} (Simon, 1997; Guseva et al., 2021). At the same time, we found a significant positive
647   correlation between C_{DNG} and the measurement height, which was also unexpected. This finding
648   could be the result of measurement limitationsand require a separate detailed investigation.

649

650   4.3. Bulk transfer coefficients at high wind speed

651   The estimated C_{DN} and C_{DNG} agreed closely at high wind speeds, thus, can be considered
652   identically. In comparison to the results from the COARE 3.0 algorithm, C_{DNG} at wind speeds
653   larger than 3 m s^{-1} was higher than predicted by Charnock relationship (Eq. 8). This result was
654   expected as Charnock relationship is based on the assumption that the water surface roughness is
655   controlled by fully developed surface gravity waves. When comparing with the results from the
656   modified COARE 3.0 algorithm (capillary wave instead of smooth flow approach), we found that

657   the consideration of Charnock relationship had a weak influence only, so that it could probably be
658   omitted without large changes in bulk parameterizations.

659   We found a significant correlation between C_{DNG}, C_{HNG} and lake surface area. For large
660   lakes, the transfer coefficients at high wind speed tended to be lower. At these higher wind speeds,
661   the surface gravity waves could potentially reach the fully developed state in large water bodies.
662   For C_{ENG}, the correlation with lake surface area was not significant, but a similar trend could be
663   observed. The values of C_{ENG} in our analysis were approximately a factor of two lower than in
664   previous studies (Harbeck, 1962; Brutsaert & Yeh, 1970). Our results could not confirm a bilinear
665   decrease of C_{DNG} with increasing lake size with a weaker dependence for large lakes, as suggested
666   by Woolway et al. (2017) (Figure 5a). This can potentially be attributed to the parameterization of
667   the transfer coefficients used in Woolway et al. (2017) in lack of flux measurements. In contrast
668   to the results reported in (Panin et al., 2006), we did not find evidence for the existence of an
669   influence of water depth on the bulk transfer coefficients.

670   4.4. Study limitations

671   The estimated bulk transfer coefficients show large scatter, even after filtering the data.
672   The scatter is particularly high at light winds, i.e., in the first three to four wind speed intervals
673      $(0.5 - 2 \text{ m s}^{-1})$. It could be associated with limitations of the EC measurements, namely, the validity
674   of the underlying assumptions, including the homogeneity and stationarity of the flow, as well as
675   by increasing random errors. These effects may not have been removed completely by data
676   filtering. Moreover, our estimates of C_{DNG} differ from former results obtained using different types
677   of measurements, such as water-side energy dissipation rates (Figure 3a, e.g., (Simon, 1997)).
678   Thus, the combination of water- and air side measurements could be beneficial for further
679   investigation of the bulk transfer coefficients.

680   The parameterization of gustiness used in the COARE 3.0 algorithm assumes the CBL
681   height as a constant value of 600 m, however, this model has been used mostly for open ocean
682   conditions, not for lakes. Considering the fact, that the thermal internal boundary layer can develop
683   above lakes due to temperature difference between land and water (Glazunov & Stepanenko,
684   2015), the exact layer structure of the atmosphere (corresponding to the cases of the high drag
685   coefficients - low wind speed and convection) should be studied.

686   In our analysis we considered 30-minute intervals for averaging, however, the results will
687   likely depend on it. For example, selection of longer time interval leads to larger gustiness velocity.
688   But since the 30-minute time interval is the standard averaging interval for the EC data processing,
689   we did not have an opportunity to test the effect of averaging time scale.

690   Hwang (2004) suggested that the standard height of 10 m at which the transfer coefficients
691   are reported is inappropriate for analyzing C_{DN} and its dependence on surface roughness under
692   wave conditions. They argue that the only relevant parameter that could serve as a reference height
693   is the wavelength that describes the decay rate of the waves with the distance from the water
694   surface. The adjustment of the transfer coefficients to 10 m height may not be very relevant for
695   lakes and reservoirs and the flux measurements at two different heights should be considered in
696   future measurements. These measurements would additionally provide confirmation for the
697   existence of a constant flux layer, which is another important assumption underlying EC
698   measurements.

699   4.5. Broader implications

700   Bulk transfer coefficients are usually applied in numerical models for the atmospheric
701 boundary layer, as well as in hydrodynamic models of lakes and reservoirs. Currently, the global
702 modeling studies focusing on the lake mixing and phytoplankton blooms for climate change
703 predictions use constant values for C_{DN} (Jöhnk et al., 2008; Read et al., 2014; Woolway &
704 Merchant, 2019; Grant et al., 2021), or consider C_{DN} as a tuning parameter of the models
705 (Stepanenko et al., 2014). Inadequate values of C_{DN} result in biased estimates of the current
706 velocities in lake models (Chen et al., 2020). The increase of the transfer coefficients at low wind
707 speeds observed in our analysis can therefore lead to significant errors, as these conditions are the
708 most prevailing conditions for lakes. We found that instead of the standard formulation of the
709 transfer coefficients, their gustiness counterparts C_{DNG} , C_{HNG} and C_{ENG} can improve flux
710 parameterizations in lake models.

711   In the absence of data for the gustiness approach, the empirical parameterizations of the
712 wind-speed dependence of the bulk transfer coefficients provided in Table 1 can potentially be
713 applied in modeling lake-atmosphere interactions. The observed dependence on the lake surface
714 area is more complicated to implement, as we observed contrary dependencies at low and high
715 wind speeds.

716   While the Stanton and Dalton numbers are commonly assumed to be equal, we found that
717 C_{HNG} was on average by a factor of 1.3 higher than C_{ENG} (averaged over all wind speeds and all
718 water bodies under study). The finding of C_{HNG} being higher than C_{ENG} confirmed the results
719 reported by, e.g., (Wei et al., 2016; Dias & Vissotto, 2017). The mean value of C_{ENG} for high wind
720 speeds ($1.0 \cdot 10^{-3}$) was found to be the same as in (Kantha & Clayson, 2000), but C_{HNG} was larger
721 ($1.4 \cdot 10^{-3}$) as in (Harbeck, 1962; Hicks, 1972). The fact that $C_{HN} > C_{EN}$ may have significant
722 implications, because it results in biased estimates of lake evaporation based on the energy-budget
723 (Bowen ratio method). In particular, it would result in larger (smaller) sensible heat (latent heat)
724 fluxes than those predicted under that assumption. Both the physical mechanisms underlying their
725 difference and the extent of the differences in the predicted sensible and latent heat fluxes require
726 further investigation.

727   In state-of-the-art weather and earth system models, lakes are included as separate tiles in
728 the model cells, where the surface fluxes over the tiles are computed via Monin-Obukhov
729 similarity scaling. The models provide constant meteorological variables for each grid cell, which
730 is a so-called blending height concept (von Salzen et al., 1996). To use the bulk transfer
731 coefficients derived in this study to compute fluxes, specific values of wind, temperature and
732 humidity over lakes should be used, which can be obtained in generalization of the tile approach,
733 involving the parameterization of internal boundary layers over contrasting surfaces (Arola, 1999;
734 Molod et al., 2003; de Vrese et al., 2016). MacKay (2019) presents a specific example of such an
735 approach developed for lakes and wind speed only.

736 **5 Conclusions**

737   We were the first to analyze the bulk transfer coefficients of momentum, sensible and latent
738 heat from directly measured surface fluxes above various lakes and reservoirs. We observed a
739 pronounced increase of the transfer coefficients at low wind speeds (< 3 m s^{-1}) and relatively
740 constant values at high wind speeds (> 3 m s^{-1}). The strong increase in the transfer coefficients at
741 low wind speed was found to be associated with the existence of gusts. It is recommended to use
742 the gustiness approach in calculation of the transfer coefficients. The reduced, yet still increasing
743 values of the gustiness drag coefficient and Stanton number at low wind speeds can be explained

by capillary wave roughness. The gustiness Dalton number, however, remains constant at all wind speeds and is better described by the smooth flow roughness. The Stanton number was systematically higher than the Dalton number by a factor of 1.3, which has implications for the Bowen ratio method. At high wind speed, the drag coefficient and the Stanton number decreased with increasing surface area of the water body and with increasing fetch length, whereas the opposite was found at low wind speed. No significant correlation was found between the transfer coefficients and lake depth. In a simplified approach, the bulk transfer coefficients can be calculated without consideration of gustiness by using empirical function that has been proposed for the land surface and that we fitted to data measured over lake and reservoir surfaces. The COARE algorithm adequately describes the gustiness drag coefficient and Stanton number if capillary wave roughness is considered instead of that for smooth flow. We underline the need for simultaneous measurements of waterside and airside turbulent fluxes in future investigations, as well as experimental confirmation of the validity of the assumptions underlying eddy-covariance flux measurements at low wind speed.

Acknowledgments

Open Research

787 Derived quantities such as the bulk transfer coefficients are available in the open data repository
788 Zenodo: [10.5281/zenodo.6597828](https://doi.org/10.5281/zenodo.6597828), (Guseva et al., 2022). Original datasets are available from the
789 open data repositories or from the co-authors (see details in Table S1).
790

791 **References**

792 Akylas, E., Tsakos, Y., Tombrou, M., & Lalas, D. P. (2003). Considerations on minimum friction velocity.
793   *Quarterly Journal of the Royal Meteorological Society*, *129*(591), 1929–1943.
794   https://doi.org/10.1256/qj.01.73
795 Arola, A. (1999). Parameterization of Turbulent and Mesoscale Fluxes for Heterogeneous Surfaces. *Journal of the*
796   *Atmospheric Sciences*, *56*(4), 584–598. https://doi.org/10.1175/1520-
797   0469(1999)056<0584:POTAMF>2.0.CO;2
798 Ataktürk, S. S., & Katsaros, K. B. (1999). *Wind Stress and Surface Waves Observed on Lake Washington*. *29*(4),
799   633–650. https://doi.org/10.1175/1520-0485(1999)029<0633:WSASWO>2.0.CO;2
800 Babanin, A. V., & Makin, V. K. (2008). Effects of wind trend and gustiness on the sea drag: Lake George study.
801   *Journal of Geophysical Research*, *113*(C2), C02015. https://doi.org/10.1029/2007JC004233
802 Balsamo, G., Salgado, R., Dutra, E., Boussetta, S., Stockdale, T., & Potes, M. (2012). On the contribution of lakes in
803   predicting near-surface temperature in a global weather forecasting model. *Tellus A: Dynamic Meteorology*
804   *and Oceanography*, *64*(1), 15829. https://doi.org/10.3402/tellusa.v64i0.15829
805 Beljaars, A. C. M. (1995). The parametrization of surface fluxes in large-scale models under free convection.
806   *Quarterly Journal of the Royal Meteorological Society*, *121*(522), 255–270.
807   https://doi.org/10.1002/qj.49712152203
808 Blanken, P. D., Rouse, W. R., Culf, A. D., Spence, C., Boudreau, L. D., Jasper, J. N., Kochtubajda, B., Schertzer,
809   W. M., Marsh, P., & Verseghy, D. (2000). Eddy covariance measurements of evaporation from Great Slave
810   Lake, Northwest Territories, Canada. *Water Resources Research*, *36*(4), 1069–1077.
811   https://doi.org/10.1029/1999WR900338
812 Brutsaert, W., & Yeh, G.-T. (1970). Implications of a Type of Empirical Evaporation Formula for Lakes and Pans.
813   *Water Resources Research*, *6*(4), 1202–1208. https://doi.org/10.1029/WR006i004p01202
814 Burba, G. G., & Anderson, D. J. (2010). *A Brief Practical Guide to Eddy Covariance Flux Measurements:*
815   *Principles and Workflow Examples for Scientific and Industrial Applications*. LI-COR Biosciences.
816 Businger, J. A., Wyngaard, J. C., Izumi, Y., & Bradley, E. F. (1971). Flux-Profile Relationships in the Atmospheric
817   Surface Layer. *Journal of the Atmospheric Sciences*, *28*(2), 181–189. https://doi.org/10.1175/1520-
818   0469(1971)028<0181:FPRITA>2.0.CO;2
819 Changnon, S. A., & Jones, D. M. A. (1972). Review of the influences of the Great Lakes on weather. *Water*
820   *Resources Research*, *8*(2), 360–371. https://doi.org/10.1029/WR008i002p00360
821 Charnock, H. (1955). Wind stress on a water surface. *Quarterly Journal of the Royal Meteorological Society*,
822   *81*(350), 639–640. https://doi.org/10.1002/qj.49708135027
823 Chen, F., Zhang, C., Brett, M. T., & Nielsen, J. M. (2020). The importance of the wind-drag coefficient
824   parameterization for hydrodynamic modeling of a large shallow lake. *Ecological Informatics*, *59*, 101106.
825   https://doi.org/10.1016/j.ecoinf.2020.101106
826 Crosman, E. T., & Horel, J. D. (2012). Idealized Large-Eddy Simulations of Sea and Lake Breezes: Sensitivity to
827   Lake Diameter, Heat Flux and Stability. *Boundary-Layer Meteorology*, *144*(3), 309–328.
828   https://doi.org/10.1007/s10546-012-9721-x
829 de Vrese, P., Schulz, J.-P., & Hagemann, S. (2016). On the Representation of Heterogeneity in Land-Surface–
830   Atmosphere Coupling. *Boundary-Layer Meteorology*, *160*(1), 157–183. https://doi.org/10.1007/s10546-
831   016-0133-1
832 DeCosmo, J., Katsaros, K. B., Smith, S. D., Anderson, R. J., Oost, W. A., Bumke, K., & Chadwick, H. (1996). Air-
833   sea exchange of water vapor and sensible heat: The Humidity Exchange Over the Sea (HEXOS) results.
834   *Journal of Geophysical Research: Oceans*, *101*(C5), 12001–12016. https://doi.org/10.1029/95JC03796
835 DelSontro, T., Beaulieu, J. J., & Downing, J. A. (2018). Greenhouse gas emissions from lakes and impoundments:
836   Upscaling in the face of global change. *Limnology and Oceanography Letters*, *3*(3), 64–75.
837   https://doi.org/10.1002/lol2.10073

838   Desai, A. R., Austin, J. A., Bennington, V., & McKinley, G. A. (2009). Stronger winds over a large lake in response
839   to weakening air-to-lake temperature gradient. *Nature Geoscience*, *2*(12), 855–858.
840   https://doi.org/10.1038/ngeo693
841   Dias, N. L., & Vissotto, D. (2017). The effect of temperature-humidity similarity on Bowen ratios, dimensionless
842   standard deviations, and mass transfer coefficients over a lake: Temperature-Humidity Similarity over a
843   Lake. *Hydrological Processes*, *31*(2), 256–269. https://doi.org/10.1002/hyp.10925
844   Donelan, A. (1990). Air-sea interaction. In *The Sea* (Vol. 9, pp. 239–292). Environment and Climate Change
845   Canada.
846   Donelan, M. (1982). The dependence of the aerodynamic drag coefficient on wave parameters. *Proc.. First Int.*
847   *Conf. on Meteorology and Air-Sea Interaction of the Coastal Zone*, 381–387.
848   Downing, J. A., Prairie, Y. T., Cole, J. J., Duarte, C. M., Tranvik, L. J., Striegl, R. G., McDowell, W. H.,
849   Kortelainen, P., Caraco, N. F., Melack, J. M., & Middelburg, J. J. (2006). The global abundance and size
850   distribution of lakes, ponds, and impoundments. *Limnology and Oceanography*, *51*(5), 2388–2397.
851   https://doi.org/10.4319/lo.2006.51.5.2388
852   Edson, J. B., Jampana, V., Weller, R. A., Bigorre, S. P., Plueddemann, A. J., Fairall, C. W., Miller, S. D., Mahrt, L.,
853   Vickers, D., & Hersbach, H. (2013). On the Exchange of Momentum over the Open Ocean. *Journal of*
854   *Physical Oceanography*, *43*(8), 1589–1610. https://doi.org/10.1175/JPO-D-12-0173.1
855   Eerola, K., Rontu, L., Kourzeneva, E., Pour, H. K., & Duguay, C. (2014). Impact of partly ice-free Lake Ladoga on
856   temperature and cloudiness in an anticyclonic winter situation – a case study using a limited area model.
857   *Tellus A: Dynamic Meteorology and Oceanography*, *66*(1), 23929.
858   https://doi.org/10.3402/tellusa.v66.23929
859   Fairall, C. W., Bradley, E. F., Hare, J. E., Grachev, A. A., & Edson, J. B. (2003). Bulk Parameterization of Air–Sea
860   Fluxes: Updates and Verification for the COARE Algorithm. *Journal of Climate*, *16*(4), 571–591.
861   https://doi.org/10.1175/1520-0442(2003)016<0571:BPOASF>2.0.CO;2
862   Fairall, C. W., Bradley, E. F., Rogers, D. P., Edson, J. B., & Young, G. S. (1996). Bulk parameterization of air-sea
863   fluxes for Tropical Ocean-Global Atmosphere Coupled-Ocean Atmosphere Response Experiment. *Journal*
864   *of Geophysical Research: Oceans*, *101*(C2), 3747–3764. https://doi.org/10.1029/95JC03205
865   Foken, T. (2008). *Micrometeorology*. Springer Berlin Heidelberg. https://doi.org/10.1007/978-3-540-74666-9
866   Foken, T., Aubinet, M., & Leuning, R. (2012). The Eddy Covariance Method. In M. Aubinet, T. Vesala, & D.
867   Papale (Eds.), *Eddy Covariance* (pp. 1–19). Springer Netherlands. https://doi.org/10.1007/978-94-007-
868   2351-1_1
869   Foken, T., Göckede, M., Mauder, M., Mahrt, L., Amiro, D., & Munger, J. W. (2004). Post-field data quality control.
870   In *Handbook of micrometeorology: A guide for surface flux measurement and analysis* (pp. 181–208).
871   Foken, Th., & Wichura, B. (1996). Tools for quality assessment of surface-based flux measurements. *Agricultural*
872   *and Forest Meteorology*, *78*(1–2), 83–105. https://doi.org/10.1016/0168-1923(95)02248-1
873   Fujisaki-Manome, A., Mann, G. E., Anderson, E. J., Chu, P. Y., Fitzpatrick, L. E., Benjamin, S. G., James, E. P.,
874   Smirnova, T. G., Alexander, C. R., & Wright, D. M. (2020). Improvements to Lake-Effect Snow Forecasts
875   Using a One-Way Air–Lake Model Coupling Approach. *Journal of Hydrometeorology*, *21*(12), 2813–2828.
876   https://doi.org/10.1175/JHM-D-20-0079.1
877   Garratt, J. (1994). Review: The atmospheric boundary layer. *Earth-Science Reviews*, *37*(1–2), 89–134.
878   https://doi.org/10.1016/0012-8252(94)90026-4
879   Garratt, J. R. (1977). Review of Drag Coefficients over Oceans and Continents. *Monthly Weather Review*, *105*(7),
880   915–929. https://doi.org/10.1175/1520-0493(1977)105<0915:RODCOO>2.0.CO;2
881   Geernaert, G. L. (1990). Bulk Parameterizations for the Wind Stress and Heat Fluxes. In G. L. Geernaert & W. L.
882   Plant (Eds.), *Surface Waves and Fluxes* (pp. 91–172). Springer Netherlands. https://doi.org/10.1007/978-
883   94-009-2069-9_5
884   Glazunov, A. V., & Stepanenko, V. M. (2015). Large-eddy simulation of stratified turbulent flows over
885   heterogeneous landscapes. *Izvestiya, Atmospheric and Oceanic Physics*, *51*(4), 351–361.
886   https://doi.org/10.1134/S0001433815040027
887   Godfrey, J. S., & Beljaars, A. C. M. (1991). On the turbulent fluxes of buoyancy, heat and moisture at the air-sea
888   interface at low wind speeds. *Journal of Geophysical Research*, *96*(C12), 22043.
889   https://doi.org/10.1029/91JC02015
890   Golub, M., Desai, A. R., Vesala, T., Mammarella, I., Ojala, A., Bohrer, G., Weyhenmeyer, G. A., Blanken, P. D.,
891   Eugster, W., Koebsch, F., Chen, J., Czajkowski, K. P., Deshmukh, C., Guérin, F., Heiskanen, J. J.,
892   Humphreys, E. R., Jonsson, A., Karlsson, J., Kling, G. W., … Xiao, W. (2021). *New insights into diel to*

893   *interannual variation in carbon dioxide emissions from lakes and reservoirs* [Preprint]. Environmental
894   Sciences. https://doi.org/10.1002/essoar.10507313.1
895 Grachev, A. A., Bariteau, L., Fairall, C. W., Hare, J. E., Helmig, D., Hueber, J., & Lang, E. K. (2011). Turbulent
896   fluxes and transfer of trace gases from ship-based measurements during TexAQS 2006. *Journal of*
897   *Geophysical Research*, *116*(D13), D13110. https://doi.org/10.1029/2010JD015502
898 Grachev, A. A., Fairall, C. W., & Larsen, S. E. (1998). On the Determination of the Neutral Drag Coefficient in the
899   Convective Boundary Layer. *Boundary-Layer Meteorology*, *86*(2), 257–278.
900   https://doi.org/10.1023/A:1000617300732
901 Graf, W. H., Merzi, N., & Perrinjaquet, C. (1984). Aerodynamic drag: Measured at a nearshore platform on lake of
902   Geneva. *Archives for Meteorology, Geophysics, and Bioclimatology Series A*, *33*(2–3), 151–173.
903   https://doi.org/10.1007/BF02257722
904 Grant, L., Vanderkelen, I., Gudmundsson, L., Tan, Z., Perroud, M., Stepanenko, V. M., Debolskiy, A. V., Droppers,
905   B., Janssen, A. B. G., Woolway, R. I., Choulga, M., Balsamo, G., Kirillin, G., Schewe, J., Zhao, F., del
906   Valle, I. V., Golub, M., Pierson, D., Marcé, R., … Thiery, W. (2021). Attribution of global lake systems
907   change to anthropogenic forcing. *Nature Geoscience*, *14*(11), 849–854. https://doi.org/10.1038/s41561-
908   021-00833-x
909 Guseva, S., Armani, F., Desai, A. R., Dias, N. L., Friborg, T., Iwata, H., Jansen, J., Lükő, G., Mammarella, I.,
910   Repina, I., Rutgersson, A., Sachs, T., Scholz, K., Spank, U., Stepanenko, V., Torma, P., Vesala, T., &
911   Lorke, A. (2022). *Data associated with article 'Bulk Transfer Coefficients Estimated from Eddy-*
912   *Covariance Measurements Over Lakes and Reservoirs' by Guseva et al., 2022* (Version V2) [Data set].
913   Zenodo. https://doi.org/10.5281/ZENODO.6597828
914 Guseva, S., Casper, P., Sachs, T., Spank, U., & Lorke, A. (2021). Energy Flux Paths in Lakes and Reservoirs.
915   *Water*, *13*(22), 3270. https://doi.org/10.3390/w13223270
916 Harbeck, G. E. (1962). *A Practical Field Technique for Measuring Reservoir Evaporation Utilizing Mass-Transfer*
917   *Theory*. 101–105.
918 Heikinheimo, M., Kangas, M., Tourula, T., Venäläinen, A., & Tattari, S. (1999). Momentum and heat fluxes over
919   lakes Tämnaren and Råksjö determined by the bulk-aerodynamic and eddy-correlation methods.
920   *Agricultural and Forest Meteorology*, *98–99*, 521–534. https://doi.org/10.1016/S0168-1923(99)00121-5
921 Hicks, B. B. (1972). Some evaluations of drag and bulk transfer coefficients over water bodies of different sizes.
922   *Boundary-Layer Meteorology*, *3*(2), 201–213. https://doi.org/10.1007/BF02033919
923 Högström, U. (1988). Non-Dimensional Wind and Temperature Profiles in the Atmospheric Surface Layer: A Re-
924   Evaluation. In B. B. Hicks (Ed.), *Topics in Micrometeorology. A Festschrift for Arch Dyer* (pp. 55–78).
925   Springer Netherlands. https://doi.org/10.1007/978-94-009-2935-7_6
926 Hwang, P. A. (2004). Influence of wavelength on the parameterization of drag coefficient and surface roughness.
927   *Journal of Oceanography*, *60*(5), 835–841. https://doi.org/10.1007/s10872-005-5776-3
928 Jöhnk, K. D., Huisman, J., Sharples, J., Sommeijer, B., Visser, P. M., & Stroom, J. M. (2008). Summer heatwaves
929   promote blooms of harmful cyanobacteria: HEATWAVES PROMOTE HARMFUL CYANOBACTERIA.
930   *Global Change Biology*, *14*(3), 495–512. https://doi.org/10.1111/j.1365-2486.2007.01510.x
931 Kaimal, J. C., & Finnigan, J. J. (1994). *Atmospheric Boundary Layer Flows: Their Structure and Measurement*.
932   Oxford University Press. https://doi.org/10.1093/oso/9780195062397.001.0001
933 Kantha, L., & Clayson, C. (2000). *Small Scale Processes in Geophysical Fluid Flows* (1st Edition, Vol. 67).
934   Academic Press.
935 Kato, H., & Takahashi, H. (1981). Local Climate near the Small Lake. *Journal of Agricultural Meteorology*, *37*(1),
936   29–37. https://doi.org/10.2480/agrmet.37.29
937 Kuznetsova, A., Baydakov, G., Papko, V., Kandaurov, A., Vdovin, M., Sergeev, D., & Troitskaya, Y. (2016). Field
938   and numerical study of the wind-wave regime on the Gorky Reservoir. *GEOGRAPHY, ENVIRONMENT,*
939   *SUSTAINABILITY*, *9*(2), 19–37. https://doi.org/10.15356/2071-9388_02v09_2016_02
940 Large, W. G., & Pond, S. (1981). *Open ocean momentum flux measurements in moderate to strong winds*. *11*(3),
941   324–336. https://doi.org/10.1175/1520-0485(1981)011<0324:OOMFMI>2.0.CO;2
942 Lee, X., Liu, S., Xiao, W., Wang, W., Gao, Z., Cao, C., Hu, C., Hu, Z., Shen, S., Wang, Y., Wen, X., Xiao, Q., Xu,
943   J., Yang, J., & Zhang, M. (2014). The Taihu Eddy Flux Network: An Observational Program on Energy,
944   Water, and Greenhouse Gas Fluxes of a Large Freshwater Lake. *Bulletin of the American Meteorological*
945   *Society*, *95*(10), 1583–1594. https://doi.org/10.1175/BAMS-D-13-00136.1
946 Lenschow, D. H., Mann, J., & Kristensen, L. (1994). How Long Is Long Enough When Measuring Fluxes and Other
947   Turbulence Statistics? *Journal of Atmospheric and Oceanic Technology*, *11*(3), 661–673.
948   https://doi.org/10.1175/1520-0426(1994)011<0661:HLILEW>2.0.CO;2

Li, Z., Lyu, S., Zhao, L., Wen, L., Ao, Y., & Wang, S. (2016). Turbulent transfer coefficient and roughness length in a high-altitude lake, Tibetan Plateau. *Theoretical and Applied Climatology*, *124*(3–4), 723–735. https://doi.org/10.1007/s00704-015-1440-z

LI-COR, Inc. (2021). *EddyPro® Software (Version 7.0)*, [Software], LI-COR. https://www.licor.com/env/support/EddyPro/home.html

Lin, W., Sanford, L. P., Suttles, S. E., & Valigura, R. (2002). Drag Coefficients with Fetch-Limited Wind Waves*. *Journal of Physical Oceanography*, *32*(11), 3058–3074. https://doi.org/10.1175/1520-0485(2002)032<3058:DCWFLW>2.0.CO;2

Liu, C., Li, Y., Gao, Z., Zhang, H., Wu, T., Lu, Y., & Zhang, X. (2020). Improvement of Drag Coefficient Calculation Under Near-Neutral Conditions in Light Winds Over land. *Journal of Geophysical Research: Atmospheres*, *125*(24). https://doi.org/10.1029/2020JD033472

Ljungemyr, P., Gustafsson, N., & Omstedt, A. (1996). Parameterization of lake thermodynamics in a high-resolution weather forecasting model. *Tellus A*, *48*(5), 608–621. https://doi.org/10.1034/j.1600-0870.1996.t01-4-00002.x

Lükő, G., Torma, P., Krámer, T., Weidinger, T., Vecenaj, Z., & Grisogono, B. (2020). Observation of wave-driven air–water turbulent momentum exchange in a large but fetch-limited shallow lake. *Advances in Science and Research*, *17*, 175–182. https://doi.org/10.5194/asr-17-175-2020

MacKay, M. D. (2019). Incorporating wind sheltering and sediment heat flux into 1-D models of small boreal lakes: A case study with the Canadian Small Lake Model V2.0. *Geoscientific Model Development*, *12*(7), 3045–3054. https://doi.org/10.5194/gmd-12-3045-2019

Mammarella, I., Nordbo, A., Rannik, Ü., Haapanala, S., Levula, J., Laakso, H., Ojala, A., Peltola, O., Heiskanen, J., Pumpanen, J., & Vesala, T. (2015). Carbon dioxide and energy fluxes over a small boreal lake in Southern Finland: CO_2 and Energy Fluxes Over Lake. *Journal of Geophysical Research: Biogeosciences*, *120*(7), 1296–1314. https://doi.org/10.1002/2014JG002873

Mammarella, I., Peltola, O., Nordbo, A., Järvi, L., & Rannik, Ü. (2016). Quantifying the uncertainty of eddy covariance fluxes due to the use ofdifferent software packages and combinations of processing steps in twocontrasting ecosystems. *Atmospheric Measurement Techniques*, *9*(10), 4915–4933. https://doi.org/10.5194/amt-9-4915-2016

Mauder, M., & Foken, T. (2015). *Eddy-Covariance Software TK3* [Software], Zenodo. https://doi.org/10.5281/ZENODO.20349

Mironov, D., Heise, E., Kourzeneva, E., Ritter, B., Schneider, N., & Terzhevik, A. (2010). Implementation of the lake parameterization scheme FLake into the numerical weather prediction model COSMO. *Boreal Environment Research*. *15*, 218-- 230.

Molod, A., Salmun, H., & Waugh, D. W. (2003). A New Look at Modeling Surface Heterogeneity: Extending Its Influence in the Vertical. *Journal of Hydrometeorology*, *4*(5), 810–825. https://doi.org/10.1175/1525-7541(2003)004<0810:ANLAMS>2.0.CO;2

Monin, A. S., & Obukhov, A. M. (1954). *Basic laws of turbulent mixing in the ground layer of the atmosphere* (Vol. 151). Akad. Nauk. SSSR Geofiz. Inst. Tr.

Nordbo, A., Launiainen, S., Mammarella, I., Leppäranta, M., Huotari, J., Ojala, A., & Vesala, T. (2011). Long-term energy flux measurements and energy balance over a small boreal lake using eddy covariance technique. *Journal of Geophysical Research*, *116*(D2), D02119. https://doi.org/10.1029/2010JD014542

Obukhov, A. M. (1971). Turbulence in an atmosphere with a non-uniform temperature. *Boundary-Layer Meteorology*, *2*(1), 7–29. https://doi.org/10.1007/BF00718085

Panin, G. N., Nasonov, A. E., & Foken, T. (2006). Evaporation and heat exchange of a body of water with the atmosphere in a shallow zone. *Izvestiya, Atmospheric and Oceanic Physics*, *42*(3), 337–352. https://doi.org/10.1134/S0001433806030078

Paulson, C. A. (1970). *The mathematical representation of wind speed and temperature profiles in the unstable atmospheric surface layer*. *9*(6), 857–861. https://doi.org/10.1175/1520-0450(1970)009<0857:TMROWS>2.0.CO;2

Pawlowicz, R. (2020). *M_Map: A mapping package for MATLAB* (1.4m) [Software]. Available online at www.eoas.ubc.ca/~rich/map.html

Read, J. S., Hamilton, D. P., Desai, A. R., Rose, K. C., MacIntyre, S., Lenters, J. D., Smyth, R. L., Hanson, P. C., Cole, J. J., Staehr, P. A., Rusak, J. A., Pierson, D. C., Brookes, J. D., Laas, A., & Wu, C. H. (2012). Lake-size dependency of wind shear and convection as controls on gas exchange. *Geophysical Research Letters*, *39*(9). https://doi.org/10.1029/2012GL051886

Read, J. S., Winslow, L. A., Hansen, G. J. A., Van Den Hoek, J., Hanson, P. C., Bruce, L. C., & Markfort, C. D. (2014). Simulating 2368 temperate lakes reveals weak coherence in stratification phenology. *Ecological Modelling*, *291*, 142–150. https://doi.org/10.1016/j.ecolmodel.2014.07.029

Rosentreter, J. A., Borges, A. V., Deemer, B. R., Holgerson, M. A., Liu, S., Song, C., Melack, J., Raymond, P. A., Duarte, C. M., Allen, G. H., Olefeldt, D., Poulter, B., Battin, T. I., & Eyre, B. D. (2021). Half of global methane emissions come from highly variable aquatic ecosystem sources. *Nature Geoscience*, *14*(4), 225–230. https://doi.org/10.1038/s41561-021-00715-2

Sahlée, E., Rutgersson, A., Podgrajsek, E., & Bergström, H. (2014). Influence from Surrounding Land on the Turbulence Measurements Above a Lake. *Boundary-Layer Meteorology*, *150*(2), 235–258. https://doi.org/10.1007/s10546-013-9868-0

Salgado, R., & Le Mogne, P. (2010). Coupling the FLake model to the Surfex externalized surface model. *Boreal Environment Research*, *15*, 231-- 244.

Schlichting, H. (1968). *Boundary-Layer Theory* (6th Edition). McGraw-Hill Book Company.

Simon, A. (1997). *Turbulent mixing in the surface boundary layer of lakes* [Dissertation No 12272]. Swiss Federal Institute of Technology.

Smith, S. D., Fairall, C. W., Geernaert, G. L., & Hasse, L. (1996). Air-sea fluxes: 25 years of progress. *Boundary-Layer Meteorology*, *78*(3–4), 247–290. https://doi.org/10.1007/BF00120938

Spank, U., Hehn, M., Keller, P., Koschorreck, M., & Bernhofer, C. (2020). A Season of Eddy-Covariance Fluxes Above an Extensive Water Body Based on Observations from a Floating Platform. *Boundary-Layer Meteorology*, *174*(3), 433–464. https://doi.org/10.1007/s10546-019-00490-z

Stepanenko, V., Jöhnk, K. D., Machulskaya, E., Perroud, M., Subin, Z., Nordbo, A., Mammarella, I., & Mironov, D. (2014). Simulation of surface energy fluxes and stratification of a small boreal lake by a set of one-dimensional models. *Tellus A: Dynamic Meteorology and Oceanography*, *66*(1), 21389. https://doi.org/10.3402/tellusa.v66.21389

Strub, T. P., & Powell, T. M. (1987). The exchange coefficients for latent and sensible heat flux over lakes: Dependence upon atmospheric stability. *Boundary-Layer Meteorology*, *40*(4), 349–362. https://doi.org/10.1007/BF00116102

Stull, R. B. (Ed.). (1988). *An Introduction to Boundary Layer Meteorology*. Springer Netherlands. https://doi.org/10.1007/978-94-009-3027-8

Sun, J., Lenschow, D. H., Mahrt, L., Crawford, T. L., Davis, K. J., Oncley, S. P., MacPherson, J. I., Wang, Q., Dobosy, R. J., & Desjardins, R. L. (1997). Lake-induced atmospheric circulations during BOREAS. *Journal of Geophysical Research: Atmospheres*, *102*(D24), 29155–29166. https://doi.org/10.1029/97JD01114

Sun, X.-M., Zhu, Z.-L., Wen, X.-F., Yuan, G.-F., & Yu, G.-R. (2006). The impact of averaging period on eddy fluxes observed at ChinaFLUX sites. *Agricultural and Forest Meteorology*, *137*(3–4), 188–193. https://doi.org/10.1016/j.agrformet.2006.02.012

Thiery, W., Davin, E. L., Seneviratne, S. I., Bedka, K., Lhermitte, S., & van Lipzig, N. P. M. (2016). Hazardous thunderstorm intensification over Lake Victoria. *Nature Communications*, *7*(1), 12786. https://doi.org/10.1038/ncomms12786

Vesala, T., Huotari, J., Rannik, Ü., Suni, T., Smolander, S., Sogachev, A., Launiainen, S., & Ojala, A. (2006). Eddy covariance measurements of carbon exchange and latent and sensible heat fluxes over a boreal lake for a full open-water period. *Journal of Geophysical Research*, *111*(D11), D11101. https://doi.org/10.1029/2005JD006365

Vickers, D., & Mahrt, L. (1997). Fetch Limited Drag Coefficients. *Boundary-Layer Meteorology*, *85*(1), 53–79. https://doi.org/10.1023/A:1000472623187

von Salzen, K., M. Claussen, M., & Schlünzen, K. H. (1996). Anwendung des Konzepts der Blendhöhe zur Berechnung von bodennahen Flüssen in einem mesoskaligen Modell. *Meteorologische Zeitschrift*, *5*(2), 60–66. https://doi.org/10.1127/metz/5/1996/60

Wei, Z., Miyano, A., & Sugita, M. (2016). Drag and Bulk Transfer Coefficients Over Water Surfaces in Light Winds. *Boundary-Layer Meteorology*, *160*(2), 319–346. https://doi.org/10.1007/s10546-016-0147-8

Woolway, R. I., & Merchant, C. J. (2019). Worldwide alteration of lake mixing regimes in response to climate change. *Nature Geoscience*, *12*(4), 271–276. https://doi.org/10.1038/s41561-019-0322-x

Woolway, R. I., Verburg, P., Lenters, J. D., Merchant, C. J., Hamilton, D. P., Brookes, J., Eyto, E., Kelly, S., Healey, N. C., Hook, S., Laas, A., Pierson, D., Rusak, J. A., Kuha, J., Karjalainen, J., Kallio, K., Lepistö, A., & Jones, I. D. (2018). Geographic and temporal variations in turbulent heat loss from lakes: A global

1059   analysis across 45 lakes. *Limnology and Oceanography*, *63*(6), 2436–2449.
1060   https://doi.org/10.1002/lno.10950
1061 Woolway, R. I., Verburg, P., Merchant, C. J., Lenters, J. D., Hamilton, D. P., Brookes, J., Kelly, S., Hook, S., Laas,
1062   A., Pierson, D., Rimmer, A., Rusak, J. A., & Jones, I. D. (2017). Latitude and lake size are important
1063   predictors of over-lake atmospheric stability: Atmospheric Stability Above Lakes. *Geophysical Research*
1064   *Letters*, *44*(17), 8875–8883. https://doi.org/10.1002/2017GL073941
1065 Wu, J. (1988). Wind-Stress Coefficients at Light Winds. *Journal of Atmospheric and Oceanic Technology*, *5*(6),
1066   885–888. https://doi.org/10.1175/1520-0426(1988)005<0885:WSCALW>2.0.CO;2
1067 Wu, J. (1994). The sea surface is aerodynamically rough even under light winds. *Boundary-Layer Meteorology*,
1068   *69*(1–2), 149–158. https://doi.org/10.1007/BF00713300
1069 Wu, L., Breivik, Ø., & Rutgersson, A. (2019). Ocean-Wave-Atmosphere Interaction Processes in a Fully Coupled
1070   Modeling System. *Journal of Advances in Modeling Earth Systems*, *11*(11), 3852–3874.
1071   https://doi.org/10.1029/2019MS001761
1072 Wüest, A., & Lorke, A. (2003). Small-Scale Hydrodynamics in Lakes. *Annual Review of Fluid Mechanics*, *35*(1),
1073   373–412. https://doi.org/10.1146/annurev.fluid.35.101101.161220
1074 Xiao, W., Liu, S., Wang, W., Yang, D., Xu, J., Cao, C., Li, H., & Lee, X. (2013). Transfer Coefficients of
1075   Momentum, Heat and Water Vapour in the Atmospheric Surface Layer of a Large Freshwater Lake.
1076   *Boundary-Layer Meteorology*, *148*(3), 479–494. https://doi.org/10.1007/s10546-013-9827-9
1077 Zhu, P., & Furst, J. (2013). On the parameterization of surface momentum transport via drag coefficient in low-wind
1078   conditions. *Geophysical Research Letters*, *40*(11), 2824–2828. https://doi.org/10.1002/grl.50518
1079 Zilitinkevich, S., & Calanca, P. (2010). An extended similarity theory for the stably stratified atmospheric surface
1080   layer. *Quarterly Journal of the Royal Meteorological Society*, *126*(566), 1913–1923.
1081   https://doi.org/10.1002/qj.49712656617
1082
1083

Appendix III

Variable physical drivers of near-surface turbulence in a regulated river

S. Guseva[1], M. Aurela[2], A. Cortés[3], R. Kivi[4], E. Lotsari[5,6], S. MacIntyre[3],

I. Mammarella[7], A. Ojala[8,9,10], V. Stepanenko[11,12,13], P. Uotila[7], A. Vähä[7],

T. Vesala[7,9,14], M. B. Wallin[15,16], and A. Lorke[1]

[1] Institute for Environmental Sciences, University of Koblenz-Landau, 76829 Landau, Germany;
[2] Climate Research Programme, Finnish Meteorological Institute, Helsinki, Finland;
[3] Earth Research Institute, University of California, Santa Barbara, CA, USA;
[4] Space and Earth Observation Centre, Finnish Meteorological Institute, Sodankylä, Finland;
[5] Department of Geographical and Historical Studies, University of Eastern Finland, Joensuu, Finland;
[6] Department of Geography and Geology, University of Turku, Turku, Finland;
[7] Institute of Atmospheric and Earth System Research (INAR)/ Physics, University of Helsinki, Helsinki, Finland;
[8] Ecosystems and Environment Research Programme, Faculty of Biological and Environmental Sciences, University of Helsinki, Helsinki, Finland;
[9] Institute for Atmosphere and Earth System Research/Forest Sciences, Faculty of Agriculture and Forestry, University of Helsinki, Helsinki, Finland;
[10] Helsinki Institute of Sustainability Science (HELSUS), Faculty of Biological and Environmental Sciences, University of Helsinki, Helsinki, Finland;
[11] Laboratory for Supercomputer Modeling of Climate System Processes, Research Computing Center, Lomonosov Moscow State University, Moscow, Russia;
[12] Department of Meteorology and Climatology, Faculty of Geography, Lomonosov Moscow State University, Moscow, Russia;
[13] Moscow Center for Fundamental and Applied Mathematics, Moscow, Russia;
[14] Yugra State University, Khanty-Mansiysk, Russia;
[15] Department of Earth Sciences: Air, Water and Landscape, Uppsala University, Uppsala, Sweden;
[16] Department of Aquatic Sciences and Assessment, Swedish University of Agricultural Sciences, Uppsala, Sweden.

Please click on the following link to read the publication

https://doi.org/10.1029/2020WR027939

Variable Physical Drivers of Near-Surface Turbulence in a Regulated River

S. Guseva[1] ![ORCID], M. Aurela[2], A. Cortés[3] ![ORCID], R. Kivi[4] ![ORCID], E. Lotsari[5,6], S. MacIntyre[3], I. Mammarella[7] ![ORCID], A. Ojala[8,9,10], V. Stepanenko[11,12,13] ![ORCID], P. Uotila[7] ![ORCID], A. Vähä[7] ![ORCID], T. Vesala[7,9,14] ![ORCID], M. B. Wallin[15,16] ![ORCID], and A. Lorke[1] ![ORCID]

[1]Institute for Environmental Sciences, University of Koblenz-Landau, Landau, Germany, [2]Climate Research Programme, Finnish Meteorological Institute, Helsinki, Finland, [3]Earth Research Institute, University of California, Santa Barbara, CA, USA, [4]Space and Earth Observation Centre, Finnish Meteorological Institute, Sodankylä, Finland, [5]Department of Geographical and Historical Studies, University of Eastern Finland, Joensuu, Finland, [6]Department of Geography and Geology, University of Turku, Turku, Finland, [7]Institute of Atmospheric and Earth System Research (INAR)/ Physics, University of Helsinki, Helsinki, Finland, [8]Ecosystems and Environment Research Programme, Faculty of Biological and Environmental Sciences, University of Helsinki, Helsinki, Finland, [9]Institute for Atmosphere and Earth System Research/Forest Sciences, Faculty of Agriculture and Forestry, University of Helsinki, Helsinki, Finland, [10]Helsinki Institute of Sustainability Science (HELSUS), Faculty of Biological and Environmental Sciences, University of Helsinki, Helsinki, Finland, [11]Laboratory for Supercomputer Modeling of Climate System Processes, Research Computing Center, Lomonosov Moscow State University, Moscow, Russia, [12]Department of Meteorology and Climatology, Faculty of Geography, Lomonosov Moscow State University, Moscow, Russia, [13]Moscow Center for Fundamental and Applied Mathematics, Moscow, Russia, [14]Yugra State University, Khanty-Mansiysk, Russia, [15]Department of Earth Sciences: Air, Water and Landscape, Uppsala University, Uppsala, Sweden, [16]Department of Aquatic Sciences and Assessment, Swedish University of Agricultural Sciences, Uppsala, Sweden

Abstract Inland waters, such as lakes, reservoirs and rivers, are important sources of climate forcing trace gases. A key parameter that regulates the gas exchange between water and the atmosphere is the gas transfer velocity, which itself is controlled by near-surface turbulence in the water. While in lakes and reservoirs, near-surface turbulence is mainly driven by atmospheric forcing, in shallow rivers and streams it is generated by bottom friction of gravity-forced flow. Large rivers represent a transition between these two cases. Near-surface turbulence has rarely been measured in rivers and the drivers of turbulence have not been quantified. We analyzed continuous measurements of flow velocity and quantified turbulence as the rate of dissipation of turbulent kinetic energy over the ice-free season in a large regulated river in Northern Finland. Measured dissipation rates agreed with predictions from bulk parameters, including mean flow velocity, wind speed, surface heat flux, and with a one-dimensional numerical turbulence model. Values ranged from $\sim 10^{-10} \, \mathrm{m^2 s^{-3}}$ to $10^{-5} \, \mathrm{m^2 s^{-3}}$. Atmospheric forcing or gravity was the dominant driver of near-surface turbulence for similar fraction of the time. Large variability in near-surface dissipation rate occurred at diel time scales, when the flow velocity was strongly affected by downstream dam operation. By combining scaling relations for boundary-layer turbulence at the river bed and at the air-water interface, we derived a simple model for estimating the relative contributions of wind speed and bottom friction of river flow as a function of depth.

Plain Language Summary Inland water bodies such as lakes, reservoirs and rivers are an important source of climate forcing trace gases to the atmosphere. Gas exchange between water and the atmosphere is regulated by the gas transfer velocity and the concentration difference between the water surface and the atmosphere. The gas transfer velocity depends on near-surface turbulence, but robust formulations have not been developed for river systems. Their surface area is sufficiently large for meteorological forcing to cause turbulence, as in lakes and reservoirs, but turbulence generated from bed and internal friction of gravity-driven flows is also expected to contribute. Here we quantify near-surface turbulence using data from continuous air and water side measurements conducted over the ice-free season in a large subarctic regulated river in Finland. We find that turbulence, quantified as the dissipation rate of turbulent kinetic energy, is well described using equations for predicting turbulence from meteorological data for sufficiently high wind speeds whereas the contribution from bottom shear dominated at higher flow velocities. A one-dimensional river model successfully captured these processes.

We provide a fundamental model for estimating the relative contributions of atmospheric forcing and bottom friction as a function of depth.

1. Introduction

Inland waters produce, receive, transport and process organic and inorganic carbon and, relative to their surface area, are disproportionately important to regional and global carbon cycling (Aufdenkampe et al., 2011; Cole et al., 2007; Tranvik et al., 2009). River systems are often supersaturated in carbon dioxide (CO_2) and methane (CH_4), and release these radiatively-active gases to the atmosphere (Borges et al., 2015; Richey et al., 2002; Raymond et al., 2013). These gases are derived from terrestrial carbon sources and organic carbon fixed in aquatic ecosystems, and the relative importance of these sources and their response to anthropogenic disturbance remain uncertain in most systems (Alin et al., 2011; Butman & Raymond, 2011).

A key parameter that regulates the gas exchange across the air-water interface is the gas transfer velocity, which is mainly controlled by turbulence on the water side of the interface. Both surface renewal and thin-film theories result in a dependence of the gas transfer velocity on the dissipation rate of turbulent kinetic energy near the water surface (Katul & Liu, 2017; Lamont & Scott, 1970; Zappa et al., 2007). Several mechanisms can contribute to the generation of turbulence in the surface boundary layer (SBL). In lentic aquatic systems, such as lakes and reservoirs, near-surface turbulence is mainly driven by atmospheric forcing, including wind shear, convective cooling and surface wave breaking (Brumer et al., 2017; MacIntyre et al., 2010, 2020). Turbulence generation by wind shear can be described by boundary layer theory and energy dissipation rates scale with wind speed, while decreasing with increasing distance from the water surface (Tedford et al., 2014; Wüest & Lorke, 2003). In the open ocean, there is an increasing contribution of breaking surface waves to near-surface turbulence at wind speeds exceeding 10 m s^{-1} (Brumer et al., 2017). Convective mixing may occur if the net heat flux across the air-water interface is negative, and under such conditions, dissipation rates of turbulent kinetic energy scale with the surface buoyancy flux although the contribution has been found to be minimal (Bouffard & Wüest, 2019; MacIntyre et al., 2018, 2020). In shallow lotic ecosystems, such as streams, turbulence is mainly generated by bed friction induced by currents, that is, gravity-driven flow, and dissipation rates of turbulent kinetic energy scale with the mean flow velocity and decrease with increasing distance from the bed (Lorke & MacIntyre, 2009). It should be noted, that the term "bottom-generated turbulence" is often used for turbulence generated by bed friction in oceans and lakes. However, in rivers bottom shear can result from wind forcing and from gravity-driven river flow. Here we refer to bottom-generated turbulence as turbulence resulting from the latter forcing. Alin et al., (2011) suggested a conceptual scheme, in which the physical control of the gas transfer velocity in rivers undergoes a transition from the dominance of wind control in large rivers and estuaries toward increasing dominance of water current velocity and depth in smaller channels. Such scheme can provide the basis for a quantitative framework for estimating dissipation rates and gas transfer velocities in rivers, but requires improved mechanistic understanding of the drivers that regulate near-surface turbulence in rivers of different size.

With the need to quantify gas fluxes from rivers, and with minimal measurements of turbulence at this time to test key hypotheses, empirical relations between the gas exchange velocity and bulk flow properties have been developed including channel slope, discharge, mean flow speed, and water depth (Natchimuthu et al., 2017; Raymond et al., 2012; Ulseth et al., 2019; Wallin et al., 2018). Although these parameterizations have mainly been derived for streams, they are applied to larger streams and rivers because direct measurements of gas exchange velocities in large rivers are currently lacking, or restricted to estuaries and tidal rivers. Measurements in an estuary suggested that the principal controlling factor for near-surface dissipation rates was wind and that the surface heat flux and tidal currents played a secondary role (Orton, McGillis, & Zappa, 2010; Orton, Zappa, & McGillis, 2010). These studies underlined the important role of the density stratification in estuaries with seawater intrusions, which reduced the contribution of bed shear to near-surface turbulence. Density stratification can be expected to be less important in inland rivers. However, worldwide many rivers are altered and regulated for human demands (Grill et al., 2019). River regulation is characterized by anthropogenic control of the water level and discharge by dams. Hence, flow regulation is associated with alterations of the magnitude and temporal dynamics of flow velocity (Grill et al., 2019; Poff et al., 2007) and can be expected to affect gas exchange.
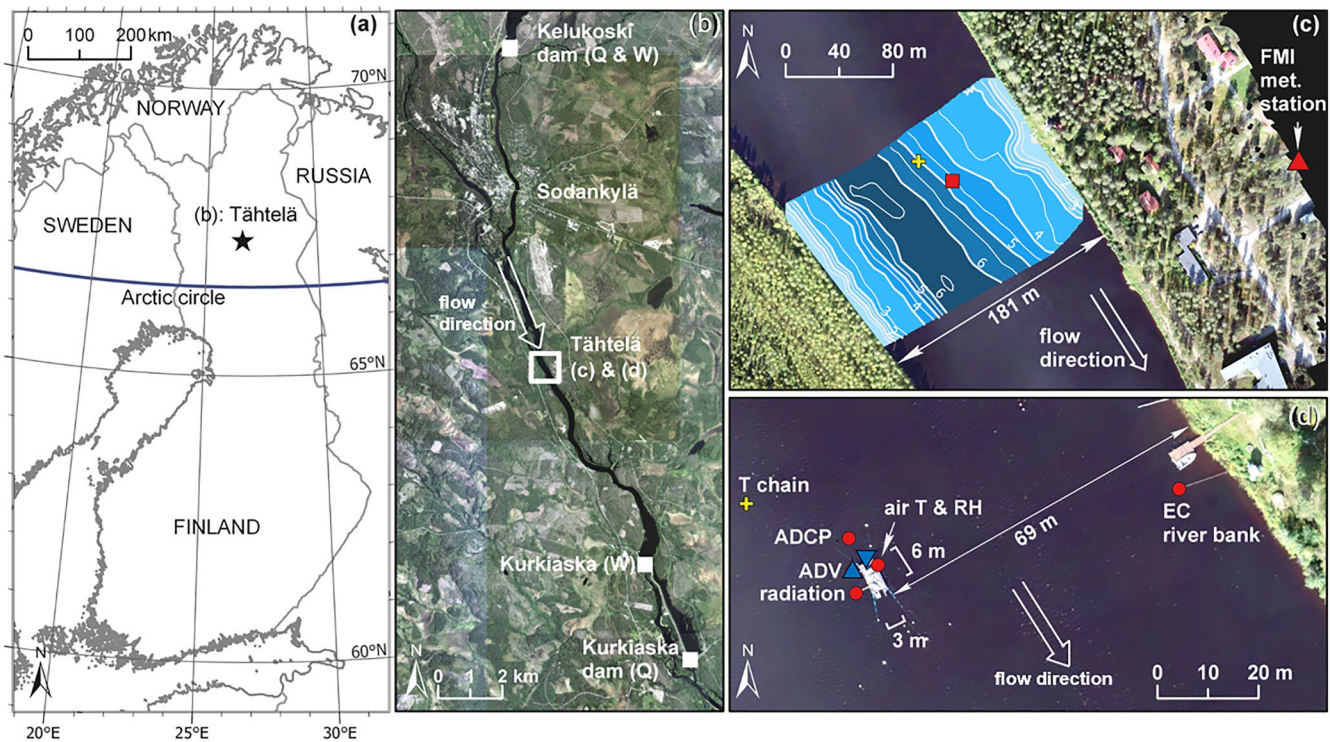
The country borders are downloaded from Eurostat (a).
The orthomosaic is from National Land Survey of Finland (b).

The aerial orthophoto has been measured on 31st August 2018
by University of Eastern Finland (Pasi Korpelainen) (c and d).

Figure 1. Location of the River Kitinen and the study site (a, b). The study site is marked by the black star in (a) and by the white box in (b). (c) shows the river bathymetry at the study site, text labels refer to water depth in meters. The yellow and red symbols mark in (c), (d) the location of the thermistor chain and floating platform, respectively. The red triangle indicates the location of the land meteorological station operated by the Finnish Meteorological Institute (FMI). (d) Areal photograph of the instrument platform and locations of instruments. The downward- and upward-facing blue triangles show two locations of the acoustic Doppler velocimeter (ADV) during the first month (June 10 to July 10, 2018) and the remaining period (July 10 to September 24, 2018), respectively. Red circles indicate the locations of the acoustic Doppler current profiler (ADCP), air temperature, relative humidity and radiation sensors and eddy covariance (EC) mast. Large white arrow in (c, b, d) show the flow direction.

In this study we identify the key drivers for near-surface turbulence in a regulated river and their temporal variations from hourly to seasonal time scales. Based on intensive field observations in a subarctic river, we quantify the contributions of gravity-driven flow and atmospheric forcing (wind shear, buoyancy flux, surface waves) to energy dissipation rates near the water surface. We compare our observations to dissipation estimates obtained from bulk parameters using commonly applied scaling relations, as well as to predictions made by a one-dimensional numerical turbulence model. Based on our findings, we derive a mechanistic concept for quantifying the contributions of wind shear and bottom friction to near-surface turbulence, which can be applied to a range of river sizes. To validate our methods for the estimation and predictions of the dissipation rates, we verify the assumption of an equilibrium between production and dissipation of turbulent kinetic energy (TKE) using the model simulations of the individual components of TKE budget.

2. Materials and Methods

2.1. Site Description

The present study was conducted in summer 2018 as part of the KITEX experiment, which was an international measurement campaign designed to improve the understanding of river-atmosphere greenhouse gas exchange. The study combines atmospheric and water-side measurements throughout the ice-free season (June to September) in a regulated river located in continental subarctic climate.

The study was conducted in the River Kitinen, 5 km south of the town Sodankylä in Northern Finland (67.3665°N, 26.6230°E; Figures 1a and 1b). At our study site, the river is a Strahler order 5 river according

Table 1

Hydraulic Parameters During the Observations: S_B [m km^{-1}] Is Bed Slope, Q [m^3 s^{-1}] Is River Discharge, H [m] Is Water Depth at the Sampling Location, W [m] Is River Width, $\bar{u}_{flow}$ [m s^{-1}] Is Mean Longitudinal Flow Velocity at 0.4 m Water Depth (See Following Section 2.2), Re $= \frac{\bar{u}_{flow} H}{\nu}$ *[–] is Bulk Reynolds Number, ν [m^2 s^{-1}] Kinematic Viscosity of Water (at 15°C), $Fr = \frac{\bar{u}_{flow}}{\sqrt{gH}}$ [–] Is Froude Number, g [m s^{-2}] Is Gravitational Acceleration*

S_B [m km^{-1}]	Q [m^3 s^{-1}]	H [m]	W [m]	$\bar{u}_{flow}$ [m s^{-1}]	Re [–]	Fr [–]
0.5	84 (1; 166)	4.2	181	0.13 (0.001; 0.34)	$4.7 \cdot 10^5$; ($2.8 \cdot 10^3$; $1.2 \cdot 10^6$)	0.02 ($1.2 \cdot 10^{-4}$; 0.05)

Note. Each number corresponds to the mean value during the observational period. For temporary varying parameters, the numbers in parentheses are minimum and maximum values.

to HydroSHEDS database (Lehner et al., 2008). The River Kitinen is the main tributary of the River Kemijoki, which is the longest (ca. 600 km) river in Finland. The construction of two large reservoirs, Lokka and Porttipahta, in the drainage area (ca. 51,000 km^2) of the River Kitinen in 1960, as well as seven hydroelectric power plants, modified the river hydrology drastically. One of the consequences is that the spring flooding is no longer present (Åberg et al., 2019). The power company regulates the river discharge at the power stations in such a way that the production of hydroelectricity increases in the morning and decreases during the night. In addition, less electricity is generated on the weekends than on weekdays (Krause, 2011).

The measuring site was located between the two dams of the operating power plants: Kelukoski (ca. 10 km) to the north and Kurkiaska (ca. 10 km) to the south (Figure 1b). The river width at the study location was 181 m and the maximum water depth was 6.5 m. The surrounding area was flat and the mean bed slope was only 0.5 m km^{-1}. The mean Froude number during the observational period was 0.02, which indicates slow subcritical flow (Table 1). A floating platform 6 m long and 3 m wide with measurement instruments was installed near the middle of the river where the water depth reached 4.5 m. The platform had an anchor system with surface buoys. The ropes from the platform corners were attached to surface buoys which were approximately 8–14 m distance from the platform. Ropes from the buoys extended to the bottom where they were fixed to concrete anchors approximately 20–30 m distance from the platform. The ropes connecting the platform, surface buoys and the anchors were tight and made the whole construction stable even in the presence of surface waves.

An eddy covariance (EC) mast was installed at the bank of the river, at a distance of approximately 80 m from the platform. Additionally, meteorological data were collected at meteorological station located at about 247 m east from the floating platform and operated by the Finnish Meteorological Institute (FMI).

2.2. Water-Side Measurements

The instruments and their deployment configurations of the water-side measurements are summarized in Table 2 and Figures 1c and 1d. An Acoustic Doppler Velocimeter (ADV, Nortek Vector) was installed twice during the measurement campaign. For the first month (June 10 to July 10, 2018) it was deployed at the northern (upstream) side of the platform and for the remaining period (July 10 to September 24, 2018) at the western side. The ADV was oriented downwards with its transducer located at a water depth of 0.24–0.25 m in both deployments, providing continuous measurements of flow velocity at the depth of the measurement volume, 0.4 m below the water surface (Figure 2). The instrument measured three components of flow velocity in a nearly cylindrical sampling volume (15 mm diameter, 14.9 mm length), located at a distance of 0.15 m from the transducer. An upward-facing Acoustic Doppler Current Profiler (ADCP, RDI Workhorse 600 kHz) was deployed on the bottom of the river, approximately 10 m upstream of the platform. Its profiling range extended from ∼0.7 m above the bottom (including the blanking distance of 0.2 m and the instrument height of 0.4 m) to ∼0.3–0.4 m below the surface with a vertical resolution of 0.1 m. The ADCP operated in pulse-coherent mode (high-resolution water profiling mode) and provided along-beam components of flow velocity from four acoustic beams which rise from the transducer at an angle of 20° (transducer diameter: 86 mm, beam width 1.5°). The size of the sampling volume varied from $6.7 \cdot 10^{-4}$ m^3 near the transducer (at 0.2 m blanking distance) to $2.4 \cdot 10^{-3}$ m^3 at 0.4 m below the water surface. Three-dimensional velocity vectors at each depth cell were estimated by combining radial along-beam velocities from all four beams. With a beam separation distance of 2.6 m at the water surface (0.4 m depth),

Table 2
Water-Side Measurements Conducted in the River Kitinen

Parameter	Instrument	Period of measurements	Sampling frequency (Hz)	Sampling depth (m)
Flow velocity	ADV Nortek vector	June 10 to September 24, 2018	32	~0.4
Velocity profile	ADCP RDI workhorse 600 kHz	June 7 to September 10, 2018	1–1.5	~0.4–3.5
Water level	RBR duet	June 10 to September 24, 2018	Wave burst mode: every 5 min 512 measurements with 16 Hz	0.43
Water Temperature	RBR solo	June 6 to September 24, 2018	0.1	6 June to 17 June 2018: 0.35, 1.35, 2.35, 3.35, 4.3517 June to 24 September 2018: 0.07, 1.05, 2.05, 3.05, 4.05
Photosynthetically active radiation (PAR)	LI-COR LI-192 Directional PAR sensor (0.3 m, 1 m); LI-COR LI-193 omnidirectional PAR sensor (0.65 m)	May 31 to October 2, 2018	1/60	0.3. 0.65, 0.1

turbulent velocity fluctuations could only be resolved along radial (along-beam) directions, while vertical profiles of mean flow velocities were obtained in Cartesian coordinates. A thermistor chain was deployed to measure water temperature at five different depths (Table 2). Water level fluctuations and surface waves were observed using a wave recorder (RBR duet), which was rigidly deployed on the base of the EC mast at 0.4 m below the water surface. Photosynthetically active radiation (PAR) was measured at the platform at three different water depths. It was used to estimate the attenuation coefficient (k_d [m^{-1}]) in water at noon using the Beer-Lambert law. Daily mean discharge and water level measurements were provided by the Kurkiaska power station located downstream from the study site (source of data: Finnish Environment Institute SYKE/ Hydrologian ja vesien käytön tietojärjestelmä HYDRO, available at http://www.syke.fi/avoindata, last access: 03.01.2019).
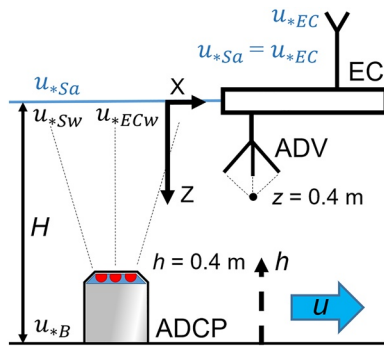

Figure 2. Schematic representation of (a) instruments location (Acoustic Doppler Velocimeter [ADV] and Acoustic Doppler Current Profiler [ADCP]). The upward-facing ADCP was installed on the river bottom. The sampling volume of the downward-oriented ADV was at 0.4 m below the water surface (black dot). Vertical coordinate z [m] is measured positive downward, h [m] corresponds to the distance from the bottom. Blue labels u_{*Sa}, u_{*EC} [m s^{-1}] correspond to the surface air-side friction and atmospheric friction velocity. The former is the generic descriptor of the air-side friction velocity and the latter is calculated from eddy covariance (EC) measurements 2 m above the water surface. In the atmospheric boundary layer, we assume a constant shear stress distribution, thus, both friction velocities are equal. Black labels u_{*Sw} and u_{*ECw} indicate generic surface water-side friction velocity and surface water-side friction velocity converted from u_{*EC} using the assumption of continuity of shearing stress across the air-water interface, respectively. u_{*B} is bed friction velocity. The large blue arrow indicates the direction of the mean flow velocity (u).

2.3. Air-Side Measurements

The meteorological measurements are summarized in Table 3. The eddy covariance system included a USA-1 (METEK) three-axis sonic anemometer/thermometer, which was mounted on a mast in the river at a distance of 10 m from the river bank and at a height of 2 m. The EC system provided mean wind speed $\bar{u}_{wind}$ [m s^{-1}], wind direction w_{dir} [°] and atmospheric friction velocity u_{*EC} [m s^{-1}] at 2 m height. Gaps in the time series measurements of wind speed and direction measured at the platform were filled using linearly regressed values from the corresponding station on land (FMI). We used incoming shortwave and longwave radiation from the land station, which were nearly identical to the values measured at the platform, but without gaps. The outgoing shortwave radiation was calculated as a product of albedo and incoming shortwave radiation, where albedo was estimated from Fresnal's Law (Neumann & Pierson, 1966). Outgoing longwave radiation was calculated as a function of surface water temperature (MacIntyre et al., 2002). Air temperature and relative humidity were measured at the platform (Rotronic HC2-S3CO3), and were also gap-filled using linear regression between the platform data and the land station data.

Table 3
Meteorological Measurements Conducted at the Study Site

Parameter	Instrument/Manufacturer	Period of measurements	Sampling frequency (Hz)	Instrument height (m)	Location
Wind speed, wind direction, atmospheric friction velocity	USA-1 (METEK)	May 29 to 17 October, 2018	10	2	>10 m from river bank
Wind speed, wind direction	UA2D Adolf Thies GmbH & Co. KG	May 01 to October 31, 2018	1/60	22.7	Land meteorological station (FMI)
Incoming short-and longwave radiation	CM11, Kipp & Zonen B.V.	May 01 to October 31, 2018	1/60	17.5	Land meteorological station (FMI)
Air temperature, relative humidity	Rotronic HC2-S3CO3	31 May to 20 September 2018	1/60	2	Measurement platform
Air temperature	Pt100 sensor, Pentronic AB	May 01 to October 31, 2018	1/60	2	Land meteorological station (FMI)
Relative humidity	HMP155D, Vaisala Oy	May 01 to October 17, 2018	1/60	2	Land meteorological station (FMI)

2.4. Data Processing

2.4.1. Turbulent Kinetic Energy Budget

In the turbulent boundary layer, we consider the following budget of turbulent kinetic energy K [m^2 s^{-2}] (Foken & Napo, 2008; Kundu et al., 2010):

$$\underbrace{\frac{\partial K}{\partial t}}_{(1)} + \underbrace{\bar{u}_j \frac{\partial \overline{K}}{\partial x_j}}_{(2)} + \underbrace{\frac{\partial \overline{u_j' K}}{\partial x_j}}_{(3)} = -\underbrace{\frac{1}{\rho_\mathrm{w}} \frac{\partial \overline{u_i' p'}}{\partial x_i}}_{(4)} - \underbrace{g\alpha \overline{w'T'}}_{(5)} - \underbrace{\overline{u_i' u_j'} \frac{\partial \overline{u}_i}{\partial x_j}}_{(6)} - \underbrace{\varepsilon}_{(7)} \tag{1}$$

where $K = \frac{1}{2}\overline{u_i'^2}$ is the turbulent kinetic energy, $\bar{u}_i$, $i = 1, 2, 3$ which corresponds to u, v, w, u_i' which corresponds to u', v', w' [m s^{-1}] are the mean velocities and the turbulent velocity fluctuations, respectively, resulted from Reynolds decomposition of each of the velocity component. ρ_w [kg m^{-3}] is the water density, p' [Pa] are the turbulent pressure fluctuations, x_i [m] are the coordinates where x_1, x_2, x_3 correspond to x, y, z, T' [K] are the temperature fluctuations, ε [W m^{-2}] is the dissipation rate of turbulent kinetic energy (summation convention is implied over the indices i and j). For steady-state conditions and homogeneous turbulence, the rate-of-change of TKE term (1) and the turbulent transport terms (2) – (3), as well as pressure correlation term (4) are neglected. By further assuming two-dimensional flow conditions (uniform flow except for vertical variations of the mean longitudinal flow velocity $\bar{u}_\mathrm{flow}$ [m s^{-1}]), leads to an approximate equilibrium between the sum of the shear production term (6) and buoyant production or consumption term (5) and the rate of energy dissipation (7) (Equation 2).

$$\varepsilon = -g\alpha \overline{w'T'} - \overline{w'u'} \frac{\partial \overline{u}_\mathrm{flow}}{\partial z} \tag{2}$$

Note that, in comparison with, for example (Nikora & Roy, 2012), we consider the buoyancy term here, as a source of TKE during convective cooling.

2.4.2. Estimation of Near-Surface Dissipation Rates From ADV Data

Data analysis procedures for the ADV and the ADCP were similar in that, first, the data went through quality control procedures and then dissipation rates were computed using the inertial subrange method. The ADV resolved the vertical velocity component of flow directly. It had high quality data and could be used to estimate dissipation rates when surface waves were present. Thus, dissipation rates from the ADV measurements were primarily used in the results and discussion sections when characterizing near-surface turbulence. The sampling rate of the ADV was 32 Hz. Data were quality-checked by removing measurements with a correlation magnitude less than 70% (a standard statistical measure of velocity data quality [Nortek, 2015]). Outliers were removed following the procedures described in (Goring & Nikora, 2002;

Wahl, 2003). Subsequent analysis was performed for 10 min periods following established methods (Cannon & Troy, 2018; Guerra & Thomson, 2017; Jabbari et al., 2020; McCaffrey et al., 2015; McMillan & Hay, 2017; Orton, McGillis, & Zappa, 2010). If more than 20% of the data within each period were removed by the quality check, then the period was discarded, otherwise the missing velocities were linearly interpolated. In Text S1 in Supporting Information S1 we demonstrate that the chosen threshold of 20% results in an uncertainty of dissipation rate estimates of less than 10% (Figure S1 in Supporting Information S1). Velocities measured in instrument coordinates were rotated into the direction of the mean flow for each interval. Mean flow velocity was calculated for each 10 min time interval as the mean longitudinal velocity component $\bar{u}_{\text{flow}}$. In total, 11% of the data were removed during quality screening and averaging.

Dissipation rates of turbulent kinetic energy ε_{ADV} [W kg^{-1}] were estimated using the inertial dissipation technique also known as inertial subrange fitting (ISF), following (Bluteau et al., 2011). This method is based on general theories of turbulence describing a cascade of energy from the larger to the smaller scales (Tennekes & Lumley, 1972) and an implicit assumption of an equilibrium between production and dissipation of TKE. We estimated the dissipation rate using the following equation:

$$\varepsilon = \left(\frac{E(k)}{A \alpha_{\text{K}} k^{-5/3}} \right)^{\frac{3}{2}}. \tag{3}$$

Here, E [m^3 s^{-2} rad^{-1}] is the one-dimensional wave number spectrum of turbulent velocity fluctuations. $\alpha_{\text{K}} = 1.5$ [–] is the Kolmogorov constant, k is the longitudinal wave number [rad m^{-1}], and A is a constant which depends on the direction of velocity fluctuations: for vertical and transversal components $A = \frac{4}{3} \times \frac{18}{55}$ [–] and for horizontal component $A = 1 \times \frac{18}{55}$ [–] (Pope, 2000).

Velocity power spectra in the frequency domain $S(\omega)$ [m^2 s^{-1} rad^{-1}] were calculated using Welch's method (Thomson & Emery, 2001). Each 10 min segment of velocity time series was divided into overlapping (50%) sections with 8192 individual samples on which a fast Fourier transform was applied after subtraction of a linear trend and multiplication with a Hanning window function. Power spectra were estimated as the average squared magnitude of the periodograms. We converted the spectra from frequency to the wave number domain ($\omega = \bar{u}_{\text{flow}} k$) using Taylor's frozen turbulence hypothesis, which assumes that the turbulent flow does not change its characteristics while passing through the sensor and that turbulent velocity fluctuations are much smaller than the mean flow. The validity of this approach was tested as $\overline{(u_i'^2)}^{\frac{1}{2}} / \bar{u}_{\text{flow}} \leqslant 0.15$ (Bluteau et al., 2011).

The spectral range used for inertial subrange fitting was limited by the instrument noise at a high frequency limit ω_{up} [rad s^{-1}] and by the size of energy-containing eddies at a lower frequency limit ω_{low} [rad s^{-1}]. We defined the upper cutoff frequency as the frequency for which the ratio of power spectral density to the noise level became smaller than one. The noise level was calculated for each spectrum as the logarithmic mean of S at frequencies larger than 50 rad s^{-1} where noise was always observed even for high flow velocity, see Figure 3a. The lower frequency limit was estimated by identifying a breakpoint in spectral slope at the beginning of the inertial subrange (IS) in each spectrum (see Text S2, Figure S2a in Supporting Information S1). If this breakpoint corresponded to the distance larger than the distance to the boundary $-l = 0.4$ m and 4.2 m for vertical and horizontal velocity components, respectively, then the lower IS limit was set to the frequencies corresponding to this distance ($\omega_{\text{low}} = 2\pi \bar{u}_{\text{flow}}/l$) (see an example for vertical component in Figure S2b in Supporting Information S1).

Many spectra had a pronounced peak caused by surface waves ($\sim$10 rad s^{-1} or 1 s period, see Figure 3b). For these spectra, an upper frequency limit for ISF was defined as the frequency where the function $f = S(\omega) \cdot \omega$ had a minimum value within the interval $0.5 \leqslant \omega_{up} \leqslant 3$ [rad s^{-1}]. The minimum marks the transition from the $-5/3$ power law to the wave peak.

Following the suggestions in Bluteau et al. (2011), we applied the following quality criteria to the inertial subrange fits: (a) validity of Taylor's frozen turbulence hypothesis (15% of the fits were rejected); (b) coefficient of determination should be larger than 0 (26% of fits were rejected). In addition, the following optional quality criterion was applied: (c) length of the fitted inertial subrange (10% of fits were rejected). We applied the three criteria to all the data (the threshold for the last one was 10/8 of a decade as an compromise
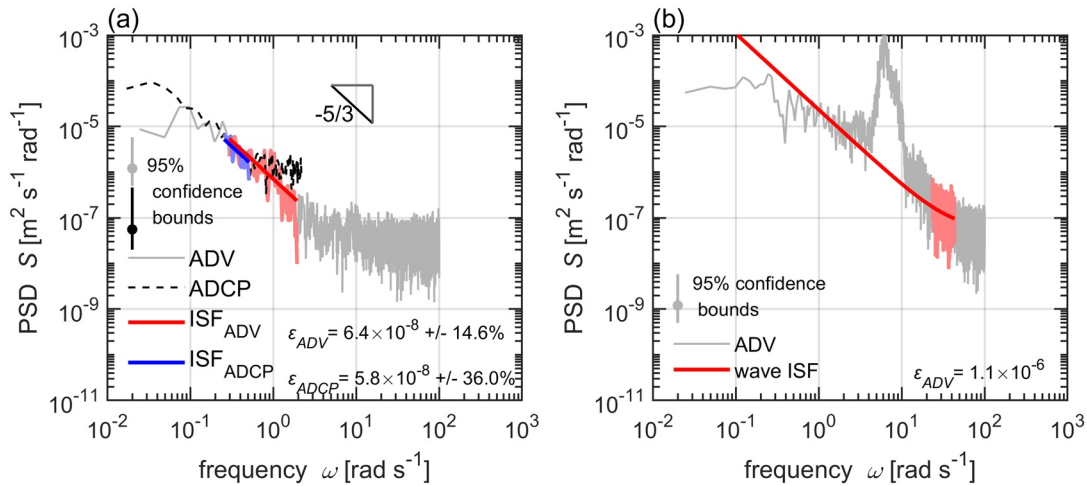
Figure 3. (a) Typical frequency spectrum (power spectral density, PSD) of vertical velocity fluctuations measured by ADV (gray line) and along-beam velocity fluctuations measured by ADCP (dashed black line) for a period without surface waves. Blue and red parts of the spectra represent the selected range for estimating dissipation rates by inertial subrange fitting (ISF, −5/3 slope) for ADCP and ADV, respectively. Thick blue and red lines show the corresponding fits. The dissipation rates obtained from ISF ε_{ADV}, ε_{ADCP} [W kg^{-1}] with confidence bounds (in percent) are provided as labels. Gray and black lines with dots indicate the 95% confidence bounds of the spectra for ADV and ADCP, respectively. (b) ADV frequency spectrum for a period with surface waves (wave peak at around 10 rad s^{-1}). The frequency range marked by red color was used for spectral fitting of the wave affected inertial subrange method (Equation 4). The extrapolated fit from the wave-affected part is shown as a thick red line.

between reasonable amount of data and avoiding too short inertial subrange) and rejected fits were discarded from further analyses of dissipation rates. Application of these three criteria led to 58% reduction of the fits.

We visually inspected the spectra of all three velocity components. Most of the horizontal and transversal velocity spectra were strongly contaminated by noise (see a typical example in Figure S3a in Supporting Information S1). In contrast to that, the vertical component was found to be less affected by noise. To validate the assumption of isotropic turbulence, we compared the quality assured dissipation rate estimates from horizontal and vertical velocity components (see Figure S3b in Supporting Information S1). We found a good agreement on average, however, at higher dissipation rates there was a discrepancy of at least a factor of 3–5. We used only the vertical velocity component for the calculation of dissipation rates, as in other studies, (e.g. Feddersen et al., 2007).

When surface waves were present, we fitted spectra at frequencies higher than the surface waves and lower than the noise limit (see Figure 3b). Advection by wave orbital velocities additionally was accounted for:

$$\varepsilon = \exp\left\langle \ln\left(\frac{(S_{\text{ww}}(\omega) - \text{Noise} \quad \text{level}) \; \omega^{5/3}}{\alpha_{\text{K}} \, J_{\text{ww}}} \right)^{3/2} \right\rangle, \tag{4}$$

where $J_{\text{ww}} = f(\sigma_1, \sigma_2, \sigma_3, \bar{u}, \bar{v})$ is a function describing the effect of the wave advection in terms of the standard deviations of all three velocity components σ, and mean horizontal flow velocities $(\bar{u}, \bar{v})$ (Gerbi et al., 2009). The subscript "ww" is used for vertical velocity component. The angled brackets denote averaging over all frequencies ω for which the inertial subrange fit was applied. This method is a slightly modified version of the one proposed by (Feddersen et al., 2007). The spectra which were affected by surface waves and the range of the frequencies for wave peaks were selected manually. These selected spectra were fitted according to Equation 4. A comparison of both fitting procedures for spectra where an inertial subrange could be fitted at both sides of the wave peak, revealed good agreement of the resulting dissipation rates. Resulting dissipation rates consisted of 54% and 46% estimates using Equations 3 and 4, respectively.

To exclude time periods for which the observed flow was potentially affected by the platform, we discarded dissipation rate estimates for which the sampling location was at the downwind end of the platform, that is, for wind direction (a) $80° \leqslant w_{dir} \leqslant 245°$ for the first and (b) $20° \leqslant w_{dir} \leqslant 150°$ for the second deployment.

This led to a further 25% reduction of the quality-checked data resulting in a total of 7,452 dissipation rate estimates based on ADV data (0.4 m water depth).

2.4.3. Estimation of Dissipation Rates From ADCP Data

The overall procedure to analyze ADCP data was similar to that with the ADV. That is, the first steps involved obtaining valid data using quality controls followed by calculating dissipation rates in the inertial subrange. Measurements with a magnitude of signal correlation less than 70 were removed and velocity time series at each depth were despiked using the same parameters as for the ADV data. For the first 33 days, we applied a bin mapping procedure using linear interpolation (Ott, 2002) due to a significant instrument tilt during this deployment ($\sim 8°$). Frequently occurring losses of connection to the ADCP resulted in missing data and a slight reduction of actual sampling frequency. If the number of missing velocity measurements in 10 min analysis intervals was less than 20%, we applied linear interpolation to fill these gaps using the mean sampling frequency for this period.

Velocities were measured in beam coordinates, which were transformed to orthogonal (instrument) coordinates before being rotated into the mean flow direction (longitudinal, transversal and vertical velocity components) for 10 min averaging intervals. After quality screening and averaging, the temporal coverage of valid velocity measurements was ~50% of the total deployment duration in the middle of the water column, and slightly less (44%) near the water surface (0.4 m water depth).

Frequency spectra were calculated from beam velocities over 10 min periods (number of samples used for the fast Fourier transform is 256) and log-averaged over all 4 beams. The identification of the lower and upper frequencies of the inertial subrange was the same as described above for the ADV. For each individual depth the distance to the boundary (except cases when the breakpoint in the in the optimization procedure was smaller than this distance), was fixed as the lower frequency limit.

Since the ADCP measures velocity fluctuations along the four acoustic beams, the direction of the turbulent velocity fluctuations, that is, the constant A (Equation 3) is undetermined. In this study the constant was set to $A = 1.16 \times \frac{18}{55}$, which corresponds to the average of 1 and 4/3. We applied the same quality criteria to spectral fits as for the ADV data.

The sampling frequency of the ADCP was too low to resolve wave orbital velocities, and we could not estimate dissipation rates during wave-affected periods. As described above, we primarily used the ADV data in subsequent analyses. The ADCP based estimates are used in Sections 2.6, 3.2, where we specifically analyze bottom-generated turbulence and provide vertical profiles of dissipation rates.

2.4.4. Shear Stress Obtained From Eddy Covariance

A double rotation of the coordinate system was performed with the wind velocity measurements of the anemometer (McMillen, 1988). The atmospheric friction velocity was calculated from the original 10 Hz data as 5 min block-averages as a square root of the Reynolds stress in the air:

$$u_{*EC} = \left(\overline{u'_{EC} w'_{EC}}^2 + \overline{v'_{EC} w'_{EC}}^2 \right)^{\frac{1}{4}}.$$

(5)

Here, the subscript "EC" is used showing that these turbulent velocity fluctuations were measured in the air. Screening for weak turbulence with a specific friction velocity limit was not performed, but the cases with upward momentum flux ($\overline{u'_{EC} w'_{EC}} < 0$) were discarded. The 5 min u_{*EC}, wind speed and wind direction data were further averaged to 10-min mean values to enable direct comparison with other data. Acceptable wind directions were $151° \leqslant w_{dir} \leqslant 190°$ and $290° \leqslant w_{dir} \leqslant 323°$ to ensure sufficient fetch with an open water surface.

2.5. Turbulence From Atmospheric Forcing

To estimate dissipation rates in the water from bulk measurements of atmospheric forcing, we used Monin-Obukhov similarity scaling described in Tedford et al. (2014). During periods of heating of the water surface (the surface buoyancy flux, $J_{BO} > 0$ [W kg^{-1}]), dissipation rates were estimated as:

$$\varepsilon_{\text{SBL}} = \varepsilon_{\text{SBL, wind}} = C_1 \frac{u_{*\text{Sw}}^3}{\kappa z}, \tag{6}$$

where $\kappa = 0.41$ [–] is the von Kármán constant, $C_1 = 0.6$ is a constant, z [m] is the distance from the water surface. $u_{*\text{Sw}}$ [m s^{-1}] is the surface water-side friction velocity computed from surface wind shear stress τ_{S} [N m^{-2}] assuming continuity of shear stress at the interface $\tau_{\text{S}} = \rho_{\text{a}} u_{*\text{Sa}}^2 = \rho_{\text{w}} u_{*\text{Sw}}^2$, where ρ_{a} [kg m^{-3}] is the air density, $u_{*\text{Sa}}$ [m s^{-1}] is the surface air-side friction velocity. Using this assumption we calculated $u_{*\text{Sw}} = (\tau_{\text{S}}/\rho_{\text{w}})^{\frac{1}{2}}$. Surface wind shear stress was calculated from the wind speed as $\tau_{\text{S}} = \rho_{\text{a}} C_{\text{Da}} \bar{u}_{\text{wind}}^2$, where C_{Da} [–] is the drag coefficient. We assumed a neutral drag coefficient at 10 m height of $C_{\text{Da 10m}} = 1.3 \cdot 10^{-3}$ (Foken & Napo, 2008), which gives $C_{\text{Da 2m}} = 1.8 \cdot 10^{-3}$ at the 2 m measurement height using boundary-layer scaling. Note, that "neutral" refers to the neutral stratification in the atmosphere. $C_{\text{Da 2m}}$ was corrected for atmospheric stability following (Hicks, 1972).

The buoyancy flux was calculated as $J_{\text{BO}} = g\alpha Q_{\text{heat}}/(C_{\text{pw}}\rho_{\text{w}})$ [W kg^{-1}], where Q_{heat} [W m^{-2}] is the effective heat flux at the water surface, α is the thermal expansion coefficient of water, C_{pw} [J kg^{-1} °C^{-1}] is the specific heat capacity of water. The surface heat flux was computed as the sum of latent heat flux, sensible heat flux and net longwave radiation, and the effective heat flux for the actively mixing layer as the sum of the surface heat flux plus the shortwave radiation retained within the actively mixing layer. The mixing layer depth was estimated as the depth where the water temperature difference from the surface was exceeding 0.02°C. All calculations above were based on formulations from (Imberger, 1985; MacIntyre et al., 2002, 2014).

During water cooling ($J_{\text{BO}} \leqslant 0$), when convective mixing also contributed to the dissipation rate (Tedford et al., 2014), ε_{SBL} was estimated as:

$$\varepsilon_{\text{SBL}} = \varepsilon_{\text{SBL, wind}} + \varepsilon_{\text{SBL, buoy}} = C_1 \frac{u_{*\text{Sw}}^3}{\kappa z} + 0.77|J_{\text{BO}}|, \tag{7}$$

Additionally, we used surface boundary layer scaling to estimate wind-generated energy dissipation rates (Equation 6) in the water from atmospheric momentum fluxes measured by EC:

$$\varepsilon_{\text{SBL,EC}} = C_1 \frac{u_{*\text{ECw}}^3}{\kappa z}, \tag{8}$$

where the surface water-side friction velocity $u_{*\text{ECw}}$ was estimated from the atmospheric friction velocity $u_{*\text{EC}}$ calculated from the EC system as $u_{*\text{ECw}} = u_{*\text{EC}}(\rho_{\text{a}}/\rho_{\text{w}})^{\frac{1}{2}}$. Shear stress is assumed constant in the atmospheric boundary layer ($u_{*\text{EC}} = u_{*\text{Sa}}$).

2.6. Bottom-Generated Turbulence

In addition to turbulence generated by atmospheric forcing, we consider the contribution of bed friction of gravity-driven river flow. This source of turbulence comes from the mean kinetic energy through the shear production term (6) in Equation 1. We used the variance of ADCP beam velocities to compute vertical profiles of Reynolds shear stresses $\tau_{\text{T}} = \left(\overline{u'w'}^2 + \overline{v'w'}^2\right)^{\frac{1}{2}}$ [N m^{-2}] following (Stacey et al., 1999). The bed friction velocity $u_{*\text{B}}$ [m s^{-1}] was calculated as:

$$u_{*\text{B}} = \left(\frac{\tau_{\text{T}}}{\rho_{\text{w}}\left(1 - \frac{h}{H}\right)}\right)^{\frac{1}{2}}, \tag{9}$$

where h [m] is the distance from the bottom, H is the total water depth at the ADCP location.

To estimate the near-surface dissipation rates generated by turbulence production by bed shear we used three approaches, which are all based on the assumption of a steady, two-dimensional boundary-layer flow. The first simple dissipation scaling is based on the assumption that the shear stress is constant over the water column and equal to bed shear stress τ_{B} [N m^{-2}]:

$$\varepsilon_{\text{BBL}} = \frac{u_{*\text{B}}^3}{\kappa h}. \tag{10}$$

A commonly used empirical approach in open channel flows, where the shear stress is decreasing linearly from the bed to zero at the water surface (Nezu, 1977), results in a stronger exponential decay of dissipation rates with distance from the bed:

$$\varepsilon_{\text{BBL, Nezu}} = \frac{u_{*B}^3}{H} \frac{E}{\sqrt{h/H}} \exp\left(-\frac{3h}{H}\right),$$ (11)

where E [–] is an empirical constant for which we assigned a value of $E = 9.8$, as suggested by Nezu (1977). In addition, we used the model proposed in Nikora and Smart (1996):

$$\varepsilon_{\text{BBL, NS}} = \frac{u_{*B}^3}{\kappa h}\left(1 - \frac{h}{H}\right),$$ (12)

where apart from linearly-decreasing shear stress a logarithmic profile of the mean flow velocity is taken into account. Note, that the assumption of an equilibrium between production and dissipation of turbulent kinetic energy is implied in all above equations and density stratification is not considered.

To identify periods when bed shear stress was the dominating generation mechanism for near surface turbulence, we estimated u_{*B} from ADCP data (Equation 9) as the mean value over 18 bins (0.7–2.4 m above the bed). We then selected cases when the dissipation rate at 0.4 m water depth predicted by Equation 10 exceeded the dissipation rate from atmospheric forcing (Equation 6 and 7). For these cases, we compared the vertical distribution of dissipation rates obtained from ADCP data with the three scaling approaches described by Equation 10–12.

For the selected cases for which bed-shear was the dominating source of near-surface turbulence, we estimated the bed drag coefficient C_{Dw} [–], which relates bed shear stress to the mean flow velocity at a given height above the bed:

$$C_{\text{Dw}} = \frac{u_{*B}^2}{\bar{u}_{\text{flow 1m}}^2}.$$ (13)

C_{Dw} was first estimated for a height of 1 m above the bed using the mean flow velocity measured by the ADCP. Unrealistically high values of the drag coefficient were excluded from averaging. We chose an upper threshold of ($C_{\text{Dw}} \leqslant 7.4 \cdot 10^{-3}$, which corresponds to the upper limit of Manning's roughness coefficient $n_M = 0.035$ s m$^{-1/3}$ reported for the rivers with sand bed and the straight uniform channel where grain roughness is predominant (Arcement & Schneider, 1989; Chow, 1959). To take advantage of the longer time series of mean flow velocity measured by the ADV, we subsequently scaled the bed drag coefficient to 0.4 m water depth following two equations where we first derived the bed roughness length z_0 [m]:

$$z_0 = h \cdot e^{-\frac{\kappa}{\sqrt{C_{\text{Dw}}}}},$$ (14)

where $h = 1$ m. Then we calculated the bed drag coefficient at 0.4 m water depth ($h = 3.8$ m):

$$C_{\text{Dw}} = \frac{\kappa^2}{\ln\left(\frac{h}{z_0}\right)^2}.$$ (15)

By combining expressions for the bed shear stress $\tau_B = \rho_w C_{\text{Dw}} \bar{u}_{\text{flow}}^2$, and the bed friction velocity $u_{*B} = (\tau_B/\rho_w)^{\frac{1}{2}}$ and Equation 10, the mean flow velocity measured by the ADV was used to estimate the near-surface dissipation rate generated by bed shear ($\varepsilon_{\text{BBL, ADV}}$) as:

$$\varepsilon_{\text{BBL,ADV}} = C_{\text{Dw}}^{\frac{3}{2}} \frac{\bar{u}_{\text{flow}}^3}{\kappa h}.$$ (16)

2.7. One-Dimensional $k - \varepsilon$ Model

Both bottom shear stress and atmospheric forcing are taken into account while simulating dissipation rates below the water surface using a vertically resolving turbulence model of a river flow. The one-dimensional (in vertical direction) modeling of turbulent river flow should be sufficient to reproduce the vertical structure of thermo- and hydrodynamic properties, if the marginal effects at river banks are negligible; this is the case when depth-to-width ratio is small (about 0.02 for the River Kitinen at the location of the raft). The $k - \varepsilon$ model used in this study is a 1D version of Reynolds-Averaged Navier-Stokes (RANS) equation system. This system is an exact result of spatial averaging of 3D RANS-equations over a horizontal cross-section of a river stream, in which the shape of horizontal and vertical cross-sections are assumed rectangular, neglecting heat and momentum fluxes at the channel banks and omitting longitudinal advection; the system is provided with boundary conditions from atmospheric and river discharge measurements (the complete description of the model is given in Text S4 in Supporting Information S1). The full system is solved using LAKE2.0 model code (Stepanenko et al., 2016) as it uses horizontal averaging of thermo- and hydrodynamic equations as well. The only modification to the lake model algorithm was an addition of a method to compute longitudinal pressure gradient, driving the river flow (Text S4 in Supporting Information S1).

The model provided TKE transport terms, which we use in Section 3.6 to verify the assumption of an equilibrium between the production and the dissipation underlying dissipation rate estimates.

2.8. Statistical Analyses

Cumulative distribution functions of dissipation rate estimates are approximately lognormal (Baker & Gibson, 1987). Averaging of dissipation rates was therefore done with log-transformed values. Similarly, also estimates of the bottom drag coefficient log-averaged. For visual comparison of different dissipation rate estimates we applied a bin-averaging procedure, which is described in Supporting Information S1 (Text S3, Figure S8).

3. Results

3.1. Overview of the Measurements

The variations of wind speed, flow velocity and surface buoyancy flux as the main drivers for near-surface turbulence are shown in Figure 4. Wind speed varied over diel and synoptic scales with a range of 0 and 8.4 m s^{-1}. Mean flow velocity also changed over diel cycles due to the downstream dam operations and ranged between 0.001 and 0.34 m s^{-1}. River discharge at the downstream Kurkiaska power station (Figure 4b) varied between 1 and 166 m^3 s^{-1}, with no pronounced seasonal pattern. The mean discharge during the time period from June 1 to September 30 was 84 m^3 s^{-1}. Daily mean measured flow velocity and the discharge were strongly correlated ($\rho = 0.9$, $p < 0.05$, where ρ is a correlation coefficient and p is a significance level for the correlation coefficient). The surface buoyancy flux generally showed a pronounced diel pattern with seasonally varying amplitude. Maximum ($3.2 \cdot 10^{-7}$ W kg^{-1}) and minimum ($-1.7 \cdot 10^{-7}$ W kg^{-1}) values were observed at the beginning of August. Nighttime buoyancy fluxes were negative throughout the observational period as expected and indicative of periods when convective mixing could occur. The dissipation rate at 0.4 m depth varied between $9.7 \cdot 10^{-10}$ and $2.4 \cdot 10^{-5}$ W kg^{-1} (Figure 4d). Dissipation rates less than 10^{-8} W kg^{-1} were observed when flow velocities were low, that is, at low discharge.

Air temperature varied between -0.8°C on September 15 and 30.3°C on July 13 and also showed a diel pattern (Figure S4a in Supporting Information S1). Surface water temperature increased during summer, reaching its maximum value of 23°C on August 2, and slowly decreased toward autumn to the minimum value of 8.7°C on September 22. Weak thermal stratification developed primarily during the first half of the summer June–July (Figure S5 in Supporting Information S1). The maximum value of the temperature difference between the surface and bottom was 2.3°C on June 18 (Figure S5a in Supporting Information S1). Using a threshold for the temperature difference between surface and bottom of 0.05°C (Bormans & Webster, 1997), stratification was observed on 41 days and persisted for 38% of the observational period.

Significant wave height H_{sig} (defined as the average wave height, from trough to crest, of the highest one-third of the waves) was correlated to wind speed ($\rho = 0.7$, $p < 0.05$) and was mostly below 0.05 m reaching
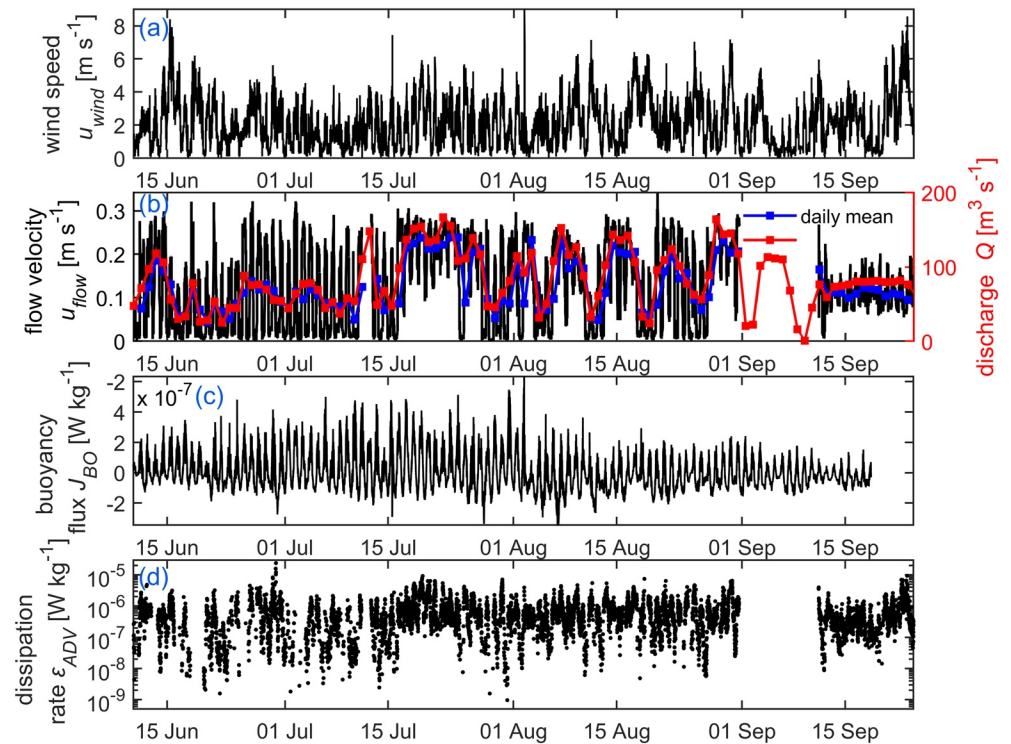
Figure 4. Time series of drivers of near-surface turbulence during the study period: (a) wind speed; (b) longitudinal flow velocity at 0.4 m water depth (ADV, black line), daily mean flow velocity (blue line) and daily mean discharge at Kurkiaska power station (red line with square symbols); (c) buoyancy flux; (d) dissipation rate of turbulent kinetic energy at 0.4 m depth. Except for daily mean values in (b), all data are shown with 10 min resolution.

a maximum value of 0.11 m (Figure S4c in Supporting Information S1). We found weaker correlation between H_{sig} and $\bar{u}_{wind}$ when the wind blew along the main flow direction ($\rho = 0.5$, $p < 0.05$, Figure S6a in Supporting Information S1) in comparison with a relatively strong correlation and linear relationship ($\rho = 0.8$, $p < 0.05$) when the wind direction was in opposition to the main flow direction (Figure S6b in Supporting Information S1).

The diel variability in flow was not only observed at the surface but throughout the full water column (Figure 5). Maxima occured during daytime (Figures 5b and 5c). The change from high to low flow velocity occurred rapidly, with mean flow velocity often decreasing by 50% within 30–60 min. The direction of the mean flow near the water surface was aligned either with the wind direction or with the direction of river flow (Figure 5a). During the day, when flow velocities and wind were elevated, incoming heat was sometimes mixed throughout the water column and water temperature increased; on the other days temperature declined. After flow speed and wind speed decreased at night, weak thermal stratification occurred and persisted until midnight (see 1–2 July in Figure 5d). Stratification usually persisted for several hours, before it was disrupted by a rapid increase in flow or by convective mixing.

3.2. Bottom-Generated Turbulence

When bed-shear was expected to dominate near-surface dissipation rates ($n = 2,967$), the temporarily averaged dissipation rate estimated from ADCP measurements were highest near the bottom (maximum value of $3.7 \cdot 10^{-6}$ W kg^{-1} at a distance of 0.7 m above the bottom) and decreased by a factor of five to $7.1 \cdot 10^{-7}$ W kg^{-1} near the water surface (Figure 6a). The vertical profile agreed well with the simple dissipation scaling based on assumption of the constant shear stress distribution (Equation 10). The extrapolation to 0.4 m water depth was in close agreement with the mean dissipation rate estimated from ADV measurements for the selected cases. This agreement was unexpected as the extrapolation of the dissipation rates up to water surface using Equations 10 and 12 is only valid for a distance from the bottom over which the velocity profile
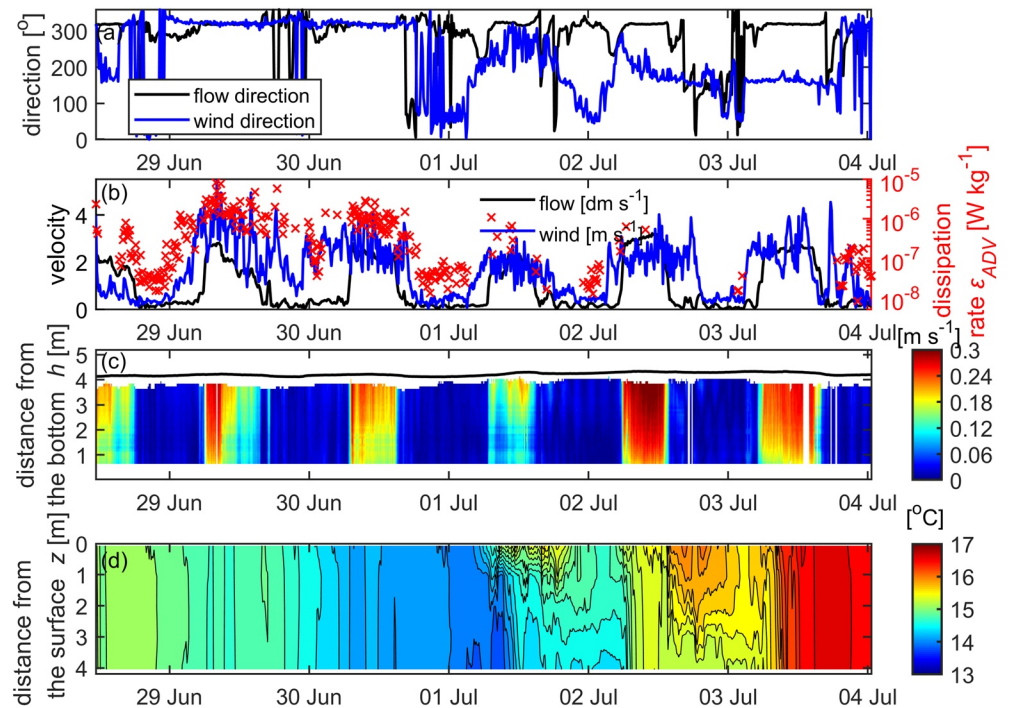
Figure 5. Time series of (a) flow direction (ADV, black line) and wind direction (blue line); (b) flow velocity (ADV [dm s⁻¹], black line), wind speed ([m s⁻¹], blue line) and dissipation rate of turbulent kinetic energy (ADV, red crosses); (c) contours of flow velocity (ADCP), black line represents water surface; (d) water temperature. Data are from June 28 to July 04, 2018, emphasizing diel dynamics with a temporal resolution of 10 min.

is expected to be logarithmic (up to 0.6 of the water depth H). We did not find a good agreement between the mean ADCP dissipation rate profile and the two scaling relations for dissipation rates based on linearly decreasing shear stress toward the water surface (Equations 11 and 12). Both profiles agreed well with each other at a distance of 0.7 m above the bottom and deviated from the ADV dissipation rate at 0.4 m depth by a factor of 4 and 10, respectively. In contrast to the empirical approach by Nezu (1977), the model of Nikora and Smart (1996) converges to zero at the water surface (Figure 6a).

In contradiction to the scaling of vertical profiles of dissipation rates, the averaged Reynolds shear stress profile was not constant over depth, but closely followed a linear decrease toward zero at the water surface, as assumed in the derivation of Equations 11 and 12 (see, Figure S7 in Supporting Information S1).

The average value of the bottom drag coefficient at 1 m distance above the bed equaled to $C_{\mathrm{Dw}} = 0.002$. For a water depth of 0.4 m we estimated a value of $C_{\mathrm{Dw}} = 0.0015$. There was generally good agreement between bin-averaged near-surface dissipation rates estimated from the bed friction velocity derived from ADCP measurements (u_{*_B}), and dissipation rates predicted from mean flow velocity measured by the ADV ($\varepsilon_{\mathrm{BBL,ADV}}$, Equation 13, see Figure 6b).

3.3. Turbulence Generated by Atmospheric Forcing

We examined the relation between dissipation and atmospheric forcing for cases when $\varepsilon_{\mathrm{SBL}} > \varepsilon_{\mathrm{BBL}}$. Bin-averaged rates of dissipation of turbulent kinetic energy predicted from bulk atmospheric forcing ($\varepsilon_{\mathrm{SBL}}$, Equations 6 and 7) agreed reasonably well with dissipation rates estimated from ADV measurements ($\varepsilon_{\mathrm{ADV}}$) over nearly three orders of magnitude (Figure 7a). The predicted values slightly underestimated dissipation rates in the higher range of the data. Considering only data for which the wind direction was along the river (151° $\leqslant w_{\mathrm{dir}} \leqslant 190°$ and $290° \leqslant w_{\mathrm{dir}} \leqslant 323°$) did not improve the agreement significantly (a two-sample Kolmogorov-Smirnov test showed no significant difference between them) (Figure 7b). The average ratio of predicted and observed dissipation rates was $\mu = 1.2$ in both cases.
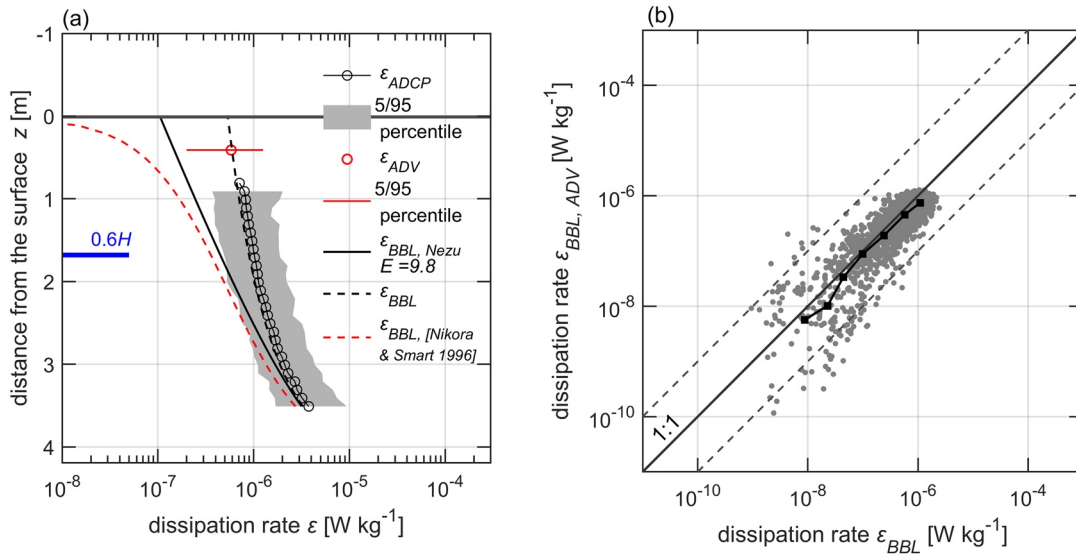
Figure 6. (a) Temporarily averaged dissipation rate profiles during conditions at which bed shear stress was expected to dominate turbulent dissipation near the water surface: the black line with open circles shows dissipation rates obtained by inertial subrange fitting from ADCP measurements (ε_{ADCP}, number of data points at 1 m distance above the bed: 53). The gray area marks the 5th to 95th percentile range of the data. The empty red circle shows the mean dissipation rate (and percentile range) estimated by inertial subrange fitting of ADV measurements (ε_{ADV}). The solid black line represents $\varepsilon_{BBL, Nezu}$ (Equation 11), the dashed black line represents ε_{BBL} (Equation 10) and dashed red line represents $\varepsilon_{BBL, NS}$ (Equation 12). For ε_{ADCP} we considered only those profiles which have at least 80% data in vertical direction and at least 20 time intervals. The thick horizontal line marks the water surface. The thick blue line corresponds to the depth up to which the logarithmic velocity law is valid (0.6 of water depth H). (b) Dissipation rates at 0.4 m water depth estimated from mean flow velocities measured by ADV ($\varepsilon_{BBL,ADV}$, Equation 16) versus dissipation rates estimated from shear stresses obtained from ADCP data (ε_{BBL}, Equation 10). The black line with square symbols shows bin-averaged data. Number of data points in the plot is 1714. The solid gray line shows the 1:1 relationship and two dashed lines indicate differences of one order of magnitude.

Dissipation rates estimated from measured momentum fluxes by the EC system ($\varepsilon_{SBL,EC}$, Equation 8) exceeded observed dissipation rates by a factor of five on average (Figure 8a). The large difference between the two dissipation rates estimated from atmospheric forcing were related to the difference between measured wind friction velocity and that estimated from mean wind speed in the bulk scaling (Figure 8b), with the latter
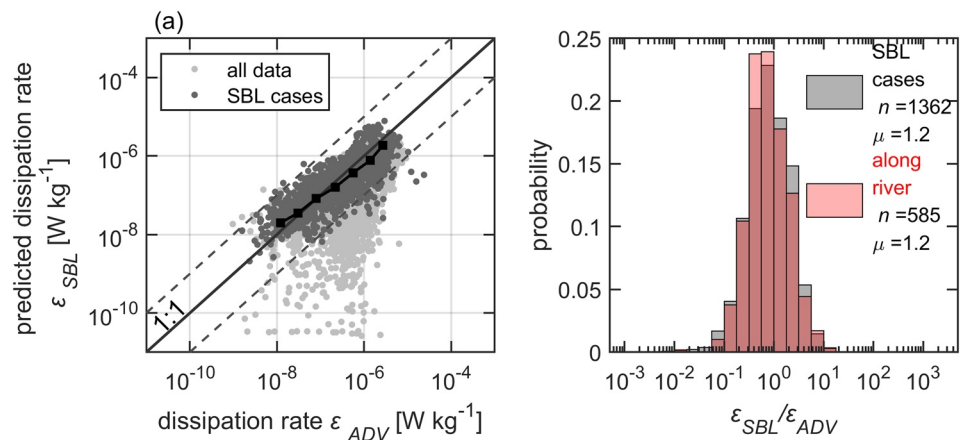

Figure 7. (a) Predicted dissipation rate of turbulent kinetic energy from bulk meteorological forcing ε_{SBL} versus observed dissipation rate ε_{ADV} at 0.4 m water depth. Light gray symbols show all data, dark gray symbols mark data for the selected cases for which near-surface turbulence was driven by atmospheric forcing (SBL cases). The black line with square symbols shows bin-averaged selected data. The solid gray line shows the 1:1 relation and two dashed lines indicate differences of one order of magnitude. (b) Probability distributions (bar graphs) of the ratio of ε_{SBL} and ε_{ADV} for all data with predominant atmospheric forcing (gray), and for the subset of this selection for which the wind directions were along the river ($151° \leqslant w_{dir} \leqslant 190°$ and $290° \leqslant w_{dir} \leqslant 323°$) (red). The number of data points n and the mean values μ of both distributions are provided in the legend.
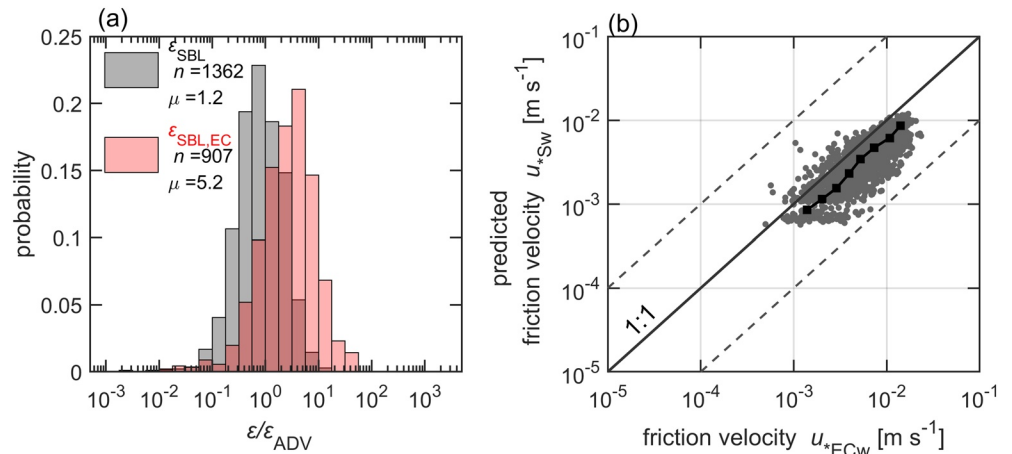
Figure 8. (a) Probability distributions (bar charts) of the ratio of dissipation rates estimated from atmospheric forcing and dissipation rates computed from measurements at 0.4 m depth. The gray bars show the distribution for bulk scaling (ε_{SBL}, Equations 6 and 7) and the red chart shows the ratio for dissipation rates estimated from measured momentum fluxes by the eddy covariance system ($\varepsilon_{SBL, EC}$, Equation 8). Only selected data for periods when atmospheric forcing is expected to dominate near-surface turbulence are shown. The number of data points n and mean values of the ratio μ are shown in the legend. (b) Measured wind friction velocity by EC u_{*ECw} versus predicted friction velocity calculated from the bulk approach u_{*Sw}. The solid black line indicates a bin-average of the data, the gray solid line shows a 1:1 ratio and the two gray dashed lines represent one order of magnitude difference.

being consistently smaller than those derived from measurements. The agreement between the measured and predicted friction velocities was not improved if only wind directions along the river were considered.

We additionally tested a scaling relation for near-surface dissipation rates under breaking surface waves proposed for large lakes (Wang et al., 2013, 2015) (see Appendix A for details). We estimated the dissipation rate by taking measured significant wave height into account (see Appendix A, Figure S9a in Supporting Information S1). In comparison to dissipation rates predicted from bulk atmospheric forcing (ε_{SBL}), the wave scaling (ε_{wave}) did not improve the prediction quality (mean value of the ratio of ε_{wave} and ε_{ADV} $\mu = 0.1$, see, Figure S9b in Supporting Information S1). On average, ADV dissipation rates were a factor of 10 higher than the prediction ε_{wave}. The wave contribution to the dissipation rate was small due to much larger relative depth (depth of the dissipation rate measurements over the significant wave height) than in the former observations made in large lakes.

Table 4
Relative Contribution of Different Forcing Mechanisms to Near-Surface Dissipation Rates (0.4 m depth)

Dominance of:	Wind, buoyancy flux and mean flow	Wind and mean flow
$\varepsilon_{SBL,wind}$	$n = 5564$	$n = 7199$
	44%	60%
$\varepsilon_{SBL,buoy}$	$n = 1839$	
	15%	
ε_{BBL}	$n = 5081$	$n = 6266$
	40%	40%
Total amount of data	$n = 12,646$	$n = 13,465$
	100%	100%

Note. As an indicator for the dominating forcing mechanism, the first column shows the predicted dissipation with the maximum magnitude: ε_{SBL}, wind estimated from wind speed, ε_{SBL}, buoy estimated from buoyancy flux and ε_{BBL} estimated from mean flow velocity. n is a number of observations (10 min sampling intervals) and percentages refer to relative occurrence during the observational period. The second column shows the relative contributions of wind and mean flow velocity with disregarding the buoyancy flux.

3.4. Relative Importance of Atmospheric Forcing and Bottom-Generated Turbulence

To evaluate the relative contributions of different generation mechanisms to turbulence near the water surface, we classified all 10 min data segments throughout the observational period according to the highest values of predicted dissipation rates at 0.4 m water depth. For this analysis we used dissipation rates estimated from mean flow velocity observed by the ADV ($\varepsilon_{BBL,ADV}$) and from bulk atmospheric forcing ($\varepsilon_{SBL,wind}$, $\varepsilon_{SBL, buoy}$). Conditions for which $\varepsilon_{BBL, ADV}$ was larger than $\varepsilon_{SBL,wind}$ and $\varepsilon_{SBL, buoy}$, but smaller than their sum, were only 1% of total cases and are not included in further analyses.

Between June and September bottom-generated turbulence dominated for 40% of the time, wind 44%, and convective cooling 15% of the time (Table 4). Despite the large scatter of individual 10-min estimates, bin-averaged dissipation rates predicted from mean flow velocity and atmospheric forcing agree well with our observations ($\rho = 0.5$, $p < 0.05$,
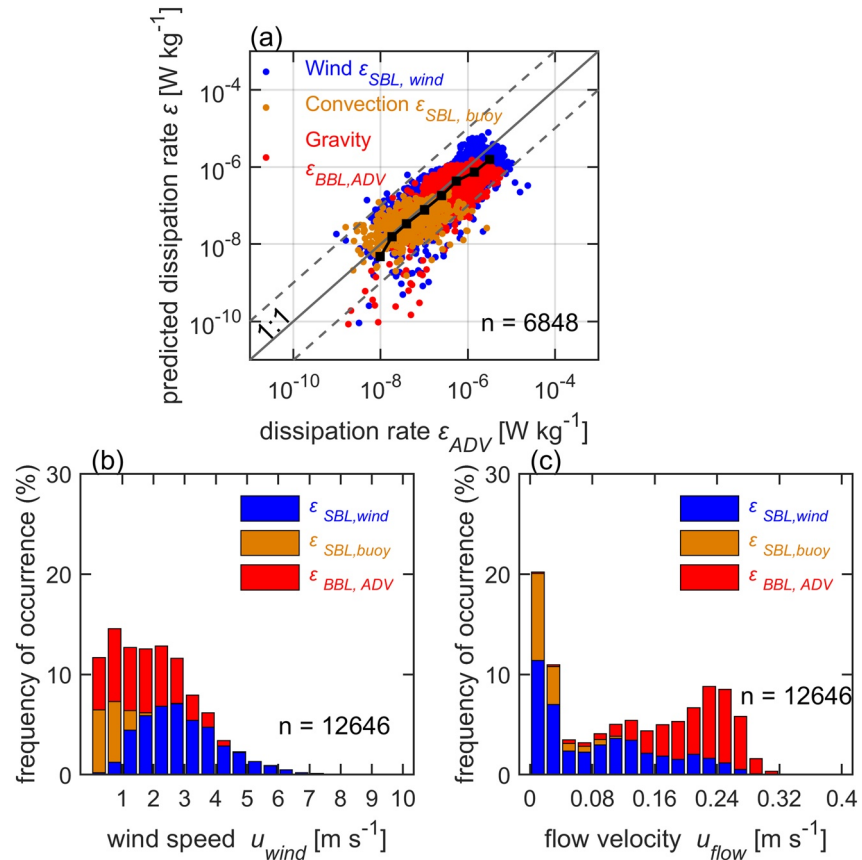
Figure 9. (a) Predicted dissipation rates of turbulent kinetic energy at 0.4 m water depth vs. observed values ε_{ADV} (n = 6,848 number of the data points resulted from the intersection of the ADV dissipation rate measurements (7,452) and combined predicted dissipation rate). Predictions are based on wind speed $\varepsilon_{SBL,wind}$ and buoyancy flux $\varepsilon_{SBL,buoy}$ if atmospheric forcing was the dominant driver of the near surface turbulence (blue and orange symbols, respectively). The predictions are based on bottom-boundary layer scaling estimated from mean flow velocity $\varepsilon_{BBL,ADV}$ when the bottom-generated turbulence was dominant (red symbols). The dominant forcing mechanism was identified as the largest value of the three predictions. The black line with square symbols indicates bin-averaged data over all forcing conditions. The solid gray line shows a 1:1 relation, dashed lines represent a one order of magnitude difference. The symbols are partly overlapping, red and orange were plotted on top of blue. (b) Relative frequency of occurrence of dominant forcing conditions as a function of wind speed and (c) mean flow velocity. n indicates number of data points.

Figure 9a). The mean ratio of predicted and observed dissipation rates was 1.0. We additionally estimated the relative contributions of turbulence from wind speed and from gravity-generated flows, while disregarding buoyancy flux which is not always available in all studies. In this analysis we predicted the dissipation rate at 0.4 m water depth either from Equation 16 or (6), depending on which of both predictions was higher. The statistics of the dominant forcing mechanisms changed only slightly. Wind- and bottom-generated turbulence dominated in 53% and 47% of total time, respectively (Table 4).

Wind shear affected near-surface dissipation rates for wind speeds greater than 1 m s^{-1} and was the dominant mechanism for wind speeds exceeding 3 m s^{-1} (Figure 9b). When the flow velocity exceeded 9–10 cm s^{-1}, the bottom-generated turbulence dominated the near surface energy dissipation (Figure 9c). The contribution of the buoyancy flux was important at night, when the convective cooling coincided with low flow velocity and low wind speed. It was the most frequent cause of turbulence at wind speeds less than 2 m s^{-1} and flow velocities less than 9–10 cm s^{-1}.

The effect of thermal stratification is not included in the scaling approaches that we used to estimate near-surface dissipation rates from bulk forcing variables. To test its importance, we comparing the probability distributions of the ratio of predicted and observed dissipation rates for cases with and without thermal stratification (temperature difference > 0.05°C). Except for periods of convective cooling, stratification

did not change the agreement between predictions and observations significantly (mean value of the ratio differed by less than 20%). In the rare case of convective turbulence in the presence of thermal stratification (3% of the observational period), the predictions based on buoyancy flux overestimated observed dissipation rates by 40% on average (Figure S10b in Supporting Information S1).

To test the effect of wind direction relative to the flow direction on near-surface dissipation rates, we separated the data into cases when the wind directions was along the longitudinal river flow direction ($290° \leqslant w_{dir} \leqslant 323°$) and against ($151° \leqslant w_{dir} \leqslant 190°$). Significant differences between predictions and observations were found between both cases, if wind or gravity was the dominant forcing mechanism (Figure S11 in Supporting Information S1). For wind-generated turbulence, the predictions underestimated near-surface dissipation rates by 10% for the periods when wind direction was along river flow in comparison to the periods when the wind direction was against the river flow. When bottom-generated turbulence was dominant, the predicted dissipation rates were lower than observed values by 10% and 20% for wind direction against and along the river, respectively.

3.5. Effect of Water Depth

To assess the extent to which dominant controls depend on water depth as well as on the distance below the surface, at which dissipation rates are evaluated, we calculated the ratio of dissipation rates resulting from bed friction (Equation 16) and from wind forcing (Equation 6). We derived a "critical" wind speed, for which both dissipation rates are equal, that is, for wind speeds greater than the critical wind speed, wind is the dominant forcing of near-surface turbulence:

$$u_{\text{wind crit}} = \bar{u}_{\text{flow}} \frac{1}{C_1} \left(\frac{\rho_w}{\rho_a} \right)^{\frac{1}{2}} \left(\frac{C_{Dw}}{C_{Da}} \right)^{\frac{1}{2}} \left(\frac{z}{H-z} \right)^{\frac{1}{3}}. \tag{17}$$

Note, that we did not consider the cases where buoyancy-driven turbulence dominated because we assumed its contribution was not significant in time. This equation is not accurate during stable density stratification (see Figure S10 in Supporting Information S1).

We calculated the critical wind speed $u_{\text{wind crit}}$ for the depth of 0.4 m using estimated for this depth the drag coefficient (ADV measurements). For the water depth at our sampling site of 4.2 m, $u_{\text{wind crit}}$ increased from 1 to 7.2 m s^{-1} for mean flow velocities between 0.1 and 0.35 m s^{-1}. For a flow velocity of 0.35 m s^{-1}, the critical wind speed decreases from 13.4 m s^{-1} for a flow depth of 1–2.4 m s^{-1} for 100 m depth (Figure 10a).

The critical wind speed increases strongly with increasing depth at which wind and bottom-generated turbulence are compared. Using Equation 17, we computed the mean critical wind speed as a function sampling depth below the surface for the range of observed mean flow velocities (at 1 m above the river bed). At the ADV sampling depth (0.4 m below the surface), the mean critical wind is a factor of 6.8 higher compared to $u_{\text{wind crit}}$ estimated for a sampling depth of 1 mm below the surface. This depth corresponds to the Kolmogorov microscale of turbulence $L_k = (v^3/\varepsilon)^{\frac{1}{4}}$, which defines the thickness of a viscous sublayer at the water surface and the depth at which turbulent energy dissipation rates are maximal (Lorke & Peeters, 2006). The value of the Kolmogorov microscale was calculated from the the log-averaged value of the observed dissipation rates at 0.4 m depth.

3.6. Verification of Equilibrium Between Production and Dissipation of TKE

We used the numerical 1D $k - \varepsilon$ model to validate the assumption of local equilibrium between production and dissipation rates of turbulent kinetic energy (Equation 2). The model includes the effects of wind (excluding surface waves), river flow and vertical heat transport on turbulence throughout the water column. In general, results from the $k - \varepsilon$ model showed good agreement with observed dissipation rates at 0.4 m water depth ($\rho = 0.5$, $p < 0.05$, Figure S12 in Supporting Information S1). However, there was a systematic difference at lower dissipation rates, for which the $k - \varepsilon$ model underestimated the dissipation rates by up to a factor of 5–10 on average. On average, the model slightly underestimated the dissipation rate at 0.4 m water depth by 10% (Figure S12b in Supporting Information S1). The results of the model revealed that
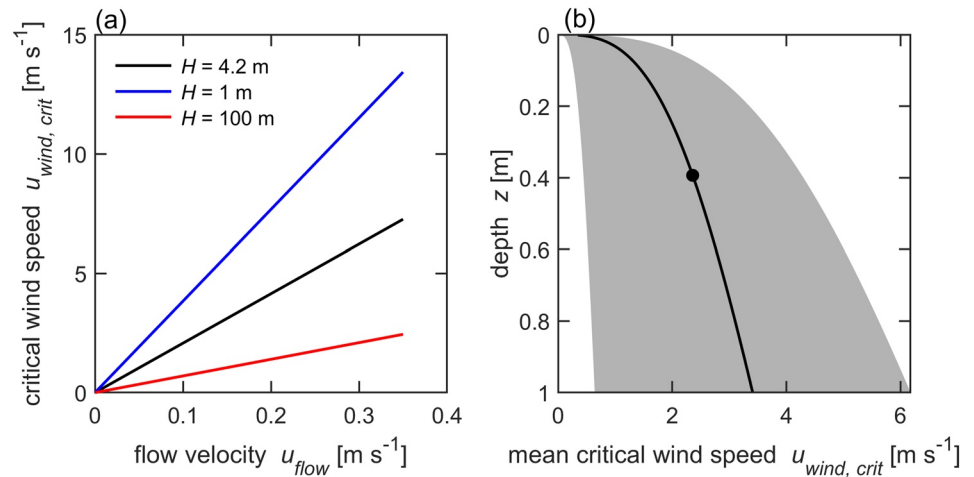
Figure 10. (a) Critical wind speed, above which near-surface turbulence is dominated by wind forcing (Equation 17 with the drag coefficient estimated for the depth of 0.4 m $C_{\mathrm{Dw}} = 0.0015$) versus mean flow velocity for water depths H of 4.2 m (black line), 1 m (blue line), 100 m (red line). The depth at which wind- and bottom-generated dissipation rates are compared is 0.4 m (ADV sampling depth). (b) Vertical distribution of mean critical wind speed (black line) calculated for the mean flow velocity observed at 1 m above the bed. The drag coefficient corresponded to 1 m above the bed $C_{\mathrm{Dw}} = 0.002$. The gray area encompasses the range of measured mean flow velocities (plus/minus one standard deviation). The black circle marks the depth of 0.4 m for which the critical wind speed in panel (a) was estimated. The uppermost depth corresponds to the lower edge of the viscous sublayer (equal to the mean Kolmogorov microscale of 1 mm).

TKE production was balanced by dissipation during most of the observational period. Only for 13% and 2% of the total data (1,463 and 166 10-min periods), turbulent transport of TKE (terms [2, 3] in Equation 1), and TKE tendency (term [1]) were larger than the sum of the production terms (terms [6,7]), respectively (Figure 11a). Disregarding data from time periods when the model predicted significant contributions of TKE transport or unsteadiness did not improve the agreement between dissipation rates obtained from measurements and from bulk forcing variables (Figure 11b). The mean value of the transport terms was
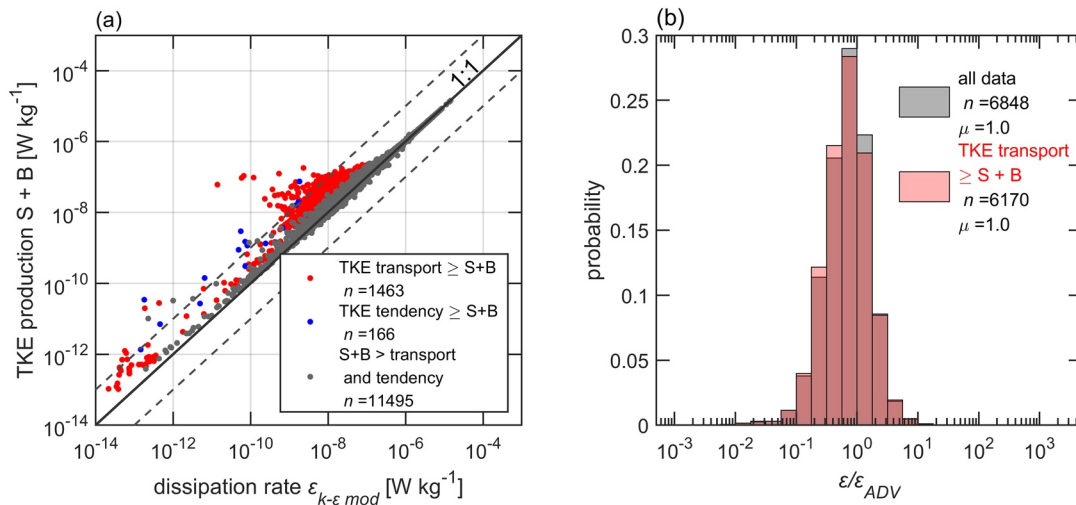

Figure 11. (a) Sum of production rates turbulent kinetic energy (TKE) by mean shear (S) and buoyancy flux (B) vs. TKE dissipation rates (Equation 1) simulated by the $k - \varepsilon$ model. Gray dots (11,495 data points) show cases for which local TKE production rates was the dominant source of dissipated energy. Red and blue dots represent the cases when turbulent transport of TKE (1,463 data points) or TKE tendency (166 data points) exceeded the sum of the two production terms. (b) Probability distributions of the ratio of predicted and observed dissipation rates $\varepsilon_{\mathrm{ADV}}$. Gray bars correspond to the ratio of the predicted dissipation rates from bulk approaches ($\varepsilon_{\mathrm{SBL}}$, $\varepsilon_{\mathrm{BBL}}$) and $\varepsilon_{\mathrm{ADV}}$, red bars show the same ratio but without the data for which TKE production and dissipation were not in balance (marked by blue or red color in [a]). The respective number of data points (n, also in [a]) and the mean value (μ) of the ratio are shown the legend.

equal to $4.3 \cdot 10^{-9}$ [W kg^{-1}], which was smaller than most of our measured dissipation rates (ε_{ADV} was less than this value only in 1% of the total number of measurements). These findings validate the assumption of a local equilibrium between TKE production and dissipation, which we made for inertial subrange fitting and bulk approaches.

Surface water temperature was slightly underestimated by the $k - \varepsilon$ model, with a mean difference between modeled and observed temperature of $-0.8°C$ (Figure S13 in Supporting Information S1). The inaccuracies in prediction of dissipation rate occurred when the water was stratified (Figure S12a in Supporting Information S1). The modeled flow velocity profile (Figure S14 in Supporting Information S1) was characterized by the patterns of flow regulation similar to what was observed.

4. Discussion

4.1. Magnitude, Drivers and Dynamics of Near-Surface Turbulence

Our measurements are the first to identify the dominant forcing mechanisms of near-surface turbulence in a large regulated river and their dynamics from minutes to seasonal time scales. Bed friction of gravity-driven flow and wind shear were nearly equally important forcing mechanisms and made dominant contributions to near-surface energy dissipation during 40% and 44% of the observational period, respectively. Convective cooling dominated energy dissipation rates only during 15% of the time. The temporal dynamics resulted from diel variability in wind speed, buoyancy flux and flow velocity. The latter was strongly affected by flow regulation. The nocturnal reduction of flow velocity due to demand-following hydropower production was frequently associated with a transition from the dominance of bottom-generated turbulence to atmospheric forcing and a change of the water body from a lotic to a more lentic-like system.

With a Strahler stream order of 5 and a width of approximately 100 m at the study site, the River Kitinen belongs to the class of moderately sized rivers (orders 5–9), which contribute the largest surface area globally, with less area covered by lower and higher order streams (Downing et al., 2012). Despite their widespread distribution, turbulence measurements in such rivers are rare. In the River Kitinen, dissipation rates of turbulent kinetic energy varied over five orders of magnitude 10^{-10} and 10^{-5} W kg^{-1} during the ice-free season, with a log-averaged mean value of $4.2 \cdot 10^{-7}$ W kg^{-1}. This range is comparable to dissipation rates reported from shorter-term observations in a river of similar size in Germany (Lorke et al., 2012). In low-order streams, dissipation rates can be up to four orders of magnitude higher (Kokic et al., 2018), similiar to tidal estuaries where dissipation estimates rates range from 10^{-6}–10^{-4} W kg^{-1} (Chickadel et al., 2011; Zappa et al., 2007). The comparably low dissipation rates in the River Kitinen were similar in magnitude to dissipation rates observed in the near-surface layer of lakes, where they typically vary between 10^{-9} and 10^{-5} W kg^{-1} (Tedford et al., 2014; Wüest & Lorke, 2003).

Our study also showed that the contribution of surface waves to dissipation rates was insignificant, probably due to the small amplitude of the observed waves. Wind direction relative to the flow influenced dissipation rates only up to 10%, which is within the error of the measurements. Weak thermal stratification caused a slight suppression of turbulence. This result is in contrast to observations in a strongly stratified estuary, where wind was identified as the primary driver of near-surface turbulence. In these studies, turbulence from bed friction was attenuated by vertical density stratification caused by seawater intrusions (Orton, McGillis, & Zappa, 2010; Orton, Zappa, & McGillis, 2010).

4.2. Scaling and Modeling Near-Surface Turbulence

When atmospheric forcing dominated, near-surface dissipation rates followed a similarity scaling, as it been found in lakes and oceans (Lombardo & Gregg, 1989; Tedford et al., 2014) and could be well predicted from bulk parameters, including wind speed and surface buoyancy flux. Similarly, bottom-generated turbulence followed boundary-layer scaling and its vertical distribution could be well predicted from mean flow velocity after adjusting the bed roughness coefficient. Surprisingly, our observations showed that the vertical decline of bottom-generated turbulence was better described by the law-of-the-wall scaling, which is based on the assumption of a constant shear stress. This finding was in contrast to studies (Nezu, 1977; Nikora & Smart, 1996) in which empirical and theoretical approaches in open-channel flows are commonly applied.

The latter approaches have been found to agree well with vertical profiles of dissipation rates measured in smaller rivers (Sukhodolov et al., 1998) and in laboratory flumes (Johnson & Cowen, 2017; Nezu & Rodi, 1986). By combining both approaches for atmospheric and bottom-generated turbulence, we obtained a good prediction of near-surface dissipation rates as a function of bulk atmospheric forcing and mean flow velocity (Figure 9). Although the scatter of individual (10-min based) dissipation rates is large, bin-averaged data revealed an unbiased agreement between prediction and observation.

To assess the relative importance of bottom- and wind generated turbulence in rivers of arbitrary depth, we defined a critical wind speed, derived with the assumption that at some depth the surface boundary-induced turbulence is equal to the bottom boundary-induced turbulence. We combined both boundary-layer scaling approaches and derived an expression for the critical wind speed as a function of mean flow velocity and water depth (Equation 17). For wind speeds exceeding this critical value, near-surface turbulence is expected to be controlled by wind, in contrast to the predominance of bed friction for wind speed below the the critical value.

In addition to bulk forcing and water depth, the relative importance of wind and bottom-generated turbulence depends strongly on the distance from the surface at which turbulence is observed. Particularly, wind-generated turbulence declines below the water surface and dissipation rates are expected to be highest at the base of the viscous sublayer at the water surface (Lorke & Peeters, 2006). As in most field observations of near-surface turbulence, the distance below the water surface at which turbulence was observed (0.4 m) was limited by the physical dimension of the velocimeter. Spatially resolving measurements of turbulence in the wind-mixed surface layer of a lake using particle image velocimetry, confirmed the existence of a power-law decline of dissipation rates, even within the uppermost centimeter of the water column (Wang et al., 2013). The relative importance of wind or flow generated turbulence can be estimated as a function of distance from the water surface using law-of-the-wall scaling (Equation 17).

A 1D $k - \varepsilon$ model for rivers has been applied to quantify the turbulence throughout the water column. Despite the higher numerical complexity and more comprehensive physics compared to bulk approaches, the $k - \varepsilon$ model results did not demonstrate substantial improvement in simulating subsurface dissipation rates compared to the similarity-based estimates. The model results were comparable to surface similarity scaling when the atmospheric forcing was dominant, because the top boundary condition used in he model is of the same type as that used in the scaling. When the turbulence was dominated by bed friction, the $k - \varepsilon$ model slightly underestimated the dissipation rates. This result should be interpreted with caution, since the dissipation rate measurements contain significant uncertainties themselves (discussed below). The discrepancies may also result from the well-known knowledge gaps in the construction of optimal two-parameter (e.g., $k - \varepsilon$) turbulence closures, namely, specification of stability functions and non-dimensional constants (Mortikov et al., 2019), setup of the surface boundary conditions (Burchard, 2002), and inclusion of TKE production by wave-induced motions (Ghantous & Babanin, 2014), to mention a few. This study also indicates, that model improvements will need to address the overestimation of solar heating below the water column top (and corresponding diminishing of turbulence) under low wind and flow speed conditions.

4.3. Uncertainties in Dissipation Rate Estimates

The unique longer-term observations of near-surface TKE dissipation rates were obtained by invoking a number of rigorous assumptions and simplifications. The most complete data set was obtained from the ADV observations at a fixed depth of 0.4 m below the water surface. While we aimed at estimating dissipation rates in close proximity to the water surface, the sampling depth of the ADV was limited by deployment considerations, which ensured that the transducer head remained submerged below the water surface also in the presence of wind-generated waves. The ADCP measurements provided support for choosing a relationship describing the vertical profile of turbulence generated by bed friction, although the sampling volume of the ADCP was three orders of magnitude larger than that of the ADV. This limitation, an addition to the undetermined isotropy constant for the radial along-beam velocities (Lorke & Wüest, 2005), made the ADCP measurements less favorable for estimating dissipation rates near the water surface.

Dissipation rates were estimated from measured flow velocities and bulk scaling approaches by assuming a simplified balance of turbulent kinetic energy, in which production and dissipation are in equilibrium.

In studies of bottom-generated turbulence in rivers with high flow speeds this assumption is challenged by theoretical considerations (Nezu & Nakagawa, 1993) and by observations (Scully et al., 2011; Talke et al., 2013). In these cases, energy dissipation rates near the water surface exceeded local production rates and were balanced by upward transport of TKE from the near-bed region. We tested whether such vertical transport would occur for the flow conditions in the Kitinen River using the $k - \varepsilon$ model. Results indicated that TKE transport and unsteadiness of the TKE balance (TKE tendency) were small compared to TKE production near the surface by shear and buoyancy flux and the near-equal dissipation rates. This finding was true for 85% of the observational period. Disregarding observations from the brief periods when the simulations showed significant contributions from turbulent transport and TKE tendency did not improve the predictions based on bulk approaches (Figure 11).

Our results differ from those in the more energetic tidal rivers. In these, dissipation rates were about two order of magnitude higher than in the Kitinen River and vertical TKE flux divergence was observed (Scully et al., 2011; Talke et al., 2013). At these energetic sites, coherent flow structures enhanced TKE transport from the river bed to the surface (Talke et al., 2013). Such coherent structures, or boils, consist of localized upwelling motions which constantly disrupt the water surface. While these structures cannot be resolved by the one-dimensional $k - \varepsilon$ model, energetic boils were not observed visually in our velocity measurements. TKE divergence due to larger-scale vertical motions would not affect the presence of an inertial subrange in spectra of near-surface velocity fluctuations (Flores et al., 2017; Scully et al., 2011; Talke et al., 2013). However, bulk scaling approaches relying on the law-of-the-wall would not apply (Equations 10 and 12), which is in contrary to our observations.

The validity of our estimates of dissipation rates also requires that the turbulence be isotropic over the range in which we did our calculation. In energetic river flows, anisotropy has been found near the water surface where vertical velocity fluctuations can be suppressed. However, both observations (Talke et al., 2013) and direct numerical simulations (Flores et al., 2017) show that an inertial subrange, exists for the horizontal velocity components near the free water surface. Within an integral length (corresponding to the distance from the boundary), the flow has adjusted to isotropic turbulence and dissipation rates can be obtained from vertical velocity fluctuations using the inertial dissipation method. We validated that the flow was isotropic based on comparisons of dissipation rates of the three components of velocity when the noise in the horizontal velocities was low enough for the measurement to be conducted (Figure S3 in Supporting Information S1). By bounding the lower limit of the wave number range that we used for inertial subrange fitting by that corresponding to the ADV sampling depth (0.4 m), we excluded the larger anisotropic scales. The vertical velocity component was used in analysis due to its lower noise.

Estimates of dissipation rates using the inertial dissipation method have been found to be in good agreement with those obtained from other estimation techniques (e.g., the structure function method McMillan & Hay, 2017, temperature microstructure measurements Lorke & Wüest, 2005 and direct dissipation estimates from particle image velocimetry Wang et al., 2013), over a wide range of boundary-layer flows. The cumulative uncertainties in the measurement related to dissipation rates has been estimated to be within a factor of two (Moum et al., 1995). Bin-averaged dissipation rates predicted using bulk scaling approaches generally agreed with the measurements within a factor of two (e.g., Figures 6b, 7a and 9a). For further understanding of processes affecting near-surface dissipation rate in regulated rivers, future studies should include measurements to resolve additional components of the TKE budget (such as in Talke et al., 2013), and explore the application of optical remote sensing of surface flow structures for improved identification of coherent structures (Branch et al., 2021).

4.4. Implications for Gas Exchange in Regulated Rivers

Near-surface turbulence constitutes the primary control on the gas transfer velocity (k_g) at the air-water interface (MacIntyre et al., 2010; Zappa et al., 2007). k_g is related to the dissipation rate of turbulent kinetic energy as $k_g = c_1(\varepsilon \nu)^{1/4} Sc^{-1/2}$, where Sc is a Schmidt number, c_1 is a scaling parameter (Lamont & Scott, 1970). The mean observed dissipation rate of $4.2 \cdot 10^{-7}$ W kg^{-1} corresponds to the normalized value of k_{600} (i.e., for $Sc = 600$) of 1.5 m d^{-1} (using $c_1 = 0.5$ MacIntyre et al., 2010). This gas transfer velocity is approximately 4 times lower than what has been used for a river with Strahler order of 5 in a global analysis of inland water CO_2 emissions (Raymond et al., 2013). Moreover, the range of variability of dissipation rates

spanned four orders of magnitude, which corresponds to temporal variations in k_g of one order of magnitude (0.3–4 m d^{-1}), with most of the variability occurring at a diel time scale. As dissolved gas concentrations also often show diel variations in response to light and temperature, the diel variability of gas fluxes to the atmosphere can be amplified or attenuated, depending on the superposition of both cycles. To the best of our knowledge, direct measurements of gas fluxes from rivers using floating chamber or tracer methods have been conducted during daytime, which can potentially result in a significant bias if these fluxes are assumed to present daily or longer-term mean values in larger-scale estimates. To date, temporal variability of the gas transfer velocity has not been resolved in larger-scale models of riverine CO_2 emissions, where the gas transfer velocity is typically considered as constant for a stream segment or reach (Magin et al., 2017; Raymond et al., 2013; Lauerwald et al., 2015). Future field observations and modeling efforts are required to analyze the extent to which diel variability may affect longer-term emission rates.

Alin et al., (2011) suggested a conceptual scheme for the transition of the physical control of gas transfer velocities and fluxes in river systems from the dominance of wind control in estuaries and large rivers toward increasing importance of water current velocity and depth at progressively lower stream orders. Our findings confirm this scheme, with the Kitinen River being located in the transition zone, where wind and water currents are of nearly equal importance. Moreover, we provide a quantitative evaluation of this concept, by combining scaling relations for energy dissipation rates generated by wind and water currents as a function of river depth. Our concept of a critical wind speed can be used to separate the two physical forcing regimes and to estimate near-surface dissipation rates and corresponding gas transfer velocities from mean flow velocity or from wind speed.

The temporal dynamics of the near-surface turbulence were strongly affected by flow regulation. Demand-following hydropower generation resulted in diel changes of flow velocity from 0.2–0.3 m s^{-1} during daytime to some mm s^{-1} at night, changing the physical characteristics of the river from lotic to lentic. As the majority of river systems are affected by flow regulation (Grill et al., 2019), this situation can probably considered as typical. Flow regulation has been shown to decrease flow variability at seasonal scales by homogenization of river discharge (Poff et al., 2007; Long et al., 2019). The effect of flow regulation on shorter, including diel time scales has received comparably less attention. In the regulated river Saar in central Europe, diel variations in flow velocity have been shown to modulate the oxygen flux into the river bed by a factor of two (Lorke et al., 2012). The availability of oxygen in river sediment can be expected to affect mineralization rates and the production of greenhouse gases. Therefore, flow regulation not only modulates near-surface turbulence and, therewith the temporal dynamics of gas fluxes, it may additionally affect the total amount of greenhouse gases emitted from rivers. Despite its global relevance, this potential implication has not been explored and should be addressed in future studies. Such studies can be based on the scaling approaches or on the 1D $k - \varepsilon$ model, which can be combined with biogeochemical models for water and sediment as has also been done for lakes at regional scales (e.g., Sabrekov et al., 2017). These models can be used to explore and to optimize management strategies for flow regulation, that can potentially mitigate adverse effects of river damming on greenhouse gas emissions.

5. Conclusion

Our study provides the first continuous turbulence measurements in a large regulated river. We found nearly equal contributions from atmospheric forcing and bottom-generated turbulence to near-surface dissipation rates with wind being the dominant driver for wind speeds exceeding 3 ms^{-1}, and bottom-generated shear when flow speeds exceeded 0.09–0.1 ms^{-1}. After validation of individual scaling approaches, we developed a scaling approach to quantify the dominant forcing mechanism (wind or flow) using a critical value of the wind speed, which depends on mean flow velocity and flow depth. As flow regulation proved to be important for the temporal dynamics of the near-surface turbulence, future studies should address the implications of daily and sub-daily flow variations on both the temporal dynamics of fluxes and biogeochemical cycling in such rivers.

Appendix A: Wave-Breaking Scaling

Based on measurements in large lakes and in the coastal ocean, Terray et al. (1996); Feddersen et al. (2007) proposed the following scaling for near-surface dissipation rates under breaking surface waves in deep water:

$$\frac{\varepsilon_{\text{wave}} H_{\text{sign}}}{\alpha (u_{*\text{Sw}})^3} = \beta \left(\frac{z}{H_{\text{sign}}} \right)^m, \tag{A1}$$

where z is the distance from the water surface, H_{sign} is the significant wave height, $\alpha \sim c_p/u_{*\text{Sw}}$ (where c_p is the wave phase speed) is a coefficient which has been found in (Feddersen et al., 2007) equal to 250 for the coastal ocean, $\beta = 0.3$ and $m = -2$ are the constants. However, measurements conducted by (Wang et al., 2013, 2015) in a large lake suggested scaling constants of $\beta = 0.04$, $m = -0.73$ within the top layer of water column.

We obtained α and m using a linear regression model for filtered data with wind speed exceeding 1 m s^{-1} and wind directions along the river (see Figure S9a in Supporting Information S1). The friction velocity $u_{*\text{Sw}}$ was calculated from from mean wind speed. We found $\alpha = 54$ and $m = -0.9$ which were close to the result in (Wang et al., 2013, 2015). With these values we estimated the dissipation rate including the effect of waves $\varepsilon_{\text{wave}}$ using Equation A2:

$$\varepsilon_{\text{wave}} = \beta \alpha (u_{*\text{Sw}})^3 \frac{H_{\text{sign}}}{z^2}. \tag{A2}$$

Conflict of Interest

The authors declare no conflicts of interest relevant to this study.

Data Availability Statement

The data used in this study is available at the Mendeley repository Guseva et al., 2020 [doi: 10.17632/jnbx-wyybcn.2]. We are grateful for the scripts provided by Cynthia Bluteau and Galen Charles Egan.

References

Åberg, S. C., Korkka-Niemi, K., Rautio, A., Salonen, V.-P., & Åberg, A. K. (2019). Groundwater recharge/discharge patterns and groundwater–surface water interactions in a sedimentary aquifer along the River Kitinen in Sodankylä, northern Finland. *Boreal Environment Research*, *24*, 155–187.

Alin, S. R., de FátimaRasera, F. L. M., Salimon, C. I., Richey, J. E., Holtgrieve, G. W., Krusche, A. V., & Snidvongs, A. (2011). Physical controls on carbon dioxide transfer velocity and flux in low-gradient river systems and implications for regional carbon budgets. *Journal of Geophysical Research: Biogeosciences*, *116*(G1). https://doi.org/10.1029/2010JG001398

Arcement, G. J., & Schneider, V. R. (1989). *Guide for selecting Manning's roughness coefficients for natural channels and flood plains*. US Government Printing Office.

Aufdenkampe, A. K., Mayorga, E., Raymond, P. A., Melack, J. M., Doney, S. C., Alin, S. R., et al. (2011). Riverine coupling of biogeochemical cycles between land, oceans, and atmosphere. *Frontiers in Ecology and the Environment*, *9*(1), 53–60. https://doi.org/10.1890/100014

Baker, M. A., & Gibson, C. H. (1987). Sampling turbulence in the stratified ocean: Statistical Consequences of strong intermittency. *Journal of Physical Oceanography*, *17*(10), 1817–1836. https://doi.org/10.1175/1520-0485(1987)017<1817:stitso>2.0.co;2

Bluteau, C. E., Jones, N. L., & Ivey, G. N. (2011). Estimating turbulent kinetic energy dissipation using the inertial subrange method in environmental flows. *Limnology and Oceanography: Methods*, *9*(7), 302–321. https://doi.org/10.4319/lom.2011.9.302

Borges, A. V., Darchambeau, F., Teodoru, C. R., Marwick, T. R., Tamooh, F., Geeraert, N., et al. (2015). Globally significant greenhouse-gas emissions from African inland waters. *Nature Geoscience*, *8*(8), 637–642. https://doi.org/10.1038/ngeo2486

Bormans, M., & Webster, I. T. (1997). A mixing criterion for turbid rivers. *Environmental Modelling & Software*, *12*(4), 329–333. https://doi.org/10.1016/S1364-8152(97)00032-7

Bouffard, D., & Wüest, A. (2019). Convection in lakes. *Annual Review of Fluid Mechanics*, *51*, 189–215. https://doi.org/10.1146/annurev-fluid-010518-040506

Branch, R., Horner-Devine, A. R., Chickadel, C. C., Talke, S. A., Clark, D., & Jessup, A. (2021). Surface turbulence reveals riverbed drag coefficient. *Geophysical Research Letters*, *48*(10), e2020GL092326. https://doi.org/10.1029/2020GL092326

Brumer, S. E., Zappa, C. J., Blomquist, B. W., Fairall, C. W., Cifuentes-Lorenzen, A., Edson, J. B., et al. (2017). Wave-related Reynolds number parameterizations of CO$_2$ and DMS transfer velocities. *Geophysical Research Letters*, *44*(19), 9865–9875. https://doi.org/10.1002/2017GL074979

Burchard, H. (2002). *Applied turbulence modelling in marine waters* (Vol. 100). Springer Science & Business Media. https://doi.org/10.1007/3-540-45419-5

Butman, D., & Raymond, P. A. (2011). Significant efflux of carbon dioxide from streams and rivers in the United States. *Nature Geoscience*, *4*(12), 839–842. https://doi.org/10.1038/ngeo1294

Cannon, D. J., & Troy, C. D. (2018). Observations of turbulence and mean flow in the low-energy hypolimnetic boundary layer of a large lake. *Limnology and Oceanography*, *63*(6), 2762–2776. https://doi.org/10.1002/lno.11007

Chickadel, C. C., Talke, S. A., Horner-Devine, A. R., & Jessup, A. T. (2011). Infrared-based measurements of velocity, turbulent kinetic energy, and dissipation at the water surface in a tidal river. *IEEE Geoscience and Remote Sensing Letters*, *8*(5), 849–853. https://doi.org/10.1109/LGRS.2011.2125942

Chow, V. T. (1959). *Open-channel hydraulics*. McGraw-Hill Book Co.

Cole, J. J., Prairie, Y. T., Caraco, N. F., McDowell, W. H., Tranvik, L. J., Striegl, R. G., et al. (2007). Plumbing the global carbon cycle: Integrating inland waters into the terrestrial carbon budget. *Ecosystems*, *10*(1), 172–185. https://doi.org/10.1007/s10021-006-9013-8

Downing, J. A., Cole, J. J., Duarte, C., Middelburg, J. J., Melack, J. M., Prairie, Y. T., et al. (2012). Global abundance and size distribution of streams and rivers. *Inland waters*, *2*(4), 229–236. https://doi.org/10.5268/IW-2.4.502

Feddersen, F., Trowbridge, J. H., & Williams, A., III. (2007). Vertical structure of dissipation in the nearshore. *Journal of Physical Oceanography*, *37*(7), 1764–1777. https://doi.org/10.1175/JPO3098.1

Flores, O., Riley, J. J., & Horner-Devine, A. R. (2017). On the dynamics of turbulence near a free surface. *Journal of Fluid Mechanics*, *821*, 248–265. https://doi.org/10.1017/jfm.2017.209

Foken, T. (2008). *Micrometeorology* (1st ed.). Springer, Berlin, Heidelberg. https://doi.org/10.1007/978-3-540-74666-9

Gerbi, G. P., Trowbridge, J. H., Terray, E. A., Plueddemann, A. J., & Kukulka, T. (2009). Observations of turbulence in the ocean surface boundary layer: Energetics and transport. *Journal of Physical Oceanography*, *39*(5), 1077–1096. https://doi.org/10.1175/2008JPO4044.1

Ghantous, M., & Babanin, A. (2014). One-dimensional modelling of upper ocean mixing by turbulence due to wave orbital motion. *Nonlinear Processes in Geophysics*, *21*(1), 325–338. https://doi.org/10.5194/npg-21-325-2014

Goring, D. G., & Nikora, V. I. (2002). Despiking acoustic doppler velocimeter data. *Journal of Hydraulic Engineering*, *128*(1), 117–126. https://doi.org/10.1061/(asce)0733-9429(2002)128:1(117)

Grill, G., Lehner, B., Thieme, M., Geenen, B., Tickner, D., Antonelli, F., et al. (2019). Mapping the world's free-flowing rivers. *Nature*, *569*(7755), 215–221. https://doi.org/10.1038/s41586-019-1111-9

Guerra, M., & Thomson, J. (2017). Turbulence measurements from five-beam acoustic Doppler current profilers. *Journal of Atmospheric and Oceanic Technology*, *34*(6), 1267–1284. https://doi.org/10.1175/JTECH-D-16-0148.1

Hicks, B. (1972). Some evaluations of drag and bulk transfer coefficients over water bodies of different sizes. *Boundary-Layer Meteorology*, *3*(2), 201–213. https://doi.org/10.1007/BF02033919

Imberger, J. (1985). The diurnal mixed layer. *Limnology and oceanography*, *30*(4), 737–770. https://doi.org/10.4319/lo.1985.30.4.0737

Jabbari, A., Boegman, L., Valipour, R., Wain, D., & Bouffard, D. (2020). Dissipation of turbulent kinetic energy in the oscillating bottom boundary layer of a large shallow lake. *Journal of Atmospheric and Oceanic Technology*, *37*(3), 517–531. https://doi.org/10.1175/JTECH-D-19-0083.1

Johnson, E. D., & Cowen, E. A. (2017). Estimating bed shear stress from remotely measured surface turbulent dissipation fields in open channel flows. *Water Resources Research*, *53*(3), 1982–1996. https://doi.org/10.1002/2016WR018898

Katul, G., & Liu, H. (2017). Multiple mechanisms generate a universal scaling with dissipation for the air-water gas transfer velocity. *Geophysical Research Letters*, *44*(4), 1892–1898. https://doi.org/10.1002/2016GL072256

Kokic, J., Sahlée, E., Sobek, S., Vachon, D., & Wallin, M. B. (2018). High spatial variability of gas transfer velocity in streams revealed by turbulence measurements. *Inland Waters*, *8*(4), 461–473. https://doi.org/10.1080/20442041.2018.1500228

Krause, F. (2011). River management. Technological challenge or conceptual illusion? Salmon weirs and hydroelectric dams on the Kemi River in Northern Finland. In *Implementing environmental and resource management* (pp. 229–248). Springer. https://doi.org/10.1007/978-3-540-77568-3_19

Kundu, P. K., Cohen, I., & Dowling, D. (2010). *Fluid mechanics* (4th ed.). Academic Press.

Lamont, J. C., & Scott, D. (1970). An eddy cell model of mass transfer into the surface of a turbulent liquid. *AIChE Journal*, *16*(4), 513–519. https://doi.org/10.1002/aic.690160403

Lauerwald, R., Laruelle, G. G., Hartmann, J., Ciais, P., & Regnier, P. A. (2015). Spatial patterns in CO_2 evasion from the global river network. *Global Biogeochemical Cycles*, *29*(5), 534–554. https://doi.org/10.1002/2014GB004941

Lehner, B., Verdin, K., & Jarvis, A. (2008). New global hydrography derived from spaceborne elevation data. *Eos, Transactions American Geophysical Union*, *89*(10), 93–94. https://doi.org/10.1029/2008EO100001

Lombardo, C. P., & Gregg, M. C. (1989). Similarity scaling of viscous and thermal dissipation in a convecting surface boundary layer. *Journal of Geophysical Research: Oceans*, *94*(C5), 6273–6284. https://doi.org/10.1029/JC094iC05p06273

Long, L., Ji, D., Liu, D., Yang, Z., & Lorke, A. (2019). Effect of cascading reservoirs on the flow variation and thermal regime in the lower reaches of the Jinsha River. *Water*, *11*(5), 1008. https://doi.org/10.3390/w11051008

Lorke, A., & MacIntyre, S. (2009). The benthic boundary layer (in rivers, lakes, and reservoirs). In G. E. Likens (Ed.), *Encyclopedia of inland waters* (pp. 505–514): Academic Press. https://doi.org/10.1016/B978-012370626-3.00079-X

Lorke, A., McGinnis, D. F., Maeck, A., & Fischer, H. (2012). Effect of ship locking on sediment oxygen uptake in impounded rivers. *Water Resources Research*, *48*(12). https://doi.org/10.1029/2012WR012483

Lorke, A., & Peeters, F. (2006). Toward a Unified Scaling Relation for Interfacial Fluxes. *Journal of Physical Oceanography*, *36*(5), 955–961. https://doi.org/10.1175/JPO2903.1

Lorke, A., & Wüest, A. (2005). Application of coherent ADCP for turbulence measurements in the bottom boundary layer. *Journal of Atmospheric and Oceanic Technology*, *22*(11), 1821–1828. https://doi.org/10.1175/JTECH1813.1

MacIntyre, S., Bastviken, D., Arneborg, L., Crowe, A. T., Karlsson, J., Andersson, A., et al. (2020). Turbulence in a small boreal lake: Consequences for air–water gas exchange. *Limnology and Oceanography*, *66*(3), 827–854. https://doi.org/10.1002/lno.11645

MacIntyre, S., Crowe, A. T., Cortés, A., & Arneborg, L. (2018). Turbulence in a small arctic pond. *Limnology and Oceanography*, *63*(6), 2337–2358. https://doi.org/10.1002/lno.10941

MacIntyre, S., Jonsson, A., Jansson, M., Aberg, J., Turney, D. E., & Miller, S. D. (2010). Buoyancy flux, turbulence, and the gas transfer coefficient in a stratified lake. *Geophysical Research Letters*, *37*(24). https://doi.org/10.1029/2010GL044164

MacIntyre, S., Romero, J. R., & Kling, G. W. (2002). Spatial-temporal variability in surface layer deepening and lateral advection in an embayment of Lake Victoria, East Africa. *Limnology and Oceanography*, *47*(3), 656–671. https://doi.org/10.4319/lo.2002.47.3.0656

MacIntyre, S., Romero, J. R., Silsbe, G. M., & Emery, B. M. (2014). Stratification and horizontal exchange in Lake Victoria, East Africa. *Limnology and Oceanography*, *59*(6), 1805–1838. https://doi.org/10.4319/lo.2014.59.6.1805

Magin, K., Somlai-Haase, C., Schäfer, R. B., & Lorke, A. (2017). Regional-scale lateral carbon transport and CO_2 evasion in temperate stream catchments. *Biogeosciences*, *14*(21), 5003–5014. https://doi.org/10.5194/bg-14-5003-2017

McCaffrey, K., Fox-Kemper, B., Hamlington, P. E., & Thomson, J. (2015). Characterization of turbulence anisotropy, coherence, and intermittency at a prospective tidal energy site: Observational data analysis. *Renewable Energy*, *76*, 441–453. https://doi.org/10.1016/j.renene.2014.11.063

McMillan, J. M., & Hay, A. E. (2017). Spectral and structure function estimates of turbulence dissipation rates in a high-flow tidal channel using broadband ADCPs. *Journal of Atmospheric and Oceanic Technology*, *34*(1), 5–20. https://doi.org/10.1175/JTECH-D-16-0131.1

McMillen, R. T. (1988). An eddy correlation technique with extended applicability to non-simple terrain. *Boundary-Layer Meteorology*, *43*(3), 231–245. https://doi.org/10.1007/BF00128405

Mortikov, E., Glazunov, A., Debolskiy, A., Lykosov, V., & Zilitinkevich, S. (2019). Modeling of the dissipation rate of turbulent kinetic energy. *Doklady Earth Sciences*, *489*(2), 1440–1443. https://doi.org/10.1134/S1028334X19120067

Moum, J. N., Gregg, M. C., Lien, R. C., & Carr, M. E. (1995). Comparison of turbulence kinetic energy dissipation rate estimates from two ocean microstructure profilers. *Journal of Atmospheric and Oceanic Technology*, *12*(2), 346–366. https://doi.org/10.1175/1520-0426(1995)012<0346:cotked>2.0.co;2

Natchimuthu, S., Wallin, M. B., Klemedtsson, L., & Bastviken, D. (2017). Spatio-temporal patterns of stream methane and carbon dioxide emissions in a hemiboreal catchment in Southwest Sweden. *Scientific Reports*, *7*, 39729. https://doi.org/10.1038/srep39729

Neumann, G., & Pierson, W. (1966). *Principles of physical oceanography*. Prentice-Hall.

Nezu, I. (1977). *Turbulent structure in open-channel flows (PhD dissertation)*. Kyoto University.

Nezu, I., & Nakagawa, H. (1993). *Turbulence in open-channel flows* (pp. 281). IAHR Monograph.

Nezu, I., & Rodi, W. (1986). Open-channel flow measurements with a laser Doppler anemometer. *Journal of Hydraulic Engineering*, *112*(5), 335–355. https://doi.org/10.1061/(asce)0733-9429(1986)112:5(335)

Nikora, V., & Roy, A. G. (2012). Secondary flows in rivers: Theoretical framework, recent advances, and current challenges. *Gravel bed rivers: Processes, tools, environments*. (3–22). Wiley Online Library.

Nikora, V., & Smart, G. (1996). A simple model of turbulence intensity and turbulence scale distribution in gravel bed rivers. In *Advances in turbulence VI* (pp. 171–174). Springer. https://doi.org/10.1007/978-94-009-0297-8_47

Nortek, A. S. (2015). *The comprehensive manual [computer software manual]*. Retrieved from http://www.nortek.no/en/support/manuals

Orton, P. M., McGillis, W. R., & Zappa, C. J. (2010). Sea breeze forcing of estuary turbulence and air-water co2 exchange. *Geophysical Research Letters*, *37*(13). https://doi.org/10.1029/2010GL043159

Orton, P. M., Zappa, C. J., & McGillis, W. R. (2010). Tidal and atmospheric influences on near-surface turbulence in an estuary. *Journal of Geophysical Research: Oceans*, *115*(C12). https://doi.org/10.1029/2010JC006312

Ott, M. W. (2002). An improvement in the calculation of ADCP velocities. *Journal of Atmospheric and Oceanic Technology*, *19*(10), 1738–1741. https://doi.org/10.1175/1520-0426(2002)019<1738:aiitco>2.0.co;2

Poff, N. L., Olden, J. D., Merritt, D. M., & Pepin, D. M. (2007). Homogenization of regional river dynamics by dams and global biodiversity implications. *Proceedings of the National Academy of Sciences*, *104*(14), 5732–5737. https://doi.org/10.1073/pnas.0609812104

Pope, S. B. (2000). *Turbulent flows*. Cambridge University Press. https://doi.org/10.1017/CBO9780511840531

Raymond, P. A., Hartmann, J., Lauerwald, R., Sobek, S., McDonald, C., Hoover, M., et al. (2013). Global carbon dioxide emissions from inland waters. *Nature*, *503*(7476), 355–359. https://doi.org/10.1038/nature12760

Raymond, P. A., Zappa, C. J., Butman, D., Bott, T. L., Potter, J., Mulholland, P., et al. (2012). Scaling the gas transfer velocity and hydraulic geometry in streams and small rivers. *Limnology and Oceanography: Fluids and Environments*, *2*(1), 41–53. https://doi.org/10.1215/21573689-1597669

Richey, J. E., Melack, J. M., Aufdenkampe, A. K., Ballester, V. M., & Hess, L. L. (2002). Outgassing from Amazonian rivers and wetlands as a large tropical source of atmospheric CO_2. *Nature*, *416*(6881), 617–620. https://doi.org/10.1038/416617a

Sabrekov, A. F., Runkle, B. R. K., Glagolev, M. V., Terentieva, I. E., Stepanenko, V. M., Kotsyurbenko, O. R., et al. (2017). Variability in methane emissions from west Siberia's shallow boreal lakes on a regional scale and its environmental controls. *Biogeosciences*, *14*(15), 3715–3742. https://doi.org/10.5194/bg-14-3715-2017

Scully, M. E., Geyer, W. R., & Trowbridge, J. H. (2011). The influence of stratification and nonlocal turbulent production on estuarine turbulence: An assessment of turbulence closure with field observations. *Journal of Physical Oceanography*, *41*(1), 166–185. https://doi.org/10.1175/2010JPO4470.1

Stacey, M. T., Monismith, S. G., & Burau, J. R. (1999). Measurements of Reynolds stress profiles in unstratified tidal flow. *Journal of Geophysical Research: Oceans*, *104*(C5), 10933–10949. https://doi.org/10.1029/1998JC900095

Stepanenko, V., Mammarella, I., Ojala, A., Miettinen, H., Lykosov, V., & Vesala, T. (2016). LAKE 2.0: A model for temperature, methane, carbon dioxide and oxygen dynamics in lakes. *Geoscientific Model Development*, *9*(5), 1977–2006. https://doi.org/10.5194/gmd-9-1977-2016

Sukhodolov, A., Thiele, M., & Bungartz, H. (1998). Turbulence structure in a river reach with sand bed. *Water Resources Research*, *34*(5), 1317–1334. https://doi.org/10.1029/98WR00269

Talke, S. A., Horner-Devine, A. R., Chickadel, C. C., & Jessup, A. T. (2013). Turbulent kinetic energy and coherent structures in a tidal river. *Journal of Geophysical Research: Oceans*, *118*(12), 6965–6981. https://doi.org/10.1002/2012JC008103

Tedford, E. W., MacIntyre, S., Miller, S. D., & Czikowsky, M. J. (2014). Similarity scaling of turbulence in a temperate lake during fall cooling. *Journal of Geophysical Research: Oceans*, *119*(8), 4689–4713. https://doi.org/10.1002/2014JC010135

Tennekes, H., & Lumley, J. L. (1972). *A first course in turbulence*. MIT press.

Terray, E., Donelan, M., Agrawal, Y., Drennan, W. M., Kahma, K., Williams, A. J., et al. (1996). Estimates of kinetic energy dissipation under breaking waves. *Journal of Physical Oceanography*, *26*(5), 792–807. https://doi.org/10.1175/1520-0485(1996)026<0792:eokedu>2.0.co;2

Thomson, R. E., & Emery, W. J. (2001). *Data analysis methods in physical oceanography*. Elsevier Science. https://doi.org/10.1016/B978-0-444-50756-3.X5000-X

Tranvik, L. J., Downing, J. A., Cotner, J. B., Loiselle, S. A., Striegl, R. G., Ballatore, T. J., et al. (2009). Lakes and reservoirs as regulators of carbon cycling and climate. *Limnology and Oceanography*, *54*(6part2), 2298–2314. https://doi.org/10.4319/lo.2009.54.6_part_2.2298

Ulseth, A. J., Hall, R. O., Canadell, M. B., Madinger, H. L., Niayifar, A., & Battin, T. J. (2019). Distinct air–water gas exchange regimes in low-and high-energy streams. *Nature Geoscience*, *12*(4), 259–263. https://doi.org/10.1038/s41561-019-0324-8

Wahl, T. L. (2003). Discussion of "Despiking Acoustic Doppler Velocimeter Data" by Derek G. Goring and Vladimir I. Nikora. *Journal of Hydraulic Engineering*, *129*(6), 484–487. https://doi.org/10.1061/(asce)0733-9429(2003)129:6(484)

Wallin, M. B., Campeau, A., Audet, J., Bastviken, D., Bishop, K., Kokic, J., et al. (2018). othersCarbon dioxide and methane emissions of Swedish low-order streams—A national estimate and lessons learnt from more than a decade of observations. *Limnology and Oceanography Letters*, *3*(3), 156–167. https://doi.org/10.1002/lol2.10061

Wang, B., Liao, Q., Fillingham, J. H., & Bootsma, H. A. (2015). On the coefficients of small eddy and surface divergence models for the air-water gas transfer velocity. *Journal of Geophysical Research: Oceans*, *120*(3), 2129–2146. https://doi.org/10.1002/2014JC010253

Wang, B., Liao, Q., Xiao, J., & Bootsma, H. A. (2013). A free-floating PIV system: Measurements of small-scale turbulence under the wind wave surface. *Journal of Atmospheric and Oceanic Technology*, *30*(7), 1494–1510. https://doi.org/10.1175/JTECH-D-12-00092.1

Wüest, A., & Lorke, A. (2003). Small-scale hydrodynamics in lakes. *Annual Review of Fluid Mechanics*, *35*(1), 373–412. https://doi.org/10.1146/annurev.fluid.35.101101.161220

Zappa, C. J., McGillis, W. R., Raymond, P. A., Edson, J. B., Hintsa, E. J., Zemmelink, H. J., et al. (2007). Environmental turbulent mixing controls on air-water gas exchange in marine and aquatic systems. *Geophysical Research Letters*, *34*(10). https://doi.org/10.1029/2006GL028790